Of

Radio-Loud and Radio-Quiet AGN

—

Single Dish Radio Polarimetry

and

X-ray Variability Study of Polar Scattered Seyfert I Galaxies

Masterarbeit aus der Physik
Vorgelegt von

Tobias Beuchert

01.03.2013

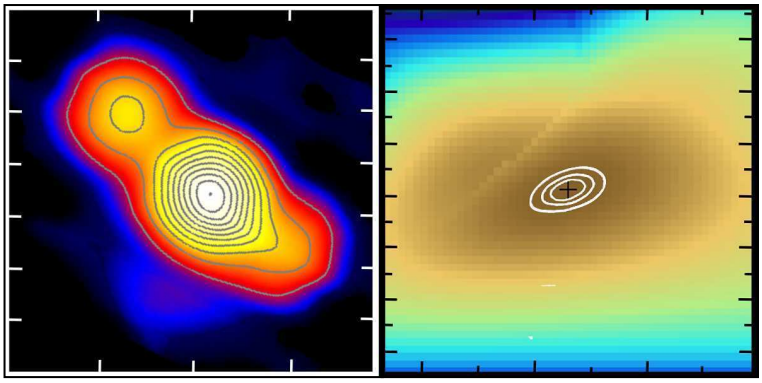

Betreuer:
Prof. Dr. Jörn Wilms (ECAP)
Prof. Dr. Matthias Kadler (Uni Würzburg)

Dr. Karl Remeis-Sternwarte
Astronomisches Institut (ECAP)
Friedrich-Alexander-Universität Erlangen-Nürnberg

ERLANGEN CENTRE
FOR ASTROPARTICLE
PHYSICS

To my

mother, Hermia Szabo-Beuchert†,
and father, Roger Beuchert,

who have been given me the strength and love
for having been able to seek and reach many dreams,
to be able to study one of them
and pass one milestone with the present work.

CONTENTS

Abstract

Polarization is an important tool in astrophysics. But what more information does polarized light harbor compared to the total intensity received by usual instruments? In general, polarization itself reveals much deeper insights into the intrinsic characteristics of astrophysical sources of radiation. It even has some symmetry breaking character. Imagine the Unified Model of Active Galactic Nuclei (AGN) embedded in so called Host Galaxies consisting of the central engine, a Supermassive Black Hole (SMBH), material being accreted from an accretion disc around it, further surrounded by a dusty torus of comparable cold material. Powerful jets are symmetrically launched by such a system perpendicular to the accretion flow and reach kilo-parsec scales until they diminish in the intergalactic medium. These jets are formed and driven by largely extended magnetic fields. As logical and clear this image might appear – there are still more questions as answers. For example, how is the magnetic field distributed starting from the surroundings of the black hole continuing deep into the jet? How does the torus look like exactly? Is it a closed dense structure or more a clumpy composite of separate clouds orbiting the central engine? In this Master thesis methods are presented to follow the tracks to the answers on these exemplary matters of dispute.

One differs two major kinds of such AGN – radio-loud ones where strong jets are present and radio-quiet ones with non detectable jets. Depending on the viewing angle towards those, each can be further classified.

The first part of the thesis deals with a set of **radio-loud AGN**, so called blazars where the system is supposed to be viewed from an angle closely aligned with the jet-axis. I present the more technical part – the calibration of Effelsberg polarimetry data of their radio jets. By now this has only been done for data taken in the time-span of a few days. I drive the demanding techniques of calibration forward to multifrequency and multi-epoch data of the F-GAMMA program taken from 2007 until now where many aspects have to be accounted for. Additionally I focus on the analysis of historical full Stokes polarimetry data of 3C111 combined with VLBI data to gain more insight into the time dependent behavior of polarized emitting regions.

The second part of this work deals with the **radio-quiet AGN**. The sources of interest form a sample of 12 sources selected by optical polarized lines. They show broad lines only in polarized light which are supposed to be polar scattered. Hence one can conclude that the viewing angle should strike through the outer layer of the torus, a structural variable region where gas is assumed to get evaporated due to in-falling radiation from the central source. In turn, also X-ray spectra are expected to be variable. To show this, all archival data is being analyzed and checked for column density variability.
Both methods in this thesis deal with the assumption of validity of the Unified Model and give a unique opportunity to probe the underlying theoretical assumptions.

Chapter 1

Introduction

> *The history of astronomy is a history of receding horizons.*
>
> Edwin P. Hubble,

In the first chapter I want to introduce the basics necessary for the understanding of the subsequent chapters. First of all, an overview over radiation physics is given which is important regarding the study of astrophysical objects of whatsoever kind. In the following part the objects of interest, highly luminous compact extragalactic objects as cores of active galaxies, are described.

1.1. Radiation Processes

For the following chapters it is crucial to understand the basics of radiation physics. Here, I summarize the most important issues. The content of this section is composed of elements from Rybicki & Lightman (2004) and Wilms (2012), notes from various lectures, such as "Astrophysical Radiation Processes" and "Active Galactic Nuclei" from J. Wilms, "Sternatmosphären und Strahlungsphänomäne" from N. Przybilla, both Dr. Remeis Observatory Bamberg & ECAP, "Theoretische Physik - Elektrodynamik" from O. Pankratov, all Univ. Erlangen-Nürnberg, the primary literature from Chandrasekhar (1960) and Mihalas (1978) as well as notes from a school on low frequency radio astronomy held at the National Centre For Radio Astrophysics (NCRA), India in 1999 (`http://gmrt.ncra.tifr.res.in/gmrt_hpage/Users/doc/WEBLF/LFRA/node1.html`).

1.1.1. Synchrotron Radiation

Synchrotron emission is *the* emission mechanism for radio astronomy and is thus derived in more detail here.
Radio emitters such as AGN produce their radiation via charges moving on helical paths along magnetic fields. The only direction a force is acting in is the Lorentz - force, i.e., perpendicular to the magnetic field. Thus the motion parallel to the field is constant which in total translates into helical trajectories with the velocity vector $\mathbf{v}$ separating into $|v_\parallel| = v\cos(\alpha)$ and $|v_\perp| = v\sin(\alpha)$ where α is the pitch angle of the helix. A photon with momentum $p = \gamma m_\mathrm{e} v$ encounters the force $F = \gamma m_\mathrm{e} dv/dt = \gamma m_\mathrm{e} a_\mathrm{ZF}$ which equals the centrifugal force. Equating the Lorentz force with the centrifugal force yields

$$\frac{q}{c}\mathbf{v} \times \mathbf{B} = \gamma m_\mathrm{e} a_\mathrm{ZF}. \tag{1.1}$$

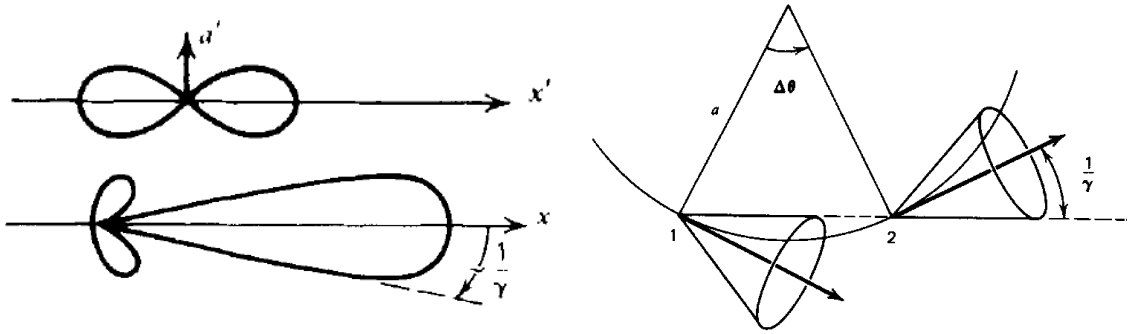

Figure 1.1.: *Top left:* radiation pattern in the frame of rest, bottom left: beamed pattern, *right:* charge on a circular trajectory around a magnetic field (Rybicki & Lightman, 2004).

For a circular motion we are only interested in the components perpendicular to the magnetic field with

$$\frac{q}{c} v_\perp B = \gamma m_\mathrm{e} \frac{v_\perp^2}{R} \tag{1.2}$$

and in a re-written form

$$\frac{v_\perp}{R} = \frac{qB}{\gamma m_\mathrm{e} c} = \frac{\omega_\mathrm{L}}{\gamma} = \omega_\mathrm{B} \tag{1.3}$$

with the gyration frequency ω_B and the Lamour frequency ω_L of an electron performing circular trajectories around the magnetic field.
Electrodynamics shows that the radiated energy of a single charge is (Rybicki & Lightman, 2004)

$$\frac{dE}{dt} = P = \frac{2}{3}\frac{q^2}{c^3}\mathbf{a}^2 \tag{1.4}$$

where $\mathbf{a}$ is the acceleration of the charge. This can be separated into components parallel and perpendicular to the magnetic field written in the charge's frame of rest $a'_\perp = \gamma^2 a_\perp$ and $a'_\parallel = \gamma^3 a_\parallel$. transforming Eq. 1.4 to

$$P = \frac{2}{3}\frac{q^2}{c^3}\gamma^4 (a_\perp^2 + \gamma^2 a_\parallel^2) \tag{1.5}$$

(Kembhavi & Narlikar, 1999). Using the relation $a_\perp = \omega_\mathrm{B} v_\perp = v \sin(\alpha)$ we can convert Eq. 1.5 to

$$P = \frac{2}{3}\frac{q^4 \gamma^2 B^2 v^2}{m_\mathrm{e}^2 c^5} \sin^2(\alpha) = 2\beta^2 \gamma^2 c \sigma_\mathrm{T} U_\mathrm{B} \sin^2(\alpha) \tag{1.6}$$

with $\beta = v/c$, the Thomson cross-section $\sigma_\mathrm{T} = 8\pi e^4 / 3 m_\mathrm{e}^2 c^4$ as derived in Sect. 1.1.2 and the magnetic energy density $U_B = B^2/8\pi$.
Averaging over all pitch angles yields a factor 2/3 in Eq. 1.6.
To derive a spectrum one transforms from the time to the frequency domain (Rybicki & Lightman, 2004). Therefore it is necessary to know the duration of one pulse of radiation per orbit of the charge around the magnetic field (Wilms, 2012). In the rest frame of the charge the radiation pattern follows Eq. 1.6 which is double-lobed perpendicular to the direction of acceleration. In the observer's frame Lorentz transformation yields a forward beamed cone (Wilms, 2012) in radial boost-direction with opening angle $\sim 1/\gamma$ (Fig. 1.1). The observer will thus receive radiation from an angle of $\Delta\theta = 2/\gamma$ in a time interval of $\Delta t = \Delta\theta/\omega_\mathrm{B} = 2/\omega_\mathrm{L}$. With respect to the Doppler effect, the difference in arrival times of radiation from a charge at the positions 1 and 2 (Fig. 1.1, right) is

$$\Delta t^\mathrm{arr} = t_1^\mathrm{arr} - t_2^\mathrm{arr} = \frac{2}{\gamma \omega_\mathrm{B}}(1 - \beta) \tag{1.7}$$

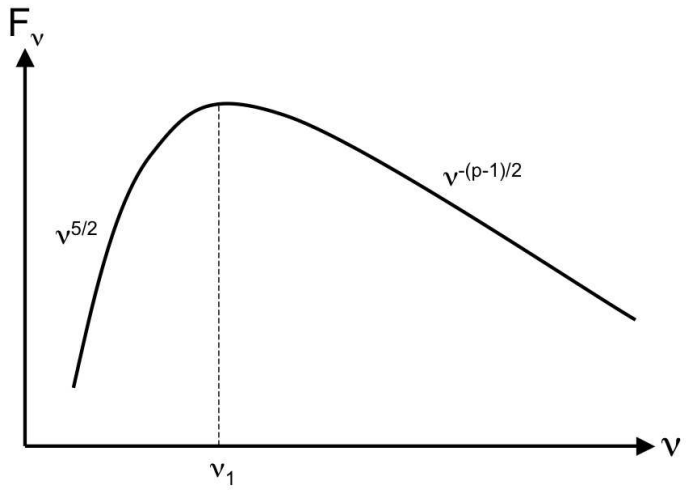

Figure 1.2.: Power-law spectral energy distribution of synchrotron radiation with a turnover to the synchrotron self absorbed regime at ν_1 (Rybicki & Lightman, 2004).

which for the case of relativistic energies $\gamma \gg 1$ turns to $\Delta t^{\mathrm{arr}} = 1/\gamma^3\omega_{\mathrm{B}}$ as the length of a pulse of radiated photons viewed tangentially to the circular track of a charge. Therewith one defines a *critical frequency* $\omega_{\mathrm{c}} \sim \gamma^3\omega_{\mathrm{B}}\sin(\alpha)$.
As shown in detail by Rybicki & Lightman (2004), one basically calculates the Fourier transformation from the time domain to the frequency domain in order to find an expression for a spectrum radiated by one single charge. The result is

$$P(\omega) = \frac{\sqrt{3}}{2\pi}\frac{q^3 B\sin(\alpha)}{m_{\mathrm{e}}c^2}F\left(\frac{\omega}{\omega_{\mathrm{c}}}\right) \tag{1.8}$$

which peaks at the critical frequency ω_{c}. Therefore the emitted frequency of a single particle is constrained via the expression $\delta(\omega - \gamma^3\omega_{\mathrm{B}})$.
In AGN and other synchrotron emitters, whole bunches of electrons are radiating each at the above derived frequency. Assume a power-law particle distribution $N(\gamma) = N_0\gamma^{-p}$ depending on the boost γ. Construct the synchrotron spectrum for a charge distribution as the integral of the radiated intensity for one charge given by Eq. 1.6 constrained at the critical frequency ω_{c} weighted with the particle distribution with the γ-factor as variable of integration

$$P_\nu = \int \frac{4}{3}\beta^2\gamma^2 c\sigma_{\mathrm{T}}U_B\delta(\omega - \omega^3\omega_{\mathrm{B}})N_0\gamma^{-p}d\gamma \tag{1.9}$$

and find (Rybicki & Lightman, 2004)

$$P_\nu = \frac{2}{3}c\sigma_{\mathrm{T}}N_0\frac{U_B}{\omega_{\mathrm{L}}}\left(\frac{\omega}{\omega_{\mathrm{L}}}\right)^{-\frac{p-1}{2}}. \tag{1.10}$$

This is again a power-law (Fig. 1.2) composed of a superposition of single electron spectra peaking at their critical frequencies.

1.1.2. Compton scattering

Compton scattering is closely related to Thomson scattering in the low energy limit of photons. Hence to start with simple elastic Thomson scattering, recall Eq. 1.4 which is the same start-

ing point for the following derivation. Without averaging over all directions of radiation, after Rybicki & Lightman (2004) the lobed emission pattern from Fig. 1.1 is given by

$$\frac{dP}{d\Omega} = \frac{\ddot{\mathbf{d}}^2}{4\pi c^3} \sin^2(\Theta). \tag{1.11}$$

Assume a charge q oscillating with $\ddot{\mathbf{r}} \sim \mathbf{E_0} \sin(\omega_0 t)$.
Define the dipole moment $\mathbf{d} = q\mathbf{r}$. From the ansatz $F = m_\mathrm{e}\ddot{\mathbf{r}} = q\mathbf{E_0} \sin(\omega_0 t)$ it follows that

$$\ddot{\mathbf{d}} = \frac{e^2 \mathbf{E_0}}{m_\mathrm{e}} \sin(\omega_0 t) \tag{1.12}$$

using the average $\langle \sin^2(\omega_0 t) \rangle = 1/2$

$$\frac{dP}{d\Omega} = \frac{e^4 E_0^2}{8\pi m_\mathrm{e}^2 c^3} \sin^2(\Theta) \tag{1.13}$$

or, averaged over all Θ,

$$P = \frac{e^4 E_0^2}{8\pi m_\mathrm{e}^2 c^3}. \tag{1.14}$$

Defining the radiation per angle via the differential cross section

$$\frac{dP}{d\Omega} = \langle S \rangle \left. \frac{d\sigma}{d\Omega} \right|_\mathrm{pol} \tag{1.15}$$

with $\langle S \rangle = cE_0^2/8\pi$ and

$$\left. \frac{d\sigma}{d\Omega} \right|_\mathrm{pol} = \frac{e^4}{m_\mathrm{e}^2 c^4} \sin^2(\Theta) = r_0^2 \sin^2(\Theta) \tag{1.16}$$

with r_0 as the *classical electron radius*.
The above differential cross-section only represents incident linear polarized waves. For unpolarized radiation, Rybicki & Lightman (2004) superpose two cross-sections of incident linear polarized waves with perpendicular pointing vectors to find

$$\left. \frac{d\sigma}{d\Omega} \right|_\mathrm{unpol} = \frac{1}{2} r_0^2 (1 + \sin^2(\Theta)). \tag{1.17}$$

Until now we treated the special case of Thomson scattering that is fully elastic meaning that the energy of the incident wave ϵ equals the one of the scattered wave ϵ_1.
Now additionally consider quantum effects that allow the photon to have a momentum itself which causes a recoil of the electron and thus energy loss for the scattering photon. Using the basic relations of Compton scattering

$$\lambda' - \lambda = \frac{h}{m_\mathrm{e} c} (1 - \cos\theta) \tag{1.18}$$

and

$$\epsilon_1 = \frac{\epsilon}{1 + \frac{\epsilon}{m_\mathrm{e} c^2} (1 - \cos\theta)}. \tag{1.19}$$

Quantum electrodynamics yield the more generic *Klein-Nishina* cross-section asymptotically turning into the *Thomson* cross-section for soft photons with $\lambda \gg \lambda_\mathrm{C}$ (Wilms, 2012)

$$\frac{d\sigma}{d\Omega} = \frac{3}{16\pi} \sigma_T \left(\frac{\epsilon_1}{\epsilon} \right)^2 \left(\frac{\epsilon}{\epsilon_1} + \frac{\epsilon_1}{\epsilon} - (\sin^2\theta) \right) \tag{1.20}$$

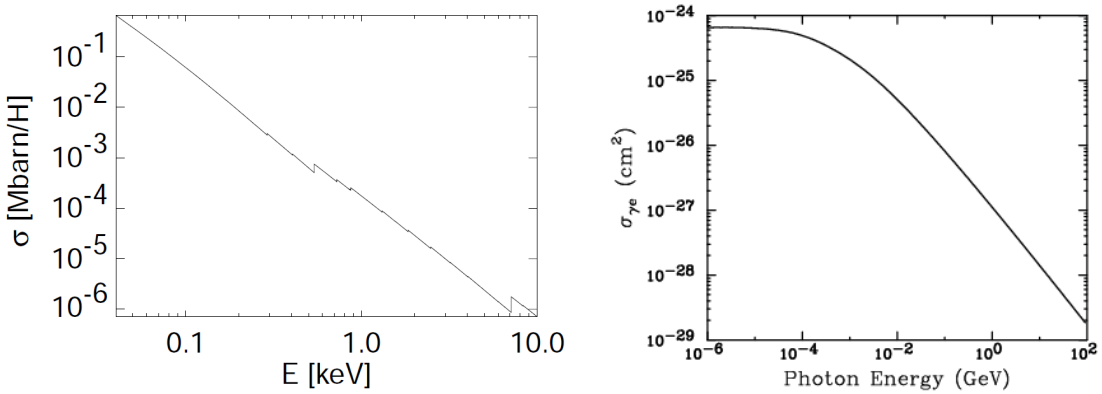

Figure 1.3.: Cross-sections for photoelectric absorption (*left*), from Wilms et al. (2000), and Compton scattering (*right*), from Belikov & Hooper (2009).

The integrated cross section is shown in the right panel of Fig. 1.3 together with the cross-section for photoelectric absorption in the interstellar gas as it is of importance for X-ray astronomy. The Klein-Nishina cross-section drops for higher photon energies, where the photon energy is sufficiently high to transfer energy to the electron. After some unit conversions (1 barn$= 10^{-24}\,\mathrm{cm}^2$) the plots tell that both cross-sections are equal at around 10 keV.
Inverse Compton scattering is a very efficient way of transferring energy for **relativistic electrons**. Assuming small photon energies, the Thomson cross-section is for the interaction with the electron and photon in the electron's frame of rest. As we now treat a highly relativistic electron gas, we have to transform from the observers frame with high energetic electrons into the rest frame where the scattering occurs. In this electron's rest frame the photon energy stays constant. After transforming back into the laboratory system, the photons' energies are amplified by a factor of γ^2 (Rybicki & Lightman, 2004):

$$\epsilon_{\mathrm{Lab}}^{\mathrm{scattered}} \sim \gamma^2 \epsilon_{\mathrm{Lab}} \tag{1.21}$$

For the case of isotropic distributions of electrons and a low energetic photon field scattering off those one has to find an average expression of the above relations. After some calculations one finds for the energy gain of the photon field due to single scattering off a whole field

$$I = \frac{d\epsilon}{dt} = \frac{4}{3}\sigma_{\mathrm{T}} c \gamma^2 U_{\mathrm{rad}} \tag{1.22}$$

with the energy density of the external photon field U_{rad}.
Until now we assumed the electrons to be highly relativistic. The photons scattering off those always gain large amounts of energy. In contrast, there is also the case of low energetic electrons which are Maxwell-distributed. Now, the γ-factor in Eq. 1.21 is nearly unity and the argument for or against amplification of the photon field is solely located in the energy of the electrons in the frame of rest. We still assume the Thomson limit to hold with no (or if so) very little relative energy transfers of $\Delta\epsilon/\epsilon = -\epsilon/m_{\mathrm{e}}c^2$ in the frame of rest. Additionally assuming Maxwell distributed electron energies we find an **amplification factor** (Wilms, 2012)

$$A = \frac{\Delta\epsilon}{\epsilon} = \frac{4kT_e - \epsilon}{m_{\mathrm{e}}c^2} \tag{1.23}$$

where A is the energy gain and T_{e} the electron plasma temperature.
Photons can either loose or gain energy in the case of non-relativistic electrons. Eq. 1.23 tells us whether the photons are getting *up-scattered* or *down-scattered* by an isotropic electron distribution or vice versa: if $E \lesssim 4kT_{\mathrm{e}}$ (**inverse Compton scattering**), energy will be transferred from

electrons to photons, and the electron-gas cools down.
In the opposite case (**Compton scattering**) with $E \gtrsim 4kT_\mathrm{e}$, energy is transferred from photons to electrons. The electron-gas heats up.
By now, only one electron is treated. We can further assume highly relativistic electrons in the hot corona of AGNs and thus the case of highly effective **inverse** Compton scattering. For multiple up-scattering, the final energy is $E_\mathrm{end} = E_\mathrm{init} A^k$ after k scattering events. The resulting photon rate at the energy E_k will in turn be $N(E_\mathrm{end}) \sim N(E_\mathrm{initial})(1+A)^k \sim N(E_\mathrm{initial})\,(E_\mathrm{end}/E_\mathrm{initial})^{-\alpha}$, which corresponds to a power-law.
Finally there is a direct link between Synchrotron radiation and (inverse-) Compton scattering (Krolik, 1999). Combining Eq. 1.6 and Eq. 1.22 gives

$$\frac{P_\mathrm{Compt}}{P_\mathrm{Synch}} = \frac{U_\mathrm{rad}}{U_\mathrm{mag}}. \tag{1.24}$$

The ratio of the Synchrotron and invers Compton luminosities are thus equal to the ratio of the energy densities of radiation field and magnetic field. This is a manifestation of the fact that in quantum electrodynamics Synchrotron radiation is just the same as inverse Compton scattering off virtual photons.

1.1.3. Radiative transport

After having treated individual radiation mechanisms it is now high time to study how such produced radiation is transported to us as observers. Standard literature besides Rybicki & Lightman (2004) mainly used in this section is by Mihalas (1978) and Chandrasekhar (1960). Radiation and thus intensity can either be *emitted* into a volume or *absorbed/scattered* by/off a certain volume. The radiated intensity is defined as the energy $\mathrm{d}E$ emitted per area $\mathrm{d}A$, in a time interval $\mathrm{d}t$, in a solid angle $\mathrm{d}\Omega$ and a frequency range $\mathrm{d}\nu$ (Chandrasekhar, 1960)

$$I = \frac{\mathrm{d}E}{\mathrm{d}A\mathrm{d}t\mathrm{d}\Omega\mathrm{d}\nu}. \tag{1.25}$$

Note that there is a fundamental difference between **spectral brightness** defined as

$$B_\nu = \frac{\mathrm{d}E}{\mathrm{d}A\mathrm{d}t\mathrm{d}\Omega\mathrm{d}\nu} \tag{1.26}$$

which is *independent of distance* due to the conservation theorem and the normalization with the solid angle $\mathrm{d}\Omega$. The **specific flux density** on the other hand is defined as

$$S_\nu = \frac{\mathrm{d}E}{\mathrm{d}A\mathrm{d}t\mathrm{d}\nu} \tag{1.27}$$

which is indeed dependent on the distance. Thus in many cases one might want to use rather the term "fluxiest source" than "brightest source" to express that a source at least *appears* to be brighter in the observer's frame. Two sources of the same intensity will have equal brightness and at all distances but different flux densities at different distances to the appropriate source. The **spectral luminosity** L_ν is defined as the energy radiated per units of time and frequency

$$L_\nu = 4\pi d^2 S_\nu \tag{1.28}$$

with d the distance to the source.
Concerning cosmology the **luminosity distance** (Wilms, 2011)

$$d_\mathrm{L} = R_0 r(1+z) \tag{1.29}$$

has to be taken into account with the current scale factor R_0, co-moving distance r and redshift z. This is because the scale factor equals $1/(1+z)$. For a flat, expanding universe the time dependent Hubble parameter $H(t) = R/R_0$ has to be expressed with the cosmological constants for matter, radiation and the dark energy and included into the luminosity distance. Thus it is possible to derive the luminosity distance just by knowing Hubble parameter and redshift. The used analysis software `ISIS` calculates the luminosity distance with the function `flux2lum`. The applied cosmological parameters are approximated to $\Omega_\mathrm{m} = 0.3$, $\Omega_\Lambda = 0.7$ and $\Omega_\mathrm{k} = 0$ for a flat universe. For more precise values see for example the recent publication of Sievers et al. (2013) analyzing the cosmic microwave background's power spectrum with the Atacama Cosmology Telescope and the Wilkinson Microwave Anisotropy Probe *WMAP*. The latest measurement of the Hubble parameter with Spitzer and the Hubble Space Telescope HST (Freedman et al., 2012) constrains a value of $74.3\,\mathrm{km\,s^{-1}Mpc^{-1}}$ excluding the by then assumed value of $\approx 70\,\mathrm{km\,s^{-1}Mpc^{-1}}$ within the errors. Furthermore the general equation of *radiative transfer* (Chandrasekhar, 1960) is given by

$$\frac{\mathrm{d}I}{\mathrm{d}s} = -\alpha_\nu I_\nu + j_\nu \tag{1.30}$$

with the specific *emission coefficient* j_ν and *absorption coefficient* $\alpha_\nu = n\sigma_\nu$ where n is the number density of absorbing material and σ_ν the cross-section of the appropriate mechanism of absorption or scattering. They represent the fractions of energy being emitted or absorbed, respectively.
The solution for absorption only can be derived by neglecting j_ν and integrating Eq. 1.30

$$I_\nu(s) = I_\nu(s_0) e^{-\int_{s_1}^{s_2} \alpha_\nu(s')\mathrm{d}s'} \tag{1.31}$$

with the *optical depth*

$$\tau_\nu = \int_{s_1}^{s_2} \alpha_\nu(s') ds'. \tag{1.32}$$

Now one can also define the *mean free path* of photons as $l_\nu = 1/\alpha_\nu = 1/n\sigma_\nu$.
In terms of X-ray astronomy the two most interesting mechanisms of attenuating source-intensity are *photoelectric absorption* and *Compton scattering* (see Sect. 1.1.2). For the interstellar medium cross-sections can be calculated for both processes. The basic equation one should have in mind while talking about the composits of X-ray spectra in terms of absorption and scattering is

$$I_\mathrm{obs} \sim e^{-\sigma N_\mathrm{H}} I_\mathrm{source} \tag{1.33}$$

with either the photoelectric or Klein-Nishina cross-sections σ_ph or σ_KN.

1.1.4. Polarization

It is additionally important to understand the physics of polarization in order to use this technique to examine astronomical sources in greater detail. This section begins with an introduction to polarized light in general with focus on the Stokes formalism.

1.1.4.1. Stokes Parameters

First, I discuss monochromatic plane waves. This is an oversimplified scenario regarding astrophysics, but important to understand the physics behind.
Monochromatic plane waves are linearly and 100 % polarized. Single photons resemble such waves. As illustrated in Fig. 1.4, every single planar wave can be expressed as superposition of two orthogonal waves – here in the linear (x, y) – basis. In particular, one can write the net-electric vector in

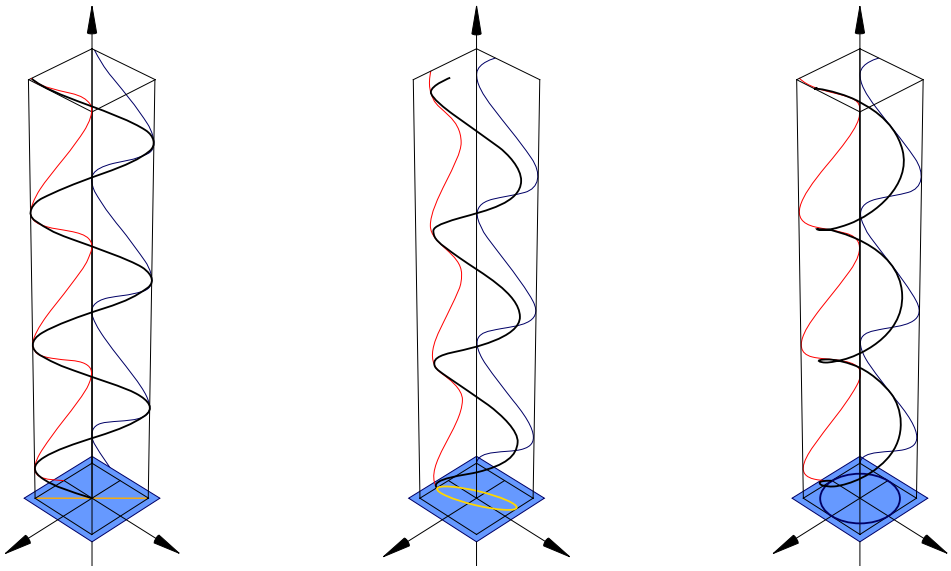

Figure 1.4.: Illustration of linear (*left*), elliptical (*middle*) and circular polarization (*right*).

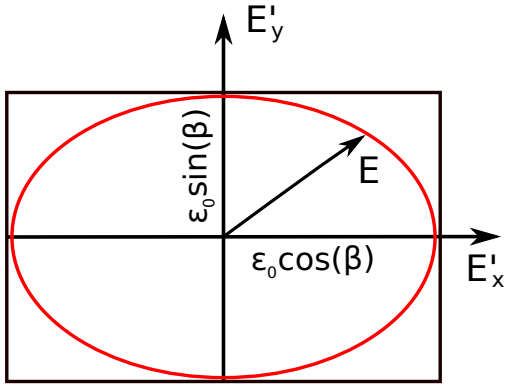

Figure 1.5.: Projection of an elliptical polarized wave in the E_x/E_y plane.

the projected plane of E_x and E_y, marked in blue in Fig. 1.4 as

$$\mathbf{E} = (\mathbf{e}_x \mathcal{E}_x e^{i\phi_x} + \mathbf{e}_y \mathcal{E}_y e^{i\phi_y}) e^{-i\omega t} = \mathbf{E}_0 e^{-i\omega t}. \tag{1.34}$$

To describe, how the electric vector behaves with respect to time, take the real parts of Eq. 1.34:

$$\mathbf{E} = (\mathbf{e}_x E_x + \mathbf{e}_y E_y) = (\mathbf{e}_x \mathcal{E}_x \cos(\phi_x - \omega t) + (\mathbf{e}_y \mathcal{E}_y \cos(\phi_y - \omega t)) \tag{1.35}$$

For **monochromatic waves**, coherence, i.e., constant phase shifts with time, allows for the two orthogonal waves to form either linear (both waves in phase or delayed by multiples of $\pi/2$), circular (phase difference $\pm\pi/4$) or as intermediate state, elliptical polarized photons for a phase difference in between both cases. Depending on the actual phase difference, the ellipse as generalization of all possible polarization states drawn by the electric vector E is tilted by an angle χ called the **e**lectric **v**ector **p**olarization **a**ngle (EVPA) towards the E_x/E_y - coordinate system. In the system of the tilted ellipse shown in Fig. 1.5, one can write Eq. 1.35 to

$$\mathbf{E} = (\mathbf{e}_x E'_x + \mathbf{e}_y E'_y) = \Big(\mathbf{e}_x \mathcal{E}'_x \cos(\beta)\cos(\omega t) - (\mathbf{e}_y \mathcal{E}'_y \sin(\beta)\sin(\omega t)\Big) \tag{1.36}$$

where the main axes of the ellipse are expressed via the phase differences described above, here called β. For the case of $\beta = 0$ or $\beta = \pi/2$, the ellipse collapses to a line, for $\beta = \pi/4$ it is a circle,

drawn by the electric vector with elapsing time. Hence, linear polarization can be treated as just an extreme case of elliptical polarization. The sign of β tells the handness of the polarization, i.e., in which sense the electric vector performs the ellipse.
One can now take Eq. 1.36 and rotate it with the EVPA χ from the coordinate system of the ellipse back into the E_x/E_y - coordinate system. The **Stokes parameters** are equations transforming between the tilted coordinate system described by the set of variables (ϕ_x, ϕ_y, $\mathcal{E}_x$, $\mathcal{E}_y$) and the system of the ellipse itself described by ($\mathcal{E}_0$, β, χ).
Realistically spoken, it is more adequate to assume incoming radiation, where phases and amplitudes of the two orthogonal waves are variable in time, i.e., $\mathcal{E}_x, \mathcal{E}_y, \phi_x(t)$ and $\phi_y(t)$. This leads to the generic case of **quasi-monochromatic** waves, that can be treated as monochromatic only on very short time scales. Therefore it is necessary to time average the electric vectors of the two orthogonal modes forming the propagating wave and contributing to the Stokes parameters. The following expressions for the Stokes parameters in a linear base are combined from Chandrasekhar (1960), Rybicki & Lightman (2004) and `http://gmrt.ncra.tifr.res.in/gmrt_hpage/Users/doc/WEBLF/LFRA/node133.html`:

$$\begin{aligned} I &= \langle E_x E_x^* \rangle + \langle E_y E_y^* \rangle = \langle \mathcal{E}_x^2 \rangle + \langle \mathcal{E}_y^2 \rangle \\ Q &= \langle E_x E_x^* \rangle - \langle E_y E_y^* \rangle = \langle \mathcal{E}_x^2 \rangle - \langle \mathcal{E}_y^2 \rangle \\ U &= \langle E_x E_y^* \rangle + \langle E_y E_x^* \rangle = 2\langle \mathcal{E}_x \rangle \langle \mathcal{E}_y \rangle \cos(\phi_x - \phi_y) \\ V &= \frac{1}{i}(\langle E_x E_y^* \rangle - \langle E_y E_x^* \rangle) = 2\langle \mathcal{E}_x \rangle \langle \mathcal{E}_y \rangle \sin(\phi_x - \phi_y) \end{aligned} \tag{1.37}$$

Most radio receivers measure the polarized radiation via the two orthogonal components E_l and E_r according to the left- and right handed circular polarized components of the electric vector instead. Hence it is important to transform Eq. 1.37 from the linear basis E_x/E_y into the circular basis E_l/E_r:

$$\begin{aligned} I &= \langle E_l E_l^* \rangle + \langle E_r E_r^* \rangle = \langle \mathcal{E}_l^2 \rangle + \langle \mathcal{E}_r^2 \rangle \\ Q &= \langle E_r E_l^* \rangle + \langle E_r^* E_l \rangle = 2\langle \mathcal{E}_r \rangle \langle \mathcal{E}_l \rangle \cos(\phi_l - \phi_r) \\ U &= \frac{1}{i}(\langle E_r E_l^* \rangle + \langle E_r^* E_l \rangle) = 2\langle \mathcal{E}_r \rangle \langle \mathcal{E}_l \rangle \sin(\phi_l - \phi_r) \\ V &= \langle E_r E_r^* \rangle - \langle E_l E_l^* \rangle = \langle \mathcal{E}_l^2 \rangle - \langle \mathcal{E}_r^2 \rangle \end{aligned} \tag{1.38}$$

The brackets denote a time averaging function (Burke & Graham-Smith, 2009) in the generic form

$$\langle E_l E_r^* \rangle = \frac{1}{T} \int_0^T E_l(t) E_r^*(t) dt. \tag{1.39}$$

As described in more detail in Sect. 2.2, radio receiver measure the power by evaluating the Fourier transform of the auto-correlation function of one signal and also cross-signals needed for Q and U. The related theorem is the Wiener-Khinchin theorem.
Having found the Stokes parameters, one can make helpful statements quantifying the received polarized signal with the degree of polarization P and the EVPA χ (Chandrasekhar, 1960) defined as

$$P = \frac{I_{\mathrm{pol}}}{I} = \frac{\sqrt{Q^2 + U^2 + V^2}}{I} \quad \text{and} \quad \chi = \frac{1}{2} \arctan\left(\frac{U}{Q}\right). \tag{1.40}$$

For **monochromatic** radiation, the degree of polarization is always 100 %. E_x and E_y trace out full ellipses or circles. Using Eq. 1.38, one can show with the Cauchy-Schwarz inequality that in general

$$I^2 \geq Q^2 + U^2 + V^2 \tag{1.41}$$

holds. In case of full polarization the square of Stokes I equals the sum of the squares of the remaining Stokes parameters Q, U, V. For **quasi-monochromatic** waves, the degree of polarization

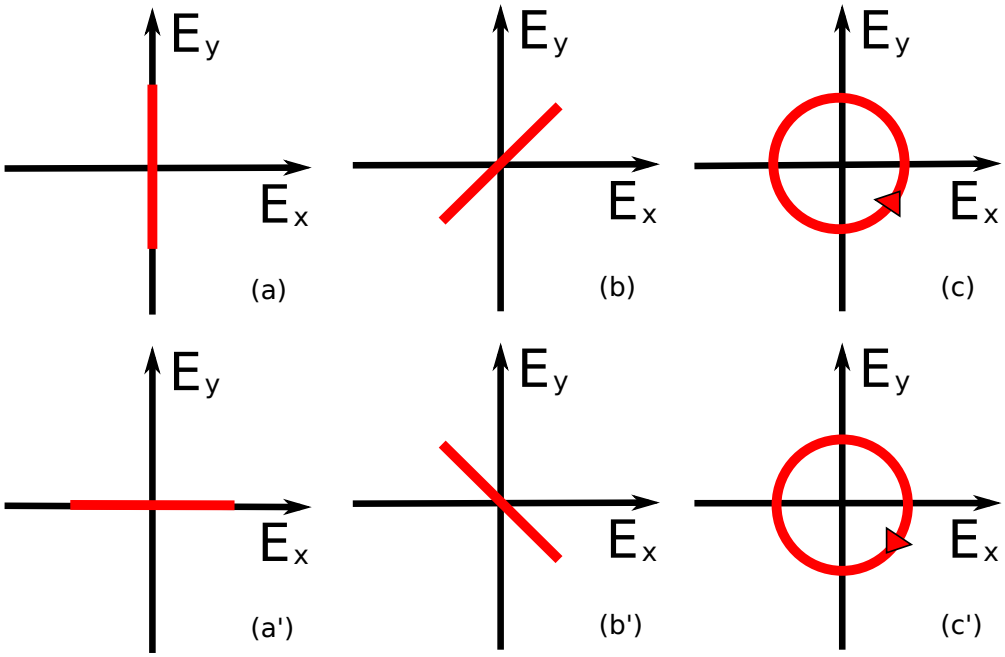

Figure 1.6.: Selected Stokes vectors in the E_x/E_y plane. Panels *(a)* and *(a')* correspond to the resp. vectors (1,1,0,0) and (1,-1,0,0), *(b)* and *(b')* to (1,0,1,0) and (1,0,-1,0) and finally *(c)* and *(c')* to (1,0,0,-1) and (1,0,0,0).

must be smaller than 100 %. Polarized radiation is usually described via the four-vector (I, Q, U, V). Figure 1.6 shows a selection of Stokes vectors. Linear polarization can be fully described with the parameters Q and U.

1.2. The Unified Model

Having revealed basics of radiative processes necessary to deal with high-luminous compact extra-galactic objects, the latter are going to be introduced in the following. The **U**nified **M**odel (UM) of **A**ctive **G**alactic **N**uclei (AGN) as suggested by Antonucci (1993) offers an explanation for a wide field of phenomena connected with such sources.
AGN are thus the core of a so called host galaxy which can be brighter than the whole galaxy itself. Reason for that is an active core with a Supermassive Black Hole (SMBH) and matter being accreted over a disc further surrounded by a torus-shaped structure of relatively cold gas and dust. **Radio-loud AGN** (Sect. 1.3) distinguish themselves from **radio-quiet AGN** (Sect. 1.4) by a jet accelerating charges up to highly relativistic speeds (Sect. 1.3.1). The basic statement that the Unified Model makes is that different sub-classes of those AGN represent the same underlying object just viewed under a different inclination angle (Fig. 1.7).
Thus, radio-quiet objects are further divided into the Seyfert sub-classes **Sy I** and **Sy II** galaxies named after Carl Seyfert (Seyfert, 1943) who stated two classes of spiral galaxies depending on their optical lines. Broad lines are typical for Sy Is, where narrow lines mostly occur in Sy II galaxies. This is because Sy IIs are supposed to appear under a line of sight intercepting the torus while a galaxy is classified as Sy I if there is an unobscured line of sight directly to the nuclear, inner region revealing hot matter spiraling around the central SMBH with large velocities. This also explains the width of optical lines emerging from those regions. The X-ray classification refers to the amount of obscuration of the soft X-ray energy band. After the primary literature of Beckmann & Shrader (2012) and Kembhavi & Narlikar (1999) objects with measured column densities of larger than $10^{22}\,\mathrm{cm}^{-2}$ are said to be Sy II types.

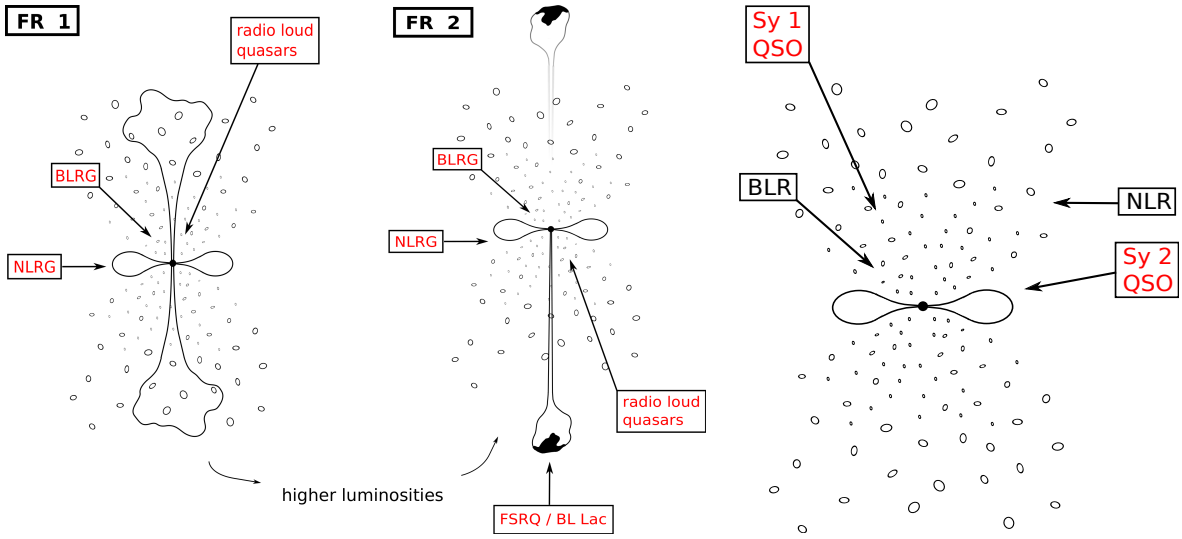

Figure 1.7.: Sketches and sub-classification of radio-loud (*left* and *center*) and radio-quiet (*right*) AGN.

Radio-loud AGN are also sub-classified depending on the inclination angle of the line of sight towards the main symmetry axis of the system, aligned with a highly relativistic jet (Kembhavi & Narlikar, 1999). However, first focusing on the morphology of the radio jets, one can distinguish two major classes, the Fanaroff-Riley classes **FR I** and **FR II** after Fanaroff & Riley (1974). FR I sources are in general less luminous. Their brightest region is the core with asymmetric uncollimated jets of extended emission. In FR II radio galaxies not the core but so called radio-lobes with bright hot-spots, fed by highly collimated spine-like jets, dominate the radio luminosity. If the source is appearing under a steep inclination angle, only one side of the jet approaching the observer is visible due to *relativistic beaming*. See (Beuchert, 2010) for analytical calculations.
Both FR I and FR II morphology-types can appear as **Narrow/Broad Line Radio Galaxies (NLRG/BLRG)** again depending of the inclination angle of the line of sight with respect to the main symmetry axis. Similar to Sy II galaxies, NLRG show narrow optical lines but additionally a strong radio dominance in the multi-wavelength spectrum. The smaller the angle between line of sight and jet, the stronger the radio luminosity. For such a steep angle, the term "radio galaxy" is replaced by "radio-loud quasar". Is the line of sight totally aligned with the jet axis, the source appears point-like and is classified as **blazar** or **BL Lac** named after the prototypical blazar BL Lacertae. Sources with only marginal jet-contribution viewed under some inclination angle are called **quasi-stellar objects (QSO)** or **quasars**.

1.3. Radio-loud AGN

This section is dedicated to the strong radio emitters of AGN. The main sources of non thermal radio emission are jets that are introduced in more detail in the following.

1.3.1. Radio-loud jets and Polarization

Jets are powerful collimated streams of matter being accelerated to relativistic speeds and launched near the Supermassive Black Hole into the symmetry axis of AGN. Jets are also seen in galactic sources (Meier, 2003) such as X-ray binaries (micro-quasars) or protostellar discs and must be considered for a generic jet model. Although micro-quasars are much closer to Earth and such easier to study, there are still many unsolved problems. Meier (2003) and Meier et al. (2001) for

example claim that X-ray binaries shall host disc driven jets, whereas AGN-jets seem to be black hole driven. This is, however, not yet proven. Some other questions are:
How are jets launched magnetohydrodynamically? How can magnetic fields collimate an accretion disc inflow and eject it to kilo-parsec scales?
Jets are besides disks very important candidates to carry away angular momentum in several systems. The angular momentum grows with the inverse of the moment of inertia.
For a complete review on the early work on extragalactic radio sources and particularly jets see Begelman et al. (1984).
Blandford & Konigl (1979) present an analytical calculation of the radio emission of a steady state jet hosted by an AGN. VLBI observations, however, rather suggest a variable configuration with moving "blobs". In their publications they also suggest the occurrence of moving clouds being accelerated by the overall jet flow and expand adiabatically on their way downstream of the jet.
Marscher & Gear (1985) followed up the idea of moving shocks. Here power-law energy distributions of electrons are fed into the jet and get accelerated to relativistic speeds. Within the frame of a moving shock electrons are also accelerated following the front and thus loose energy via synchrotron radiation while moving on helical paths around the collimating jet-magnetic field (Sect. 1.1.1).
One single shock will then emit a power-law synchrotron spectrum with a turnover frequency where the spectrum becomes opaque towards synchrotron self absorption. This frequency depends on the confining magnetic field. Assuming some turbulent magnetic field in the jet with equal parts of field components parallel as well as perpendicular to the jet axis $B_\perp \approx B_\parallel$, Marscher & Gear (1985) state two boundary conditions. Either a field lying fully aligned or perpendicular with the jet axis which results in the field to decay with $B \sim R^{-a}$ with R along the jet axis and $a = 1$ for $B = B_\perp$ or $a = 2$ for $B = B_\parallel$. Locally at the position of the shock that is compressing the turbulent magnetic field to some fraction of $B_\perp$, the case of $B \sim R^{-1}$ is realistic (Marscher, 1996, 2006). Using this assumption they find that the turnover frequency of a shock moving in a magnetic field getting weaker with R^{-1} also drops with $\approx R^{-1}$.
For the emitting radio spectrum of an overall jet this leads to a superposition of individual synchrotron spectra from several shock regions at different distances to the central engine, the SMBH, and thus a flat radio spectrum that is **steepening** if the shocked agglomeration of electrons is expanding adiabatically. The turnover frequency will now drop not only because of the decay of the embedding magnetic field but also because of the decaying opacity due to less synchrotron self absorption (Valtaoja et al., 1992). At the same time the emitted intensity drops. Although the whole model jet is adiabatic at each time, this decay stage is said to be dominated by adiabatic looses. That only means that the shock looses energy while diminishing, leading to less ordered magnetic fields and thus to less importance of synchrotron emission. While expanding adiabatically, shocks also loose density. Due to Synchrotron self absorption of Synchrotron produced photons at the electron gas (Fig. 1.2), only photons with highest frequencies can emerge electron clouds of highest density. Therefore one defines the so called $\tau = 1$ border of regions visible at a certain observing wavelength. The larger the frequency, the closer one can look towards the actual launching point of the jet – the most dense region. As one newly shocked jet-component evolves, the according flare is thus moving through the frequency space. Figure 1.8 (left panel) shows that behavior for a historic flare of 3C 111 around 1997 (Kadler et al., 2008). The appropriate spectral power-law index in the right panel is steepening with time. What is remarkable for 3C111 is that the overall flux levels of the different light curves do show a gradient with frequency at almost every time. In other words, the overall spectral index is scattering around a value of < -0.5 except of the time where the new component is ejected and the flare rises to its maximum. Here the spectrum is getting temporarily flat.
Having discussed the overall jet phenomenon, let us move towards the launching region. The part of the jet closest to the central engine being visible on high resolution VLBI images is called the

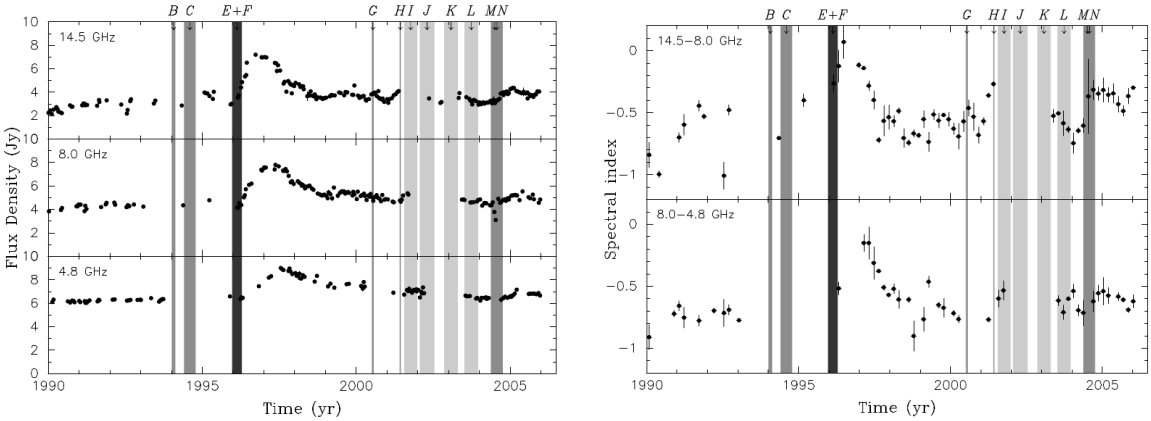

(a) Light curves provided by the University of Michigan Radio Astronomy Observatory for the three different frequencies 4.8 GHz, 8 GHz and 14.5 GHz.

(b) Development of the spectral power-law index with time.

Figure 1.8.: Light curves and Spectral index curve adapted from Kadler et al. (2008) where shaded regions correspond to evolving structures seen in radio interferometry maps.

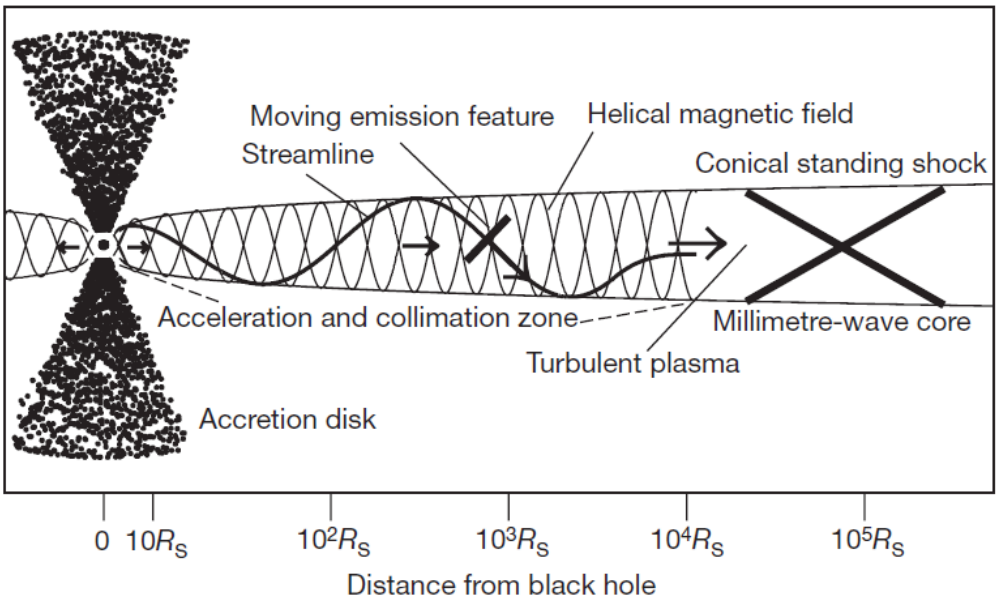

Figure 1.9.: Inner Jet model proposed by Marscher et al. (2008).

"radio core" of the jet. This is the region that is most dense but still optically thin at the observing frequency regarding synchrotron self absorption. Thus while rising the frequency at which VLBI maps are measured, the visible jet core will move towards the actual central launching point (e.g. Müller et al., 2011). Doeleman et al. (2012) even claim to reach the actual launching point of the jet of M87 using mm-VLBI at 1.3 mm.

Normally this innermost region stays obscured to radio observers but is getting observable at even higher frequencies from IR over optical bands to the UV. Marscher (1996) explicitly state an acceleration- and collimation-zone (Fig. 1.9) that is a region beyond the radio jet where an ordered helical magnetic field is proposed. The shocking region presumably consists of e^+e^- - pairs created via pair creation out of photons entering the jet nozzle in combination with the surrounding magnetic field (McKinney, 2005). The surrounding helical field is a natural configuration suggested

by theoretical MHD-calculations such as by Blandford & Znajek (1977) and Blandford & Payne (1982). However as Homan (2005) state, many different three-dimensional magnetic field configurations can produce the same two-dimensional polarization pattern such as a field composed of toroidal and polodial elements. I will further require helical fields to be the magnetic field pattern at least in inner jets. Following Vlahakis (2006) a distribution of plasma also follows helical paths within the constraining helical magnetic field but with a wider pitch angle as illustrated in Fig. 1.9. On this path the whole electron-positron distribution is most probably accelerated due to magnetic driving (Vlahakis & Königl, 2004) caused by a magnetic pressure-gradient within the jet. This acceleration mechanism is much more efficient on larger jet scales compared to centrifugally driven non relativistic jets or even thermal driving. At the distance of $\approx 10^4\,\mathrm{R_S}$ from the SMBH the shocked blob is supposed to enter some standing shock and even further upstream to develop a moving shock itself compressing a chaotic magnetic field as the authors state.
This model is very good to explain the comparatively large degree of polarization at outer expanded regions of the jet, where the magnetic field is getting locally aligned perpendicular to the jet axis due to compression. The integrated degree of polarization often exceeds 30 % here and drops to $< 10\,\%$ towards the nucleus (Saikia & Salter, 1988; Hogbom & Carlsson, 1974). Integrating over a larger region covered with helical magnetic field lines near the nucleus suppresses the overall degree of polarization. It has to be noted that the outer borders of helical fields show a larger fraction of field lines being aligned parallel to the jet axis. Thus jets with helical fields appear more polarized at the edges (Saikia & Salter, 1988). Marscher et al. (2008) also support this idea due to the detection of two distinct flares for BL Lac first appearing in the Optical, X-rays and Gamma wavelength most probably due to a new component of plasma being injected into the inner acceleration- and collimation-zone. As the authors claim, the second flare occurs while the component encounters the standing shock and forms a moving shock beyond the radio core. Additionally a swing of the optical polarization angle as also seen, i.e., for 3C 454.3 (Jorstad et al., 2010) can explain the propagation of plasma through the external helical field. Lyutikov et al. (2005) give the necessary theoretical background. They show that a hypothetical rotationally symmetric jet with embedded helical field produces a net linear polarization being oriented either perpendicular or parallel to the jet axis while electron charges are performing helical paths around the helical wounded magnetic field lines. In the model of Vlahakis (2006) the shocked plasma is itself following a helical path within the magnetic field-cone. Thus it is possible to reach intermediate EVPA orientations between the two extreme parallel or perpendicular cases. A possible observational verification can be the smoothness of EVPA rotations detected, e.g., by Marscher et al. (2008) that can not be explained by random walks of the EVPA in a turbulent field.
The study of evolution of *polarization* in general can thus trace many open questions and uncertainties in these assumptions.

1.4. Radio-quiet AGN

In opposite to radio-loud AGN, radio-quiet AGN have no, or at least no jet that would be worth to be studied in the radio. They emit both thermal and non-thermal radiation, where the latter is high-energy (X-ray to Gamma) radiation due to invers Compton up-scattering of softer photons. X-ray spectroscopy turns out to be a useful tool to get access to many physical properties of such kind of sources.

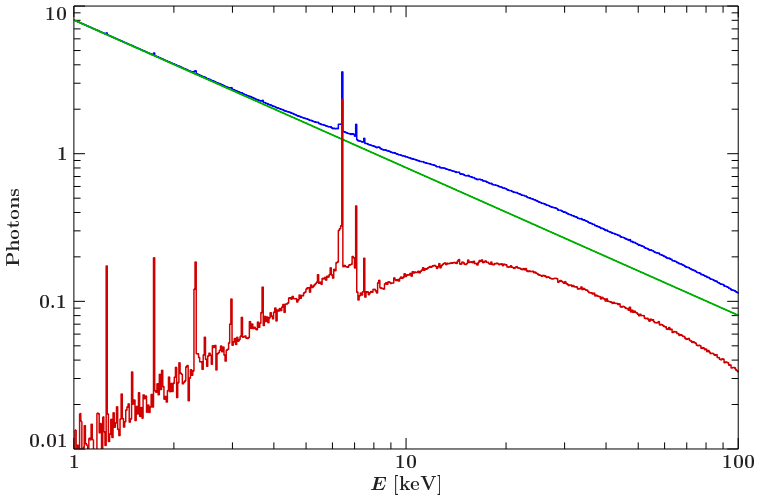

Figure 1.10.: Reflected and composite (reflected plus direct) spectra for a flat, optically thick, circular slab isotropically illuminated by primary X-rays located at some height above the center. The here shown reflection spectra are corresponding to a mean inclination angle of $\cos(i) = 0.5$ and a photon index of 2 (W. Eikmann, priv. comm.).

1.4.1. Multi wavelength and X-ray spectrum

1.4.1.1. General spectral formation

The underlying spectral continuum of all AGN in first instance is a power-law continuum produced via multiple inverse Compton up-scattering (Sect. 1.1.2) of UV-photons by coronal relativistic electrons to X-ray energies as nicely described in detail by Turner & Miller (2009).
Depending on the inclination angle of the AGN towards the line of sight, Compton reflection of incident power-law photons is more or less effective (George & Fabian, 1991; Lightman & White, 1988). Let us review the process of **Compton reflection** in general. Typical continuum shapes of a reflected power-law spectrum are shown in Fig. 1.10. The two main competing mechanisms are photoelectric absorption and Compton down-scattering. As discussed in Sect. 1.1.2, the cross-section for photoelectric absorption goes with $\approx E^{-3}$ because high Z elements necessary for photo-absorption are getting less abundant at higher energies. It reaches about the same value as the Klein-Nishina cross-section at 10 keV which is decaying starting at photon energies of around 100 keV. This means that in the energy range of interest for X-ray spectra (0.3 – 10 keV) the Klein-Nishina cross-section can be approximated with the energy independent Thomson cross-section σ_{T}. In general one can assume that power-law photons irradiate the accretion disc or the inner side of the torus (Ghisellini et al., 1994) again while getting redirected due to Compton reflection in the Thomson regime at intermediate energies and also suffer energy loss due to electron recoil at higher energies of $E \gtrsim 30$ keV where the Thomson cross-section fades into the regime of the overall Klein-Nishina cross-section where scattering events can not be treated as fully elastic any more.
The combination of **photo-absorption** at lower energies, the redirection out of the line of sight and energy attenuation of photons due to Compton (down-)scattering yield the typical Compton reflection continuum peaking at energies around 30 keV. Early work on the high energy bump as a signature of cold matter in Seyfert galaxies is also done by Matt et al. (1991) as well as Haardt & Maraschi (1991).
The continuum is accompanied also by **emission features** due to creation of new photons by recombination, bremsstrahlung, collisional excitation and fluorescence effects strongly dependent on the degree of **ionization** of the medium where also Compton reflection takes place.
The ionization parameter is defined as $\xi = L/nr^2$ with the irradiating luminosity L and the column

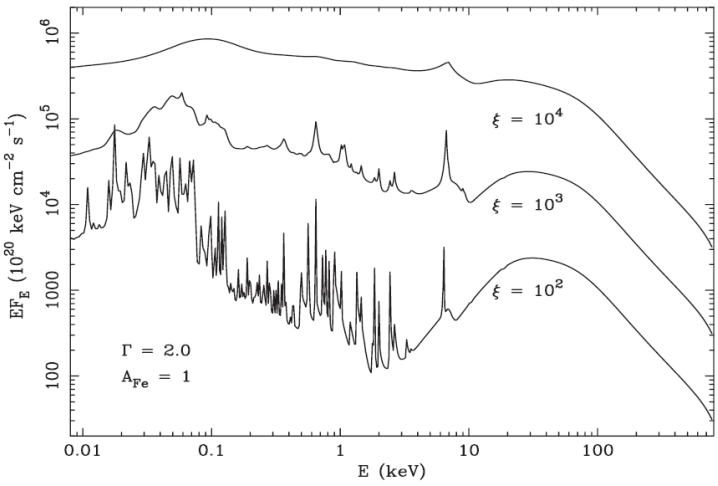

Figure 1.11.: Reflection Spectra for constant density slabs for three values of ξ getting illuminated by a power-law spectrum with photon index of 2 (Liedahl & Torres, 2005).

density n of material at a distance of r from the nucleus. It measures the degree ionization of gas situated in the upper layers of the accretion flow (corona) and the torus due to irradiation.

Two extreme cases are used in many publications, e.g., by Zycki et al. (1994), Turner & Miller (2009) and Fabian & Ross (2010). In highly ionized, hot plasma most electrons are stripped of the elements leading to a decrease of the efficiency of photoelectric absorption and in turn a dominance of the unabsorbed reflected continuum as well as less emission features in the soft X-rays. Low ionization states of the plasma in opposite allow the occurrence of emission features and a dominance of photoelectric absorption of the incident photons causing less photons to be reflected. In a cold plasma with weak external irradiation and low ξ, the thermal black body radiation from the disc as well as collisional events are still sufficient to partly ionize elements such as carbon, nitrogen and oxygen allowing the occurrence of recombination lines.

Figure 1.11 nicely shows the effects of ξ. For detailed calculations of ionized absorption and further illustrations of the effect of different ionization parameters, see García & Kallman (2010).

On top of the reflected continuum the Fe Kα line produced by fluorescence line emission is mostly dominant. Iron is the last element towards high energies with still abundant electron shells. Fluorescence is the ionization of an electron from the Iron K-shell and another electron filling that gap from the L-shell while emitting a photon at $\approx 6.4\,\mathrm{keV}$. An Iron edge at at $\approx 7.1\,\mathrm{keV}$ often appears due to the rapid fall-off of the photo-absorption cross-section (Wilms et al., 2000) in Fig. 1.3.

Moreover reflection is getting more effective for larger column densities (Ghisellini et al., 1994). Photons are scattering only several times until they emerge the disc. At each scattering event the photon can also be absorbed. As derived in Sect. 1.1.3 the opacity τ is proportional to $N_\mathrm{H}\sigma_\mathrm{KN}$ with the column density N_H. For multiple scattering events the photons encounters a total opacity of $\sum_n \tau^n$ which will get very large already for small n. That means that for additionally large N_H values, Compton scattering will be the only contribution to the measured spectrum as the photons being absorbed by the same medium of course do not reach out. In other words, when the obscuring column density is so large that the primary continuum is obscured up to (and beyond) $10\,\mathrm{keV}$ ($N_\mathrm{H} \gtrsim 10^{24}\,\mathrm{cm}^{-2}$), we speak of **"reflection-dominated"** or **"Compton-thick"** objects. Both terms are used synonymously, although the former is more the phenomenological appearance, the latter the underlying cause.

Combining the above discussed elements of

- the incident power-law spectrum
- reflection / re-procession of the incident power-law at dense, partly ionized regions around

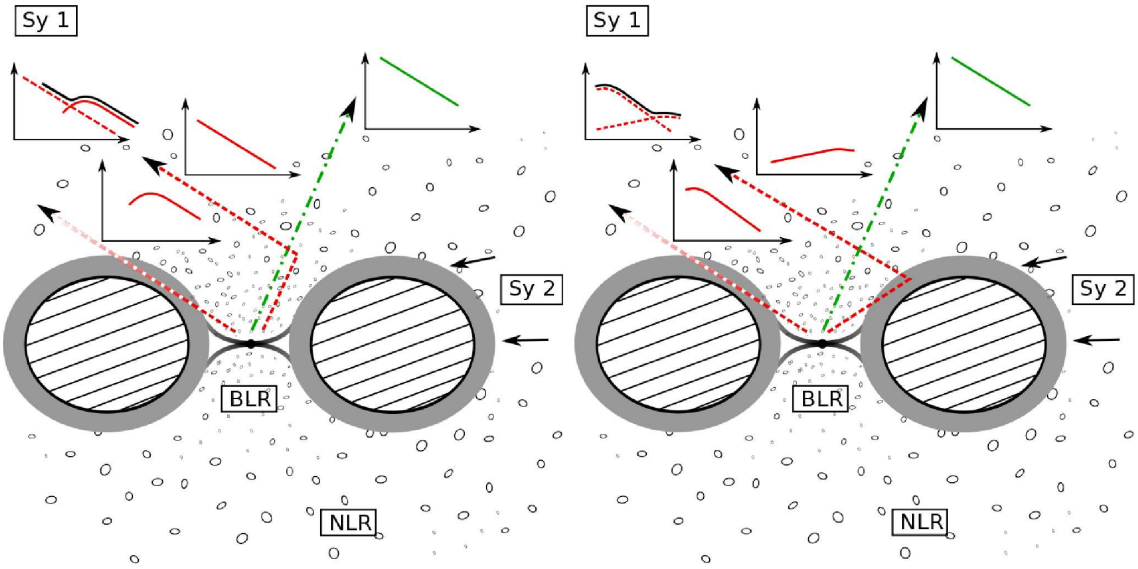

Figure 1.12.: Sketches of possible geometrical interpretations of the detected 0.3 – 10 keV band spectra for radio-quiet AGN / Seyfert galaxies seen under an inclination angle of $i = 45°$: *left:* partial covering, *right:* Compton reflection

the accretion disc or the inner side of the torus, most likely also being the source of

- emission features

we can now combine an overall spectrum emerging a region within the obscuring torus. Thus the measured spectrum can be assumed to consist of the sum of the incident power-law spectrum coming directly from the nucleus and the power-law reprocessed in the outer layers of the disc.
Now, the dusty torus as well as other surrounding gas have to be further considered as obscuring matter. In other words, we have to distinguish between Sy I and II galaxies in the following which are the same objects just viewed at different inclination angles towards the torus' symmetry axis. For some inclination angles in between it is legitimate to assume that the overall spectrum consists of continuum or line photons originating from multiple paths as illustrated in Fig. 1.12, right panel. Those are the incident power-law directly emerging the nucleus (green, dotted-dashed line), striking through the edge of the obscuring torus (red, dashed line on the left side), second the component reprocessed at the inner side of the torus seen from an unobscured line of sight (red, dashed line on the right side). If reflection occurs in the absorbing torus, it may be partially obscured and not detectable. Whether the reprocessing occurs in the torus or the accretion disc can only be judged using variability studies. The sum of the Compton reflected and the incident but absorbed power-law spectrum has a break somewhere above 10 keV (see also the composite spectrum of Fig. 1.10). Thus it is challenging if not impossible to constrain a Compton reflection component with the X-ray instruments used in this thesis as they are sensible only up to 10 keV.
Next to **cold absorption** occurring most likely in the torus consisting of relatively dense and cold gas and dust, there is also less dense gas in the NLR partially ionized by radiation from the central engine being responsible for **warm absorption** producing also absorption line features depending on the ionization state of the gas. As Costantini (2010) and many more authors conclude due to the measurement of Doppler shifted absorption lines, this is in particular evaporated gas from, e.g., the outer torus layers being driven outwards by the radiation pressure of the X-ray source. Systematic studies show that at least half of all AGN harbor such outflowing warm absorbing gas (Reynolds & Fabian, 1995; George et al., 1998; Piconcelli et al., 2005; Blustin et al., 2005; McKernan et al., 2007).
At last a very interesting feature is the **soft excess** (Guainazzi & Bianchi, 2007). This is an excess

in form of extra continuum or line emission in the soft on top of a power-law fitting to the hard 2–10 keV band, extrapolated into the soft. For the origin one has to separately consider obscured Sy II and unobscured Sy I galaxies. **Sy II** galaxies have only little intrinsic emission due to strong absorption. While Sy Is allow us a direct view onto the nucleus and emission features due to partially ionized gas as discussed above, the same is obscured with a dusty torus for Sy IIs. However the excess photons of emission features together with soft X-ray continuum photons are effectively scattered into the line of sight by the highly ionized large scale low dense gas above the torus, most likely coinciding with the NLR (Bianchi et al., 2006). The spectrum on the direct line of sight through the torus is mostly absorbed in the soft band down below 4 keV. The high ionization state of the NLR, however, makes photo-electrical absorption in general insignificant in contrast to scattering of soft X-rays and also optical to UV photons (Mushotzky et al., 1993). On the other hand the soft excess of unobscured **Sy I** galaxies can be explained by Compton reflection from dense, partially ionized gas around the accretion disc into the line of sight (Pounds et al., 2001) – an example for Compton dominance also in the soft energy band.
Popular attempts to model such soft excess that is still subject of debate are models of thermal bremsstrahlung or Comptonization (Brenneman et al., 2007), reflection from ionized medium as discussed above and black body radiation.

1.4.1.2. Partial Covering and Warm Absorption

In particular, partial covering is a frequently used model description to account for the cold absorbers partially obscuring the line of sight. Figure 1.12, left panel shows the situation. Again we assume radiation to arise from different paths for a line of sight striking through the outer edge of the torus. In principle also Fig. 1.12, right panel shows a case of partial covering. Depending on the site where Compton reflection occurs, it is generally speaking possible that one line of sight is getting obscured and the radiation is partially covered.
Here, I want to discuss partial covering visible in the observable 0.3 - 10 keV band. For the assumed line of sight towards intermediate Sy I/Sy II types incident power-law radiation again strikes through the outer edge of the torus which is moderately dense (N_{H} of the order of $10^{22}\,\mathrm{cm}^{-2}$) and thus only absorbs down to some keV. On the other hand, photons can also be Thomson scattered into the line of sight. This scattering most likely occurs in the NLR while only a fraction of the incident power-law photons arrive the observer. Thus the overall spectrum is the superposition of a power-law attenuated in normalization and the incident power-law absorbed in the soft by cold matter which gives the typical "S-shaped" spectrum. The model for such a spectrum combines as

$$[(1-c)\cdot c\cdot e^{-\sigma N_{\mathrm{H\,internal}}}](E^{-\Gamma}+\mathcal{G}_{\mathrm{Fe}})e^{-\sigma N_{\mathrm{H\,galactic}}} \tag{1.42}$$

with the covering factor c and a power-law plus Iron Kα line $\mathcal{G}_{\mathrm{Fe}}$ (Dauser et al., 2010) absorbed by the source itself and our own galaxy given by the column densities $N_{\mathrm{H\,internal}}$ and $N_{\mathrm{H\,galactic}}$.
Ceballos & Barcons (1996) nicely test the importance of partial coverers for a sample of 65 Sy I and Sy II sources by examining the relation of the soft and the hard X-ray fluxes. The partial covering model is best understood with Fig. 1.13. Here every source accords to one data point in the hardness ratio vs. flux ratio diagram. After the idea of the Unified Model, Sy II galaxies appear under a line of sight that is obscured by a molecular "torus". Experimentally one finds that those sources are obscured by column densities of $N_{\mathrm{H}} \geq 10^{23}\,\mathrm{cm}^{-2}$ whereas Sy I galaxies with average column densities of $N_{\mathrm{H}} \approx 10^{22}\,\mathrm{cm}^{-2}$ are not supposed to be absorbed by that structure as this column density is of the order of the intergalactic N_{H}. See the primary literature by Kembhavi & Narlikar (1999) for examples from modern research.
The sources discussed here, again intermediate Sy I/Sy II sources with a line of sight striking through the outer torus layer, can be assigned to the sample of Sy I in Fig. 1.13 in terms of the measured quantities of N_{H}.

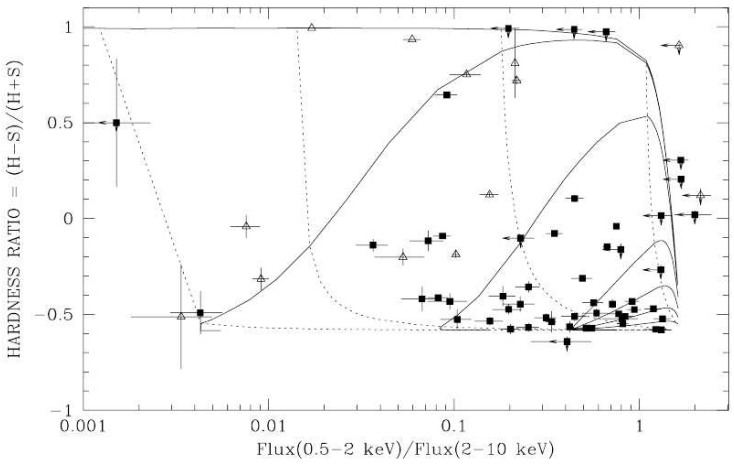

Figure 1.13.: ROSAT PSCP hardness ratio versus flux ratio for a set of 65 Sy I (filled squares) and Sy II (open triangles) sources (Ceballos & Barcons, 1996).

The figure gives an overview over the parameters of models best describing the source's spectra. Solid lines are lines of equal covering factor starting with $c = 0.2$ at the very bottom rising to $c = 1.0$ at the top of the panel. While tracing those lines of equal covering factors from right to left, the column density rises from $N_{\mathrm{H}} = 10^{20}\,\mathrm{cm}^{-2}$ to $N_{\mathrm{H}} = 3 \cdot 10^{23}\,\mathrm{cm}^{-2}$. Thus strongly absorbed sources such as Sy II (open triangles) are found at the upper left of the figure where column densities and covering fractions are large and in turn the spectra are harder. The sample of less absorbed Sy I and also the intermediate Sy I/Sy II galaxies partially included in this sample of Ceballos & Barcons (1996) conglomerate at the lower right of the figure where N_{H} values are low, covering fractions intermediate and the spectra more soft. Some soft excess might also be existent for soft sources with lower covering factors, however hard to determine with partial coverer models.
Thus the **covering fraction is directly correlated with the N_{H} parameter**. Having shown that partial coverers are indeed physical mechanisms of spectral formation one might ask if also **warm absorbers** play a role for sources of that kind. Indeed Ceballos & Barcons (1996) conclude that one needs a combination of neutral and partially ionized absorbers to fully account for both the absorption of the continuum and absorption line features.

1.4.2. Variability studies

Variability in flux and absorption is ubiquitous for Seyfert galaxies (Risaliti et al., 2002). They explicitly state **two reasons for spectral variability** that are variations in the irradiation and thus the ionization state of the warm absorber (Krolik, 1999) as well as variations of the absorber itself.
The mentioned intermediate Sy I/Sy II galaxies are sources revealing possible variability of the absorbing gas in the line of sight through the outer torus layer. The goal is to find a sample of those sources to test for the variable structure of the outer torus layer and to give a contribution to probe the verity of the Unified Model. The following section is dealing with those sources in detail defining an appropriate sample.

1.4.2.1. Polar scattered Sy I galaxies

The Unified Model of Active Galactic Nuclei (Antonucci, 1993) shows that Sy I and Sy II galaxies are the same type of galaxies, but seen under different inclination angles (Fig. 1.14). At inclinations

$\lesssim 45\,^\circ$ Sy I galaxies are typically either optically unpolarized or polarized due to predominantly equatorial scattering. Sy II galaxies have an inclination of $\gtrsim 45\,^\circ$ and show mainly optical polarization features due to polar scattering, as the line of sight of Sy II galaxies passes through the optically thick torus.
The spectra analyzed in this work do not reveal any soft emission features in the X-rays but indeed in form of scattered emission lines the optical and UV. In detail, as shown in the illustration, there are two scattering regions of polarized light. One located near the accretion disc, correlated with the broad line region (BLR), and one farther outside, to be identified with the Narrow Line Region (NLR). The former is the source of polarized light with a polarization angle (PA) parallel to the torus' symmetry- or polar-axis, also called the **equatorial scattering region** (green scattering trail in Fig. 1.14). From the latter, **polar scattering region**, one receives mainly polarized light with a PA perpendicular to the polar axis (red scattering trail). Here the measured broad, polarized line photons are scattered on large scale gas above the system as pointed out in the last section in respect of soft excess emission. Hence, the dominating mechanism for Sy I galaxies is equatorial scattering, for Sy II galaxies polar scattering. In reality, both scattering regions contribute to the effective polarization. It is important to note, that for both the degree of polarization increases for an increasing inclination of the line of sight towards the symmetry axis. Furthermore, if both regions contribute to one line of sight, one has to take into account partial cancellation of polarization, as both PAs are orthogonal. Additionally, photons from the unpolarized continuum follow the same scattering path as the polarized ones. So, also dilution of the unpolarized continuum takes place.
Using characteristics of optical polarized emission to constrain the geometrical situation, Smith et al. (2004) state a sample of 12 so called **polar scattered Sy I galaxies** with an assumed line of sight of $45\,^\circ$. But why are those still dominated by polar scattering?

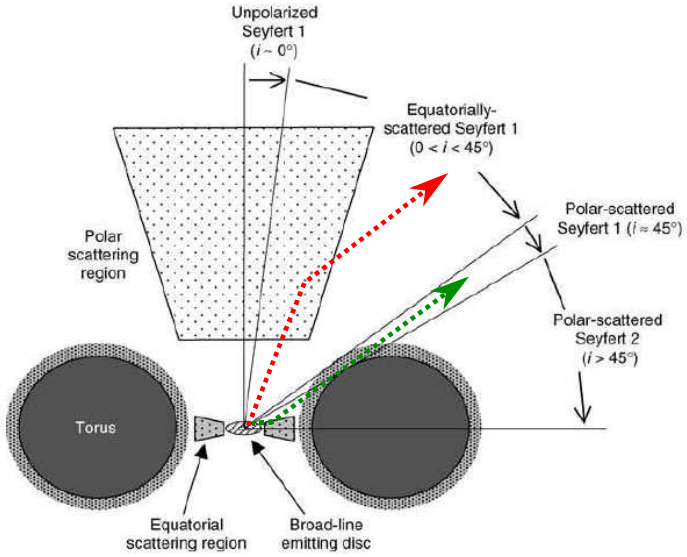

Figure 1.14.: Geometric interpretation of the observation of optically different polarized Seyfert galaxies (Smith et al., 2004).

The answer depends on the system geometry: equatorial scattered polarized light can pass the outer less dense layer of the obscuring gas as shown in Fig. 1.14 and is therefore attenuated towards the optically polar scattered light.
X-rays produced near the nucleus presumably follow the same (scattering) paths and thus also paths through the outer layer of the torus consisting of evaporated inhomogeneous gas and dust. This should result in significant soft X-ray variability due to strongly variable column densities and photoelectric absorption.

1.4.2.2. Origins of X-ray column-density variation

The basic model assumption for all sources is a partial covering of the line of sight with cold gas and dust from the outer torus layers. For the high resolution *XMM*-data it is possible to find better model descriptions including additional warm absorbers and for spectra with very high S/N even Compton reflection components. In order to stay consistent within the model descriptions of all compared observations it is necessary for more complex models to always include elementary starting models. This bottom-up procedure of starting with basic models and gradually testing more advanced ones is particularly important for comparing column densities.
After a simple absorbed power-law model, a partial coverer (Sect. 1.4.1.2) is the standard model which is successfully fitted to most of the available data. However, speaking of variability, a partial covering scenario of that kind might be less physical concerning findings of rapid dips in X-ray light curves of obscured Seyfert galaxies such as Fairall 9 (Lohfink et al., 2012), Centaurus A (Rivers et al., 2011), Mrk 348 (Akylas et al., 2002) and NGC 3227 (Lamer et al., 2003) which is also in my sample. In all cases dips are found in *RXTE* light curves. Further examples of N_{H} variations on short time-scales are given by Risaliti (2010). As a side-note: *RXTE* is not used in my analysis due to the lack of sensitivity in the soft X-ray range which is essential for a spectral identification of absorption of lower column densities of the order of $10^{22}\,\mathrm{cm}^{-2}$ as present in my sample.
Also the rapid column density changes found by Puccetti et al. (2007) in NGC 4151, a prototypical source in that case, lead to the insight that a partial coverer with homogeneous distributed cold absorbing matter obscuring the direct line of sight towards the nucleus while unobscured photons get Thomson scattered into that line of sight is less meaningful compared to the model of a **clumpy torus** proposed and applied by Holt et al. (1980) with a good model explanation provided by Nenkova et al. (2008). This model is also used as explanation in most of the above stated examples of detected X-ray dips. The basic assumption is that the absorber is no longer homogeneous but consisting of a large, Poisson distributed number of clouds each of a certain column density. Variability is said to be due to fluctuating cloud numbers in the observer's line of sight. Considering the small cloud size, a partial covering now **within** the solid angle of the observer is possible (Holt et al., 1980).
That kind of clumpy-torus model including a large number of small clouds has been tested for many sources with *RXTE*. The timescale of variability is expected to be limited by the light crossing time at the inner side of the torus. Also X-ray absorption variability detected on time scales of hours to days by Risaliti (2010) can be better explained by the notion of clouds moving in front of the line of sight. Although this ansatz of partial covering clouds opens the door to the internal structure of the obscuring torus, the partial covering with a homogeneous shield as used in this work is sufficient to describe variability itself (de Rosa et al., 2007). It is important to note that both the homogeneous shield and the clumpy torus models are successfully fitting the data. Also variability can be explained by both. The homogeneous shield assumes one cloud drifting over the line of sight, the clumpy torus model many Poisson distributed clouds instead. Measurements yield time scales of hours to days at the maximum (Risaliti, 2010). It is thus a more physical approach to include relatively small clouds directly into the underlying model as being most likely the components of obscuring torus (Krolik & Begelman, 1988).
All those assumptions are hypothetical as no one could resolve the inner regions of AGN by now. Understanding the partial coverer as partial covering of the direct line of sight towards the nucleus instead of a contribution of different regions of the system (Fig. 1.12) is a legitimate ansatz towards a more realistic understanding of the physical processes if one considers the scientific results achieved in terms of short term variability of absorption of many systems.

The model of a homogeneous shield in the line of sight can also explain homogeneous clouds performing orbits around the central SMBH and obscuring the line of sight for a certain period of time. The smallest measured time scale will then set an upper limit on the radius of orbits if assumed to be circular.
This can be determined if assuming that the obscuring cloud is moving on circular Keplerian orbits around the central SMBH. Lohfink et al. (2012) in particular use this ansatz to calculate an upper limit on the distance of the absorber for Fairall 9, where several absorption dips were found. Assume a spherical cloud of radius $r = xr_S$ with the Schwarzschild radius $r_S = GM/c^2$ where G is the gravitational constant and M the mass of the central SMBH. Let the cloud move on a circular orbit with the radius $R = Xr_S$. Equating the centrifugal force with the gravitational yields for the velocity of the cloud $v = \sqrt{GM/R} = X^{-1/2}c$. The duration of one eclipse triggered by the obscuring cloud of radius r moving in front of the line of sight is approximately $\Delta t \sim 2r/v$. Inserting the result for the velocity v yields

$$X = \left(\frac{\Delta t c^3}{2xGM} \right)^2 \tag{1.43}$$

and therefore

$$R = Xr_S = \Delta t^2 c^2 r_S \frac{1}{4r^2} \tag{1.44}$$

for the radial distance of an obscuring cloud from the central engine. Risaliti et al. (2002) re-write this equation in order to include information of density n (units cm^{-3}) and column-density, N_H (units cm^{-2}) of the obscuring cloud to

$$R \sim 3 \cdot 10^{16} \frac{M_{BH}}{10^{19}\, M_\odot} \left(\frac{n}{10^6\,\mathrm{cm}^{-3}} \right)^2 \left(\frac{\Delta t}{5\,\mathrm{Ms}} \right)^2 \left(\frac{N_H}{10^{22}\,\mathrm{cm}^{-2}} \right)^{-2} \mathrm{cm} \tag{1.45}$$

where the radius of a spherical orbiting cloud can be used to gain the cloud density out of measured column densities N_H. Additionally to this estimate of the distance of an absorber with neutral/cold N_H, Krolik (1999) derives a relation for a partially ionized absorber to be

$$R \sim 500 L_{ion}^{1/2} \left(\frac{\Delta t_{ion}}{1\,\mathrm{yr}} \right)^{1/2} \left(\frac{Z_{eff}}{4} \right)^{-2} \mathrm{pc} \tag{1.46}$$

with L_{ion} as "the ionizing luminosity [...] defined as the luminosity in the continuum corresponding to the ion in question" (Krolik, 1999) derived from X-ray model fits, Z_{eff} the charge of the ion of interest, and Δt_{ion} as the time where an order of unity change occurs in ionization.
My focus lies on the variability of neutral absorbing matter and in turn on varying column densities as derived from model fits of the data. Also visible in the data is a variation of the total flux itself due to changes in activity of the radiation emerging from the vicinity of the black hole. The ionization state of warm absorbing gas in turn also answers with variability (Zycki et al., 1994) remembering the relation for the ionization state $\xi = L/nr^2$ with the irradiating luminosity L.

Chapter 2

Polarimetry of Relativistic Jets

> *What would you be if you were attached to another object by an inclined plane, wrapped helically around an axis? Screwed!*
>
> S. Cooper, *Big Bang Theory*

In the previous chapter radiation processes and different types of AGN as sources of measurable radiation are discussed in detail. After Sect. 1.3 the radio-loud sub-types of AGN host jets embedded in magnetic fields as shown in Fig. 1.9. They are the main source of *partially polarized* Synchrotron radio emission that can be measured both in total and polarized intensity with (single-dish) radio telescopes. Saikia & Salter (1988) review the most important achievements in interferometric and single-dish polarimetry until 1988. Polarimetry is the key to the overall structure of magnetic fields as lying perpendicular to the EVPA vectors for a resolved map. The magnetic field reveals insight in the basic, yet not understood physics of jets and their formation.
One interesting finding in terms of the theories stated in Sect. 1.3.1 is that for FR I radio galaxies where both jet and counter-jet are visible, the magnetic field is mostly parallel to the jet axis behind the hot spots and perpendicular towards the core, whereas for FR II types the field is predominantly parallel to the axis.
Not only the magnetic field structure but in particular the dynamics and variability induced by shocks moving downstream the jets is measurable both in total and polarized intensity. This is done for the extended radio galaxy 3C 111 in this chapter. First I give an introduction to this source, explaining the technical issues of single-dish radio astronomy with the 100-m Effelsberg telescope in the following section to finally use those techniques to analyze and interpret data of 3C 111.

2.1. The FR II Radio Galaxy 3C 111

The nearby radio galaxy 3C111 ($z = 0.048$) is a unique source to study a broad variety of phenomena. In contrast to blazars with jets dominating the whole frequency range from radio to X-rays, 3C111 as a FR II type Broad Line Radio Galaxy (Sargent, 1977) is jet-dominated in the radio regime (see Fig. 2.1) and shows Seyfert like spectra in the optical and X-rays (Chatterjee et al., 2011). This is on the one hand because of the jet position angle of about 63 ° reported by Linfield & Perley (1984) meaning that the line of sight is highly inclined towards the jet axis. On the other hand a reason can be a probably low external photon field allowing the synchrotron peak in the radio-to-gamma spectral energy distribution (SED) not to reach X-ray wavelengths and dominate the accretion disc X-ray emission. Groups like Hartman et al. (2008), Chatterjee et al. (2011) and Tombesi et al. (2012) studied multi wavelength data especially from the radio to X-rays in order to trace the

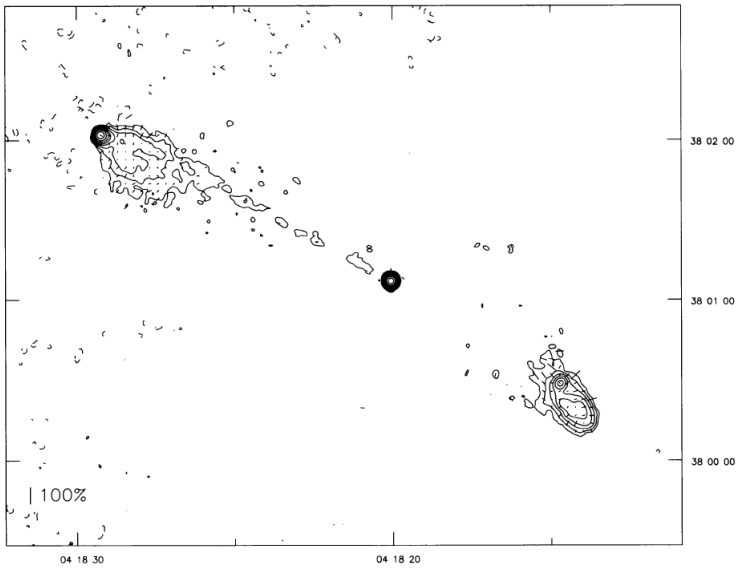

Figure 2.1.: 3C 111 mapped with the VLA at 3.6 cm, contours at 1.5×(-2,-1,1,2,4,...) mJy beam^{-1} (Leahy et al., 1997). The x-axis shows right ascension, the y-axis declination coordinates.

accretion disc – jet connection, the key to understand the feeding of jets. Studying this field is moreover implied by strong structural variability detected with VLBI experiments on parsec scales reported by Kadler et al. (2008) and Grossberger et al. (2012). The overall jet-morphology of the FR II type is shown by Linfield & Perley (1984), Leahy et al. (1997), Jorstad et al. (2005) and Chatterjee et al. (2011). In the present work I present full Stokes data measured with the 100-m Effelsberg radio telescope in the framework of the F-GAMMA project from 2007 until now. Data of the MPIfR 5 GHz and 10 GHz receivers are reduced as presented in Sect. 2.2. In addition to the work done on VLBI scales to study the remarkable variability of 3C 111 in the radio, the study is extended to global scales also considering polarization as a tool being very sensitive to variability in general. This makes it possible to both confirm the results already reached on high resolution scales and beyond that to understand the interaction of core activity with global structures as well as the morphology itself.

2.2. Single Dish Radio Analysis

A popular development besides Single Dish radio astronomy is the **Very Long Baseline Interferometry (VLBI)** using networks of single antennas spread over a large area (Kellermann & Moran, 2001). The so called synthesized beam and thus the network's spatial resolution goes with $1/D$ where D equals to the largest distance between two antennas as part of the network and is thus much smaller than the one of a single dish. Furthermore VLBI allows us to directly calculate an image out of the information of amplitude and phase recorded by each telescope. The algorithm basically cross-correlates all signals and is using Fourier techniques to reconstruct a map of the source of radio radiation. For primary literature regarding radio interferometry techniques see the textbook of Thompson et al. (2004). Also very useful is the proceeding collection of the frequent school of synthesis imaging and radio interferometry held at the NRAO in Socorro, New Mexico, edited by Taylor et al. (2008).
The only way to measure maps with **single antennas** is to slew the spot of maximal gain, also called "beam" across the source. In my Bachelor thesis (Beuchert, 2010), I calculate in detail how such beams are formed. The appropriate resolution, however, is worse. With VLBI one reaches

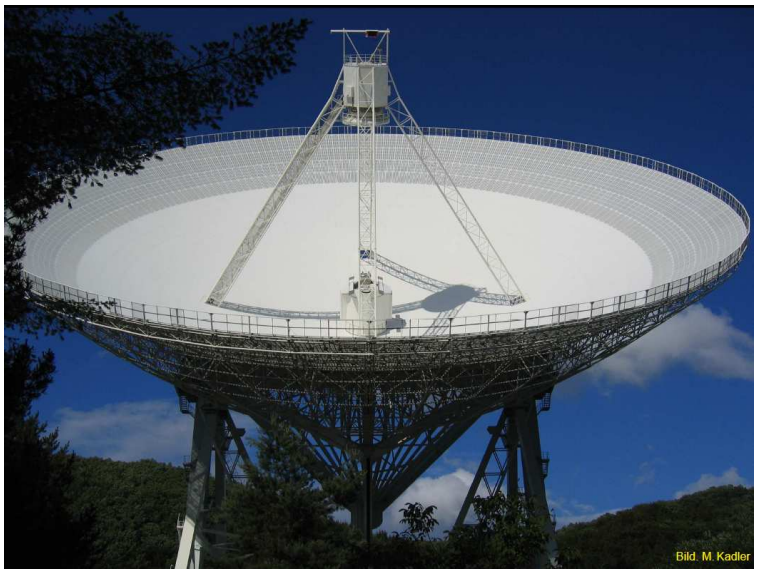

Figure 2.2.: The 100-m Effelsberg telescope, image taken by M. Kadler.

images of extragalactic radio sources with resolutions never seen before. Now one starts to ask for the necessity of single-dish observations while VLBI resolutions even allow us to study the magnetic field- and general structure in great detail, not only of AGN jets. Though, it is combined with great logistical and financial effort to maintain a VLBI network which is often spread over the whole globe. Furthermore, global networks consist of antennas of different kinds, making calibration also an elaborate task.
This leads us to the vast advantages of single-dish observations. Although the resolution is constrained to the width of a single beam being much larger than the synthesized beam of an array, such a beam covering large fractions or even the whole source for compact objects captures all information of the source at one time and in one data point. The caveat: also in terms of polarization only a value integrated over the beam can be measured. More explicitly, zones of different orientation of the polarization angles (EVPA) are washed out to one net orientation by vector addition. However, single-dish observations have easy access to a much larger field of research. Most important, long term monitorings at a wide set of different frequencies is affordable. Basic questions on the matter of AGN can only be answered by multi-frequency long term observations of the global AGN system properties. For example, the observation of megamasers by Braatz et al. (2010) allows direct measurement of the cosmological constant H_0. Another unique example for the importance of single-dish observations is the possibility of affordable long term monitorings of full Stokes polarization properties at multiple wavelength and a large set of sources. The MPIfR, Bonn leads a prominent campaign with the 100-m Effelsberg telescope together with the gamma-ray observatory *Fermi-GST* called F-GAMMA (Sect. 2.2.3.4). Historic polarimetry data of this campaign is the interest of the following sections starting with introductions to the instrument and its data analysis.

2.2.1. The Effelsberg 100-m telescope

Probably the best instrument amongst existing radio dishes for gathering polarimetry data of high quality and signal to noise is the 100-m Effelsberg telescope located in the Eifel, Germany (Fig. 2.2). It is operated from the Max-Planck Institute for Radio Astronomy in Bonn. The mount is operating in the azimuth/elevation (az/elv) coordinate system. Blazars as the target sources of the following analysis are measured using driven cross scans in azimuth and elevation.

Table 2.1.: Details for the 6 cm and 2.8 cm MPIfR receivers: central frequency, temperature of the noise diode as calibrator, the aperture efficiency and the Full Width Half Maximum of the beam.

freq [GHz]	T_{cal}	sensitivity [K/Jy]	AP efficiency [%]	FWHM [arcsec]
4.85	1.8	1.55	53	146
10.45	7.5	1.35	47	68

Table 2.2.: Channel allocation for the 5 GHz and 10 GHz receivers in Broad Band (BB) setup; TP A/B equals the total power in backend channels A and B (U. Bach, MPIfR, priv. comm.).

channel	Polarization	output signal	horn
a	LCP	TP A	1
b	RCP	TP B	1
c	cross (Q)	cos(A/B)	1
d	cross (U)	sin(A/B)	1
e	LCP	TP A	2
f	RCP	TP B	2
g	cross (Q)	cos(A/B)	2
h	cross (U)	sin(A/B)	2

2.2.1.1. 6 CM AND 2.8 CM RECEIVER

The 5 GHz/6 cm and 10 GHz/2.8 cm receivers are used for the analysis of polarimetric data. The channel allocation is listed in Table 2.1. Both receivers have approximately the same design and are operated with a main and weather horn. For total intensity it is necessary to subtract the weather horn signal from the main horn signal to reach the desired best signal-to-noise ratio. The polarimetric cross-channels cos(AB) and sin(AB), however do not include the weather due to the foregoing cross correlation. Hence a weather horn subtraction is only necessary for total intensity channels.

The feed horns themselves, i.e., circular feeds are sensitive to the polarized signal in its left- and right handed circular polarized (LCP/RCP) wave-components, which are orthogonal in the circular base. A monochromatic wave can on the other side also be decomposed into two linearly polarized waves orthogonal to each other in the linear base (see Sect. 1.1.4). As a single dipole measures only one of these orthogonal components, a linear feed in principle consisting of two orthogonal dipoles can measure both at one time. Similar, a circular feed measures both the LCP and RCP signals just as a helical formed antenna with a only one handed helix just measures one component. Hence, the feed can be understood as a combination of two of those helical antennas with opposite handing.

The necessary introduction to polarized radiation and its components is given in Sect. 1.1.4. Eq. 1.38 lists the Stokes parameters depending on the signals captured by the circular feed, namely E_l for LCP and E_r for RCP.

After the signal is divided into a LCP and RCP signal, both are treated equally within the receiver. A sketch of the MPIfR 6 cm receiver can be found in Fig. 2.3. The 6 cm receiver being described in the following is similar to the 2.8 cm one and shall be representative. The details are also discussed in Turlo et al. (1985), however referring to an older version of the 6 cm receiver.

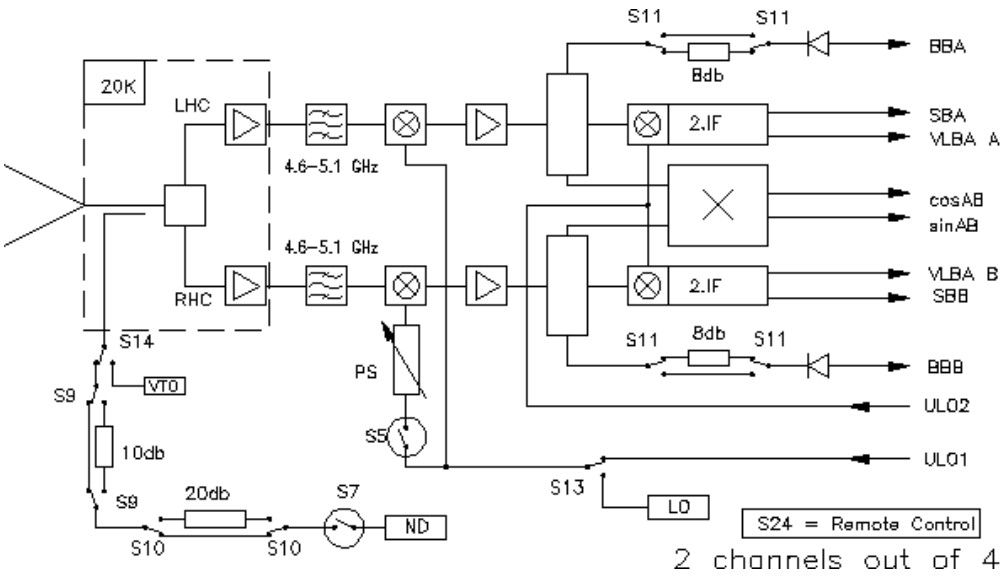

Figure 2.3.: The MPIfR 5 GHz four-channel receiver, `http://www3.mpifr-bonn.mpg.de/div/electronic/content/receivers/6cm.html`.

After passing a linear receiver and thus being amplified and trimmed to a finite bandwidth $\mathcal{B}$, the signal is getting down-converted to a lower *intermediate* frequency with the local oscillator (LO). This simply allows one to use cheaper and simpler electronic devices. Also a separate weather horn contributes a signal into the circuit which is not drawn in the sketch. At the same time when the local oscillator is fed into the path, the signals can also be phase switched with the S5 switch as drawn in Fig. 2.3. Table 2.2 includes the channel allocation of the digital backend. The total power signals of LCP and RCP are directly extracted as "TP A" and "TP B" and led to the autocorrelator stage (Eq. 1.39) to convert voltage to power. A and B simply denote the two main signal paths inside the receiver. The polarimeter in turn calculates the cross terms $\cos(A/B)$ and $\sin(A/B)$ from those signals, which will then themselves enter an autocorrelator. At this point the phase switch gets important, as it delays one signal path with 180 °. Within the polarimeter delayed and undelayed signals are subtracted in order to get rid of possible offsets formed inside the polarimeter. This is due to the fact that signals that are getting multiplied as it is the case in the polarimeter, always have positive noise that contributes to the resulting signal. A signal being delayed by 180 ° in turn will have negative noise. Subtracting both will lead to a signal scattering around zero and a more stable calibration.
In detail, the analyzed Effelsberg data are recorded by splitting the recorded signal in four phases with a length of 16 ms each. In the last two phases, the noise diode is switched into the cycle to do a Voltage – Kelvin conversion. The system records two signals (P resembles the phase, D the phase of a noise diode signal):

$$\begin{aligned} \text{sig} &= P_1 + P_2 + (P_3 + D_3) + (P_4 + D_4) = 4P + 2D \\ \text{cal} &= -P_1 - P_2 + (P_3 + D_3) + (P_4 + D_4) = 2D \end{aligned} \tag{2.1}$$

The conversion to Kelvins is performed with the equation

$$T_\mathrm{A} = \frac{\text{sig}}{2\text{cal}} T_\mathrm{cal} \tag{2.2}$$

with T_cal, the temperature of the noise diode as assumed to be constant with time (see Table 2.1) and T_A the calibrated antenna-temperature (Angelakis, 2007). In other words, this is the temperature an antenna-encircling black body would have while radiating with the same total power as the

Table 2.3.: Phase distribution of the MPIfR 5 GHz/6 cm receiver for the main horn only. Listed are the four channels a-d each carrying a different signal of polarization and combining four phases of 16 ms time-intervals to one channel-signal.

channel	Polarization	output signal	sig combination	cal combination
a	LCP	TP A (LCP)	$a_1 + a_2 + a_3 + a_4$	$-a_1 - a_2 + a_3 + a_4$
b	RCP	TP B (RCP)	$b_1 + b_2 + b_3 + b_4$	$-b_1 - b_2 + b_3 + b_4$
c	cross (Q)	cos(A/B)	$c_1 - c_2 + c_3 - c_4$	$-c_1 + c_2 + c_3 - c_4$
d	cross (U)	sin(A/B)	$d_1 - d_2 + d_3 - d_4$	$-d_1 + d_2 + d_3 - d_4$

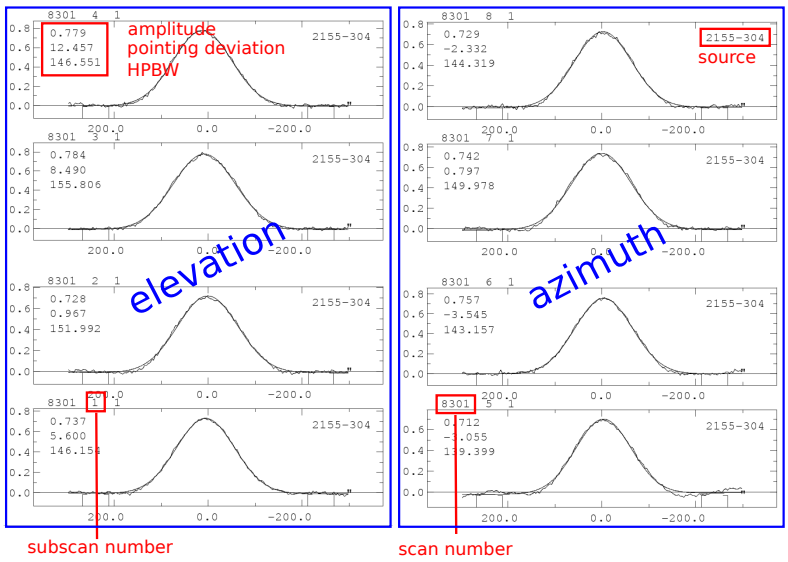

Figure 2.4.: Eight sub-scans, four in azimuth, four in elevation of the source PKS 2155-304 with the same scan number 6569.

observed source. Table 2.2 gives an overview which backend output (Fig. 2.3) accords to which phase combination plus the correct signs for the different phases used in Eq. 2.1. This is important for the data extraction. The negative signs of the cos and sin terms of $\cos(A/B)$ and $\sin(A/B)$ belong to phases delayed by 180 ° that are getting subtracted from the undelayed phases as denoted above. The phase switch of the 2.8 cm receiver was broken from July 2010 on. This can be fixed afterwards by setting the "nos5" option in the reduction software `toolbox`.

2.2.2. Stokes I calibration

After having done the Voltage-Kelvin calibration of the backend data for all four polarimeter-channels LCP, RCP, Stokes Q and Stokes U, one needs to calibrate the data to flux units measured in Jansky (Jy). The detailed steps are fully described in Sect. 3.5.3 of (Beuchert, 2010). In the available data, joint total-power cross-profiles are extracted for the channels a+b (LCP+RCP) from Table 2.3 and separate profiles for Stokes Q (channel c) and Stokes U (channel d). Figure 2.4 shows the basic scan method of Effelsberg – the cross scans. Usually, the beam is driven at least two times back and forth over the source both in azimuth and elevation. The basic analysis steps are sketched in the following. For more detailed information see Beuchert (2010).

- **Gaussian fits:**
  Gaussians represent a fairly good approximation of the beam profile as produced while sweeping over a point-source. This automatically gives a measure for the resolution of the telescope, i.e., $\theta = \lambda/D$ with λ the observed wavelength and D the aperture of the radio dish. Having fitted the Gaussian, the amplitude is the value one proceeds with. For the data file system until July 2010, the measured line profile is already pre-calibrated to Kelvins. Each data-point is thus derived by integrating the received signal over 64 ms and finding T_A with Eq. 2.2. After July 2010, no Kelvin pre-conversion is done. The Gaussian profiles appear in arbitrary units. However, all following steps are performed in the same way.

- **opacity correction:**
  Based on the equation for radiative transport (Eq. 1.30) and the elevation dependency of the atmospheric absorption $\tau_\mathrm{atm} = \tau_z(1/\sin(\mathrm{elv}))$ with τ_z the opacity in the zenith one can derive a formula for the measured system temperature with varying air-mass to be

$$T_\mathrm{sys} = T_0 + T_\mathrm{atm}(1 - e^{-\tau_\mathrm{z}(1/\sin(\mathrm{elv}))}) \overset{\tau \ll 1}{\approx} T_0 + T_\mathrm{atm}\tau_\mathrm{z}(1/\sin(\mathrm{elv})). \tag{2.3}$$

  Due to measurements of the air-mass against T_sys, which have a linear dependency following Eq. 2.3, one can directly derive $T_\mathrm{atm}\tau_\mathrm{z}$ from its' slope.

- **pointing correction**
  The high resolution of the Effelsberg beams at various frequencies, requires a pointing correction. Using the ansatz of a 2-dimensional Gaussian as approximation of the beam or point spread function (PSF) regarding a point source, it is possible to recalculate the pointing offsets in azimuth and elevation just using the driven scans in both directions.

- **gain correction and flux conversion** The az/elv mount of Effelsberg allows only elevation-dependent effects to play a role in the gain calibration. The gain of a receiving system like Effelsberg solely depends on the observing wavelength with the mean effective area[1] $\langle A \rangle = \lambda^2/4\pi$. See Table 2.1 for the aperture efficiencies of the appropriate receivers. Consequently, the antenna gain is getting worse for shorter wavelength, while the beam FWHM also shrinks with λ/D (Table 2.1). However it is sufficient to measure the gain as function of the elevation for the observed frequencies to correct for it. Reason for the gain variation with elevation is the deformation of the dish, which remains parabolic at all elevations.
  The sensitivity- or flux conversion from pre-calibrated units of Kelvin to Janskys is done by knowing the exact flux for several observed calibrator sources.

The sensitivity factors given in Table 2.1 include all calibration steps from Kelvins to Janskys.

2.2.3. Calibration of polarimetry data

2.2.3.1. Extraction of Polarimetry Data

Sect. 2.2.2 basically also describes the calibration steps for the polarized channels, however there are two caveats:

- a so called Müller matrix can be found for full Stokes polarimetry data including all internal calibration factors.

- for the new data system (change to FITS files) from July 2010 on, no Gaussian fits are applied to the Stokes Q and U profiles. The values for Q and U are read off at the position of the

[1] `http://www.cv.nrao.edu/course/astr534/ERA.shtml`

Stokes I (=LCP+RCP) maximum projected on the Stokes Q and U profile's base. The reason for this approach is the *beam squint* effect for LCP and RCP signals in a feed system being laterally displaced from the center of the focal plane (Fiebig et al., 1991). As LCP and RCP signals are orthogonal to each other in the frame of circular feeds and thus produce different beams being offsetted from each other.

2.2.3.2. Müller Calculus

The Müller formalism facilitates the complete calibration chain (Turlo et al., 1985). It relates the Stokes four-vector $\mathbf{S}_{\rm obs}$ (Sect. 1.1.4) for the observed data to $\mathbf{S}_{\rm cal}$ which is well known for the used calibrator sources by

$$\mathbf{S}_{\rm obs} = M_{ij} R_{ij} \mathbf{S}_{\rm cal}. \tag{2.4}$$

$\mathbf{S}_{\rm obs}$ and $\mathbf{S}_{\rm cal}$ are the Stokes vectors in the observer's and the source frame. Both are transformed into each other by applying the generic "Müller-matrix". It can further be separated into two matrices taking over the roles of gain calibration and instrumental effects on the one hand (M_{ij}) and a rotation ($R_{i,j}$) of the linear EVPA projected on the horizontal az/elv system just by the movement of the source on the sky on the other. It is sufficient to treat this as a purely three dimensional problem, as we do not expect an high fractional amount of circular polarization for synchrotron emission of AGN sources (Sect. 1.1.1). Writing the components of Eq. 2.4 one finds

$$\begin{pmatrix} I \\ Q \\ U \end{pmatrix}_{\rm obs} = \begin{pmatrix} m_{1,1} & m_{1,2} & m_{1,3} \\ m_{2,1} & m_{2,2} & m_{2,3} \\ m_{3,1} & m_{3,2} & m_{3,3} \end{pmatrix} \begin{pmatrix} 1 & 0 & 0 \\ 0 & \cos(2q) & \sin(2q) \\ 0 & -\sin(2q) & \cos(2q) \end{pmatrix} \begin{pmatrix} I \\ Q \\ U \end{pmatrix}_{\rm cal} \tag{2.5}$$

where the rotated vector with nominal calibrator values $(I, Q, U)_{\rm cal}$ can be parallactically rotated with the matrix $R_{i,j}$ to $(I, Q, U)_{\rm p}$ which yields

$$\begin{pmatrix} I \\ Q \\ U \end{pmatrix}_{\rm obs} = \begin{pmatrix} m_{1,1} & m_{1,2} & m_{1,3} \\ m_{2,1} & m_{2,2} & m_{2,3} \\ m_{3,1} & m_{3,2} & m_{3,3} \end{pmatrix} \begin{pmatrix} I \\ Q \\ U \end{pmatrix}_{\rm p}. \tag{2.6}$$

Figure 2.5 relates the equatorial to the horizontal coordinate system as it could be seen from the latitude of the 100-m Effelsberg telescope. It has an az-elv mount and is thus constrained to the horizontal system here shown in green. The tilted earth equator projected to the sky is the base for the equatorial coordinate system marked as blue. An observed source follows tracks parallel to the celestial equator. In Fig. 2.5 a possible tracking path of the radio telescope is drawn as an orange dashed line. As a source moves with time, also the parallactic angle

$$q = \arctan\left(\frac{\pm\cos(\Phi)\sin(H)}{\sin(\Phi)\cos(\delta) - \cos(\Phi)\sin(\delta)\cos(H)}\right) \tag{2.7}$$

being included in the overall Müller matrix as a transformation from the observer's to the source's system changes. In Eq. 2.7, Φ is the geographical latitude staying constant for the present telescope, $H = \mathrm{LST} - \alpha$ the hour angle with LST as the local sidereal time, α the right ascension and δ the declination.

The hour angle is just the angle between the plane through the observer's zenith and the earth axis (meridian) and the plane through the source and the earth axis. Combined with the right ascension as measured from the vernal equinox, the hour angle measures how much sidereal time has passed after the source was intersecting the meridian. Sidereal time is a time related to the earth rotation and the resulting propagation of stars on the sky.

The source of interest – 3C111 – (Sect. 2.1) shows extended morphology. Thus, it changes it's

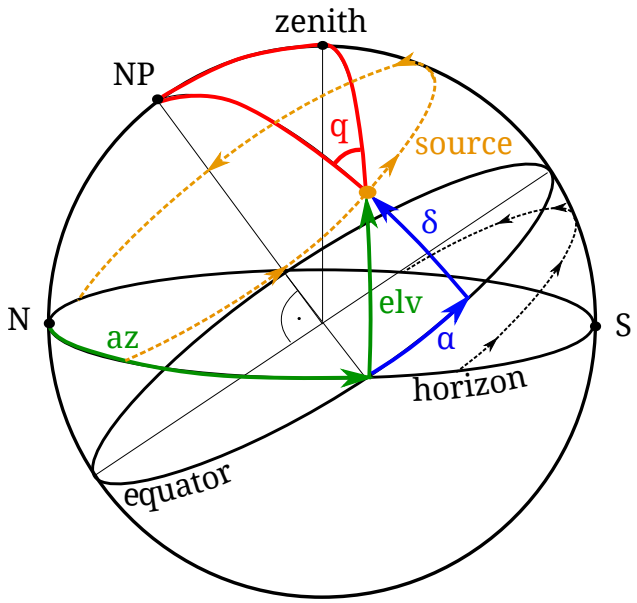

Figure 2.5.: Equatorial and horizontal coordinate system with right-ascension α/declination δ and azimuth/elevation. The parallactic angle q is the angle between the main axes of declination and elevation.

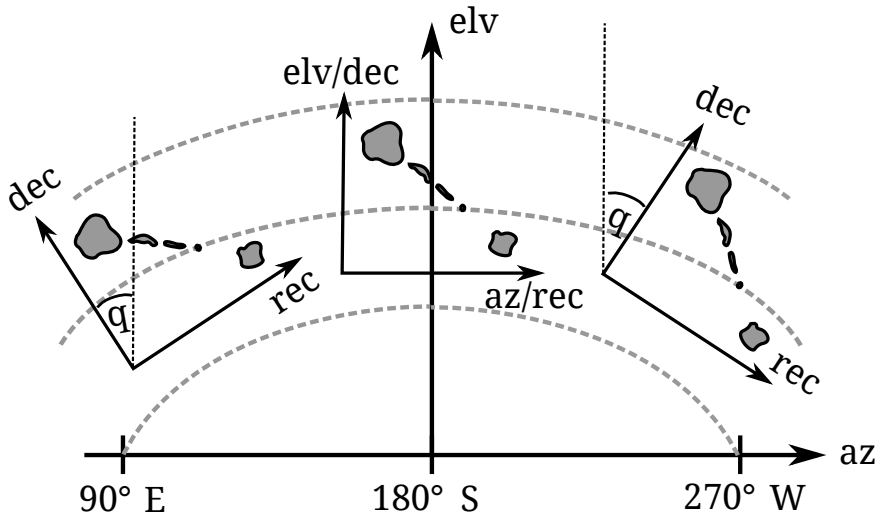

Figure 2.6.: The path of an extended source such as 3C 111 over the sky.

orientation projected on the horizontal observer's and here also the telescope's coordinate system while propagating over the sky as shown in Fig. 2.6. The *parallactic angle* is the angle between the main axes of declination and elevation of the source- and telescope's coordinate systems where the source is measured in. In other words: while the orientation of the source in the ra/dec coordinates never changes, it changes direction on the observed in az/elv coordinates with the parallactic angle q. This is the same rotation as described by the rotation matrix R_{ij} in Eq. 2.4.

Determining the Müller matrix elements is the main task of the analysis part of this thesis. As one might imagine, it is demanding and related to many aspects one has to be aware of.

The principle idea behind in turn is very simple and follows Turlo et al. (1985) and Kraus (1997). Thus, expand Eq. 2.6 to three dependent equations

$$\begin{aligned} S_1 = I_{\rm obs} &= m_{11} I_{\rm p} + m_{12} Q_{\rm p} + m_{13} U_{\rm p} \\ S_2 = Q_{\rm obs} &= m_{21} I_{\rm p} + m_{22} Q_{\rm p} + m_{23} U_{\rm p} \\ S_1 = U_{\rm obs} &= m_{31} I_{\rm p} + m_{32} Q_{\rm p} + m_{33} U_{\rm p} \end{aligned} \tag{2.8}$$

insert the observed and known calibrator data and perform a linear regression (Sect. 2.2.3.3). One can account for the fact of the correlation afterwards by varying the calibrator values to find the best fit for all three equations. This is possible as calibrators such as 3C 286 have been observed frequently enough in the past to state reliable and constant values for the Stokes parameters. The whole fitting process requires knowledge about the rough behavior and meaning of the individual matrix components. Again referring to Eq. 2.4, it is clear that the diagonal elements are the sensitivity factors [K/Jy] or [arbitrary unit/Jy] for Stokes I,Q and U assuming the calibrator values to be in flux units of Janskys and the raw data in pre-calibrated Kelvins or uncalibrated arbitrary units. The observed values within the F-GAMMA campaign (sec. 2.2.3.4) of monthly observations have been pre-calibrated to units of Kelvin using the noise diode until July 2010. After that data are provided in arbitrary units without pre-calibrating the cross scans themselves. The matrix formalism however does not depend on the input units. The result will be different calibration factors for whatsoever units the raw-data has.

Having already separated off the rotation matrix between Stokes Q and U due to the parallactic angle, there still remains an instrumental rotation due to the elements $m_{22}, m_{23}, m_{32}, m_{33}$ (Turlo et al., 1985). In other words, these components describe the relation between the measured and nominal source-values of Stokes Q and U. As shown in Sect. 2.2.3.4, the measured uncorrected data will spread over a deformed circle in the Q-U plane when measured at different parallactic angles. The amount of deformation gives information about these 2×2 matrix elements making use of the parallactic rotation spreading the data over a circular shape.

The entries m_{12} and m_{13} describe the overflow of polarized intensity to total intensity by the so called "depolarization"

$$p_{\rm depol} = \frac{\sqrt{m_{12}^2 + m_{13}^2}}{|m_{11}|}. \tag{2.9}$$

In opposite, also total intensity can flow over to polarized intensity. This is then called the "instrumental polarization"

$$p_{\rm instr} = \frac{\sqrt{m_{21}^2 + m_{31}^2}}{|m_{11}|}. \tag{2.10}$$

The EVPA rotation angle induced by instrumental effects is thus defined as

$$\chi_{\rm instr} = \arctan\left(\frac{m_{31}}{m_{21}}\right) \tag{2.11}$$

while the additional rotation of the EVPN itself described by the sub-2x2 matrix $m_{22}, m_{23}, m_{32}, m_{33}$

is given by

$$\arctan\left(\frac{m_{32}-m_{23}}{m_{22}+m_{33}}\right). \tag{2.12}$$

2.2.3.3. Log-Likelihood and Linear Regression

Having derived Eq. 2.8, one has to fit these equations to the observed data. One observing epoch of the F-GAMMA program (Sect. 2.2.3.4) contains cross scan observations of approximately 70 extragalactic sources. In each epoch, also several calibrator sources with more or less known Stokes values are observed multiple times in the best case. To also study the time dependent behavior of the Müller matrix, different matrices for every observing epoch are determined. Thus the input of Eq. 2.8 for one epoch is all calibrator measurements for $(I,Q,U)_{\mathrm{obs}}$ and the appropriate assumed default values for $(I,Q,U)_{\mathrm{cal}}$ or, respectively, $(I,Q,U)_{\mathrm{p}}$ when corrected for the well known parallactic angle at the present observing time. In the best case, the measurements of the Stokes Parameters are linearly aligned in the $(I,Q,U)_{\mathrm{p}}$-space, whilst the parameters m_{ij} represent some kind of slope of the linear dependency in the multi-dimensional space.
The general approach is to minimize the deviation of model and data for each equation separately. Therefore let the set $\{s_1,\ldots,s_n\}$ be measurements of S_1, S_2 or S_3 of Eq. 2.8.
The Likelihood[1] function is defined as

$$L(s_1,\ldots,s_n|m)=\prod_{i=1}^{n} f(s_i|m) \tag{2.13}$$

with $m=\{m_1,\ldots,m_m\}$ as the set of parameters, here for $m=1,2,3$ and a probability density function f being equal to the Gaussian distribution for normal distributed data around the model. σ_i denotes the Gaussian distributed error of each measurement. Assuming a fit with a model being equal to the representative equation $\mu_i = m_1 I_p^i + m_2 Q_p^i + m_3 U_p^i$, the Likelihood then turns out to be

$$L(s_1,\ldots,s_n|m_1,m_1,m_1)=\prod_{i=1}^{n}\frac{1}{\sqrt{2\pi\sigma^2}}e^{-\frac{(s_i-\mu)^2}{2\sigma^2}}. \tag{2.14}$$

There is one model function $\mu_i(m)$ per measurement s_i equaling to I_p^i, Q_p^i or U_p^i depending on which equation one wants to fit, as the parallactic angle changing from observation to observation is also included in the parallactic rotated Stokes calibrator values. Furthermore, it is more convenient to use the log-Likelihood

$$\ln(L(s_1,\ldots,s_n|m_1,m_2,m_3))=\ln\left(\frac{1}{\sqrt{2\pi\sigma^2}}\right)-\sum_{i=1}^{n}\frac{(s_i-\mu_i)^2}{2\sigma^2}. \tag{2.15}$$

The absolute value of the second term is equal to the known χ^2, which is basically Eq. 2.15 with opposite sign. After summing up all the individual error-weighted deviations from the model for each data point, the Log-Likelihood $\ln L(m)$ is just a function of the parameters m. The aim is to *maximize* this Log-Likelihood function to *find* the best fit of the model to the data. The appropriate χ^2 function, being defined as the sum only, then has to be minimized.
Depending on the amount of data n, the number of free parameters and the individual errors, the parameter space – meaning the Log-Likelihood function within the coordinate system given by the free parameters – looks more or less smooth and the global maximum is more or less prominent and clear. In some cases as it is pointed out in Sect. 3.1, it is very difficult to find a global maximum (or minimum for the χ^2, respectively). The global extremum might be covered with multiple local extrema, where the algorithm can get stuck.

[1] `http://www-zeuthen.desy.de/~kolanosk/smd_ss02/skripte/ls.pdf`

The following calculations are after Bevington & Robinson (2002) and the lecture script of van Eldik (2010). For simplicity we assume the extremum to be prominent around the center equaling the best fit value of the given set of parameters $\hat{m} = \{\hat{m_1}, \hat{m_2}, \hat{m_3}\}$. This is equal with developing the Log-Likelihood around this maximum and neglecting the series after the second order:

$$\ln L(m) = \ln L(\hat{m}) + \left[\frac{\partial(\ln L)}{\partial m}\right]_{\hat{m}} (m - \hat{m}) + \frac{1}{2}\left[\frac{\partial^2(\ln L)}{\partial m^2}\right]_{\hat{m}} (m - \hat{m})^2 + \dots . \tag{2.16}$$

At the best fit value, the second term is zero by definition. Hence, the Log-Likelihood function turns out to be a parabola around the best fit value. The Likelihood function in turn is the Gaussian

$$L(m) = L(\hat{m}) e^{\frac{1}{2}\left(\frac{\partial^2 \ln L}{\partial^2 m}\right)(m-\hat{m})^2} \tag{2.17}$$

in first approximation. In other words, understanding this result as the Gaussian distribution of possible parameters m around the best parameter $\hat{m}$, the appropriate squared error must be

$$\sigma^2 = -\left[\frac{\partial^2 \ln L}{\partial^2 m}\right]^{-1}_{\hat{m}}, \tag{2.18}$$

which is the *variance*. In Eq. 2.16 we disregarded correlated terms. Being more accurate the second term approximation in the Taylor series should be

$$\frac{1}{2}(m_i - \hat{m}_i)(m_j - \hat{m}_j)\frac{\partial^2 L}{\partial m_i \partial m_j}\bigg|_{\hat{m}} \tag{2.19}$$

which leads to the generic expression for the *co*variance matrix

$$V^{-1}_{ij} = -\frac{\partial^2 L}{\partial m_i \partial m_j}\bigg|_{\hat{m}}. \tag{2.20}$$

Back to the linear model we want to fit to the observed data. The Log-Likelihood is

$$\ln(L(s_1, \dots, s_n | m_1, m_2, m_3)) = \ln\left(\frac{1}{\sqrt{2\pi\sigma^2}}\right) - \sum_{i=1}^{n} \frac{(s_i - m_1 I^i_p + m_2 Q^i_p + m_3 U^i_p)^2}{2\sigma^2}. \tag{2.21}$$

After calculating the according derivations, we find for the appropriate covariance matrix

$$V^{-1} = \frac{1}{\sigma_i^2}\begin{pmatrix} \sum (I^i_p)^2 & \sum_i I^i_p Q^i_p & \sum_i I^i_p U^i_p \\ 0 & \sum_i (Q^i_p)^2 & \sum_i Q^i_p U^i_p \\ 0 & 0 & \sum_i (U^i_p)^2 \end{pmatrix}. \tag{2.22}$$

The 1σ parameter errors are then included in the inverse V of Eq. 2.22. Get the best fit values $\{m_1, m_2, m_3\}$ by evaluating the first derivative of the Log-Likelihood function. Some intermediate calculations yield the solution for the best fit parameters to be

$$\begin{pmatrix} m_1 \\ m_2 \\ m_3 \end{pmatrix} = V \sum_i \frac{1}{\sigma_i^2} s_i \begin{pmatrix} I^i_p \\ Q^i_p \\ U^i_p \end{pmatrix} = V \begin{pmatrix} \beta_1 \\ \beta_2 \\ \beta_3 \end{pmatrix}. \tag{2.23}$$

So the whole linear regression or maximization of the Log-Likelihood can thus be solved analytically starting from a very generic ansatz. For more complicated and non-linear model functions as it is the case in X-ray astronomy (see Sect. 3.1) an algorithm has to be chosen to iteratively search for the maximum of the $\ln L$ parameter space.

Performing this above described fitting for all three equations from Eq. 2.8, we in principle find three different covariance matrices. Here one just uses the diagonal variance terms $\delta m_{ij} = \sqrt{\mathrm{cov}(j,j)}$ of the three derived covariance matrices to find a matrix containing errors for the appropriate values of the Müller matrix.
After having derived the matrix, it can be inverted in order to recalculate corrected Stokes quantities. Errors of the observed Stokes quantities are propagated while applying the inverse Müller matrix using simple Gaussian error propagation. The parameter errors of the matrix elements themselves are not further used. Lefebvre et al. (2000) describe how the derived errors for the inverse covariance matrix V_{ij}^{-1} can be propagated with the operation of matrix inversion. The basic idea is to link the error propagation on a set of inverting functions relating the original matrix elements with those of the inverse functions. Applying this method and including also errors of the matrix elements into the final error of the reconstructed Stokes values, the errors do not get significantly larger. Therefore this method of propagating errors in matrix inversions is no longer pursued. Additionally, a repeatability error will be imposed due to the variability of the corrected full-Stokes data. This error will be much larger than the errors of the observed data until July 2010 (see Sect. 2.2.3.4) and especially the error imposed of the matrix inversion.

2.2.3.4. Realization with Effelsberg Data – The F-GAMMA project

The present work has been done in the framework of the F-GAMMA program[1] (Angelakis et al., 2010). Within this program, over 60 AGN are observed monthly since 2007 with the 100-m Effelsberg telescope and the IRAM 30-m telescope. Also APEX is providing even more frequent data at frequencies up to 345 GHz. The F-GAMMA project is a multi wavelength program with congruent high energy data from the *Fermi*-GST satellite.
This is the first time this historic recorded polarimetric data are getting analyzed over the full range of time from 2007 until today at the two different frequencies of 5 and 10 GHz. The first consequent application of the here presented technique for cross-scan observations with Effelsberg was performed by Kraus et al. (2003) for Stokes I, Q and U. See also the PhD thesis of A. Kraus (1997). E. Cenacchi (2009) is expanding the work of Kraus et al. (2003) by adding the Stokes V parameter and examining the formalism from a more formal point of view.
The observations are divided into epochs starting with EP0, having reached EP70 right now. In Beuchert (2010) multi wavelength Stokes I data of the blazar PKS 2155-304 are analyzed until EP42 (July 2010).
For the full Stokes analysis of all historic epochs, it is very important to be aware of the switch to a new FITS-file system and hence coming along with a new `toolbox`. Two major differences are explained in the following.

- **EP0-EP42:**
  Data recorded in binary raw tables are extracted with the `cont2` tool inside the former `toolbox`. Stokes I,Q and U cross scan profiles are formed out of four phases of recorded data for every data point in the profile. *Gaussian fits* to the profiles yield the amplitudes of the scans, the appropriate *errors* are derived from partial derivatives of the Chi-squared.

- **EP43-today:**
  The data file system changed to FITS-files. The data extraction is done with a new `toolbox` that treats the derivation of Stokes I values identically to before. Stokes Q and U values are extracted differently from the mostly deformed scan profiles, which is due to weak signals on the one hand and possible beam squinting on the other hand. Gaussians are not any more assumed to be adequate approximations of the scans. Hence, Stokes Q and U values are just the values of the profiles at the point of the maximum of the Gaussian for to the Stokes I

[1] `http://www3.mpifr-bonn.mpg.de/div/vlbi/fgamma/fgamma.html`

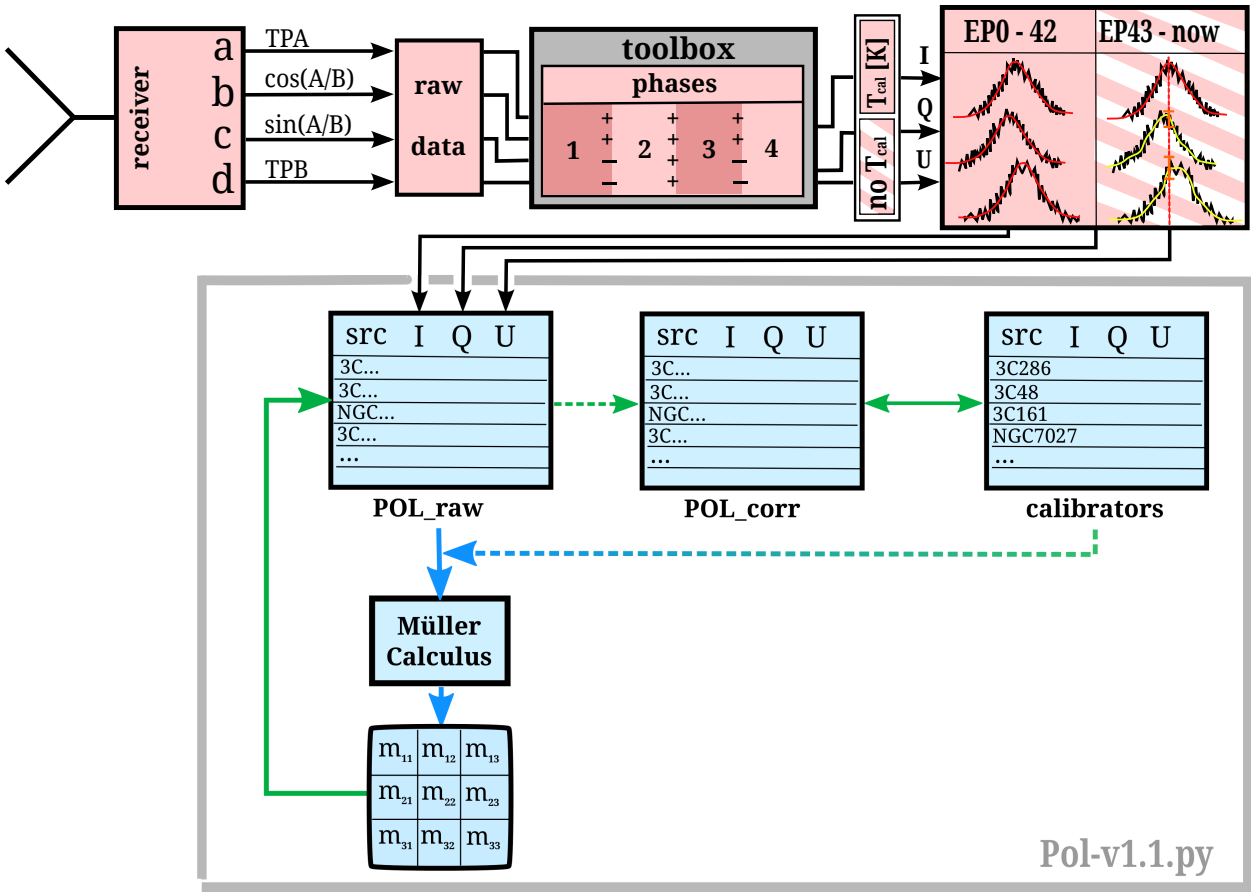

Figure 2.7.: Data processing using the MPIfR 2.8 and 6 cm receiver of the 100-m Effelsberg telescope. See the text for detailed explanation.

profile. Furthermore, the profiles are flattened by fitting a polynomial function to the Stokes Q and U scans. The appropriate errors to Q and U are the amplitude of the residuals of the polynomial fit. This yields a much more realistic guess of the error of the polarization data than just taking the calculated amplitude error from Gaussian fits, which is getting reduced due to the constraint of the Gaussian shape.

For the raw data input into the Müller calculus, the choice is not to adapt any kind of post-data calibration, as the sensitivity factors of the Müller matrix will do this at once with respect to the observed full-Stokes calibrators. Figure 2.7 illustrates the whole data processing chain. First the feed marked as open triangle is capturing the cosmic signals. The receiver rack processes them as exposed in Sect. 2.2.1.1 and passes its output to the four backend channels according to the two total power channels "TPA" and "TPB" as well as the "cos(A/B)" and "sin(A/B)" cross terms leaving the polarimeter. The next block marks the process performed by the `toolbox` software combining four phases of different kind for each channel to form the final signals of Stokes I,Q and U. Now there are two possible ways of either pre-calibrating the data to Kelvins using the noise diode, or not as it is the case for the recent epochs. In the following step, the scan-profile treatment is sketched via two boxes for either the first epochs until EP42 with included pre-calibration, or the latter epochs until today with no pre-calibration. In the former case amplitude and errors are derived due to Gaussian fits to all Stokes scan-profiles, in the latter one, the projection of the position of the Stokes I Gaussian maxima onto the Stokes Q and U profiles derives the appropriate values plus errors from the data-scatter. After all these pre-processing steps, the Stokes raw-data table including values for all observed sources of the present epoch enters the main data-loop. The

Table 2.4.: Stokes parameters of the used calibrator sources combined to total power, fractional polarization and the electric vector position angle both for the 5 GHz and 10 GHz receivers. See the according text for references.

	3C286	3C48	3C161	NGC7027
	10 GHz / 2.8 cm			
Stokes I [Jy]	4.44	2.68	2.99	5.92
fractional polarization PD [%]	11.7	5.9	2.4	0.0
EVPA [°]	33.0	116.0	93.8	0.0
	5 GHz / 6 cm			
Stokes I [Jy]	7.48	5.48	6.62	5.48
fractional polarization PD [%]	11.0	4.2	4.8	0.0
EVPA [°]	33.0	106.6	122.4	0.0

Python-script doing this calculation has been developed by M. Angelakis (MPIfR) and myself. It is basically performing the Müller calculus described in Sect. 2.2.3.2. Therefore, the raw-data are inserted into the matrix fitting code together with more or less well known calibrator values. The emerging matrix including all elements of possible data distortion due to the system is then applied to the previously inputted raw-data table yielding recalculated Stokes parameters (POL_corr table in Fig. 2.7) that should ideally accord to the well known parameters in source space. As this is not the case in reality, the double sided arrow now compares the average recalculated parameters of all observations of each calibrator at one epoch with the nominal values. The smaller the χ^2 of the Müller matrix fits are, the smaller are the deviations of the recalculated average values to the nominal values. Thus the script now gives the opportunity to change the calibrator parameters as input of the matrix-element fitting process in order to yield better fits. This is legitimate, as most calibrators are not monitored good enough in history to find their unaltered source-frame Stokes parameters. Furthermore the linear regressions in the 4-dimensional space and the too small data errors for epochs until EP42 turn the multi-epoch-consistent fitting of the three dependent equations into a challenging procedure. The calibrator parameters assumed as default values in first instance are listed in Table 2.4. For references see Tabara & Inoue (1980) as a summary of full Stokes data of a large set of radio sources published before 1978 and Turlo et al. (1985) who list a summary of published monitorings of calibrator sources themselves and the recent edition of the Astronomical Almanac[1]. For the latter, data derived with the 100-m Effelsberg telescope are listed, for other references mainly measurements of the VLA are used.

Examining all publications coming into consideration it is clear that only the calibrator 3C286 has been monitored well enough to be able to trust the stated parameters for flux, partial polarization and the EVPA. Hence, for the fitting procedure that has to be done by hand to account for the correlation between the three equations for I,Q and U of Eq. 2.8, one can legitimately use the approach of slightly varying the given calibrator parameters of sources being different of 3C286. As a consequence the values for 3C286, recalculated with each fitted Müller matrix, can be adjusted as close as possible to the default values listed in Table 2.4. Doing so, it is proven of value to, e.g., rise the calibrator value of the PD of one source, if the value for another source recalculated with a Müller matrix fitted in the former step is lower than suggested by the nominal calibrator value. This approach will iteratively find the best χ^2 for all three equations.

[1] `http://asa.usno.navy.mil/`

Table 2.5.: Systematic repeatability errors on the values Stokes I, PD and PA from histogrammed light curves at the two observing wavelengths 2.8 and 6 cm.

λ	σ_{I} [Jy]	σ_{PD} [%]	σ_{PA} [°]
2.8 cm	0.122	0.458	1.0
6 cm	0.054	0.127	1.5

2.2.3.5. Results

Following the previous exposed steps, Müller matrices are found for all analyzed epochs of data from the beginning of 2007 until mid 2012. The light curves derived both for 2.8 cm and 6 cm wavelength reveal a good quality of reconstruction of the calibrator data from literature putted into Eq. 2.4. The recovered values of the (EV)PA occasionally had to be shifted by 90 ° to coincide with the literature values. This is possible, because the PA defined as $\chi = 0.5 \arctan(U/Q)$ can together with the definition for the fractional polarization $p = \sqrt{U^2 + Q^2}/I$ be split into the two modes $Q = pI\cos(2\chi)$ and $U = pI\sin(2\chi)$. These equations imply that for the same fractional polarization p, all values of χ shifted by 90 ° yield the same values for Q and U.
Clearly apparent are the overall larger data errors from MJD 55400 on, which coincides with the switch to the new `toolbox` where the differing scan-profile analysis allows the statement of such enhanced error estimates.
However even the average of the scattering data points with underestimated errors due to the former epochs are consistent with literature values (Table 2.4). This can be further underpinned by calculating histograms along the time line (Fig. 2.12 and Fig. 2.13).

Obviously the most frequent observed calibrators are 3C286 and 3C48 which also yield the best histograms for Stokes I, PD and PA. Here "best" means the most Gaussian-shaped histograms based on the largest amount of underlying data. The width of equally binned Gaussian fits denoted as the σ-value of the fits, are in general larger for all calibrators different of 3C286. This is because we choose 3C286 as the calibrator with the highest reliability and thus adjust the fits of the Müller matrix elements such that the published calibrator values of 3C286 are preserved. Especially in the case of NGC 7027 at 6 cm the large scatter is apparent. This is mainly because of the smaller data errors of the former epochs which make the fits unstable. Thus requiring 3C286 to stay at the nominal value makes it necessary for NGC 7027 to take over some percentage of partial polarization even though being unpolarized at least as stated in literature.
All these calibrators take part in the final goal of finding those Müller matrices that keep the reconstructed calibrator parameters of Stokes I, PD and PA as close to the literature values when being applied to the observed raw data. The set of derived matrices is indeed able to keep the calibrator values recovered from observed values in average close to the nominal input values. The Gaussian width σ of the appropriate histograms will later be applied as an additional systematic error to the statistical errors from the scan profiles in first instance as propagated due to the matrix-recovering process. It is legitimate to apply the largest *repeatability error* of all observed calibrators to data of non calibrator sources as we assume calibrators to be non-variable.
Table 2.5 lists those additional errors as outcome of the histograms. These calibrator-related repeatability errors can also be interpreted as a 1σ fluctuation of a value that ought to be constant just like the background. The *detection limit* is defined to be roughly a few sigma. Of course it would be more precise to plot histograms of the background fluctuations at the base of the scans. Now knowing that the Müller matrices reproduce the calibrator parameters well, the time dependency of the matrix itself has to be studied.
Starting with the sensitivity factor m_{11} for Stokes I, Fig. 2.14 shows a constant behavior within the first and second block of epochs. As mentioned before, after EP42 (MJD 55400 or July 2010)

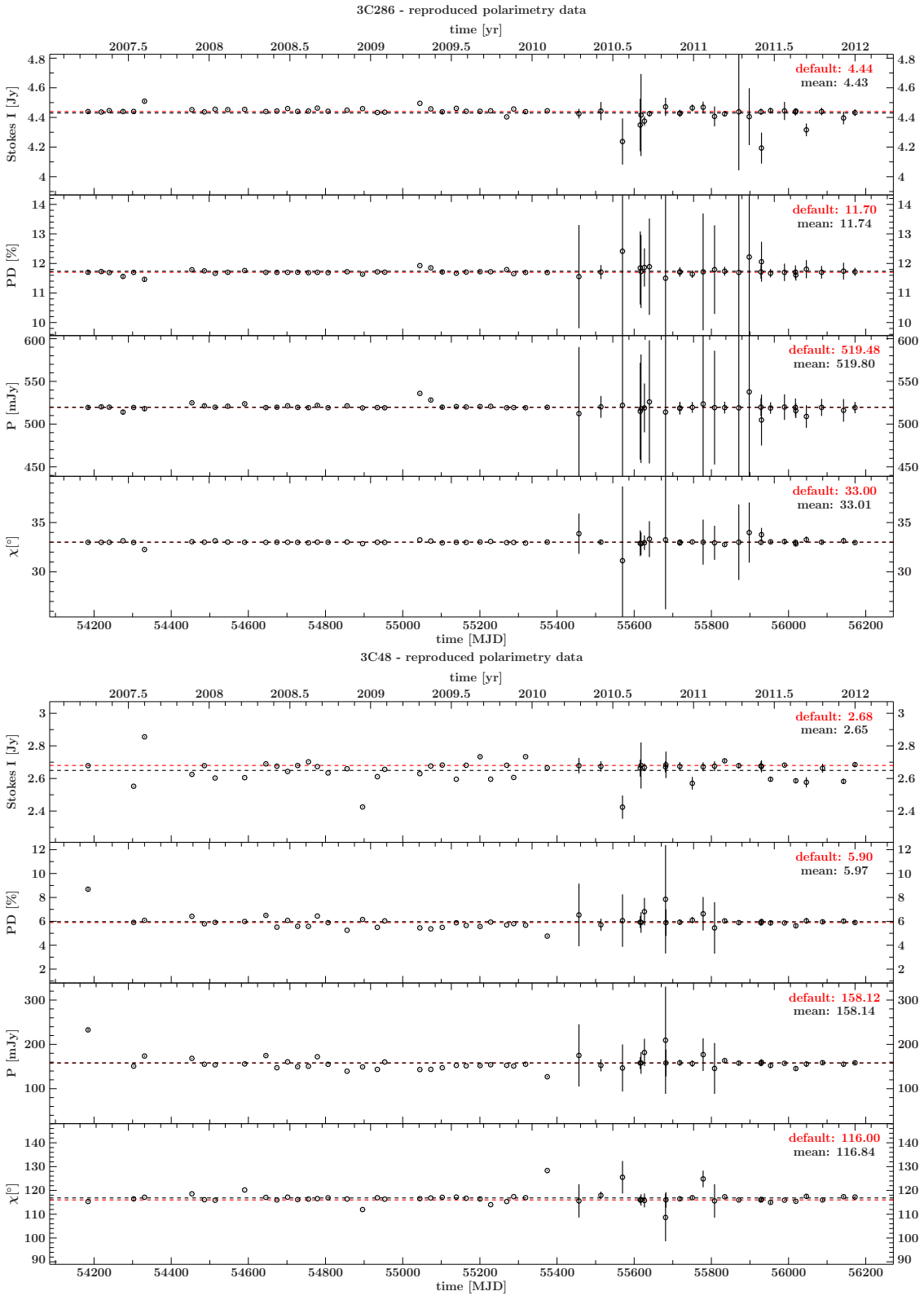

Figure 2.8.: 2.8 cm Light curves of re-calculated calibrator polarimetry data for 3C286 and 3C48; the red dashed line marks the nominal calibrator values from Table 2.4, the black dashed line the mean value of the re-calculated calibrator values based on observational data.

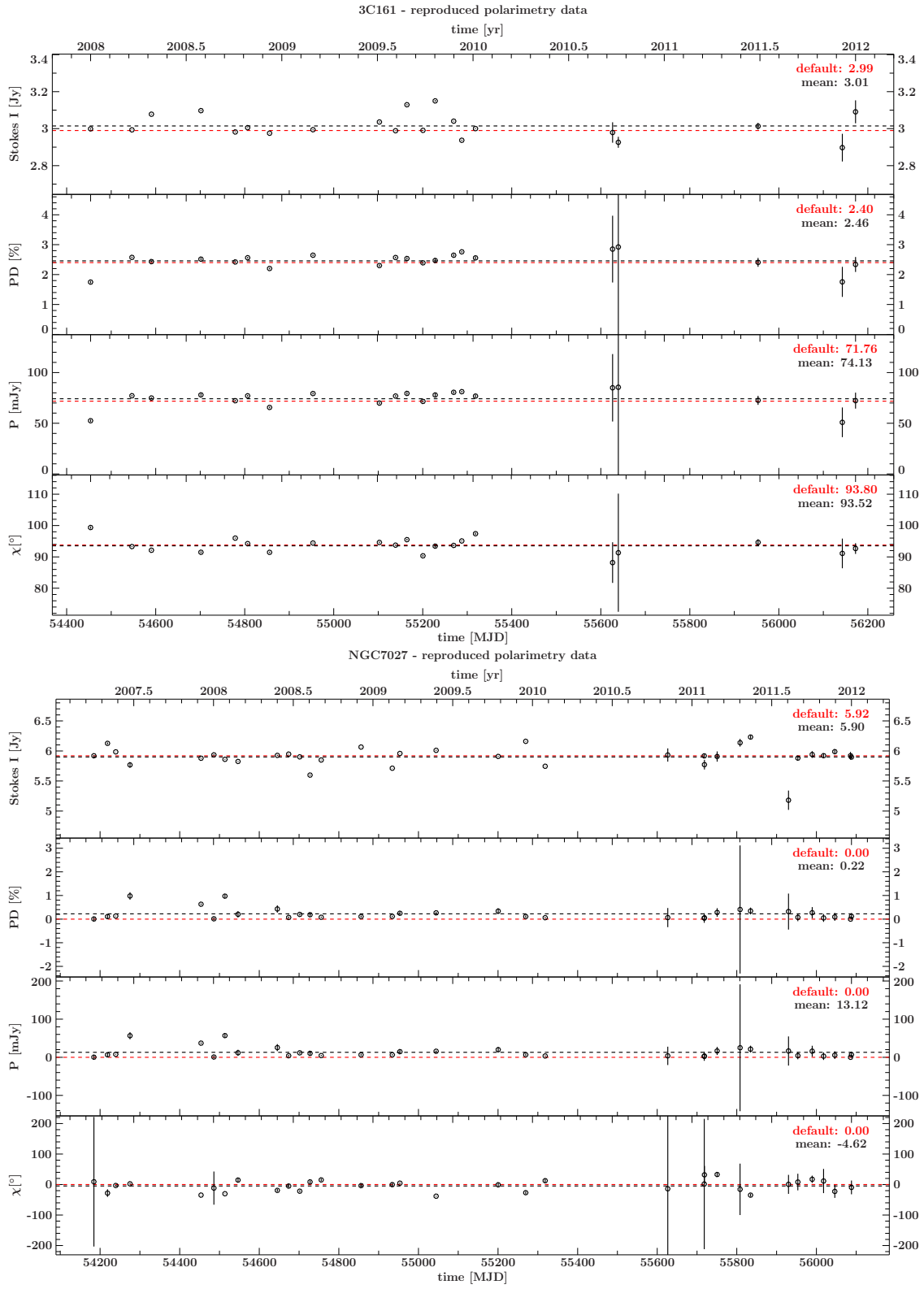

Figure 2.9.: 2.8 cm Light curves of re-calculated calibrator polarimetry data for 3C161 and NGC7027; the red dashed line marks the nominal calibrator values from Table 2.4, the black dashed line the mean value of the re-calculated calibrator values based on observational data.

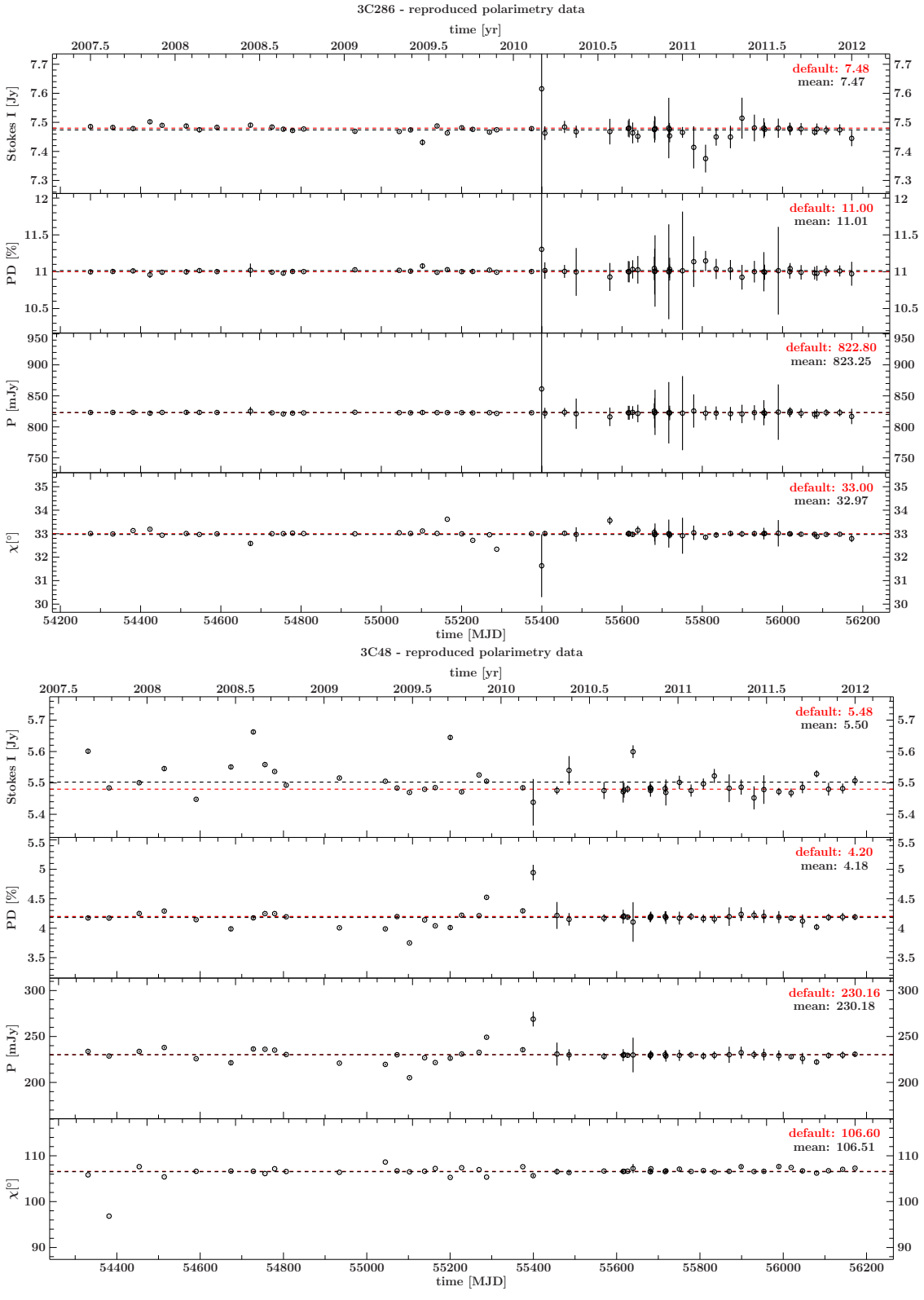

Figure 2.10.: 6 cm Light curves of re-calculated calibrator polarimetry data for 3C286 and 3C48; the red dashed line marks the nominal calibrator values from Table 2.4, the black dashed line the mean value of the re-calculated calibrator values based on observational data.

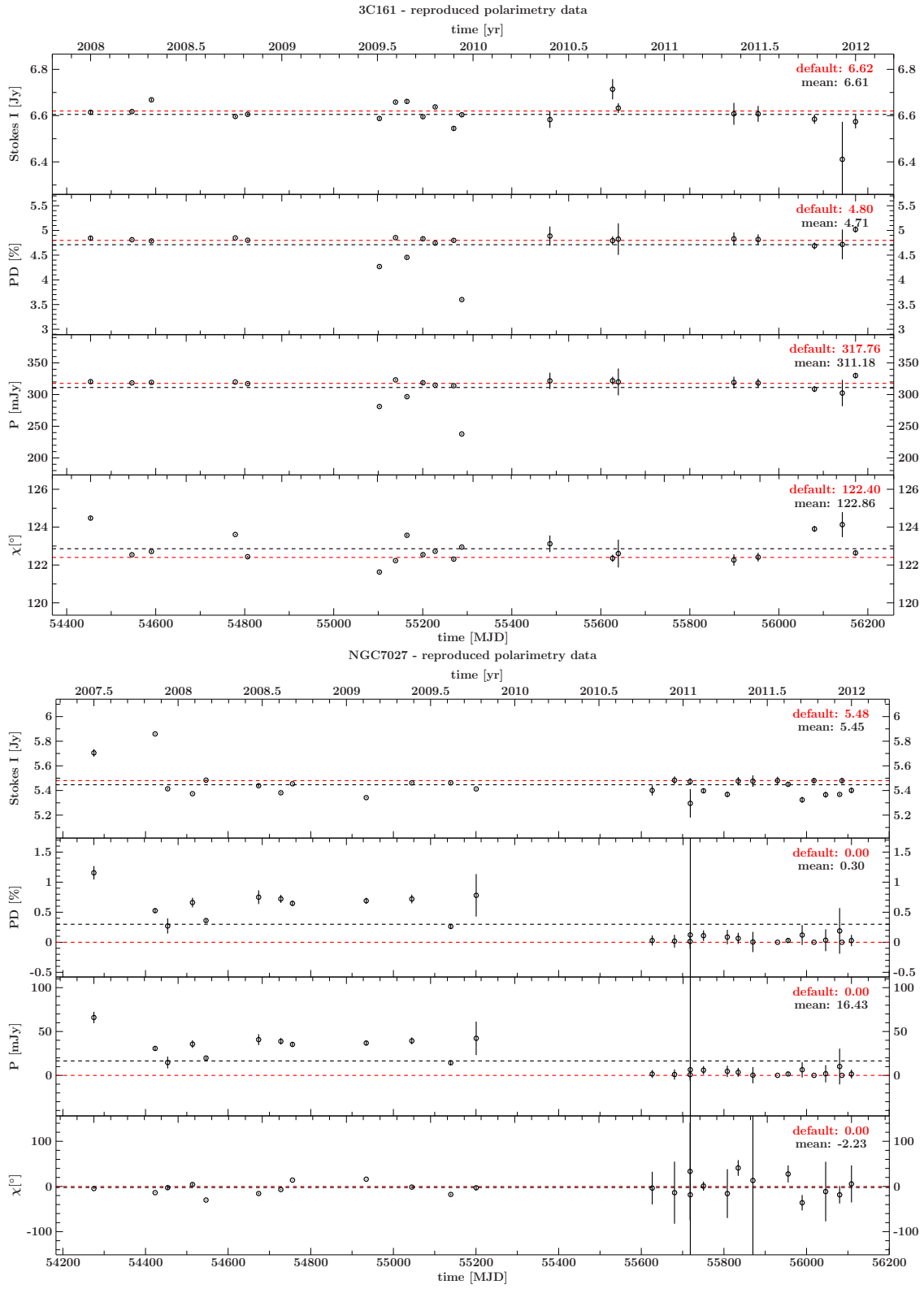

Figure 2.11.: 6 cm Light curves of re-calculated calibrator polarimetry data for 3C161 and NGC7027; the red dashed line marks the nominal calibrator values from Table 2.4, the black dashed line the mean value of the re-calculated calibrator values based on observational data.

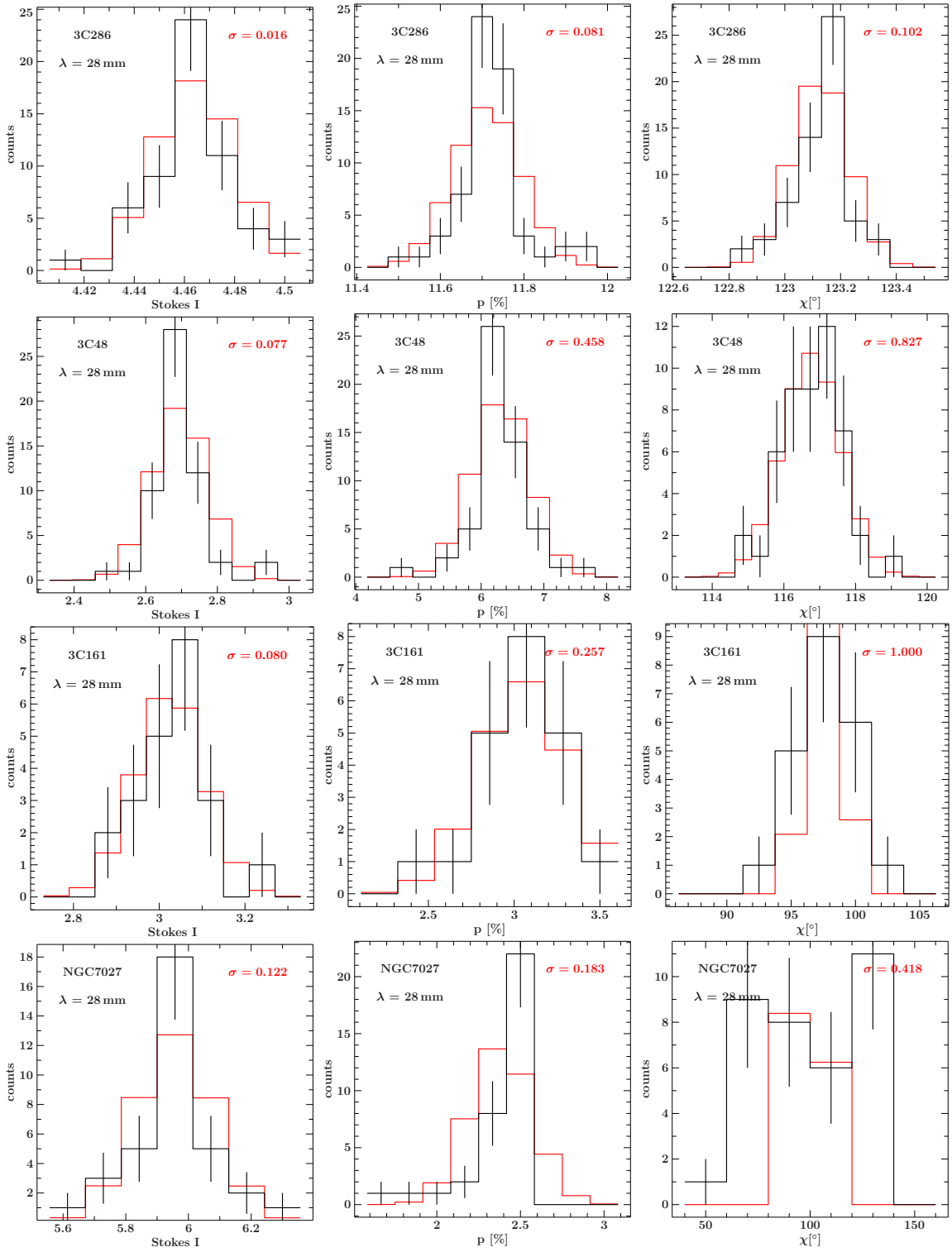

Figure 2.12.: Histograms of the 2.8 cm light curves for the observed calibrator sources 3C286, 3C48, 3C161 and NGC7027 for Stokes I (*left*), the PD (*middle*) and the PA (*right*). The red histogram resembles a Gaussian fit with the same binning. The width of the Gaussian is noted as σ inside the panels.

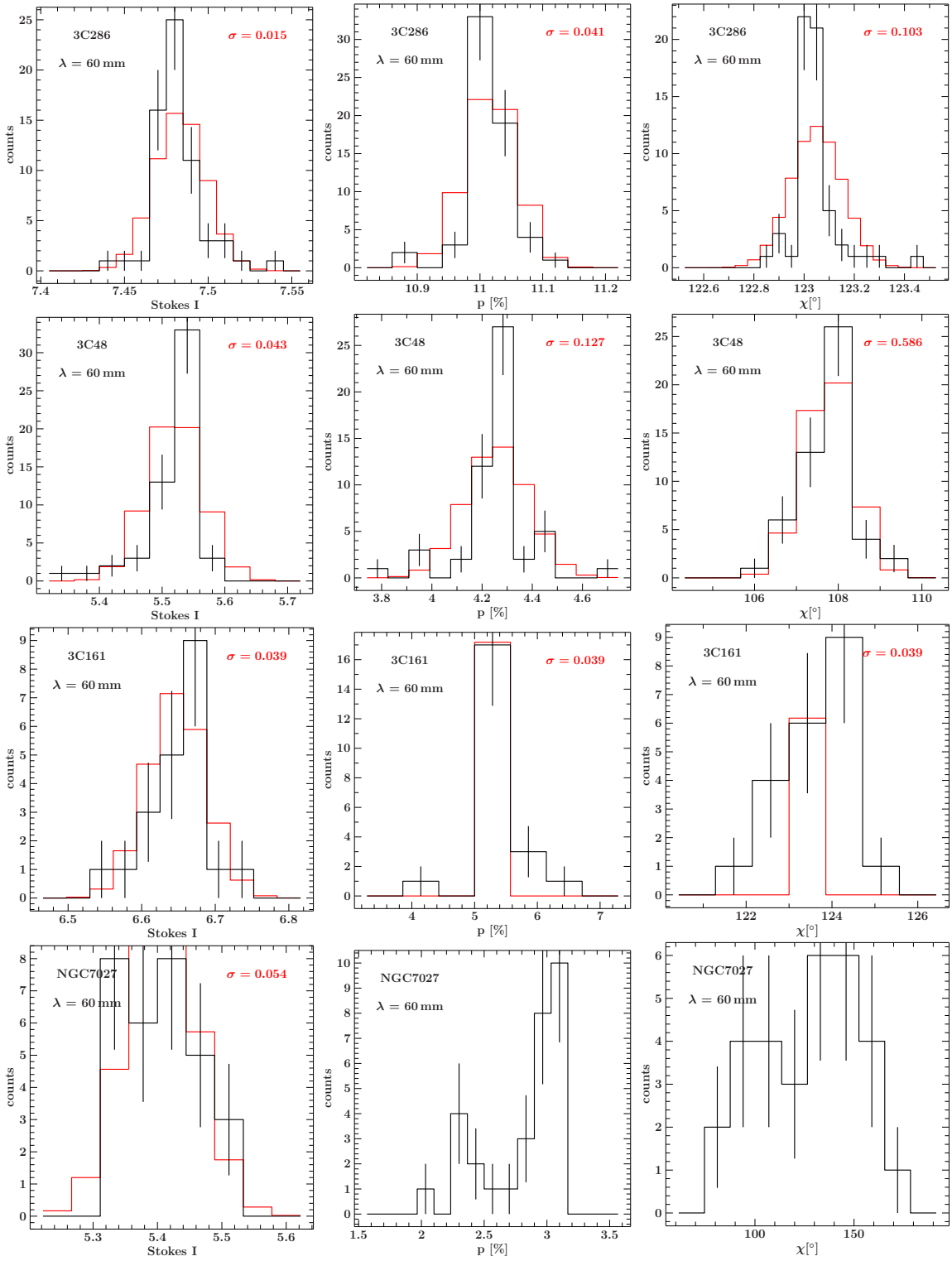

Figure 2.13.: Histograms of the 6 cm light curves for the observed calibrator sources 3C286, 3C48, 3C161 and NGC7027 for Stokes I (*left*), the PD (*middle*) and the PA (*right*). The red histogram resembles a Gaussian fit with the same binning. The width of the Gaussian is noted as σ inside the panels.

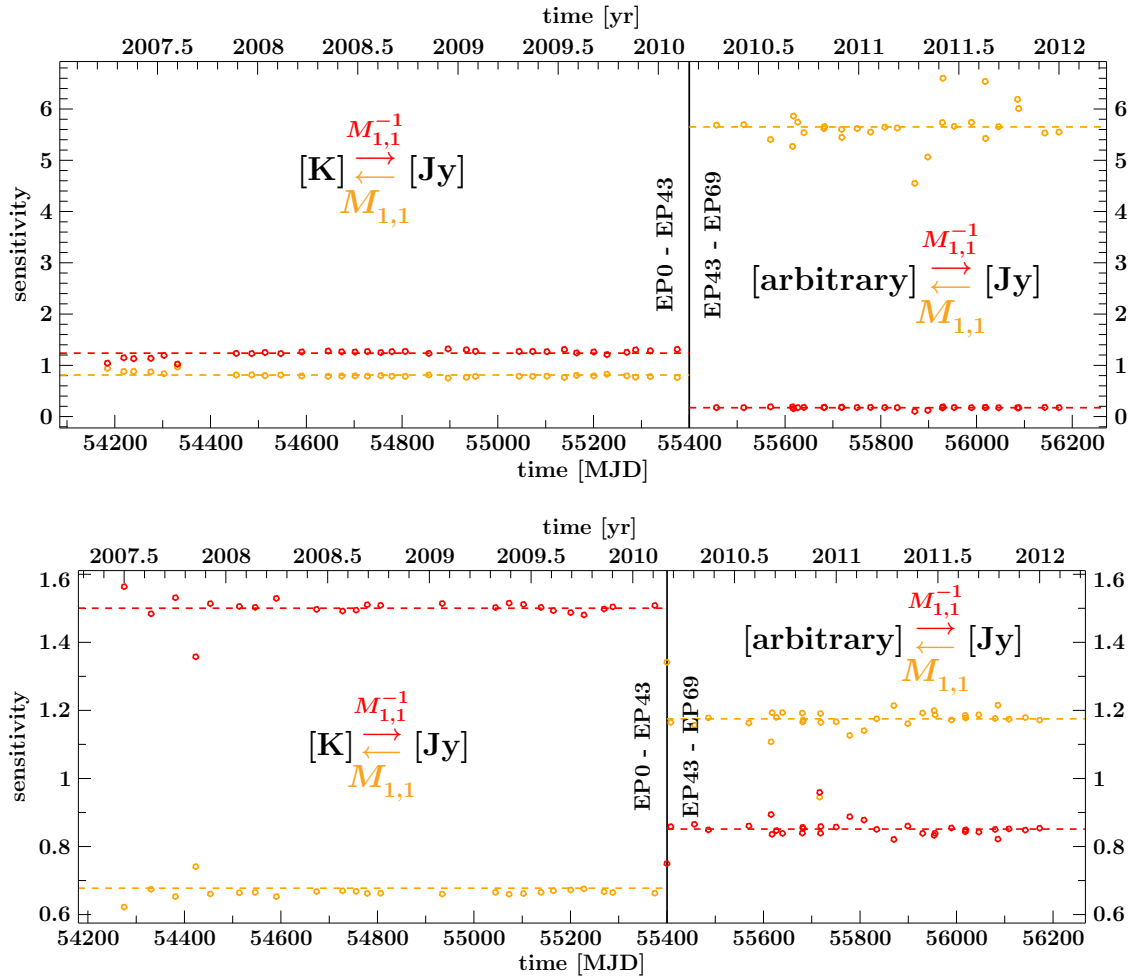

Figure 2.14.: Time evolution of the total power sensitivity factors for the MPIfR 2.8 cm (*top*) and 6 cm (*bottom*) receivers.

Table 2.6.: Sensitivity factors for the MPIfR 2.8 and 6 cm receivers.

	EP0-EP42		EP43-today	
	m_{11}	m_{11}^{-1}	m_{11}	m_{11}^{-1}
28 mm	1.24	0.81	0.17	5.65
60 mm	1.50	0.68	0.85	1.17

the file system and also the extraction procedure with the `toolbox` changed. The major change, namely the missing pre-calibration to Kelvins in the second block can be identified as jumps of the [K/Jy] to [arbitrary/Jy] sensitivity factors of different values. The mean derived sensitivity factors are listed in Table 2.6. Also the sensitivity factors of the inverse matrix are listed as they are the actual factors translating the units after data extraction (Kelvins or some non-pre-calibrated arbitrary units) directly to Janskys. These values are close to the proposed values given in the online documentation of the receivers also listed in Table 2.1. Now the rest of the matrices are further examined. Remember the equations Eq. 2.9 – Eq. 2.12 for the instrumental effects resembled by different elements of the Müller matrices. The depolarization is not further discussed, as the values seem to be strongly variable on large scales and can thus not be properly interpreted. This behavior has also been seen by A. Kraus (MPIfR, priv. comm.) in similar data.

Figure 2.15 and Fig. 2.16 plot the remaining quantities one can calculate from the derived matrices as referred to above.
Starting with the 2.8 cm receiver, Fig. 2.15 shows a clear difference in the behavior of data points before and after MJD 55900. The instrumental degree of polarization has a constant value of around 0 %–3 % before MJD 55900 and is raising to around 7 % after this break. The instrumental EVPA is scattering strongly before that date while being constant at $\approx -40°$. The vector rotation is scattering for all epochs.
Coincidental to the break seen in the data, the receiver internal "S5" switch (Sect. 2.2.1.1) got broken. The `toolbox` brings the option "nos5" to reduce polarimetry data also without this phase switch for epochs between 43 and today. Fig. 2.15 hence shows that setting this option is raising the instrumental degree of polarization and keeping the instrumental EVPA constant. It seems not to have an effect on the vector rotation. Examining the appropriate data for the 6 cm receiver shows how the instrumental polarimetric properties behave with time without a broken phase switch. The instrumental degree of polarization stays relatively constant between 0 % and 1 %. The receiver internal EVPA can roughly be said to scatter between $-50°$ and $-60°$ while the scattering is stronger below MJD 55400. This effect is much stronger for the vector rotation between Stokes Q and U. It is scattering heavily between $\approx -100°$ and $\approx 150°$ while staying constant between 80° and 90° after MJD 55400.
This is due to the change of the data analysis package to the new `toolbox` around MJD 55400. Being more explicit:

- the values for Stokes Q and U were derived from Gaussian fits in the former `toolbox` which might not be a correct and consistent procedure for polarimetry scans due to beam squinting
- as a consequence the Stokes parameter errors are larger for the new system, which makes each fit for the Müller matrix more stable and the results more consistent with each other.

Why does this only express itself in the EVPA rotation and not in the degree of polarization or the EVPA? The reproduced data for calibrator sources were free of such system-specific variations. This is because the analysis chain found those matrices that make exactly this possible. Would one use the same Müller correction-matrix for all epochs of data, the system internal changes would be visible in the reproduced data instead. This connection might be obvious but earns to be emphasized. Furthermore one should recall how the matrix elements are derived. Each line is gained in one fit where the second and third lines and columns, respectively accord to Stokes Q and U. Should there be something systematically wrong with the reduced observed values for Q and U, e.g., due to the reduction software as it is the case here, the appropriate matrix elements are derived such that the result fits best to the input Stokes I calibrator value. Ideally, the contributions of each m_{12} and m_{13} in Eq. 2.10 should be constant. But, should for some reason variations in the Stokes Q and U data require both to be different, the sum must still be the same to yield a constant reconstruction of the Stokes I calibrator value, which is how the fitting is defined. About the same argument holds also for Eq. 2.11. In contrast, Eq. 2.12 includes the whole sub-2×2 rotation matrix with $m_{22}, m_{23}, m_{32}, m_{33}$. The elements m_{22}, m_{23} and m_{32}, m_{33} most probably have to be differently adjusted to gain the required calibrator Stokes Q and U values and let the so calculated rotation angle of the instrumentally induced EVPA vary strongly with different data sets of distinct epochs.
A pretty good diagnostic tool for instrumental polarization is plotting the uncorrected raw data directly after being reduced by the `toolbox` (see Fig. 2.7 for details on the data-processing) in the $Q-U$-plane, Fig. 2.17.

The calibrator 3C286 followed by 3C48 are by far the most frequently observed calibrator sources which makes them ideal to study the instrumental effects in this plot. What conclusions can we draw just by looking at these plots?

- The black data cloud resembles fully corrected data. From the center $Q-U$ position of this

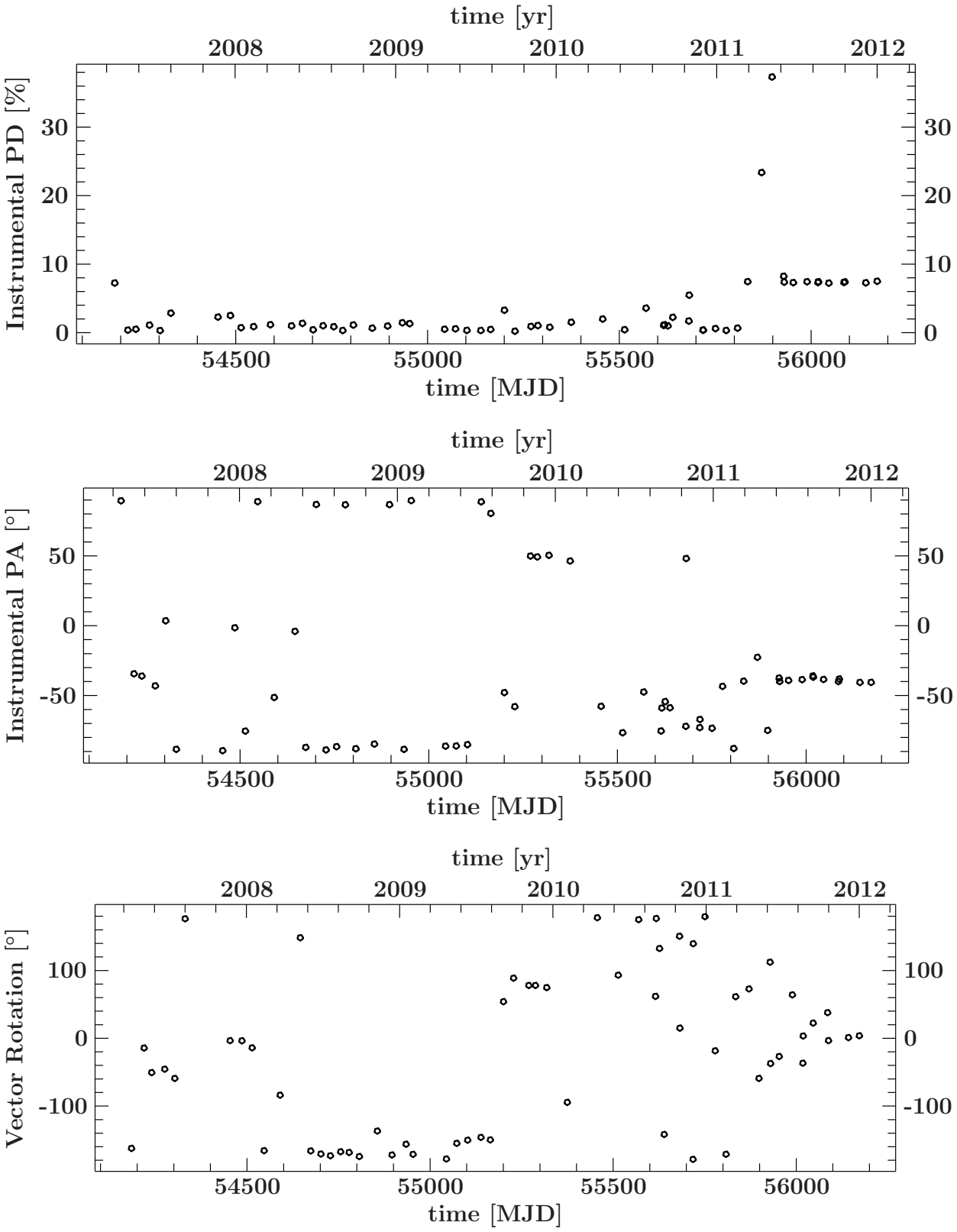

Figure 2.15.: Instrumentally imposed degree of polarization (*top*), polarized angle (EVPA) (*center*) and EVPA rotation (*bottom*) for the MPIfR 2.8 cm receiver.

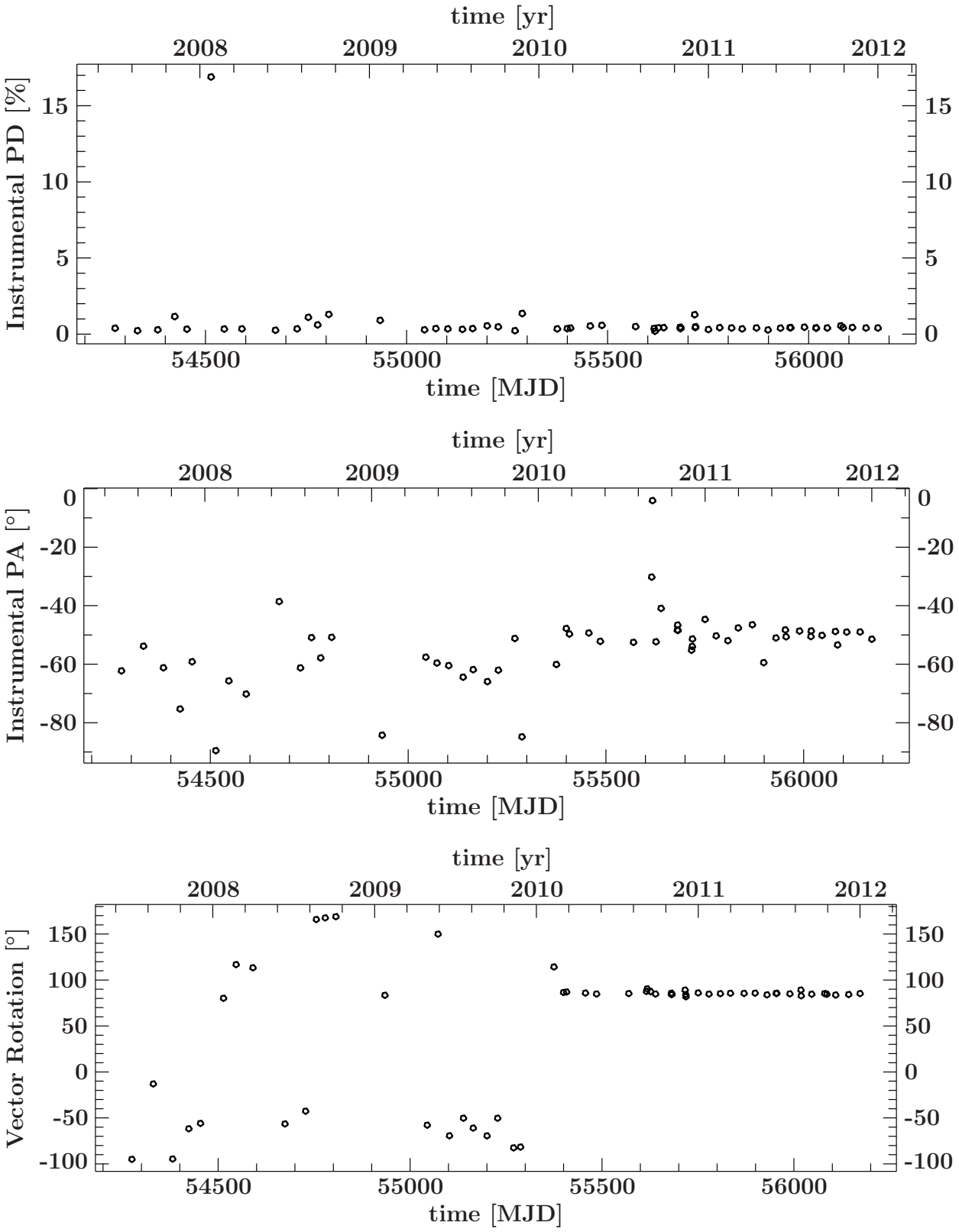

Figure 2.16.: Instrumentally imposed degree of polarization (*top*), polarized angle (EVPA) (*center*) and EVPA rotation (*bottom*) for the MPIfR 6 cm receiver.

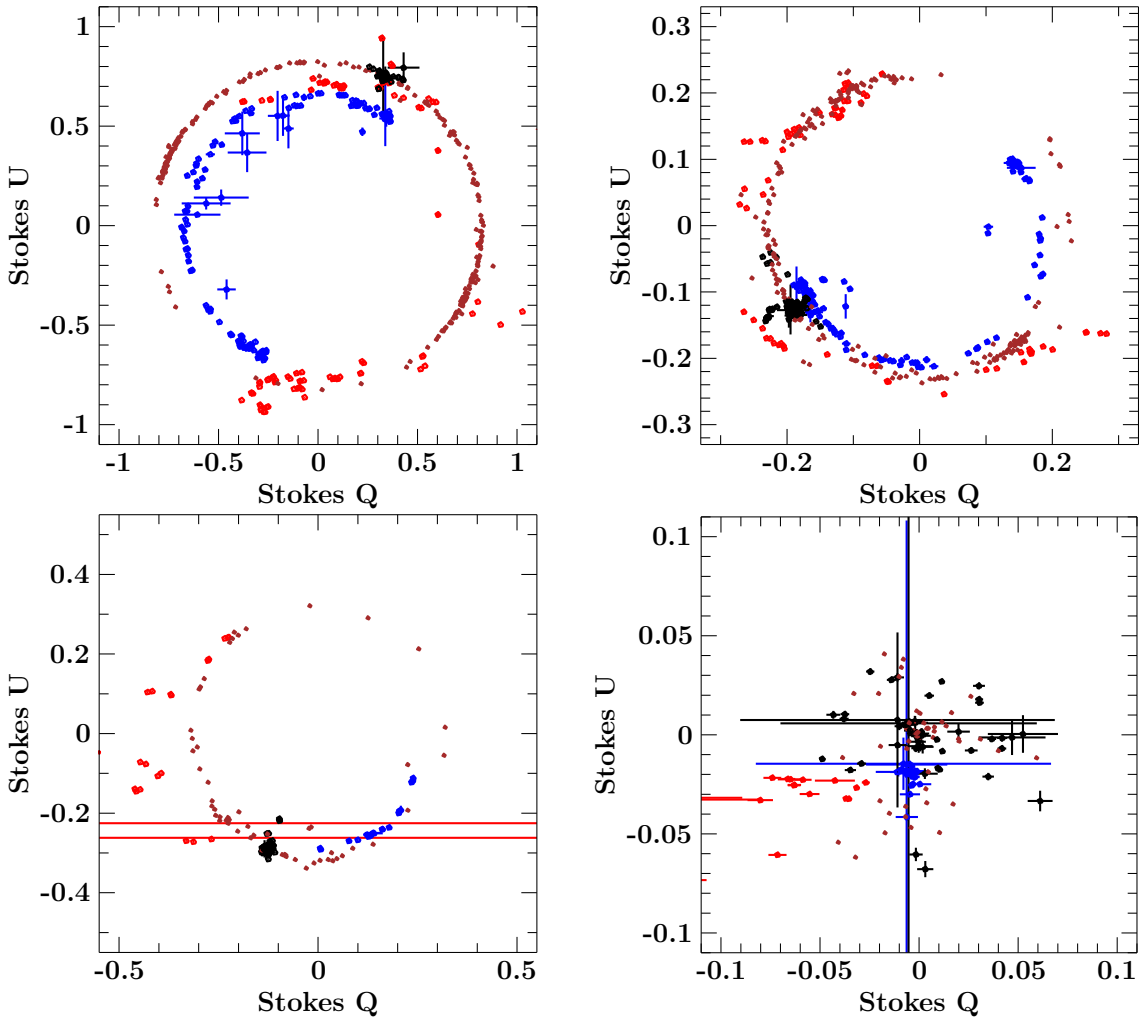

Figure 2.17.: Multi-epoch Q–U plot for 6 cm data including: uncorrected data for the new data system (EP43 and later) in blue, for the former data system in red, fully corrected data as black data cloud and in brown the corrected data rotated with the appropriate parallactic angles. *top left:* 3C286, *top right:* 3C48, *bottom left:* 3C161, *bottom right:* NGC7027.

cloud one can directly calculate the mean degree of polarization and the mean EVPA χ for the present calibrator.

- Thinking further, one could apply the rotational matrix with the changing parallactic angle q to this data cloud for each epoch. The result is shown as brown data performing a part of a circle just as far as the distribution of parallactic angles allows it from different observations of the calibrator at different positions on the sky. Any deviation from this circle gives a direct hint to instrumentally induced effects on measured polarimetry data.

- Blue data points resemble the uncorrected raw data of all epochs more recent then EP43. Data from previous epochs are plotted in red. Clearly, the recent data are drawing a nice half of an ellipse. This is just because of the constancy of the rotational angle and therefore the instrumental-rotation matrix with the elements $m_{22}, m_{23}, m_{32}, m_{33}$ for all data later than EP43 (Fig. 2.16). Before that epoch, this 2×2-matrix is highly variable which not only includes the resulting rotational angle but also the Stokes Q and U sensitivity factors m_{22} and m_{33}. This explains the wide scatter of the appropriate data points for all epochs before

EP43 plotted in red. This panel is actually too small to show the whole scattering cloud. If one would fit an ellipse to the blue data cloud, its eccentricity would gave a direct measure of the instrumental effects at least on data taken after EP43.

- The radius of the blue ellipse is smaller than the one of the final corrected data that can be found spread on a circle around it. This is because the matrix-included sensitivity makes the corrected data appear in units of Janskys. The blue raw-data however have arbitrary units. The ratio of both radii again returns the overall sensitivity factors stated in Table 2.6
- Both the nearly half-circle of parallactic rotated corrected calibrator values and the about half-ellipse of raw-data points are rotated with about 90 ° against each other. This extra rotation is the instrumental rotation angle plotted in Fig. 2.16.
- The same as stated above should also be visible in more clearness for 3C161 if there would be more observations.
- Finally, the plot for NGC 7027 just shows point clouds because of its unpolarized nature. Kraus (1997) thus argues for the necessity to include NGC 7027 as calibrator source improving the Müller matrix derivation.

To demonstrate how these plots appear for the 2.8 cm data, see Fig. 2.18. The strong scatter of the instrumental rotational angle in Fig. 2.15 already suggests the strong scatter of data from both blocks of epochs. Unlike for the 6 cm data no significant improvement of epochs reduced with the improved system is seen.

2.3. Faraday Rotation

Faraday rotation is an important effect regarding polarized signals. In order to tell the exact paths of magnetic fields out of high resolution VLBI polarimetry maps one has to correct for *Faraday rotation* (Burke & Graham-Smith, 2009) which is rotating the EVPA of a linear polarized wave in the source system as it propagates through magneto-ionic material where the LCP- and RCP-components of the wave have different phase velocities. The amount of angle rotation is $\Delta\chi = \mathrm{RM} \cdot \lambda^2$ with RM as the "rotation measure". The RM is furthermore directly proportional to the density of electrons n_e in the gas responsible for the EVPA rotation with $RM \sim \int n_\mathrm{e} B \cos\theta dl$ where B the magnetic field strength and θ the angle between the magnetic field and the line of sight. The Faraday effect for extended sources such as 3C 111 is modeled by Burn (1966). Thus plotting the RM against λ^2, the slope is proportional to the strength of the electron shield, inter-stratified with a magnetic field. Examples, e.g., for 3C 111 are included in Zavala & Taylor (2002) and for 3C 449 in Feretti et al. (1999).
Faraday rotation can be the reason for severe depolarization. Saikia & Salter (1988) review two different reasons for that. One is called "side-to-side" depolarization of an external shield (Burn, 1966). In this case the telescope's beam integrates over regions of different density and thus polarization angles. The average degree of linear polarization will be attenuated. This kind of differential depolarization is a strong function of the width of the beam and hence the resolution. This is in turn a function of observing wavelength for a single dish beam. The larger the wavelength, the larger the beam covering different regions of different properties and Faraday rotation. The decrease of the net degree of polarization with increasing wavelength, however, originates also in the steep spectra of extended radio sources (Conway et al., 1974; Liu & Pooley, 1991; Morris & Whiteoak, 1968). The steeper the radio power-law spectrum, the more the source reveals a dominance of extended, optically thin regions of thin gas at larger wavelength compared to the bright flat-spectrum core (Perley, 1982). Covering compact as well as extended regions with an additionally larger beam at longer wavelength, will thus lead to a significant contribution of Faraday shields attenuating the

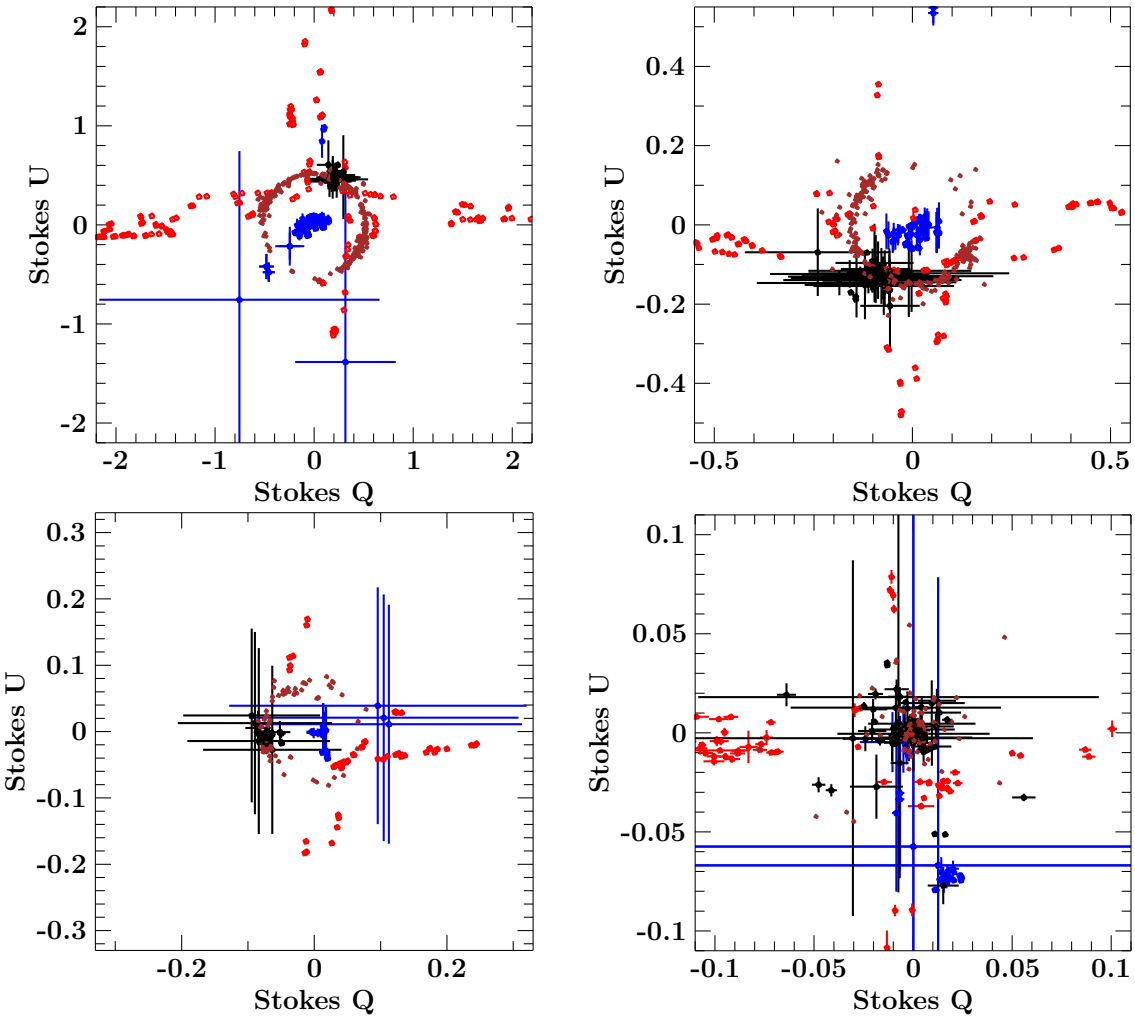

Figure 2.18.: Multi-epoch Q–U plot for 2.8 cm data including: uncorrected data for the new data system (EP43 and later) in blue, for the former data system in red, fully corrected data as black data cloud and in brown the corrected data rotated with the appropriate parallactic angles. *top left:* 3C286, *top right:* 3C48, *bottom left:* 3C161, *bottom right:* NGC7027.

net polarization.

The second reason for depolarization of radio sources is the "front-to-back" (Saikia & Salter, 1988) or intrinsic depolarization inside one line of sight due to different layers of gas with different densities of magnetoionic electron gas. Here again, decreasing degrees of polarization are expected for longer wavelength in steep-spectrum sources, as the more layers of extended gas are covering the line of sight, the longer the wavelength gets.

In such situations single-dish observations are best performed at smaller wavelength. In general for interferometers as well as single-dish antennas it is useful to derive the value of the rotation measure to account for the foreground shield or internal EVPA rotation. For VLBI maps one will be able to determine the tracks of magnetic field lines as the ones lying perpendicular to the Faraday-corrected EVPA vectors in the map.

2.4. Single Dish Radio Polarimetry of 3C 111

After understanding the instrumental behavior and having properly calibrated the polarimetry data of the whole sample of blazars for all historic epochs, now the full Stokes properties of 3C 111 can be explicitly studied.

2.4.1. Morphology at 6 cm and 2.8 cm

2.4.1.1. Observations and data analysis

For interpreting cross-scans over an extended radio galaxy such as 3C 111, we have to know it's source morphology at the appropriate wavelengths of 6 cm and 2.8 cm. Therefore full Stokes mosaic maps are measured with the 100-m Effelsberg telescope. To do so, the beams at 6 cm (FWHM: 147″) and 2.8 cm (FWHM: 70″) are gradually driven over the source.
The raw-data are delivered as FITS image files. The analysis and plotting is done with the analysis software `ISIS`. To define the background, the flux values of all pixels are plotted as histogram. The maximum lies around the background flux level which is well fitted with a Gaussian of standard deviation σ. The logarithmic color scale is defined between 3σ and the flux maximum for all displayed maps. The contour levels individually stated in the figures' captions are chosen independently of the background-σ. The main criterion is to find contour levels that encircle regions of interest such as lobe structures.
The total intensity maps are plotted in Fig. 2.19 with over-plotted directions of the cross-scans. Luckily 3C 111 was observed always around the same positions on the sky at $\pm 50°$ inclination of the az/elv to the ra/dec coordinate systems (Fig. 2.23) resulting in unchanged scanning directions across the source main axis and perpendicular to it.
Furthermore, the overall flux level of the 6 cm map is higher than the one of the 2.8 cm one with the core dominating the overall flux level at both wavelength. Note that the outer 6 cm map contours are lacking sub-structures in contrast to the 2.8 cm map where the actual core can indeed be separated from the extended lobe emission. Visible is at least a clear separation of the Western hot-spot. Maps with polarized flux are plotted in Fig. 2.20. Here even at 6 cm a separation of the western hot-spot can be identified. At 2.8 cm both hot-spots are clearly separated from the core in contrast to the total intensity map. Also here the core is dominating the map at both wavelength. The fractional polarization is mapped out in Fig. 2.21. Obviously the core does no longer dominate. Due to some unrealistic artifacts with too large values in the raw-data at 6 cm, an image is plotted such that only the inner compact region is shown. The regions of largest fractional polarization (up to 10 %) are the outer regions located at the hot-spots. The same is valid at 2.8 cm with an overall higher level of maximum 20 % at the outer edges. The core regions show polarizations of only some percent at both wavelength. There is a third information missing in terms of polarization – the EVPA. Figure 2.22 over-plots the electric vector position angles over intensity maps. The length of the vectors denote the polarized intensity that is already shown in Fig. 2.20. The vector angles at 6 cm perform a swing of over 90° from the Western to the Eastern hot-spot whereas they seem to stay at about the same angle at 2.8 cm. Averaging over both hot-spot regions and the core, the EVPA at 6 cm changes continuously from $\approx -40°$ at the western lobe over the core with $\approx -20°$ to the eastern lobe with $\approx -80°$. At 2.8 cm the EVPA changes in the same order from $\approx 40°$ over $\approx 50°$ back to $\approx 40°$. Note that the source orientation in these maps is wrong due to defective raw-data and has to be mirrored at the right-ascension axis to get a correct orientation as in the foregoing maps.

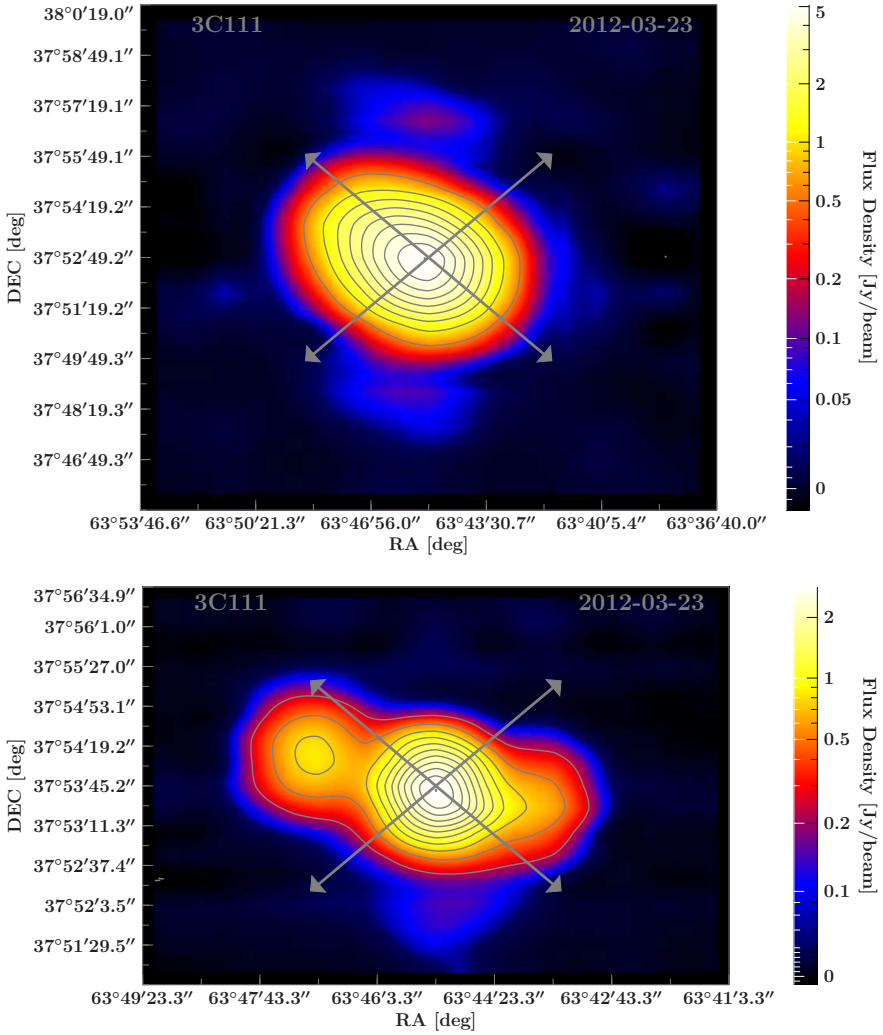

Figure 2.19.: Total intensity maps measured with the 100-m Effelsberg telescope in B1950.0 coordinates. *top:* map at 2.8 cm / 10 GHz with contour levels (-17,241,501,761,1020,1280,1540,1800,2059,2319,2579,2838) mJy beam^{-1}, *bottom:* at 6 cm / 5 GHz with contour levels (-41,530,1103,1675,2247,2819,3391,3963,4535,5107) mJy beam^{-1}. The arrows denote the driving directions of the beams across the source of 50 ° across the source extension and -50 ° perpendicular to it.

2.4.1.2. Interpretation and Discussion

Many interesting effects can be seen in the set of maps presented in the previous section. First the **total intensity** maps (Fig. 2.19) at larger wavelength that are additionally less resolved because of the larger beam, reveal more extended emission than at a shorter wavelength of 2.8 cm. The overall flux level dominated by the core is also higher at 6 cm. Why should the core have more flux when mapped at longer wavelengths? Boettcher et al. (2012) refer to the steepening of the Synchrotron power-law spectrum down the jet stream (see also Sect. 1.3.1). The result is that both extended Western and Eastern radio lobes are dominating at longer wavelength such as 6 cm and are thus over-shining the whole map. This is a common feature in extended radio sources as Perley (1982) show. In turn it offers a good explanation for the overall flux dominance of the 5 GHz light curves in Fig. 2.26. First neglect the larger beam size at 5 GHz (6 cm) compared to 10 GHz (2.8 cm). Due to the steep radio power-law spectrum, the extended radio lobes emit more Synchrotron photons at lower frequencies than the core region as the latter is still optically thick to

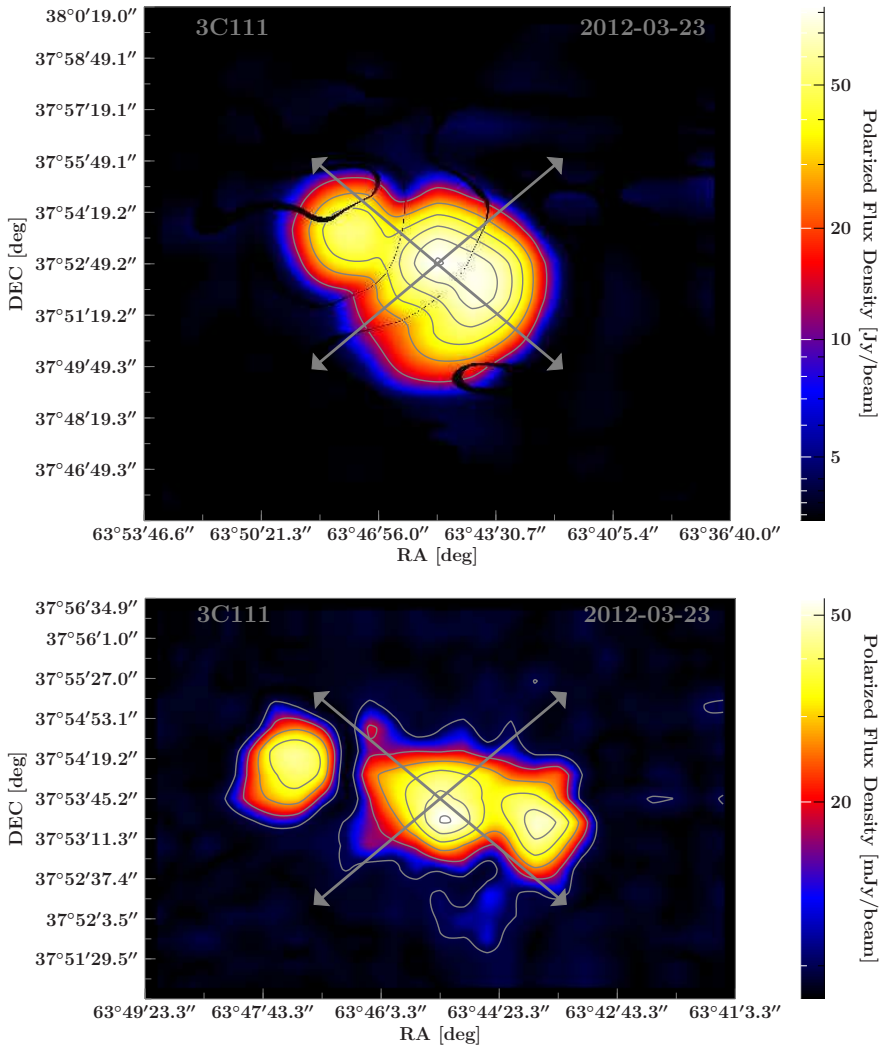

Figure 2.20.: Maps of linearly-polarized flux density measured with the 100-m Effelsberg telescope in B1950.0 coordinates. *top:* map at 2.8 cm / 10 GHz with contour levels (0,9,18,27,36,45,54) mJy beam^{-1}, *bottom:* at 6 cm / 5 GHz with contour levels (0,13,27,41,55,69,82) mJy beam^{-1}. The arrows denote the driving directions of the beams across the source of 50 ° across the source extension and -50 ° perpendicular to it.

photons of that frequency. That effect is additionally emphasized when considering that the 5 GHz beam with a FWHM of 146″ covers large fractions of 3C 111 having a total diameter of ≈ 200″ and thus capturing large fractions of extended lobe emission. Hence the maps measured in March 2012 reveal an overall higher peak flux level of ≈ 5 Jy at 5 GHz than ≈ 2 Jy at 10 GHz.
The maps of **polarized intensity** (Fig. 2.20) opposed with the maps of **fractional polarization** (Fig. 2.21) also reveal many important information. First, the fractional polarization is largest at the fronts of the extended radio lobes seen in both maps reaching 10–20 % compared to an average degree of ≈ 2 % around the core also measured by MOJAVE being sensitive to the core only. This is seen in many other extended radio galaxies (Saikia & Salter, 1988). An explanation for the enhanced degree of polarization in extended lobe-regions of steep radio spectra is given by shocks driving into the interstellar medium. This leads to a compression and local alignment of the magnetic field (Marscher, 1996, 2006), presumably the front of the produced hot-spots. Aligned magnetic field lines automatically enhance the fraction of linearly polarized Synchrotron emission

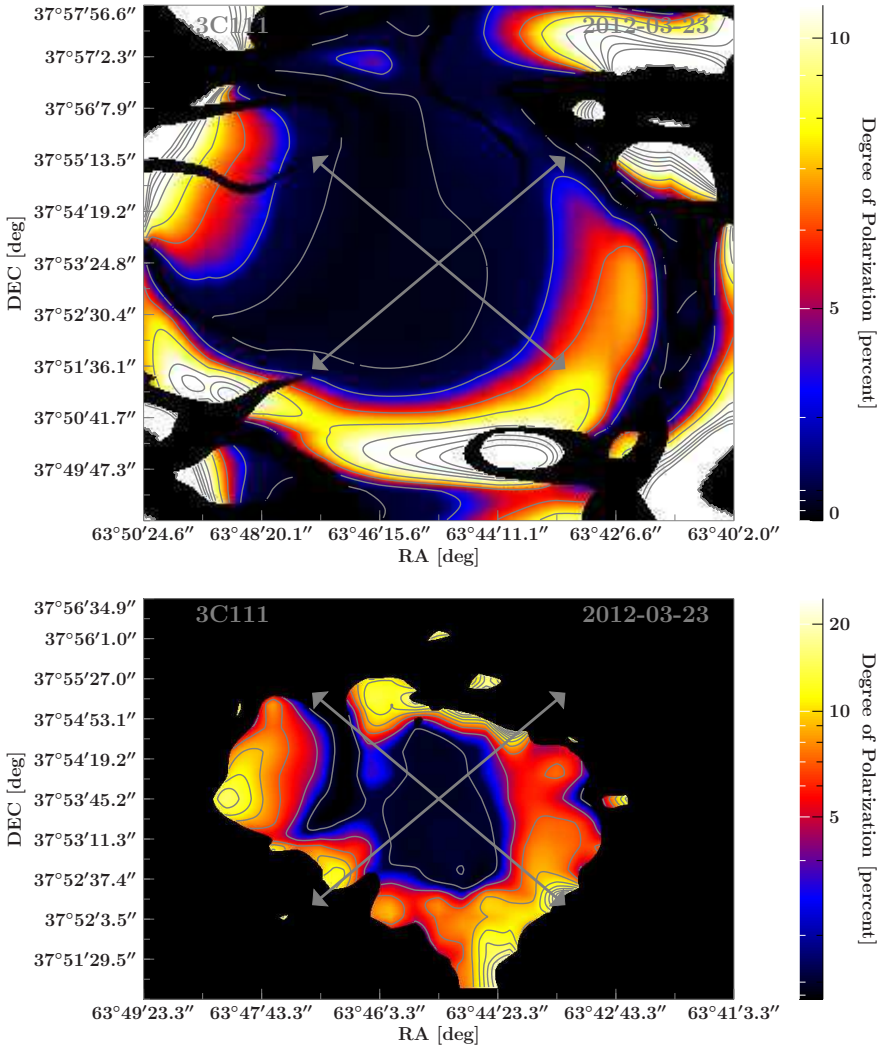

Figure 2.21.: Maps of fractional linear polarization measured with the 100-m Effelsberg telescope in B1950.0 coordinates. *top:* map at 2.8 cm / 10 GHz with contour levels (0,2,5,7,9,11,14,16,18,20,23,25) %, *bottom:* at 6 cm / 5 GHz with contour levels (0,2,4,6,8,11,13,15,17,20) %. The arrows denote the driving directions of the beams across the source of 50 ° across the source extension and -50 ° perpendicular to it.

over radiation whose net degree of polarization is lower because of an origin in more misaligned magnetic fields.

As the core is dominating the whole source in total flux, also the polarized flux is dominated by the core. Figure 2.20 shows this well, although the dominance of the core in polarized flux is not that significant as for total flux due to the also strong gradient between core and lobes in fractional polarization.

The overall level of linear polarization in terms of the degree of polarized emission is higher at the shorter wavelength of 2.8 cm. This is most likely because of intrinsic as well as external depolarization due to Faraday shields (Sect. 2.3) at the longer wavelength of 6 cm. The scanning direction being slightly misaligned with the jet-lobe-axis, however, allows 3C 111 to be studied for its core-polarization within the F-GAMMA program even though the lobes contribute significantly to the polarized flux.

At last, I want to discuss the distribution of the polarization vectors. At 6 cm the position vectors do not show the same orientation as at 2.8 cm. The average difference between the EVPAs of 2.8 cm

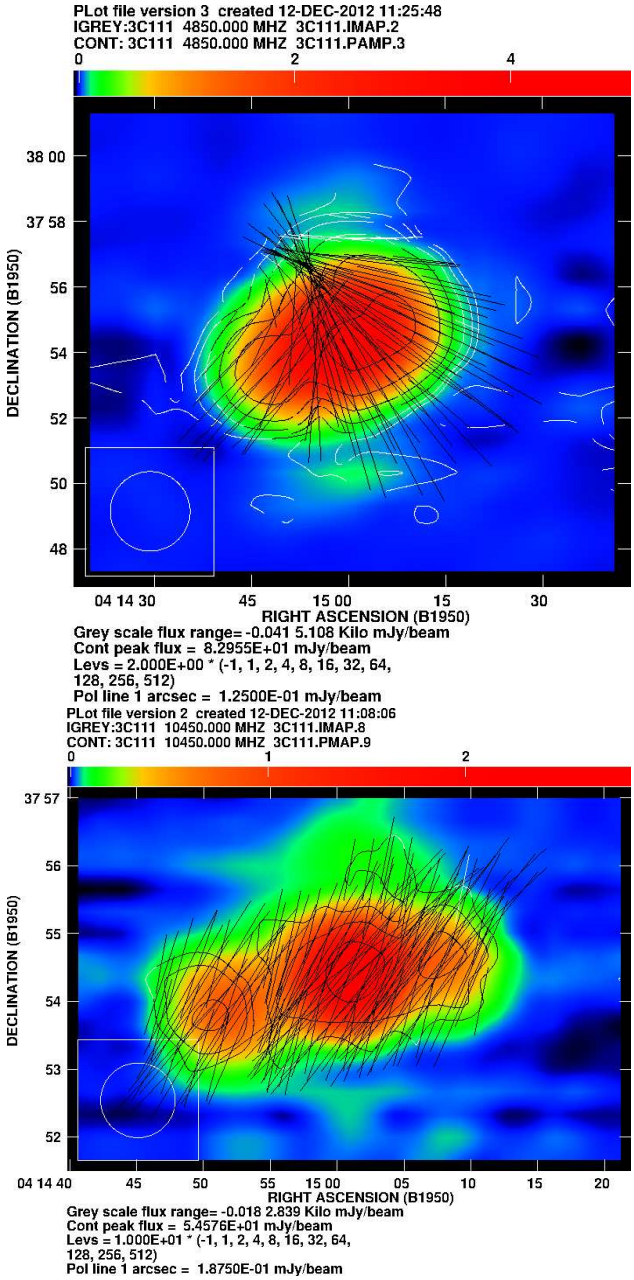

Figure 2.22.: Full Stokes maps with appropriate contours measured at the two wavelength of 6 cm (*top*) and 2.8 cm (*bottom*) in B1950.0 coordinates. Total intensity is color coded with additional contour lines. Black over-plotted vectors resemble the linearly-polarized intensity – the vector angle accords to the electric vector position angle of linear polarization, the length to the polarized flux. Due to an error in the raw-data, the present maps appear mirrored at the right ascension axis (Image courtesy: U. Bach, MPIfR).

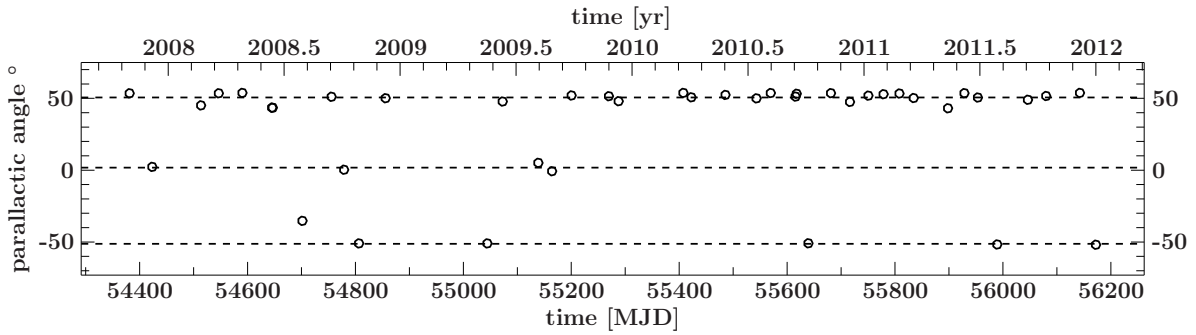

Figure 2.23.: Parallactic angles measured during observations of 3C111.

and 6 cm is between 80° and 120° due to the rotation at 6 cm. Faraday rotation (Sect. 2.3) can be a possible explanation for that. The rotation of the EVPA χ is describable by $\Delta\chi = \mathrm{RM} \cdot \lambda^2$ with the rotation measure RM, a factor proportional to the magneto-ionic matter in the line of sight. The larger the wavelength, the stronger also the rotation. This might explain the average difference between both wavelengths. The rotation of the vector angle across the source extension at 6 cm might be due to inhomogeneous extended electron gas covering the source and getting visible at longer wavelength as seen above. Additionally, the maximum level of the degree of polarization is higher at 2.8 cm with $\approx 20°$ compared to $\approx 10°$ at 6 cm. This is a second hint for Faraday rotation. As the rotation is larger at 6 cm, integrating over different depths of gas with different polarization angles with the Effelsberg beam will return a smaller net degree of polarization due to the cancellation of orthogonally aligned vector components. After Sect. 2.3 this is also called "front-to-back" depolarization (Saikia & Salter, 1988). Besides, also the integration over spatially adjacent regions will reduce the overall fraction of polarized emission due to the rotation of the position angles across the source at 6 cm. Saikia & Salter (1988) call this effect "side-to-side" depolarization. Both effects can in principle contribute. Which one dominates can not be told based on the given data.

2.4.1.3. Source extension at 6 cm

The overall diagonal diameter of extended emission from 3C 111 measured by 1997 is 215″ (Leahy et al., 1997). Compared to this, the FWHM of the 100-m Effelsberg telescope's beam at the used wavelength of 6 cm (5 GHz) is 147″ and 70″ at 2.8 cm (10 GHz). (Luckily) 3C111 was mainly observed at the same parallactic angle of +/-50 ° (Fig. 2.23) which corresponds to the angle between the horizontal and equatorial coordinate systems. The source is aligned by ≈ 60 ° towards the horizontal coordinate system (Linfield & Perley, 1984). As a result the scanning directions performed both in azimuth and elevation cut 3C 111 approximately both parallel and perpendicular to the jet-axis. The exact scanning directions are plotted as grey arrows in Fig. 2.19–Fig. 2.21. In one direction the beam thus sweeps over parts of the elongation of 3C111 resulting in broadened scan profiles only seen at 6 cm where the core is over-shined by extended emission from the radio-lobes. Exemplary sub-scans from real data are shown in in Fig. 2.24. See the sub-scans 1 and 2 for profiles broader than the actual beam-FWHM. To show this Gaussians are fitted to the upper two thirds of the recorded scans. The resulting profile's FWHMs are labeled within the plot windows.

To visualize what happens, recall the mosaic-maps presented in the previous two sections. The extended structure is not assumed to change on the timescales of the present campaign of observations from 2007 until today. Thus, the maps recorded at the beginning of 2012 can be treated as a showcase in terms of the overall source morphology.
Fig. 2.25 shows profiles gained when cutting the mosaic Effelsberg maps along the drawn lines corresponding to the az/elv scanning directions in most of the epochs. Expected are similar beam shapes and widths as seen in real data profiles such as in Fig. 2.24. Indeed those profiles that cut

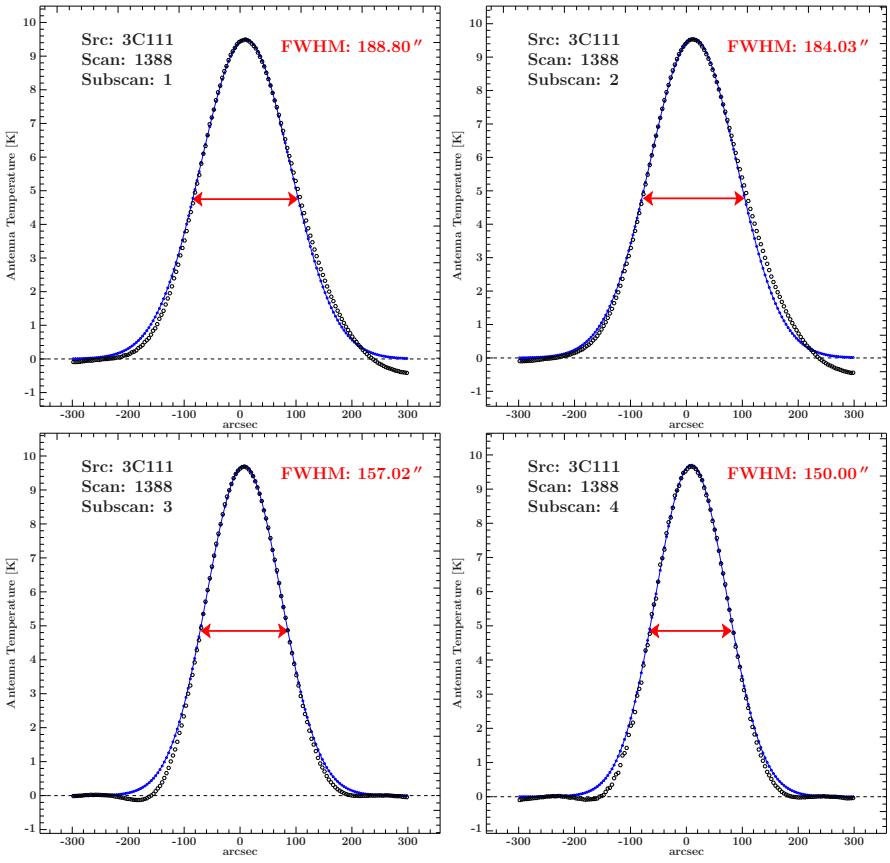

Figure 2.24.: Four sub-scans for the scan number 1388 of EP22 at 5 GHz in elevation (*top*) and azimuth (*bottom*). At the present parallactic angle of +50 ° 3C111 lies approximately aligned to the elevations axis which explains the broadened sub-scan profiles in this direction due to extended emission captured by the large beam. In azimuth the fitted Gaussian FWHM accords almost the beam FWHM of 147 °.

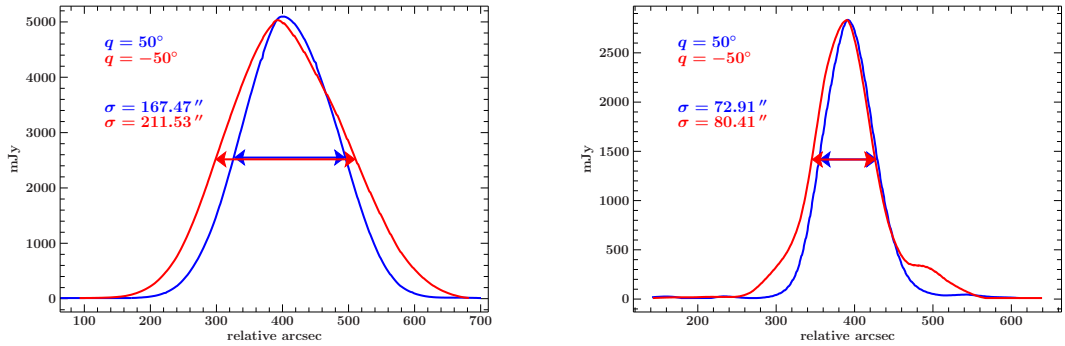

Figure 2.25.: Cuts through the maps along the arrows displayed in Fig. 2.19 yield the present scan profiles. *left:* map-extracted cross scans at 5 GHz, *right:* at 10 GHz.

the source perpendicular to the source extension (parallactic angle of ≈ 50 °) plotted in blue have smaller widths than cuts along the source extension (parallactic angle of ≈ −50 °) plotted in red. Remember the appropriate beam widths that are ≈ 146 ″ at 5 GHz and ≈ 70 ″ at 10 GHz. The measured FWHM values across and along the source extension are 167.47″ and 211.53″ at 5 GHz, and 72.91″ and 80.41″ at 10 GHz, respectively.
One observation is that at 2.8 cm / 10 GHz where the core is dominating the total intensity, the profile's FWHM values across and approximately along the jet axis are not deviating much from

the actual beam width. At 6 cm / 5 GHz, however, the source is extended in both directions being wider along the jet and narrower across the same.
As a result, 3C 111 appears more or less as a point source at 2.8 cm while being clearly extended at 6 cm. Though, as most measured cross-scans show at 6 cm, it can also be called point-like for scans driven perpendicular to the lobe extension, although the example sub-scans shown in Fig. 2.24 are indeed some arcseconds wider than the beam-FWHM in that direction. Along the extension, however, real cross-scans are clearly broadened at 6 cm as it also results from Fig. 2.25.

2.4.2. Full Stokes light curve analysis

2.4.2.1. 100-m Effelsberg long term polarimetry of 3C 111

The actual results of this part of the thesis are the full Stokes light curves shown in Fig. 2.26 at 6 cm / 5 GHz (*top*) and 2.8 cm / 10 GHz (*bottom*). The data points are measured via cross scans within the F-GAMMA campaign and thus represent particularly integrated polarimetry information. In order to demonstrate the source extension at various frequencies, blue triangles for VLBI data at 2 cm from the MOJAVE program[1] that also performs monthly observations are plotted together with Effelsberg 2.8 cm data.

The light curve at **6 cm** shows only smooth long term variability over years in total flux with a maximum stretching between 2008 and 2010 rising to ≈ 7 Jy and descending to a level of ≈ 5 Jy until today. The degree of polarization shown in the second panel stays more or less constant at about 2 % within the errors. In turn the polarized flux in the third panel rises slightly in the same time range of the total flux maximum. The integrated electric vector angle in the fourth panel also stays constant around 50° with some exceptions mostly rising to around 140° which is a difference of approximately 90°.
The **2.8 cm** light curve overall reveals more rapid variability but also larger error bars due to more sophisticated calibration. The total intensity light curve has an overall maximum in the same range as at 6 cm but with sub-structure. There are two clear peaks, one at the beginning of 2008 and one of 2009 being apart of approximately one year. The flux density is then descending from ≈ 6 Jy to ≈ 3 Jy until the last epochs. The fractional polarization is staying constant around $\approx 0\,\% - 1\,\%$ until 2010 and then starting to grow up to $\approx 2\,\%$ in 2012. The errors of the following epochs, however, are growing such that based on Effelsberg data no clear maximum of fractional polarization can be determined. The polarized flux density is varying between 0 mJy and 50 mJy with a pronounced local maximum at the beginning of 2010. The integrated EVPA shows strong variability. Starting at around 100° in 2008 and sweeping over to 50° in the mid/end of 2009, it stays constant around that value until today.
To compare the single dish data also with interferometric data being only sensitive to the compact core region, also data at 2 cm from the MOJAVE program is plotted in the panels of the 2.8 cm Effelsberg light curves. Good co-alignment of both interferometric and single dish data is found within the errors of the Effelsberg data. Exceptions are two Effelsberg data points of the EVPA at MJD 55500 and 56200 lying well below the MOJAVE data plus the EVPA for some epochs at the beginning. The MOJAVE data are in particular needed for the recent epochs between 2011 and today where the overall error-level of polarimetric data rises and no statements can be done. Assuming, however, that both data are consistent based on findings from the former epochs between 2007 and 2011, the trend of MOJAVE data is then taken as reference for further interpretations. It reveals a clear maximum of the degree of polarization around 2012. Additionally, the grey vertical bars represent exemplary epochs of MOJAVE where interferometric maps are extracted and presented in Fig. 2.27. The maps are chosen such that it is possible to identify variability events of the light curve in them. With them one is able to search for interpretations of the described trend

[1] `http://www.physics.purdue.edu/MOJAVE/`

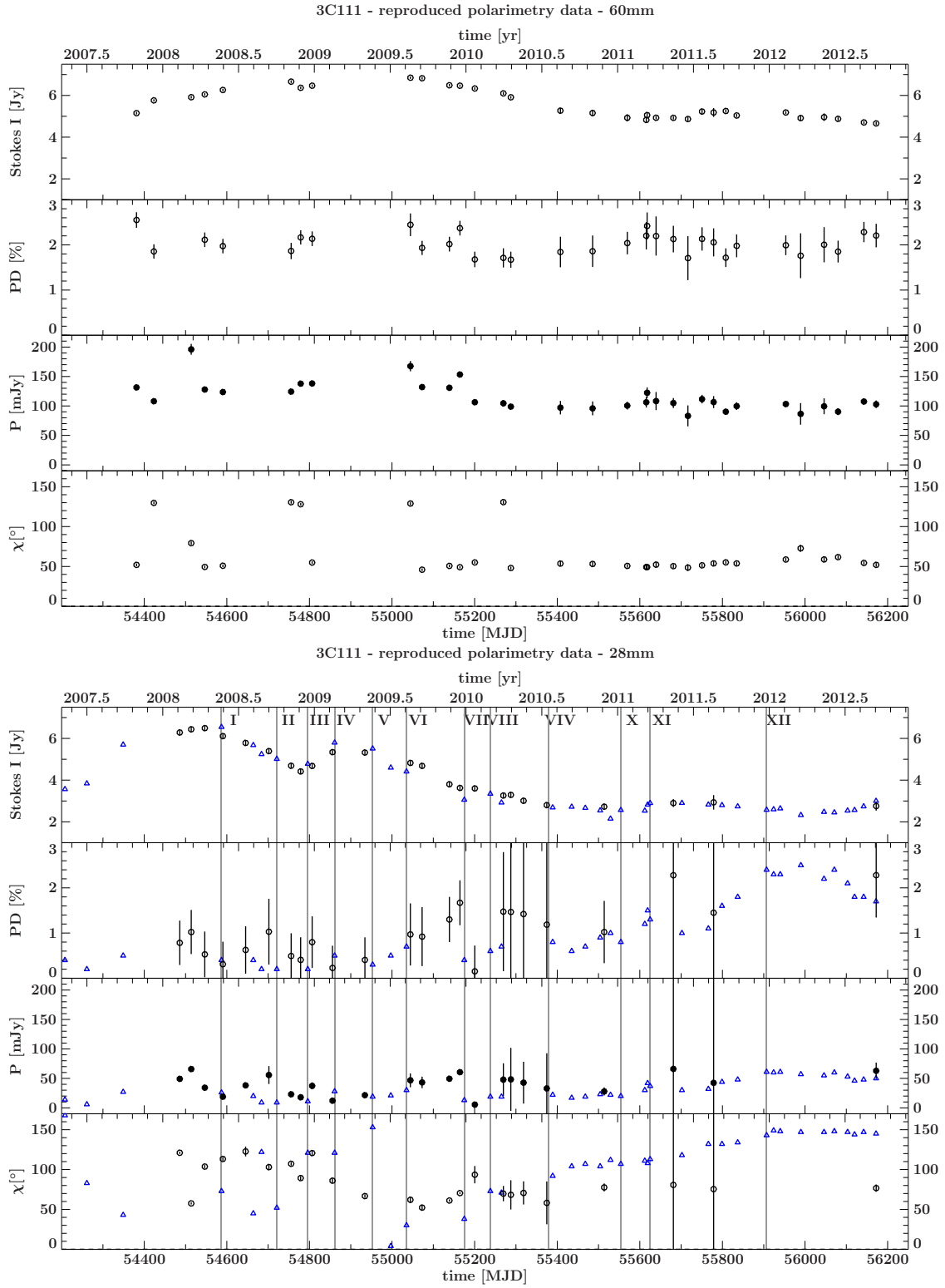

Figure 2.26.: 3C111 light curves for 6 cm / 5 GHz (*top*) and 2.8 cm / 10 GHz (*bottom*).

in both total flux and polarization in detailed maps of the core region.
Comparing the light curves between both wavelength, it appears that the total flux is overall higher at 6 cm. Also the degree of polarization with $\approx 2\,\%$ is exceeding the 2.8 cm degree and so does the polarized flux.

2.4.2.2. Interpretation and Discussion

One basic finding is that the full-Stokes-light curves of MOJAVE and Effelsberg match well at 2.8 cm. This result allows the conclusion that one is sensitive to the innermost compact core regions of 3C 111 without an over-shining of the morphologically well pronounced radio lobes as it happens to be the case at 6 cm. Why do the scan profiles not include those lobes at 2.8 cm in contrast to 6 cm if they are clearly visible in the Effelsberg maps? On the one hand, the scanning direction is slightly misaligned towards the actual jet axis, on the other hand at 2.8 cm the peak flux densities of the lobes are low compared to the core. A discussion on the flux dominance at longer wavelength as also seen in the low-state non-flaring part of the light curve from 2011 on is given in Sect. 2.4.1.2.
As the lobes contributing much to the 6 cm light curve are stable structures on the time scales examined here, the full Stokes variability is less pronounced. In contrast, the light curve reveals strong variability at 2.8 cm, which can be explained by the core dominance and high structural variability as seen in MOJAVE maps (Fig. 2.27) further resolving that core. The two subsequent flares at 2.8 cm are furthermore leading the flare at 6 cm. This is a common feature of flaring AGN in the radio and is due to the fact that the electron gas is getting optically thin first at higher frequencies. Reason for that is the Synchrotron self absorption (SSA) making flares first visible at higher and then gradually at lower frequencies. Being now sure that the 2.8 cm emission is core dominated it makes sense also to include exemplary MOJAVE maps into the discussion of the 2.8 cm light curve. The light curve reveals two flares, one in 2008 and another following in the beginning of 2009. Those can be identified in the MOJAVE maps as a primary and secondary component being ejected from the core (maps I until IV). Grossberger et al. (2012) state – based on model fits and back-extrapolation – that both are ejected from the core at about the same time. The primary component has a projected speed of $3.94 \pm 0.19\,c$ changing to $4.53 \pm 0.09\,c$ after mid 2009 and the secondary one $2.80 \pm 0.40\,c$ up to $3.32 \pm 0.19\,c$. Over the following maps both components move downstream and their total-intensity flux density decreases.
From the polarimetry maps of MOJAVE we learn that only the evolving jet components tend to be polarized. Some theoretical assumptions (Sect. 1.3.1) about the local compression of magnetic field lines by shocks are able to explain this observation interpreting such jet components as separate shocks. The integrated linearly polarized MOJAVE flux density is increasing around 2011 and forming a maximum in the beginning of 2012. In fact the MOJAVE maps show a certain degree of orthogonal alignment of the EVPAs of both the primary and secondary components in the majority of the maps before the flare in polarization. While evolving, the following secondary component's net EVPA being first oriented parallel (map VI) to the jet axis is turning in an orthogonal position aligned with the one of the leading primary component (map XI). This is giving both rise to the fractional polarization and the EVPA integrated over both components plotted as blue triangles in Fig. 2.26. The tendency of only jet components on (sub-)pc scales being polarized with EVPAs aligned to the jet axis imply an underlying chaotic magnetic field that is locally aligned by magnetic compression, most likely due to a shocking event. This finds frequent observational evidence as Saikia & Salter (1988) denote. They further argue that the irregular field is getting locally compressed or sheared around regions where enhanced linear polarization can be measured with electric vectors as direct tracer to the direction of the underlying field orientation. The effect of a rotating net EVPA of 3C 111 was also seen in former MOJAVE-epochs by Kadler et al. (2008). It is interpreted as inhomogeneities in the jet. At the point where the rotation of the net EVPA

starts the matter may flow onto external matter flowing slower. This will lead to a shear and in turn to a deformation and stretching of the initially transverse magnetic field in a direction parallel to the jet axis explaining the EVPAs to turn in an orthogonal position to it. As the MOJAVE maps are not corrected for Faraday rotation, also an external foreground shield can be responsible for some rotation. This possibility is strengthened by Zavala & Taylor (2002) who indeed find a strong Faraday rotation at the position where the EVPA rotation occurs in the MOJAVE maps. The foreground shield, however, is expected to be uniform and not variable. Thus variable EVPA rotation with time must be due to intrinsic changes of the magnetic field configuration.
Paying attention to the light curve again, one can now based on MOJAVE interferometer maps explain the nature of the sudden increase in fractional polarization at 2.8 cm in 2012. By eye this flare of polarization is delayed by approximately 3 years to the secondary component's flare in total intensity. Assuming a mean velocity of $\approx 3\,c$ measured by Grossberger et al. (2012) which corresponds to ≈ 1 mas/y, the secondary component would have moved by 3 mas in 3 years. This fits well between the spot where the trailing component was first ejected in 2009 (map III) and where it flows into the leading component around 2012 (map XII).

2.5. Conclusions

The major concern for the exceptional source 3C 111 was the unknown influence of extended emission on the overall amplitude of cross scans as performed with the monitoring program F-GAMMA. The conclusion is that at 2.8 cm the $70''$ beam is only sensitive to the compact and high-flux core of the source. No problems arise with appropriate cross-scans, the flux values derived by the high-resolution interferometer MOJAVE are in full agreement with the values measured with the 100-m Effelsberg telescope.
At 6 cm the cross scans are broadened in the scan direction along the source extension but no amplification or attenuation of the peak amplitudes are found when comparing cuts in azimuth and elevation across the Effelsberg images from March 2012 mapped out with the 6 cm beam. Also the scan-amplitudes of measured epoch-scans can not be proven to alter between sub-scans where extended emission is integrated or not integrated into the beam. This explicitly means sub-scans either across or along the source extension at a wavelength where the telescope is sensitive to that extended emission. Additionally the peak fluxes of those cuts along the same direction in which the majority of Effelsberg cross-scans are driven, are in agreement with the fluxes at the end of the Effelsberg light curve (beginning of 2012). Therefore extended emission does only affect the width, not the amplitude of cross-scans driven by a single dish beam at a sufficiently long wavelength capturing diffuse steep-spectrum emission. There is no doubt in the correctness of the here presented light curves both in total and polarized power.
Finally the importance of the 100-m Effelsberg telescope and the long term F-GAMMA campaign has to be stated. As shown above, it is possible to reproduce polarimetry data offered by MOJAVE. Unfortunately the data signal-to-noise suffered at the time of the polarization flare due to several issues of weather and calibration. However, Effelsberg is still a sufficiently good if not perfect instrument to study the long term evolution of both total and polarized intensity. It is especially *the* instrument of choice when searching for a reliable instrument for long term polarimetry monitorings of a large sample of sources at multiple wavelength facing the huge amount of financial and logistical dedicated effort to maintain VLBI networks. Notwithstanding, single dish monitorings of global source parameters yield the same results as VLBI networks for compact sources. Having VLBI maps to identify events in light curves offers lots of insights but is not always necessary to study the source in detail when taking polarimetric information into account. As the results of this work show, polarimetry data are able to interpret and identify also morphological events.

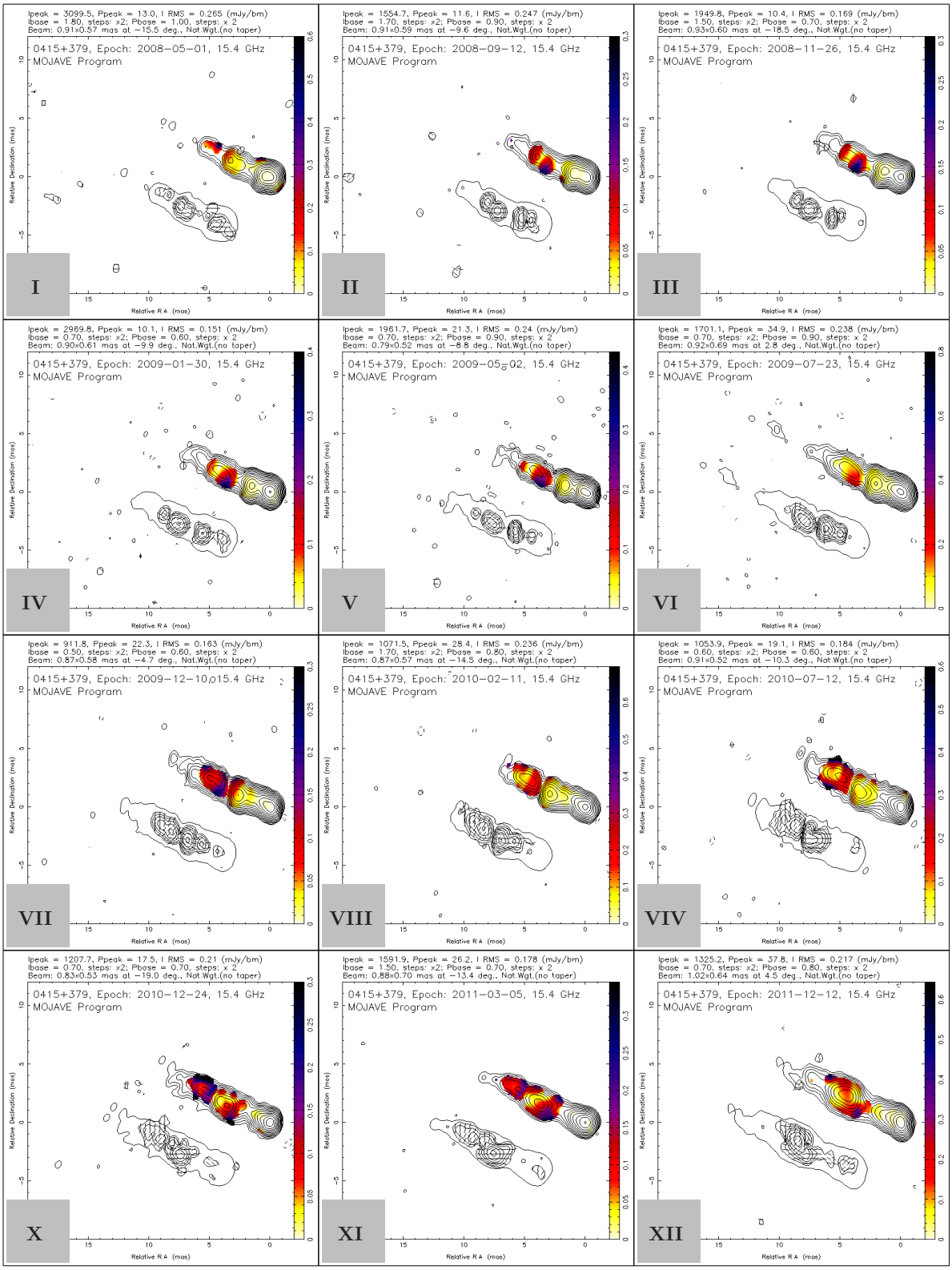

Figure 2.27.: Exemplary MOJAVE maps for the appropriate periods in the 10 GHz light curve in Fig. 2.26 (marked as roman numbers).

Chapter 3

X-ray Variability Study of Polar Scattered Sy1

> *This asteroid has been seen only once through the telescope, in 1909, by a Turkish astronomer. He had presented it in a great demonstration to the International Astronomical Congress. But nobody would believe what he said because he was in Turkish costume.*
>
> Antoine de Saint-Exupéry, *The Little Prince*, 1943

Turning over to the second part of my thesis, I want to present a special kind of radio-quiet Seyfert galaxies. After Sect. 1.4 radio-quiet AGN are the sources of interest to study the innermost regions of Active Galactic Nuclei. Under certain circumstances the measured X-ray radiation can be highly variable offering valuable clues to the geometrical nature and orientation of yet unresolved cores of some active galaxies towards our line of sight. Variability of absorption is ubiquitous in over the half of all local Seyfert galaxies (Risaliti et al., 2002). The aim of this part of my work work is to find evidence for spectral soft X-ray variability in the column density by examining all available historical observations of these sources by *XMM-Newton* and *Swift*. Despite the lower S/N ratio, *Swift* is chosen because of its higher amount of available observations. The timescales of the column variations are derived as good as the data coverage allows.
In contrast to light curve analysis with *RXTE* where several sources show rapidly following absorption events, I am implicitly interested in the long term spectral variability of my sample, especially in terms of absorption of the soft X-ray part. In addition to my work it has to be noted that such shortly following rapid absorption dips were found also for sources contained in my sample, such as NGC 3227 (Lamer et al., 2003).
This chapter first gives an overview over the technical part of X-ray astronomy including a description of X-ray detectors, instruments and the way of extracting, analyzing and interpreting data. The sample of analyzed sources is introduced in the following section followed by a more applied description of the analysis steps undertaken to gain the results on spectral variability presented in the last section.

3.1. X-ray Astronomy

Reaching higher frequencies, radio astronomy is followed by optical and ultraviolet (UV) astronomy partly still able to operate from earth. Reaching shorter wavelength starting from the UV, the atmospheric opacity is getting too large and one needs to send satellites into the orbit carrying

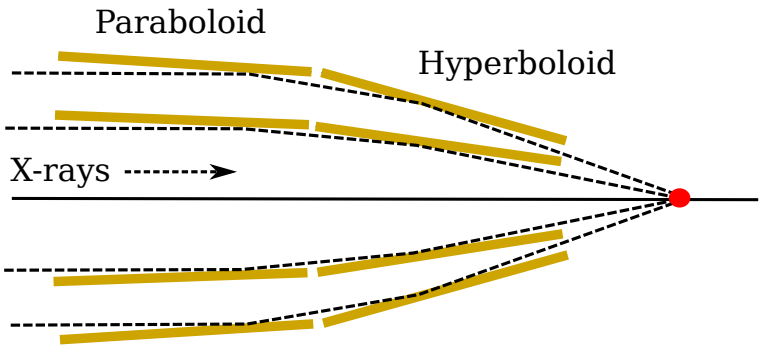

Figure 3.1.: Illustration of a Wolter telescope consisting of nested parabolic as well as hyperbolic shaped mirrors to ensure total reflection for high energetic photons such as X-rays.

appropriate telescopes and detectors. Instruments for X-ray astronomy are different to optical ones. Photons of such high energies can not be focused with optical mirrors any more. Let the angle between a ray of radiation and the normal on a surface with different index of refraction be α. Beyond the critical angle $\theta_c = \pi/2 - \alpha_c$ the photons will always be totally reflected. This is particularly the case if $\cos(\theta_c) = n$ with the index of refraction n. This would never be the case for silicate material like normal optical mirrors but for metals. Aschenbach (1985), e.g., show that the larger the density of the metal, the larger θ_c will be which is highly achievable. *XMM*-Newton uses a so called Wolter telescope consisting of 58 nested parabolic and hyperbolic mirrors of nickel covered with 250 nm layers of high purity gold. Figure 3.1 illustrates the principle of nested mirrors with X-rays entering the telescope from the left. The focus is implied as red point. The focal length is 7.5 meter to ensure a small angle of $\theta \approx 1°$ necessary for total reflection of the given medium.
The used analysis software for X-ray spectra, the **I**nteractive **S**pectral **A**nalysis **S**oftware (`ISIS`) (Houck & Denicola, 2000) is based on the S-Lang language that is developed by John E. Davis as well as the S-Lang implementation of xfig in `ISIS` (`slxfig`).

3.1.1. X-ray CCD Detectors

Besides non-imaging detectors such as proportional counters, **C**harge **C**oupled **D**evices (CCD) as semi conductor detectors, are able to both image X-ray sources and gather spectral information.
For this section several sources of literature have been taken into account. The most important ones from primary literature are the textbooks of Arnaud et al. (2011) who give a good overview over the topic of X-ray Astronomy and detectors and in particular Knoll (2010) treating (CCD) detectors in great detail. The following description mainly follows Knoll (2010). CCDs consist of a layer of doped semi-conducting material like Silicon which furthermore consists of bands at different energetic levels. One distinguishes the valence-band (electron donator) and the conduction-band (electron acceptor). Above that there is a layer of insulating material pinned with electrodes in a matrix-like pattern. Applying a voltage to the electrodes, a potential minimum (also called "drain") grows below the insulator. If the CCD is getting illuminated, a number of electrons is produced that is proportional to the incident photon energy divided by the energy needed to bring electrons from the valence band to the conduction band. These electrons are then captured in the potential drains below the electrodes. One can lower the region of minimal potential from just below the insulator to well below it in order for the electrons to accumulate inside the semi-conducting layers. This is done by adding an additional layer of an oppositely doped semi-conductor between insulator and the former semi-conductor layer. Those are called MOSFETs.
Typical gaps between the valence- and conduction bands are in the order of ≈ 1 eV (Knoll, 2010). X-ray photons, however, already carry energies of > 200 eV. Thus in X-ray sensors even single photons release a large number of electrons to the conduction band, being collected in potential

drains. In order to be sensitive to single photons and in order for the drains not to flow over, the collected charges have to be read out as fast as possible. This is done in different lines spread over the detector plane by using pulses of potentials moved towards the edge of the detector (Popp, 2004). A frequently used analogy is a number of buckets of water reached through by several people. Each bucket corresponds to one pulse with the amount of water according to the number of released electrons within one readout time-interval. By counting the amount of pulses of each line, one gains information on the second dimension of the CCD matrix. Such a configuration is able to store both the position of impact of an incident photon and its released energy.
Since this is a statistical process, the released electrons are ideally Poisson distributed with the variance $\sigma_{\text{Poisson}} = \sqrt{N}$ where N is the number of electrons being equal to E/ϵ with the incident photon energy E and the energy ϵ needed to bring electrons from the valence- to the conduction-band.
For spectroscopy the **energy resolution** R is an important quantity. One quantity included in R is the variance or uncertainty of the number of electron-hole pairs released by one photon, $\sqrt{N}$, where R equals to this variance over the mean number of released electrons N for Poisson distributed numbers of electrons x. Due to the direct proportionality of incident photon energy to released charges, it holds that $R = \Delta E/E = \Delta N/N$ where ΔE is the energy uncertainty of a given photon energy E. To be precise the numerator is not only the variance but the FWHM of the Poisson distributed number of electrons which is $2.355\,\sigma_{\text{Poisson}}$.

$$R = \frac{\Delta E}{E} = \frac{\text{FWHM}}{\langle x \rangle} \sim \frac{2.355\,\sigma_{\text{Poisson}}}{\langle x \rangle} = \frac{2.355\sqrt{N}}{N} = \frac{2.35}{\sqrt{N}} = 2.355\sqrt{\frac{\epsilon}{E}}. \tag{3.1}$$

The energy resolution at one certain photon energy is ideally only depending on ϵ being a measure for the energy gap between the donator and acceptor bands. Nevertheless there are also limiting factors such as CCD noise including dark current as well as the charge transfer efficiency. These limit R in Eq. 3.1 by some additional factor, the so called Fano factor (Knoll, 2010), depending on the detector. The Fano factor considers that due to those limitations, the statistical variance $\sigma^2 = N$ does not equal the total released number of electrons as the events are not all independent. In fact the variance will be smaller. Applying Poisson statistics is therefore only valid when considering that factor in the resolution being of the order of ≈ 0.1 for detectors of interest (Knoll, 2010). Setting this factor to a more precise value of ≈ 0.11 and the band gap to 3.62 eV for silicon (Knoll, 2010), Eq. 3.1 gives an energy uncertainty of $\Delta E \approx 110\,\text{eV}$ at an incident photon energy of $E = 6\,\text{keV}$.
In order to be able to detect single photons, the main task for X-ray CCDs is a fast readout time facing bright sources of hundreds of photons per second. **Pile up** (Popp, 2004; Schmid, 2012) can happen in pixels of very strong illumination where the readout time is too slow. Thus one can not tell if there were many photons hitting the same pixel within the integration- or readout time. In turn the according energy for this pixel within one readout cycle is the energy of many photons detected as one. This will lead to an artificial hardening extracted spectra. In general this is avoided by neglecting to strongly illuminated pixels, mostly in the center of the source.

3.1.2. X-RAY ANALYSIS

There is a basic relation (Davis, 2001; Arnaud et al., 2011) that states what bias the instrument is introducing while measuring a count spectrum:

$$c(i) = \int_0^\infty R(i, E)A(E)F(E)dE \tag{3.2}$$

It translates the incident photon flux $F(E)$ into measured counts per second $c(i)$ in the energy channel i. The **auxiliary response function (ARF)** being the effective area as function of

energy first describes the energy dependent limitations of the telescope in terms of collecting area, filters, detector efficiencies and so on. The unit of the appropriate function $A(E)$ is cm^2/photon. The **redistribution matrix function (RMF)** acts in the detector frame itself. See also Hanke (2007) and Davis (2001) for more details. It expresses that the detector's electronics often can not produce a signal of the same energy of the detected photon. The according redistribution function $\widetilde{R}(E', E)$ relates incident photon energies E to the detected ones E'. The RMF

$$R(i, E) = \int_{E'_i}^{E'_{i+1}} dE' \widetilde{R}(E', E). \tag{3.3}$$

is a function of the discrete energy bin, i, and the incident photon energy E. Unfortunately Eq. 3.2 in a discretized form relating discrete energies to detector channels is not invertible as such inversion would be unstable to small changes of $c(i)$ (Blissett & Cruise, 1979). In order to infer the real source spectrum, X-ray analysis software such as `ISIS` (Houck & Denicola, 2000) makes use of pre-determined ARF and RMF functions for the appropriate detector. Considering also background counts, the step is now to describe the detector-biased, measured source spectrum $c(i)$ with a realistic, physical model spectrum mapped into detector space using Eq. 3.2. The parameters of the model are adjusted with χ^2 minimization (Sect. 3.1.6.1) in order to find the best fit of predicted model counts $m(c)$ to measured source counts $n(c)$. This trick of inserting knowledge about the detector makes it possible to leave the detector frame and in the best case describe physical processed in the source frame.

3.1.3. *XMM*-Newton

One of the X-ray instruments used for the data analysis is the European Space Agency's **X**ray **M**ulti-**M**irror mission *XMM*-Newton launched to space in 1999. For general mission information see the user handbook or Lumb et al. (1996).
X-ray imaging instruments can be in general characterized via two competing qualities: spectral resolution vs. spatial resolution. XMM's vast advantage is the large collecting area allowing the detection of more photons at the same time as possible with other missions like *Chandra*. This particularly allows one to have well covered spectra with that many counts that it is possible to identify lines with width down to the actual hardware-limiting spectral resolution. Additionally, the more counts are detected, the more counts can be merged to one bin to raise the statistics. On the other hand it is difficult to focus rays with a set of 58 nested mirrors for each of the three Wolter telescope modules. Hence the spatial resolution measured with the **P**oint **S**pread **F**unction (PSF) – a point source as imaged with a certain instrument – is wider for *XMM* than for example for *Chandra* which has only four nested mirrors.
XMM-Newton carries three instruments, the **E**uropean **P**hoton **I**maging **C**amera, EPIC (Turner et al., 2001), further consisting of two EPIC-MOS (Holland et al., 1996) and one EPIC-pn CCD-cameras (Villa et al., 1996; Meidinger et al., 1996), the **R**eflection **G**rating **S**pectrometer, RGS (den Herder et al., 2001) and the **O**ptical **M**onitor, OM (Mason et al., 2001).
Figure 3.2 shows the three equal Wolter telescopes with a collecting area of $\sim 1500\,\mathrm{cm}^2$ each on the lower left side. The effective areas of the appropriate detectors are smaller because of detector inefficiencies and filters in front. The upper two of them are equipped with reflection grating arrays and are illuminating the two EPIC-MOS detectors in the focal plane (green radiator-horns) and also the RGS detectors sketched in light blue offsetted slightly downside in the focal plane. The lower Wolter telescope illuminates the single EPIC-PN camera beyond the purple radiator in the middle of the two reddish RGS-radiator plates. Both EPIC-MOS cameras are **front-illuminated**, whereas EPIC-pn is **back-illuminated**. The difference is that for front-illuminated sensors the wiring lies in front acting as dead layer absorbing mostly soft photons. The back-illuminated EPIC-pn sensor in contrast carries the wiring layer in behind such that the detection probability can be

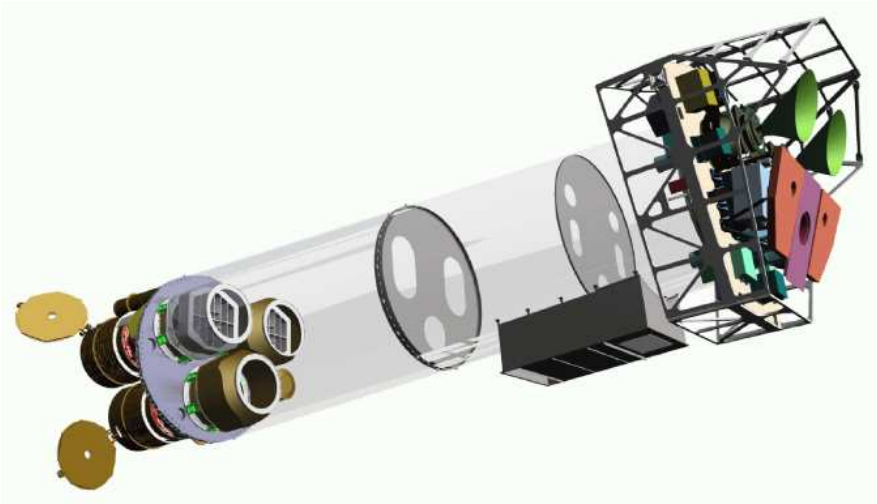

Figure 3.2.: Sketch of the *XMM* payload as extracted from the *XMM* User Handbook.

Table 3.1.: Basic characteristics of the *XMM* instruments after the *XMM* User Handbook.

	EPIC-MOS	EPIC-pn
bandpass	0.15 – 12 keV	0.15 – 12 keV
field of view	$30'$	$30'$
PSF (FWHM)	$5''$	$6''$
spectral resolution (ΔE) at 1 keV	$\sim$ 70 eV	$\sim$ 80 eV
effective area at 1 keV [cm^2]	922 each	1227

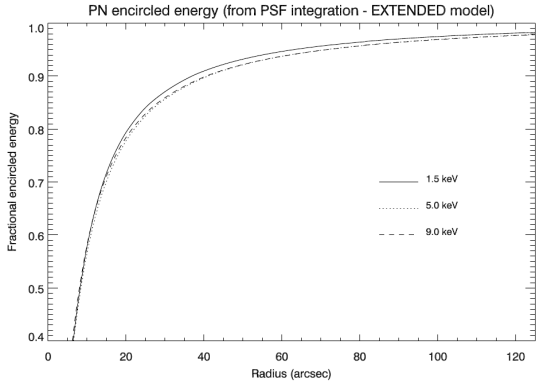

(a) Encircled energy from PSF integration of EPIC-pn.

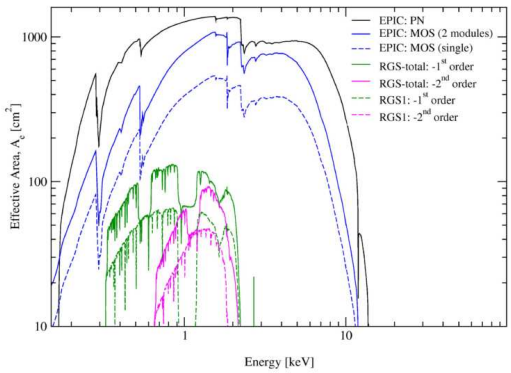

(b) Effective area of all instruments on board.

Figure 3.3.: EPIC-pn CCD properties after the *XMM* User Handbook.

raised by a significant fraction. This expresses oneself in a smaller effective area of 922 cm^2 for the EPIC-MOS detectors compared to 1227 cm^2 for the EPIC-pn detector at 1 keV. In my analysis I therefore use EPIC-pn data only.
The last instrument, the OM is a distinct telescope fixed behind the lower mirror module. The basic characteristics of the instruments are summarized in Table 3.1. The energy dependent effective area is shown in Fig. 3.3 as well as the encircled energy from the integrated point spread function of EPIC-pn. The plot of the integrated PSF tells that it is best to use source radii between $20''$

Table 3.2.: Basic characteristics of the *Swift*-instrument XRT (Gehrels et al., 2004).

	XRT
bandpass	0.2 – 10 keV
field of view	23.6′
PSF (FWHM)	18″
spectral resolution (ΔE) at 0.1 and 10 keV	$\sim$ 190 eV, $\sim$ 90 eV
effective area at 1.5 keV [cm^2]	135

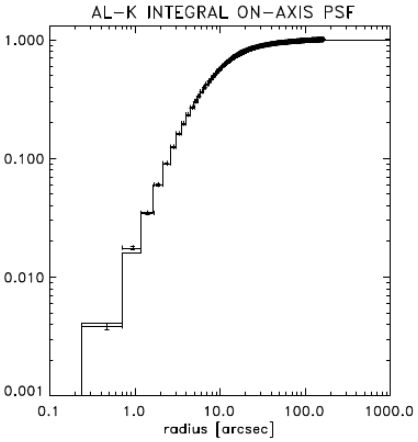

(a) *Swift*-XRT integrated PSF measured at the Panter (Moretti et al., 2004).

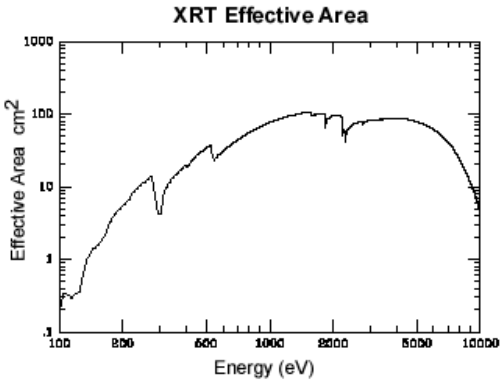

(b) Effective area of XRT (`https://heasarc.gsfc.nasa.gov/docs/swift/about_swift/xrt_desc.html`).

Figure 3.4.: XRT CCD properties

and 60″ to gain the most flux of a point source.

3.1.4. *Swift*

Swift (Gehrels et al., 2004) was designed to perform multi wavelength studies of gamma-ray bursts in the gamma ray regime with the **B**urst **A**lert **T**elecsope BAT (Barthelmy et al., 2005), the X-rays with the **X**-**R**ay **T**elescope XRT (Burrows et al., 2005) and the optical/UV with the **UV**/**O**ptical **T**elescope UVOT (Roming et al., 2005). Although not being the first science case, many observations also of Seyfert galaxies have been done by now. *Swift* has a much smaller effective area than *XMM*. It is, however, possible to have a better time coverage of observations with it, which is of enormous interest in the present study. Suffering under less detected counts, *Swift*-XRT spectra generally still bring enough information to constrain simple absorptive continuum models. For detailed information see Table 3.2. The energy dependent effective area as well as the integrated PSF are shown in Fig. 3.4. In the analysis of this work data are analyzed by setting source radii of 25″ around the point sources which collects around 90 % of all counts inside the point source folded with the PSF.

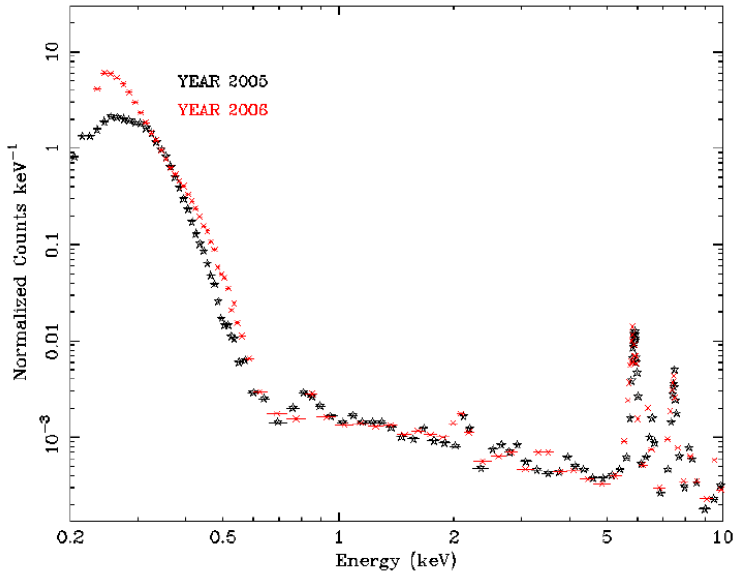

Figure 3.5.: *Swift*-XRT instrumental background for a CCD temperature of -55 C (Pagani et al., 2007).

3.1.5. Data Reduction

3.1.5.1. *XMM*-Newton

The *XMM*-Newton data are reduced with SAS v12.0.1 using the newest calibration files available at that moment. All analyzed sources are point-like. For the extraction of spectra only EPIC-pn was used. Spectra are produced using event files extracted by choosing circular regions around source and background. In the case of existent pile-up the innermost region with the strongest illuminated pixels is rejected. The diameter of the source regions strongly depends on the PSF of the instrument.

3.1.5.2. *Swift*

Swift-XRT data are analyzed using the `heasoft 6.12` package available at that time. All sources are also point-like. The event file extraction is performed as for *XMM*. In addition, sources are extracted all with source radii of 25″. In case of pile-up the innermost region is excluded.
It also has to be noted that it is dangerous to extract data below 0.5 keV with *Swift*. The reason is not only that the effective area gets quite low below that energy but primarily that the detector background is high in the range of $0-0.5$ keV especially when passing the South Atlantic Anomaly (SAA). In that case the whole detector material is getting highly activated and radiates in the whole energy range disturbing the detection of source photons. Figure 3.5 shows the instrumental background radiation of XRT measured in 2005 and 2006 at a detector temperature of $-55°$C (Pagani et al., 2007). It peaks at lower frequencies. Therefore also the uncertainty on the background distribution measured by choosing a certain background region on the CCD image is largest below 0.5 keV.

3.1.6. Spectral Fitting

After reducing the data, the techniques from Sect. 3.1.2 can be used to find a model best describing the data. As already mentioned, what matters is to reduce the difference of model counts to data counts taking into account all bins between 0.3 – 10 keV. The statistics in behind are treated in detail in the following sections.

3.1.6.1. Log-likelihood and Chi-Squared statistics

As already discussed in Sect. 2.2.3.2, the generic ansatz is the Log-likelihood function. In X-ray astronomy, spectral data are available in energy bins of certain widths according to the chosen binning. In other words, as a X-ray satellite measures a spectrum, the different energy bins are subsequently filled with photons (counts). A basic spectrum has the units of energy over counts. Thus it is all about counting experiments, where the *Poisson Statistic* holds. In turn, the 1σ uncertainty for a data point of one bin with the appropriate amount of counts per bin i, N_i is the Poisson-square-root value $\sqrt{N_i}$.
The Poisson distribution as the limit of the Binomial distribution for large total amounts of counts n but very small probabilities for one hit p is

$$P_\lambda(k) = \frac{\lambda^k}{k!} e^{-\lambda} \tag{3.4}$$

where $\lambda = np$ is the expected amount of counts and k the counts themselves. The mean amount of counts equals the expected value $\langle k \rangle = \lambda$ and the variance $\sigma = \sqrt{\lambda}$.
Another important characteristic is that the *Gaussian distribution*

$$P_\lambda(k) = \frac{1}{\sqrt{2\pi\lambda}} e^{-\frac{(k-\lambda)^2}{2\lambda}} \tag{3.5}$$

is the limit of the Poisson distribution for large λ. Gehrels (1986) and Nousek & Shue (1989) show that one can use Gaussian statistics from ≈ 20 counts per bin on. Let us rewrite the Gaussian probability to a more convenient formula using terms of X-ray astronomy:

$$G \sim e^{-\frac{(n_i - m_i)^2}{2\sigma^2}} \tag{3.6}$$

here, n_i are the observed counts and m_i the appropriate model counts of the i-th bin. Identical to Sect. 2.2.3.2 the likelihood function is the product of n Gaussian distributions with $n = 1 \ldots n$ according to n bins. Assuming a model function $m(\theta)$ as a function of parameters θ, the log-likelihood is

$$\ln(L(n_1, \ldots, n_n|\theta)) = \ln\left(\frac{1}{\sqrt{2\pi\sigma^2}}\right) - \sum_{i=1}^{n} \frac{(n_i - m_i)^2}{2\sigma^2}. \tag{3.7}$$

After summing up all n terms, the resulting function is only dependent on the model parameters θ. Again, developing the log-likelihood around its maximum just as in Eq. 2.16 yields the Gaussian shape of the likelihood function

$$L(\theta) = L(\hat{\theta}) e^{\frac{1}{2}\left(\frac{\partial^2 \ln L}{\partial^2 \theta}\right)(\theta - \hat{\theta})^2} \tag{3.8}$$

$$= L(\hat{\theta}) e^{\frac{1}{2}\frac{(\theta - \hat{\theta})^2}{\sigma^2}} \tag{3.9}$$

around its maximum $\hat{\theta}$. Considering $n\sigma$ confidence intervals one finds

$$-\ln L(\hat{\theta} \pm n\sigma) = -\ln L(\hat{\theta}) + \frac{1}{2}n^2. \tag{3.10}$$

This means that in a one-dimensional parameter space with parameter plotted against the log-likelihood, one finds the 1-dimensional error-interval of 1σ, 2σ and 3σ just by lowering the maximum about 0.5, 2 and 4.5. The intersections of lines parallel to the base with the log-likelihood-parabola are then the borders of the error-intervals (Fig. 3.6, left).
Since the **Chi-squared** formalism is equivalent to the log-likelihood, it is possible to find proper arguments for the quality of a fit as well as a derivation of the parameter uncertainties via the *chi-squared-distribution*. A certain fit will lead to a χ^2-value for the best fit as the minimum of the parameter-space with parameters plotted against the χ^2. Derived from the likelihood formalism described so far, the χ^2 with its definition

$$\chi^2 = \sum_i \left(\frac{n_i - m_i}{\sigma_i}\right)^2 \tag{3.11}$$

is the sum over the deviation of model-counts and data-counts weighted with $\sqrt{N}$ for all bins. The data confidence-interval per bin $\sigma_i = \sqrt{N_i}$ with $N_i = D_i + B_i$ being the sum of source- and background-counts must not be mixed with the σ belonging to parameter uncertainties. These are defined as described in the following.
Assume we found a best fit with $\chi^2_{\min}$. This χ^2-value is again distributed via the chi-squared distribution

$$f^n_{\chi^2}(\chi^2) = \frac{(\chi^2)^{\frac{n-2}{2}} e^{-\frac{\chi^2}{2}}}{2^{n/2}\Gamma(n/2)} \tag{3.12}$$

depending on the degrees of freedom n. See Hanke (2007) for more details and plots of the chi-squared-distribution for different degrees of freedom. For a good fit one assumes that in Eq. 3.11 the deviations of data and model $(n_i - m_i)$ are scattering just within the assumed σ-uncertainties. Thus the sum should reduce to n in total. Now one defines the *reduced chi-squared* $\chi^2_{\text{red}} = \chi^2/n$ as the chi-squared weighted with the degrees of freedom of the fit. In the best case one would reach a value of one. Everything below one resembles an overestimated, "too good" fit, everything above an underestimated, "too bad" fit.
Having achieved the best fit with $\chi^2_{\min}$, there is still the probability

$$p = \int_{\chi^2_{\min}}^{\infty} f^n_{\chi^2}(\chi^2) d\chi^2 = F^n_{\chi^2}(\chi^2_{\min}) \tag{3.13}$$

to find worse fits with larger χ^2-values. This is the so called *p-value*. If that probability p to find worse models is smaller than the probability

$$\alpha = \int_{\chi^2_\alpha}^{\infty} f^n_{\chi^2}(\chi^2) d\chi^2 = 1 - F^n_{\chi^2}(\chi^2_\alpha) \tag{3.14}$$

to still find better models, the Null-Hypothesis of the present model to be the best must be rejected within a confidence level of α. Normally one chooses a certain confidence level α of $\approx 5\,\%$. In the best case of $\chi^2_{\text{red}} \approx 1$ the p-value reaches 0.5 which means that the probability for either a larger or smaller χ^2 is identical.

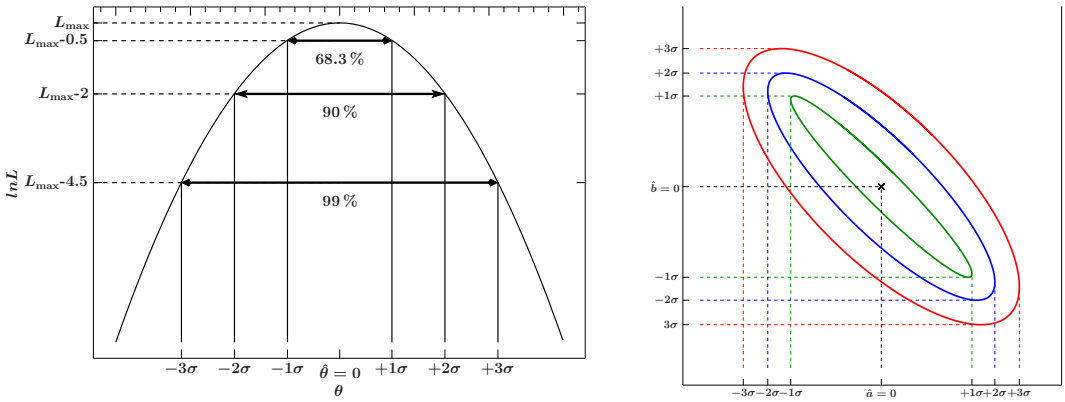

Figure 3.6.: Sketches of a one- (*left*) and two-dimensional (*right*) parameter space and the derivation of different uncertainties according to different sigma-values. The left panel plots a log-likelihood function which has to be mirrored on the parameter axis to get the chi-squared distribution $\chi^2(\theta)$.

3.1.6.2. Parameter confidence intervals and contours

For n-dimensional parameter spaces with n free parameters one can always plot 2-dimensional projections. Assuming a Gaussian distribution (> 20 counts/bin), the likelihood is the product of as many Gaussian distributions as there are bins. The product will always be Gaussian. But depending on the total amount of parameters nasty side minima/maxima can appear (recall: the χ^2-space is in general just the log-likelihood space with opposite sign). Thus, the parameter space can be complicated. In general one can say that the parameter space is getting more and more smooth and symmetric, the more bins one has with Gaussian distributed counts each bin. In simple words: if you have two bins and thus two data points in a spectrum, it is easy to fit a straight line with very few parameters to the data. In contrast, a more complicated model with dozens of parameters will produce an extremely complicated and asymmetric parameter space. The more data bins one has, the better one can constrain a model with multiple degrees of freedom.

Let's think about the case of a smooth parameter space and a well pronounced global χ^2-minimum not being patched with local minima. For simplicity assume a fit where only one parameter of p in total is varied while re-fitting all the others. For N data-bins a fit concerning a model with all p parameters varied has $N-p$ degrees of freedom and the chi-squared statistic $\chi^2(p)$. However, when varying only one parameter while re-fitting all $p-1$ others, we end up with only $N-p-1$ degrees of freedom and the according statistic $\chi^2(p-1)$. As discussed by Lampton et al. (1976) the resulting parameter space includes only the one free parameter θ plotted against the statistic $\Delta\chi^2(\theta) = \chi^2(p-1) - \chi^2(p)$ which is again χ^2-distributed according to Eq. 3.12. Chi-squared values in turn are additive values. This is a one dimensional parameter space, i.e., a simple parabola around the best fit parameter.

Having found the minimum $\chi^2(\theta)_{\rm min}$ the question is now how the confidence interval of the free parameter θ is defined. As the χ^2-distribution $f^1_{\chi^2}(\chi^2)$ holds for the statistical values on the y-axis, the probability to measure $\Delta\chi^2$ values larger than some value at a certain confidence level after re-fitting is simply $F^1_{\chi^2}\left(\Delta\chi^2(\theta)_{\rm conf}\right) = \int_{\Delta\chi^2_{\rm conf}}^{\infty} f^n_{\chi^2}(\Delta\chi^2_{\rm conf})d\Delta\chi^2$. In turn, the probability for a $\Delta\chi^2$ between the minimum $\Delta\chi^2(\theta)_{\rm min}$ and the confidence border $\Delta\chi^2(\theta)_{\rm conf}$ is $1 - F^1_{\chi^2}\left(\Delta\chi^2(\theta)_{\rm conf}\right)$. This probability is also called the **confidence limit**.

A similar approach is chosen also for two or more free parameters. In the case of two free parameters it is possible to plot **confidence contours** between both parameters (Fig. 3.6). Such contours are circular if no correlation is present. The more both parameters are correlated, the larger the confidence borders of the ellipses can get for at least one parameter.

Table 3.3.: Values of $\Delta\chi^2(\boldsymbol{\theta})^n_{\rm conf}$

significance $F^{1,2}_{\chi^2}$ $(\Delta\chi^2(\theta)_{\rm conf})$	confidence level (CL)	$\Delta\chi^2(\boldsymbol{\theta})^1_{\rm conf}$	$\Delta\chi^2(\boldsymbol{\theta})^2_{\rm conf}$
0.32	1σ (68.27 %)	1.00	2.30
0.10	2σ (90 %)	2.71	4.61
0.01	3σ (99 %)	6.63	9.21

Table 3.3 (Lampton et al., 1976) summarizes the values $\Delta\chi^2(\boldsymbol{\theta})^n_{\rm conf}$ for one and two free parameters about which one has to rise the minimum $\Delta\chi^2(\boldsymbol{\theta})_{\rm min}$ in order to include 1σ (68.27 %), 2σ (90 %) or 3σ (99 %) of all $\Delta\chi^2$ and in turn also parameters in confidence intervals as being constrained by the $\Delta\chi^2(\boldsymbol{\theta})^n_{\rm conf}$-contours projected down on the parameter space. Here $\boldsymbol{\theta}$ implies one or more free parameters. As all statements are based on relative values it is possible to infer such confidence intervals just by rising the minimum by the values given in the table.

Cash (1976) finds the confidence intervals based on a Bayesian ansatz. As a result confidence intervals are also defined in the low-count limit for less than 20 counts per bin. The appropriate statistic is often also called "Cash-statistic".

3.1.6.3. Cash Statistics

Sect. 3.1.6.1 assumes at the minimum 20 counts/bin for the Gaussian probability to be valid in each bin (Cash, 1979; Gehrels, 1986; Nousek & Shue, 1989). In the case of less counts per bin we have to go back to the Poisson statistic (Eq. 3.4). The whole χ^2 formalism is just the high-count limit of the more generic **Cash statistic**. The derivation of the statistic is identical as above. Again, the likelihood is the product of Poisson distributed data of all bins:

$$L = \prod_{i=1} (P^k_\lambda)_i = \prod_{i=1}^{N} \frac{\lambda_i^{k_i} e^{-\lambda_i}}{k_i!} \tag{3.15}$$

The Cash statistic is defined as the log-likelihood via

$$C = -2 \ln L = -2 \sum_{i=1}^{N} (k_i \ln \lambda_i - k_i - \ln k_i!). \tag{3.16}$$

As the term $\ln k_i$ cancels out when calculating ΔC, it is more convenient to use $C = 2 \sum_{i=1}^{N} (\lambda_i - k_i \ln \lambda_i)$ or aiming the topic of X-ray astronomy

$$C = 2 \sum_{i=1}^{N} (m_i - n_i \ln m_i) \tag{3.17}$$

with model counts m_i and data counts n_i per bin i.
It is important to note that ΔC is also following the χ^2 distribution. Because of this fact, contours of various confidence levels are well defined not only for the χ^2 statistic but also for the Cash- or C-statistic (Mittaz et al., 1999).
An additional issue is the reason for the choice of Cash statistics. This is, if there are definitely less than ≈ 20 counts/bin. The reason for that is in most of the cases (in particular for most *Swift* spectra) that there are only very few counts available in total. After doing some re-binning, this will mostly lead to only a small number of data points (i.e., bins). Combined with a model of several

free parameters and the use of C-statistic itself, the overall parameter space will be complicated. Global minima can be patched with side minima. Pronounced minima (if so) tend to be asymmetric in the 2-dimensional parameter space. Hence also contours calculated based on the Poisson limit in C-statistics show a lack of symmetry (Mittaz et al., 1999).
This can be challenging for minimization algorithms to find the overall minimum of the parameter space according to the "best fit" given the limiting circumstances. In `ISIS` it turns out to be useful to give data, where the C-stat is used, a first fit with the more dedicated and complex `subplex` minimization algorithm to find the global minimum within the irregular space. Then the `mpfit` Levenberg-Marquardt-algorithm following a gradient-ansatz can be used to further seek for the minimum. The latter would easily get stuck in local minima without using `subplex` at first.
In principle confidence intervals for the one dimensional and contours for the two dimensional case are also defined for Cash-statistics (Gehrels, 1986). The parameter space is of course different which results in different values of Table 3.3. `ISIS` seems to have implemented wrong numbers which leads to wrong contours. Thus the analyzed data are re-binned such that at least 20 counts/bin are reached in order to be able to use χ^2-statistics.
Have in mind that the χ^2-statistic is just a border case of the Poisson-based C-statistic. But be also aware that for continuum models without narrow line features the whole process of finding the minimum in parameter space is much more simplified by actually making use of that high-count/bin border-case without cutting back information necessary for the best achievable result.

3.1.6.4. Asymmetric uncertainties

Simple Gaussian error-propagation is only possible for symmetric and Gaussian distributed parameter uncertainties.
Within all analyzed spectra, however, there are many where the just discussed issue of the low-count or Poisson limit is the case. Asymmetric parameter contours turn into asymmetric parameter confidence-intervals. The likelihood is only parabolic in the case of a large number of bins. Besides this statistical reason, there are also systematic effects that produce such asymmetries (Barlow, 2004b). The key topic in the X-ray part of this thesis is to compare column density parameters derived from model fits of all available spectra. In particular differences of column densities, $\Delta N_{\rm H} = (N_{\rm H})_1 - (N_{\rm H})_2$, are of interest. In general consider two best fit parameters of two distinct data sets $(x_1)^{\sigma_2}_{\sigma_1}$ and $(x_2)^{\sigma_2}_{\sigma_1}$.
If the up- and down-side uncertainties are equal in the symmetric case ($\sigma_1 = \sigma_2$), the likelihood functions are known and one can state a combined likelihood for combined parameters. It does not matter whether one wants to propagate uncertainties via $(x_1 + x_2)$ or $(x_1 - x_2)$. Gaussian error-propagation gives $\delta f = \sqrt{(+1)^2\delta x_1^2 + (-1)^2\delta x_2^2} = \sqrt{\delta x_1^2 + \delta x_2^2}$ for symmetric uncertainties of x_1 and x_2 and a function $f = x_1 - x_2$. This result is the same as provided by the combined likelihood for symmetric uncertainties. The quadratic parameter-uncertainties make signs in linear combinations of error-prone parameters unimportant. In terms of the combined likelihood one can just multiply the individual ones – again only for symmetrical uncertainties:

$$L(x_1)L(x_2) = e^{-\frac{x_1^2}{2\sigma^2}-\frac{x_2^2}{2\sigma^2}} = e^{-\frac{(x_1+x_2)^2}{4\sigma^2}-\frac{(x_1-x_2)^2}{4\sigma^2}} = e^{-\frac{u^2}{4\sigma^2}-\frac{v^2}{4\sigma^2}} = L(u)L(v) \tag{3.18}$$

In the more realistic and generic case, it holds that $\sigma_1 \neq \sigma_2$. As an example Fig. 3.7 shows how contours can look like in real data sets. Here the two-dimensional parameter space for a choice of two different parameters is evaluated on a grid. The 1σ, 2σ, and 3σ contours are plotted as red, green and blue lines following the criteria of Table 3.3 based on a derived $\chi^2_{\rm min}$ for the best-fit parameters. The asymmetric 2σ confidence-intervals are the projections of the outer borders of the 2σ contour-lines onto the according parameter axes. The figure furthermore shows contours of two different data sets that are fitted with models based on a partial covered power-law. As one can

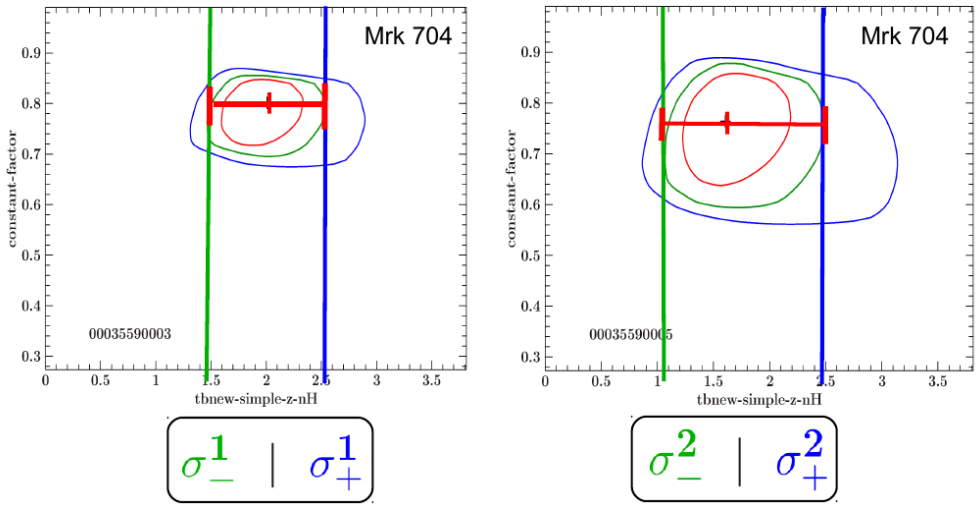

Figure 3.7.: Asymmetric uncertainties for the column density parameter derived out of two distinct data sets.

see here, the covering factor and the column densities are indeed correlated.
In most of the cases the projected 1-dimensional likelihood function according to a derived confidence-interval around the best fit parameter (a kind of cut through the parameter space parallel to both parameter axes) is unknown. Now – as so often in data analysis and applied statistics – it is again time to use the force. Barlow (2004b) and Barlow (2004a) present an elegant solution. The unknown likelihood function can be parametrized in different ways only using σ_1 and σ_2. The probably most convenient way is the ansatz of a "variable Gaussian", i.e., parabolic if taken the logarithm,

$$\ln L(\hat{\theta}, \theta) = -\frac{1}{2}\frac{(\hat{\theta} - \theta)^2}{V + V'(\theta - \hat{\theta})} \tag{3.19}$$

with a variable variance $V(\theta) = V + V'(\theta - \hat{\theta})$ and

$$V = \sigma_- \sigma_+ \qquad V' = \sigma_- + \sigma_+. \tag{3.20}$$

Now combine the just gained likelihood functions as a linear combination of parametric results θ_i to

$$\ln L(\boldsymbol{\theta}) = -\frac{1}{2}\sum_i \left(\frac{\theta_i^2}{V_i + V_i'\theta_i} \right) \tag{3.21}$$

equivalent to Eq. 3.18. The last step is to map out Eq. 3.21. For that use the technique of "undetermined multipliers", i.e., using Lagrange multipliers and some side constraint which is $u = \sum_i \theta_i$ in this case, to solve the equation. Barlow (2004b) state the solution to be

$$\theta_i = u\frac{w_i}{\sum_j w_j} \quad \text{with} \quad w_i = \frac{(V_i + V_i'\theta_i)^2}{2V_i + V_i' x_i}. \tag{3.22}$$

The numerical implementation in `ISIS` is given in Lst. 3.1.

Listing 3.1: Code excerpt for the numerical determination of a combined likelihood.

```
u = 0;
  w1 = (V[0])^2/(2*V[0]);
  w2 = (V[1])^2/(2*V[1]);
  for (i=0;i<5000;i++)
{
```

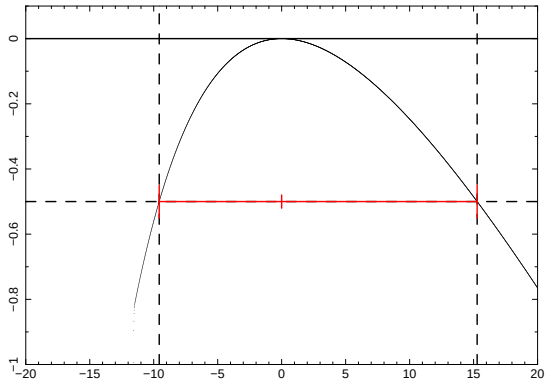

Figure 3.8.: Example for a combined likelihood numerically mapped out for initial asymmetric confidence-intervals of $\sigma^1_- = 1.41, \sigma^1_+ = 2.40$ and $\sigma^1_- = 1.03, \sigma^1_+ = 2.36$ up-scaled by a factor of 5. Plotted here is log L against the column density parameter.

```
        u -= 0.01;
        x1[i] = u*w1/(w1+w2);
        x2[i] = u*w2/(w1+w2);
        w1 = (V[0]+VV[0]*x1[i])^2/(2*V[0]+VV[0]*x1[i]);
        w2 = (V[1]+VV[1]*x2[i])^2/(2*V[1]+VV[1]*x2[i]);
        y[i] = -0.5*(x1[i]^2/(V[0]+VV[0]*x1[i]))-0.5*(x2[i]^2/(V[1]+VV[1]*x2[i]))
            ;
        if (y[i] < -0.5) conf_lo_array = [conf_lo_array,(x1+x2)[i-1]];
}
```

One example for such a combined likelihood is shown in Fig. 3.8. For this plot I use the column density uncertainties σ_- and σ_+ from Fig. 3.7 up-scaled by a factor of 5 as input for Eq. 3.21. The resulting uncertainties of the combined N_{H} can be read off that combined likelihood function by taking $L_{\max} - 1/2$ as $\sigma^1_- = 9.57/5 = 1.91$ and $\sigma^1_+ = 15.28/5 = 3.10$.

3.1.6.5. Test for Constrainability of Model functions

In many cases it is hard to constrain a certain model component. To test whether an additional model component is agreeable with the data, there are basically two ways. First of all, the **F-test** (Protassov et al., 2002) can be used especially to test for spectral lines. In the case of a model, however, that is nested and fades to its "parent"-model as parametric border case, the F-test is clearly wrong and a **Monte Carlo** ansatz has to be used. This is the case for a partial covered power-law fading into a fully absorbed power-law for a covering fraction of one.
The algorithm can be sketched as follows:
First take the model without the feature you want to test for and then, fake this spectrum using constantly the same ARF, RMF and background files. `ISIS` can do this pretty easily by loading data, background, ARF and RMF, loading a parameter file describing the model function without the feature and at last by faking data around this model.
Having a faked spectrum, it is fitted with both the input-model without the additional feature and with it. The χ^2-values for both cases are recorded. Now start again from the beginning.
Sets of around 500 simulated spectra are used to test explicitly for the constrainability of a partial covering component. Afterwards the distribution of the difference $\Delta\chi^2 = \chi^2_2 - \chi^2_1$ is plotted as histogram. The distribution is supposed to be Gaussian-distributed around the value of maximal discrepancy between both values. The p-value (Sect. 3.1.6.1) can be identified as the integral over

the distribution $f_{\Delta\chi^2}$ from the value $\Delta\chi^2$ gained with real data to infinity

$$p = \int_{\Delta\chi^2_{real}}^{\infty} f_{\Delta\chi^2} d\Delta\chi^2. \tag{3.23}$$

The p-value is the probability to find a larger discrepancy between both models than the one existent in fits to real data. Is the distribution centered around zero, it is a first indication of both models to be indistinguishable. For further statements the p-value has to be determined.

3.2. The sample of Smith et al.

Being aware of the techniques and statistical approaches of how to study X-ray spectra in general aiming the study of spectral variability, those can now be applied to real data. Of interest are sources under the reasonable suspicion of being highly variable due to aspects presented in Sect. 1.4.2. A good sample to search for such long term variability is provided by Smith et al. (2004). Although the here examined Seyfert galaxies do not reveal emission lines in the X-rays, they can indeed be found at optical/UV wavelength. Optical polarization turns out to be a tracer for a certain kind of intermediate Sy I/Sy II sources that are supposed to appear under an inclination angle of 45 °. Those are furthermore expected to be variable in absorption (see Sect. 1.4.2). Smith et al. (2004) filter 12 of those nearby (low redshift) polar scattered Sy I galaxies. On the other hand, they also find a counter-set of equatorial scattered sources that - if the geometrical assumption both of the Unified Model and of the interpretation of Smith et al. (2004) are true - should not show any variation in absorption as the line of sight is supposed not to intercept the torus. Those optically equatorial scattered sources tend to be true Sy I sources. A list of those sources together with the number of observations performed with *Swift*, *XMM* , *Suzaku* and *Chandra* is given in Table 3.4. Due to the usage of χ^2-statistics, the spectra have to be re-binned in order to guarantee at least 20 counts/bin. In turn, several observations of fainter sources have to be rejected from the analysis. All sources that have sufficient S/N ratio for model fitting are listed above the dashed line. Mrk 766 is not further analyzed in this work as several long term monitorings in literature provide enough results to confirm variability in absorption.
The analyzed sources above the dashed line are furthermore sorted after the integrated flux density in the $0.3 - 10$ keV range with the source of highest flux on top.
The sources beyond the dashed line are not able to yield values for column-density differences as there are either only single observations per source or if there are more, the S/N ratio of the data is unable to constrain absorption within the spectra.
At the time of writing, only the sample of polar scattered Sy I galaxies observed by *Swift* and *XMM* are analyzed. In the future also the control sample of equatorial scattered sources (down part of Table 3.4) will be examined to hopefully show that there is no or at least less variability than in the polar scattered sample.
Only the analyzed sources are listed in detail in Table 3.5 and Table 3.6 for *Swift*- and *XMM*-observations. The observations are sorted by observation-time per source and with decreasing integrated flux. The columns furthermore give information on the exposure time, amount of counts and thus the count-rate per observation as well as the integrated flux in the $0.3 - 10$ keV range based on the determined best-fit models. Note that only those observations are listed here that offer more than 100 counts in total. Binning the spectra to at least 20 counts/bin allowing us the usage of χ^2-statistics for model-fitting will then result in at least five bins/data points. However mostly those border cases of still too low S/N ratios also have to be rejected from the analysis chain as no reasonable column density can be constrained. Therefore the last column tells whether the appropriate observation is used for the final results. There are obviously more observations available from *Swift*. Its disadvantage is the effective area which is about one order smaller than

Table 3.4.: The sample of Smith et al.: *top half:* polar scattered Sy I galaxies, *bottom half:* equatorial scattered Sy I galaxies - the control sample.

source	*Swift* (XRT)	*XMM* (pn)	*Suzaku* (XIS)	*Chandra*	
	XRT	pn	XIS	ACIS	HEGT
NGC 3227	7	2	6	2	
NGC 4593	5	2	1		1
Mrk 704	5	2			
Fairall 51	2	2			
ESO 323-G077	3	1	1		4
Mrk 1218	7	2			
UGC 7064	2	1			
Mrk 766	33	15			
Mrk 321	1	1			
Mrk 376	2				
IRAS 15091-2107		1			
Mrk 1239		1			
Akn 120	3	1	1		
1Zwl	7	2		1	
KUV 18217+6419	1	22		4	1
Mrk 006	4	4		1	
Mrk 304		2			
Mrk 509	23	17	5		1
Mrk 841	4	5	4		3
Mrk 876	16	2			
Mrk 985					
NGC 3783	6	4	2		6
NGC 4151	4	17	3	5	5

Table 3.5.: *Swift* data

source	date	exp [ks]	rate [c/s]	flux [keV/s/cm^2]	obsid	used?
NGC 3227	2008-10-28	998.30	0.52	0.028	00037586001	
	2008-10-29	1968.67	1.30	0.048	00037586002	
	2008-11-13	2215.09	0.31	0.020	00031280004	*surd*
	2008-11-21	2121.89	0.12	0.007	00031280005	
	2008-11-22	1919.13	0.12	0.006	00031280006	
	2008-11-26	1996.28	0.19	0.014	00031280007	√
	2008-11-27	1877.27	0.12	0.010	00031280008	√
NGC 4593	2008-08-15	5029.58	0.63	0.020	00037587001	√
	2011-04-30	1917.93	0.57	0.018	00037587002	√
	2012-04-08	1131.28	0.24	0.009	00091407001	
	2012-04-16	1116.30	0.97	0.029	00091407002	
	2012-04-24	1128.79	0.71	0.025	00091407003	√
Mrk 704	2006-06-14	2218.08	0.54	0.013	00035590002	√
	2006-09-28	5006.65	0.32	0.009	00035590003	√
	2007-01-21	1718.43	0.43	0.011	00035590005	√
	2011-04-23	1832.82	0.36	0.011	00031965001	
	2011-04-23	1125.80	0.31	0.010	00031965002	
Fairall 51	2008-05-20	6087.25	0.10	0.008	00037809001	√
	2008-05-25	3182.50	0.20	0.011	00037809002	√
ESO 323-G077	2006-06-28	2279.59	0.04	0.004	00035598001	
	2006-08-17	3733.71	0.11	0.007	00035598002	√
	2006-09-14	1914.53	0.12	0.009	00035598003	√
Mrk 1218	2005-10-04	7970.89	0.01	0.001	00035167001	
	2006-09-28	3712.83	0.05	0.002	00035777001	
	2006-10-08	4212.43	0.06	0.003	00035777002	√
UGC 7064	2007-12-29	7568.04	0.02	0.002	00037137001	√
	2007-12-29	7568.04	0.02	0.002	00037137001	

Table 3.6.: *XMM* data

source	date	exp [ks]	rate [c/s]	flux [keV/s/cm^2]	obsid	used?
NGC 4593	2000-07-02	8782.68	34.66	0.048	0109970101	√
	2002-06-23	53225.81	31.43	0.047	0059830101	√
NGC 3227	2000-11-28	31089.05	1.03	0.006	0101040301	√
	2006-12-03	97408.58	13.01	0.031	0400270101	√
Fairall 51	2005-09-08	20384.15	7.26	0.020	0300240401	√
	2006-03-07	17301.79	0.95	0.005	0300240901	√
Mrk 704	2005-10-21	14875.59	2.79	0.007	0300240101	√
	2008-11-02	68436.02	9.62	0.013	0502091601	
ESO 323-G077	2006-02-07	23830.85	1.07	0.006	0300240501	√
Mrk 1218	2005-04-09	6586.68	0.72	0.002	0302260201	√
UGC 7064	2009-12-26	27604.03	0.35	0.002	0601780601	√

the one of *XMM*. This is also obvious from the count-rates. Comparing Table 3.5 and Table 3.6 the amount of counts per second is about 10 times larger for *XMM* observations that have flux comparable with *Swift* such as for ESO 323-G077.

3.3. The Analysis Chain

From the raw data to an analysis of parameters of interest several steps have to be undertaken. Here, those are shortly summarized:

- **Collect data** of all available observations.
- **Examine the data** in `ds9` which are initially only available as a CCD-image and extract source- and background regions by choosing a circular regions around the location of the source as well as somewhere off the source to collect information on the background counts. Save those region files and process them with the satellite's data extraction tools in order to **get event files** for source- and background count-spectra. For this analysis the most recent response matrix should be used as the detector efficiency changes with time due to impacts of micro-meteorites on the chip or the occurrence of dead pixels, dead columns and other aging effects of the detector. For *Swift* this is automatically performed by the scripts `xrtprepare` and `xrtextract`, for *XMM* by `xmmprepare` and `xmmextract` maintained at the Dr. Remeis-Observatory, Bamberg. One must also account for possible pile-up by excluding the central region of point sources where it can happen that the read-out time of the CCD is too slow for very luminous sources.
- **Exclude counts below 3 keV.** Facing the high uncertainties at energies even below 0.5 keV (Sect. 3.1.5) due to an enhanced expected background I still decide to accept data in the 0.3 – 10 keV range as the low S/N of most sources does hardly return many data points in the soft energy range after re-binning. Data in the soft X-ray regime are essential to find well constrained $N_{\rm H}$ values. Loosing data in the soft while increasing the degrees of freedom is not a compromise in my eyes. Hence I agree in dealing with additional correlations between $N_{\rm H}$ and the power-law slope Γ instead of having less spectral information below 2 keV.
- **Load the event files into** `ISIS` to examine and **rebin** the spectra. The used criteria are to fulfill the border of at least 20 counts/bin to be able to apply χ^2-statistics.
- **Find models** for the data and fit the data. Using χ^2-statistics and a Levenberg-Marquardt gradient minimization algorithm such as `mpfit` work fine for continuum models.
- After having found a proper model explanation of the data run an **error calculation** to iteratively step the parameter space for single parameters to find the confidence intervals for a 90 % confidence level. At the `Remeis cluster` this can be done parallelized using the script `mpi_fit_pars`.
- To also account for possible correlations between parameters, it is essential to additionally **calculate contour maps** and read off the 90 % confidence intervals from those. For calculating parameter maps always two parameters are kept fixed while all others are getting re-fitted at each position of the map.
  Similar to the error-calculation, the contour map calculation can be done parallelized with the `ISIS`-script `contour_trq` allocating each calculation to a different core. The `Remeis-cluster` consists of 204 separate cores which makes such time consuming calculations easy to handle.
- The column density parameter $N_{\rm H}$ in absorption models is of special interest. Having calculated necessary contours, read off the appropriate **$N_{\rm H}$-uncertainties** and

Table 3.7.: Model name allocations with the ISIS model names.

Phenomenological name	ISIS model component
Power-law	power-law(1)
Galactic absorption	tbnew_simple(1)
Internal cold absorption	tbnew_simple(1)
Gauss	zgauss(1)
Partial covering with cold absorption	zpcfabs(1)
Covering Factor	constant(1)
Warm absorbing zone	zxipcf(1)
Ionized Absorber	absori(1)
Comptonization of soft photons	comptt(1)

- use them to derive a **combined uncertainty** for the difference of two measurements of N_{H}, ΔN_{H}, belonging to two different observations.
- a plot of the ΔN_{H} against the time-difference Δt between two observations finally tells, whether the amount of absorption in two observations is consistent or inconsistent with each other. In the latter case one has found **proof for variability of absorption**.

In terms of testing model functions a bottom-up procedure is chosen starting with a simple absorbed power-law model over to more complex models. The following list ranks the successfully applied models by complexity.

$$\begin{aligned} e^{-\sigma N_{\mathrm{H\,internal}}} e^{-\sigma N_{\mathrm{H\,galactic}}} (E^{-\Gamma} + \mathcal{G}_{\mathtt{Fe}}) \quad & \text{absorbed power-law} \\ [(1-c)\cdot c \cdot e^{-\sigma N_{\mathrm{H\,internal}}} e^{-\sigma N_{\mathrm{H\,galactic}}}](E^{-\Gamma} + \mathcal{G}_{\mathtt{Fe}}) \quad & \text{partial coverer} \\ \mathrm{WA}(1)\cdot \mathrm{WA}(2) \cdot e^{-\sigma N_{\mathrm{H\,internal}}} e^{-\sigma N_{\mathrm{H\,galactic}}}](E^{-\Gamma} + \mathcal{G}_{\mathtt{Fe}}) \quad & \text{power-law warm and cold absorbed} \end{aligned} \tag{3.24}$$

Here the source internal absorption is separated off the galactic one. Additionally the mostly prominent Iron Kα line at 6.4 keV is fitted with a Gaussian component $\mathcal{G}_{\mathrm{Fe}}$ in all attempts.

3.4. Spectral Variability results

In this section the results based on the considerations in the introductory part of this thesis are presented. Tables of the best-fit parameters are attached in the appendix. Table 3.7 gives the connection of the phenomenological model component names in Sect. 4 with the notations of ISIS. Occasionally, *XMM* data allow us to fit several (absorption) line components. The only emission line found in all spectra with a high S/N ratio, is the Iron Kα line. For other absorption lines corresponding most likely to warm absorbers, find the central energies in Sect. 4 and take Guainazzi & Bianchi (2007) as a reference who list the most important lines seen in comparable sources. As the objective of my thesis solely depends on continuum models, the detected lines are not discussed in the following.
Data that are insufficient to fit a N_{H} component are not analyzed at all and do not further appear in the tables.
Regarding the applied warm absorbers it has to be noted that the covering fraction is always fixed to unity as warm absorbing material is most likely outflowing, thin and partially ionized gas on large spatial scales (Sect. 1.4). To account for possible outflowing gas measured for many similar sources as well as for many of the sources in the present sample, the redshift is left free to vary while fitting. Often redshifts are constrained that are less than the system redshift suggesting the

shield to move towards the observer.
In the following each source is discussed in detail, where special focus is payed to the spectral model components of the high-S/N data of *XMM*.

3.4.1. Fairall 51

3.4.1.1. Introduction and Observations

Archival data taken from the Sy I galaxy Fairall 51 ($z \approx 0.014$) by *Swift* and *XMM* reveal relatively low luminosities from $L_{\mathrm{X}} = 3.12 \cdot 10^{42}\,\mathrm{erg/s}$ to $L_{\mathrm{X}} = 1.25 \cdot 10^{43}\,\mathrm{erg/s}$ ($0.3-10\,\mathrm{keV}$). See Sect. 1.1.3 for a proper derivation of the luminosity with given cosmological parameters and redshift.
Fairall 51 was observed two times by *Swift* at 2008 May 20 and 2008 May 25 as well as two times by *XMM*-Newton at 2005 September 8 and 2006 March 7. The time coverage allows one a test for short (days) and long-term (years) variations in absorption. As for all following sources and appropriate observations both for *Swift* and *XMM*-Newton counts are extracted in a $0.3-10\,\mathrm{keV}$ range from the detector's event-files. All counts below $0.3\,\mathrm{keV}$ are excluded.

3.4.1.2. Spectral Fits

Starting with the ***XMM*-Newton** observations without going into detail regarding the step-by-step procedure of finding the best fit, for both observations solely two components of partial covering absorption by partially ionized material are needed to account for the absorbed soft X-ray flux. One warm absorber component has an ionization parameter of $\log \xi \approx 0.7$, the other $\log \xi \approx 2.3$ for both observations. The best-fit models applied to both observations consist of an initial power law, attenuated in the soft by two warm absorbers and one component addressing the well known galactic absorption as well as several additional line components. In `ISIS` the total fit-function is called

```
zxipcf(1)*zxipcf(2)*powerlaw+zgauss(1)+zgauss(2)+zgauss(3))*tbnew_simple
```

According to Sect. 1.4, the ionization parameter is a measure for the amount of ionization and thus the central sources' luminosity. Both components have constant ionization factors within the errors which can be understood by looking at Fig. 3.9 and Fig. 3.10 where in the hard X-ray regime, both initial power-laws have comparable normalization. Thus the initial irradiation emerging from regions in the vicinity of the SMBH is hardly variable – just as implied by the ionization parameters. Distinguishing the components with higher and lower ξ is straight forward when looking at Fig. 3.9. The component `zxipcf(1)` with lower ξ has more an effect of a neutral absorber, mainly absorbing the continuum in the soft. The second absorbing component (blue line) is stronger ionized and has less effect in soft absorption. Reason for that is that highly ionized elements lack of electrons in outer shells being important for photo-electrical absorption. As high-Z elements are mainly found in the soft, this is also the regime where photo-electrical absorption has most effect.
Furthermore comparing both observations, model-fits of the second reveal larger column densities of the partially ionized shields. Such N_{H}-variability without significant variation of the initial power-law flux is best visible in Fig. 3.10 where also *Swift* data are included in between of both *XMM*-observations.
The best-fit model for both ***Swift***-observations boils down to only one warm absorber and the galactic-absorbed initial power law

```
zxipcf*powerlaw*tbnew_simple.
```

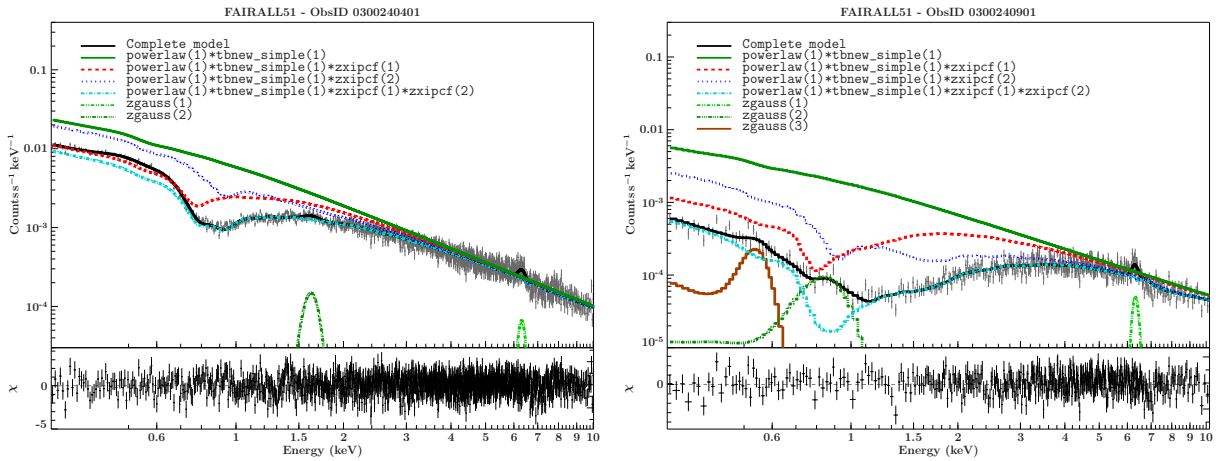

Figure 3.9.: Best-fit model components of the Fairall 51 – *XMM*-spectra (EPIC-pn) from 2005-09-08 and 2006-03-07.

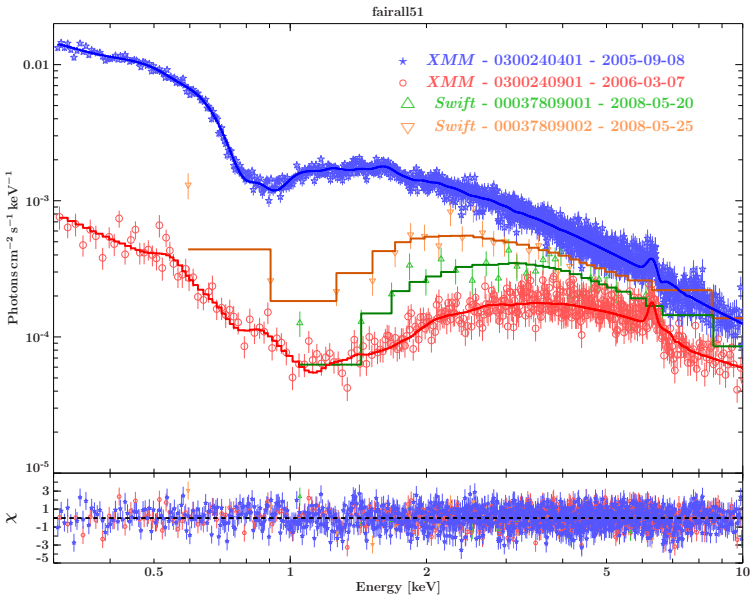

Figure 3.10.: Plot of all four data-sets recorded with *Swift* (XRT) and *XMM* (EPIC-pn) for Fairall 51.

The ionization parameter is frozen to the values of the lower ionized components derived with *XMM* for both cases as, again, the irradiation on the system can be said to be relatively constant. It is only possible to constrain lower ionized absorbers for *Swift* observations of the same kind if possible at all. The low S/N ratio of the data is too low to constrain any absorption line structures. For basically all following *Swift* observations it is sufficient to describe the shield with a model of cold, neutral gas. The results obtained here are more or less consistent with those from Ricci et al. (2010). The difference is that they claim to find a better model with a third warm absorber layer of higher ionization. As my results show, two partially ionized absorbers are sufficient to describe the continuum well enough.

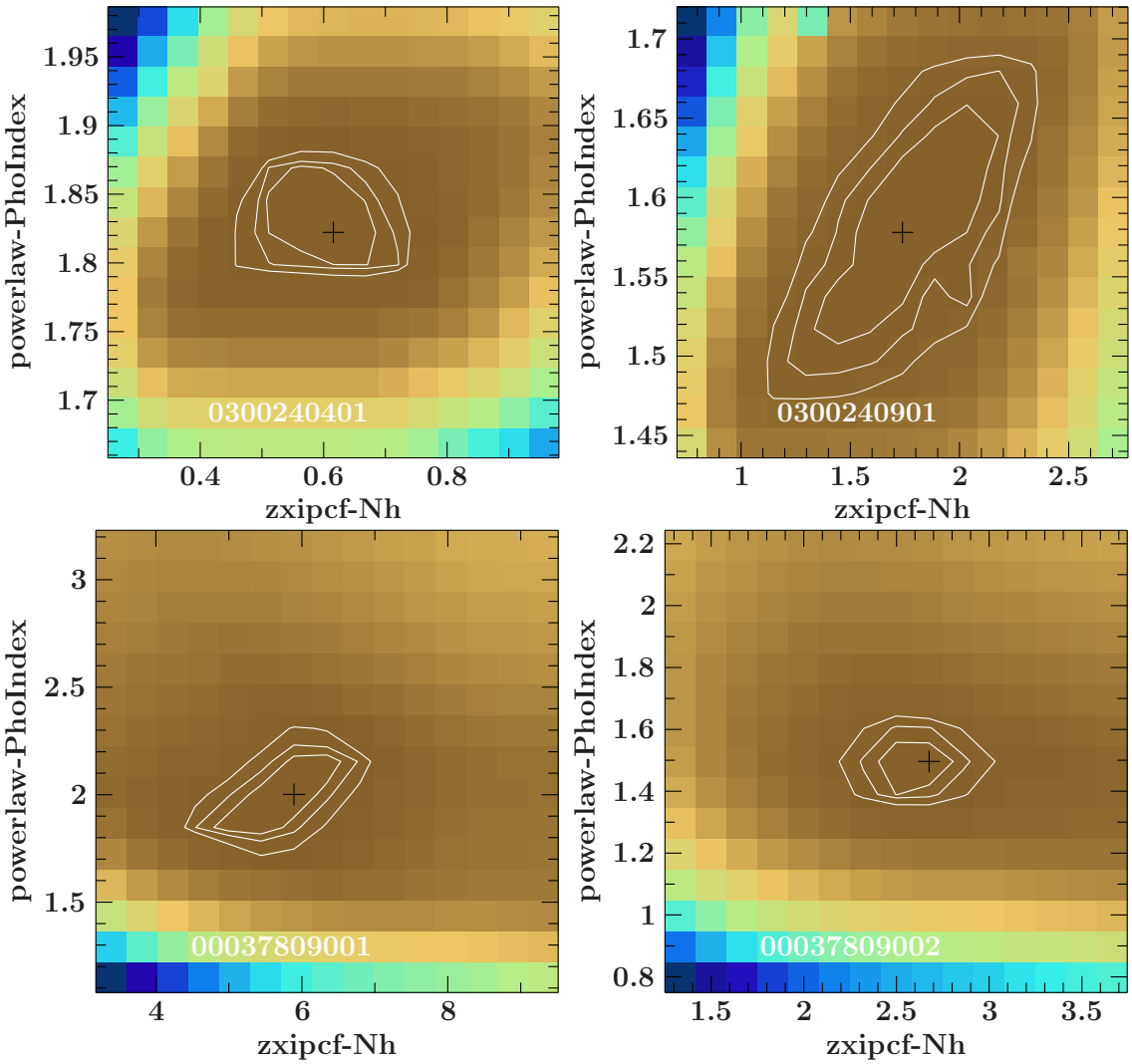

Figure 3.11.: Colored contour plots between the column density N_{H} [$10^{22}\,\mathrm{cm}^{-2}$] and power-law slope Γ in the data of all *XMM* (*top*) and *Swift* (*bottom*) observations of Fairall 51 for a 25×25 grid. Shown are 68 %, 90 % and 99 % confidence levels.

3.4.1.3. N_{H}-VARIABILITY STUDY

For the study of N_{H} variability it is necessary to further process with the column densities of the lower ionized warm absorber components, as no separate cold absorber is needed to fully describe the absorption.

Being interested not only in the N_{H} values themselves, but also in the errors that are essential to make tentative variability-statements, first the one-dimensional 90 % confidence intervals are calculated using `ISIS`. This is, however, not enough. Correlations between several free parameters also have to be taken into account. Therefore, contour plots between those parameters are calculated. In this case a possible correlation can exist between the N_{H} and the power-law slope. A model with a too soft slope will have to be additionally attenuated in the soft to still fit to the data. Large column densities are thus coming along with large slopes. The figures show all calculated contours both in a color-coded (Fig. 3.11) and interpolated (Fig. 3.12) representation. Contours calculated for *XMM* spectra constrain much narrower confidence intervals than *Swift* observations which is clear from comparing the effective areas and thus the data-S/N ratio of both instruments.

Arguing whether the contours are consistent with each other in terms of a 90 % confidence level

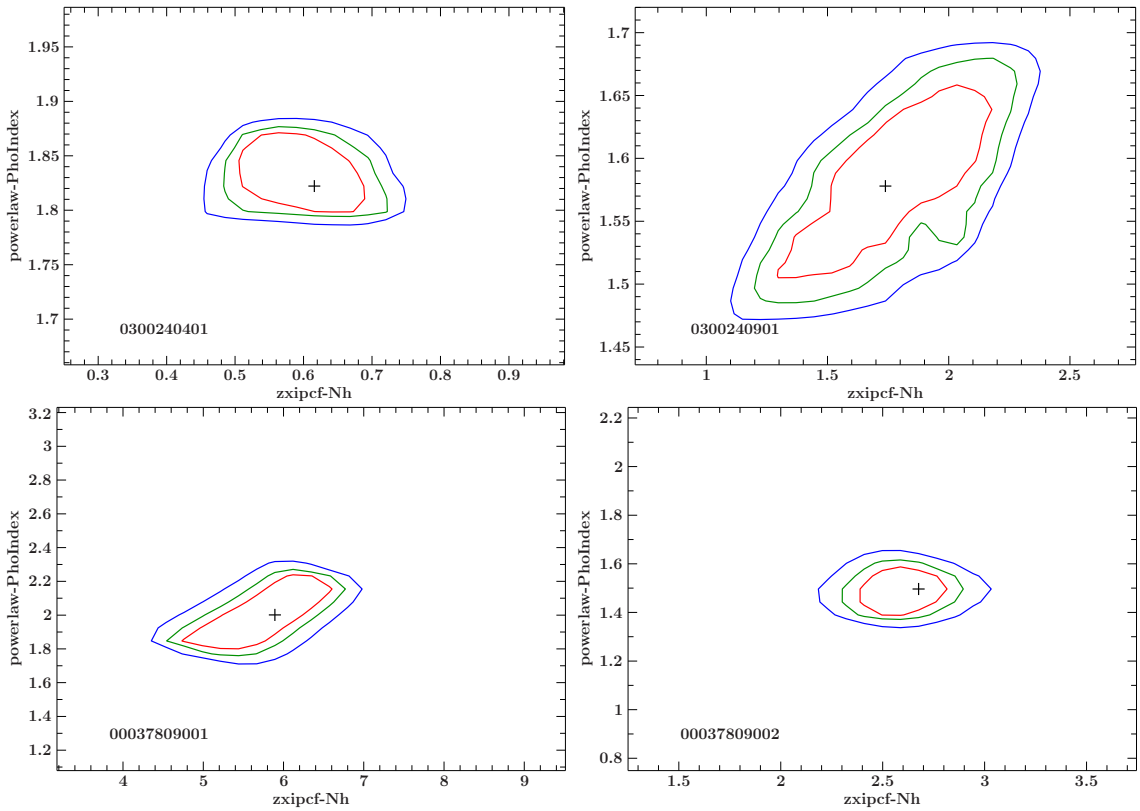

Figure 3.12.: Interpolated contour plots between the column density $N_{\rm H}$ [$10^{22}\,{\rm cm}^{-2}$] and power-law slope Γ in the data of all *XMM* (*top*) and *Swift* (*bottom*) observations of Fairall 51 for a 25×25 grid. Shown are 68 %, 90 % and 99 % confidence levels.

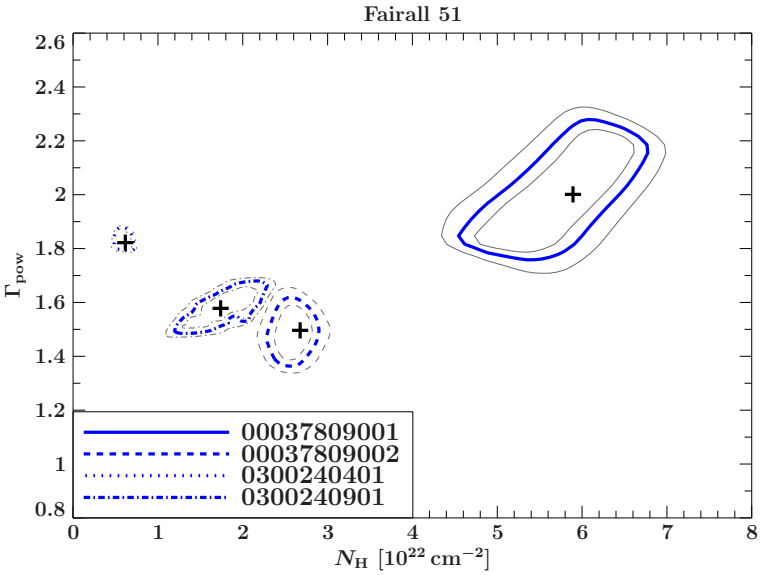

Figure 3.13.: Plot of all interpolated contours for Fairall 51. The blue, thick lines in the middle represent the 90 % contours, the thin, gray lines the 68 % and 99 % contours.

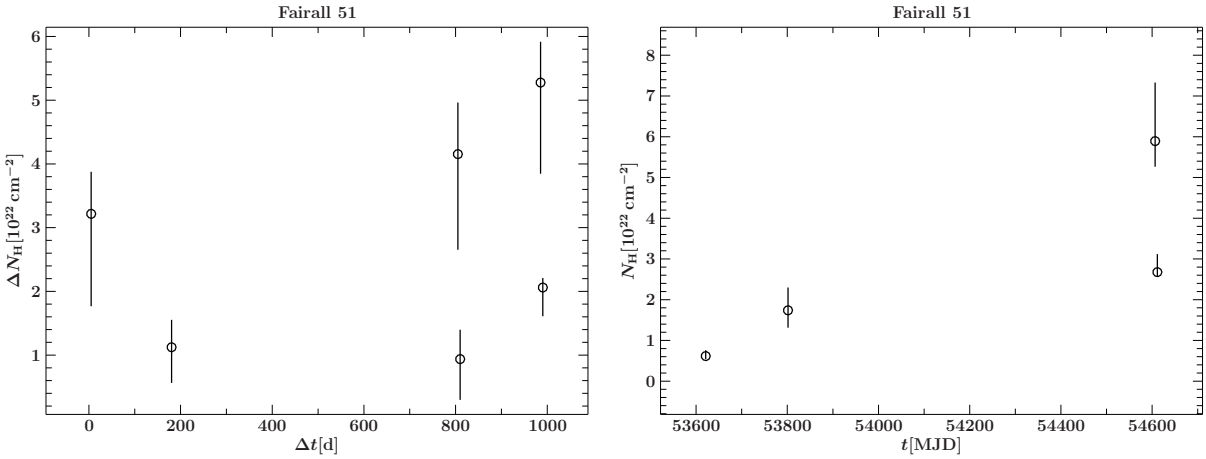

Figure 3.14.: *Left:* ΔN_H over Δt for all possible combinations of observations of Fairall 51, *right:* absolute values of N_H with errors plotted over time.

of N_H is best done by over-plotting all interpolated contours (Fig. 3.13). The figure clearly shows that the contours are inconsistent with each other on a 90 % confidence level. From this result N_H-variability is already shown. To be more accurate in terms of stating numbers, one can calculate the difference of N_H between all possible combinations of observations. The amount of possible ΔN_H values is thus given by the number of possible 2-sets out of a n-set of observations $n!/2!(n-2)!$ where the order does not matter. To find the time-scales of variation, plot the derived ΔN_H values between two observations against the time difference between both (Fig. 3.14, left figure). This plot reveals that the smallest time-scale of variability is around 5 days. As the contours already suggest, variability can be constrained for all combinations of observations. This is because the errors of all ΔN_H are inconsistent with zero. For the following sources this is not always the case. Although there are only four observations available in total, the time coverage allows one both the study of variability on short and long time scales of years. The figure in the right panel plots absolute N_H values over time which additionally suggests variable behavior in particular increasing absorption with time as also visible in the spectra in Fig. 3.10.

3.4.2. NGC 4593

3.4.2.1. Introduction and Observations

The Sy I galaxy NGC 4593 was observed twice by *XMM* in 2000 July 2 and 2002 June 23 as well as five times by *Swift* between 2008 and 2012. However, due to low S/N ratio only three *Swift* observations in 2008 August 15, 2011 April 30 and 2012 April 24 are further analyzed here. Furthermore there are two more archival pointings by *Suzaku* in 2007 and *Chandra* in 2001 which are currently getting analyzed and thus not included in this thesis.
The galaxy is close by with a redshift of $z = 0.009$. Compared to the other sources in this sample it is among the most luminous ones with luminosities ranging from $L_{\mathrm{X}} = 1.12 \cdot 10^{43}\,\mathrm{erg/s}$ to $L_{\mathrm{X}} = 2.99 \cdot 10^{43}\,\mathrm{erg/s}$ based on my derived models in the $0.3 - 10\,\mathrm{keV}$ range. Brenneman et al. (2007) cite X-ray luminosities derived with ASCA and *Chandra* in the $2 - 10\,\mathrm{keV}$ range of 8.53 and $5.37 \cdot 10^{42}\,\mathrm{erg/s}$.
Due to the luminosity of the source, *XMM* was operating in the small window mode with the possibility of much faster readout to account for possible pile-up.

3.4.2.2. Spectral Fits

I will again start with the ***XMM*-Newton** data.
The model fits are adapted from Brenneman et al. (2007) for the observation from 2002 June 23. The earlier observation in 2000 July 2 is discussed by Steenbrugge et al. (2003). They constrain on the RGS grating instrument of *XMM* as the background was too high for analyzing the EPIC-pn data as they argue. To loose no continuum data, I, however, do so and gain a spectrum which is similar to the one from 2002 (see Fig. 3.16). I thus used the same continuum model for both observations. The achieved best-fit model is

```
((powerlaw+comptt)*zpcfabs*zxipcf(1)*zxipcf(2)+zgauss(1)+zgauss(2))*tbnew_simple
```

which differs from the one used by Brenneman et al. (2007) in the partial coverer that is additionally used here to try to explicitly constrain cold absorption. This, however, leads to a very small covering factor of $c \approx 0.14$ with a medium N_{H} of $3 - 4 \cdot 10^{22}\,\mathrm{cm}^{-2}$ for both observation. Therefore I conclude that it is indeed possible to separate off a cold absorber from the two warm absorbers only used by Brenneman et al. (2007) which has only relatively low – but still visible (Fig. 3.15, red, dashed line) – effect on the continuum attenuation in the soft because of the low covering. Also visible in that figure are again two different ionization states of the low ionized absorber with $\xi \approx 2$ and the higher ionized one with $\xi \approx 3 - 4$. Both stay relatively constant which involves the constant normalization of both observations. Brenneman et al. (2007) constrain even lower ionization parameters to account for the existing contribution of cold absorption as separated of here.
NGC 4593 furthermore shows a prominent soft excess that is tried to be modeled with a bremsstrahlung component and thermal Comptonization of soft photons in a hot plasma. Here I do not particularly need the bremsstrahlung component. The further three analyzed ***Swift*** observations use the simple partial coverer model as derived in the introductory part of this thesis.

```
(((1-constant)+constant*tbnew_simple_z)*powerlaw+zgauss)*tbnew_simple
```

The constrained column densities range from $N_{\mathrm{H}} \approx 1.2 \cdot 10^{22}\,\mathrm{cm}^{-2}$ to $N_{\mathrm{H}} \approx 1.9 \cdot 10^{22}\,\mathrm{cm}^{-2}$ and appropriate covering factors from $c = 0.5$ up to $c = 0.6$. From Fig. 3.16 it is not clear by eye that a partial coverer is indeed needed for the obs-ids 00037587001 and 00037587002. Monte Carlo simulations yield p-values of the $\Delta\chi^2$-distribution of 0.094 for the observation 00037587001 and

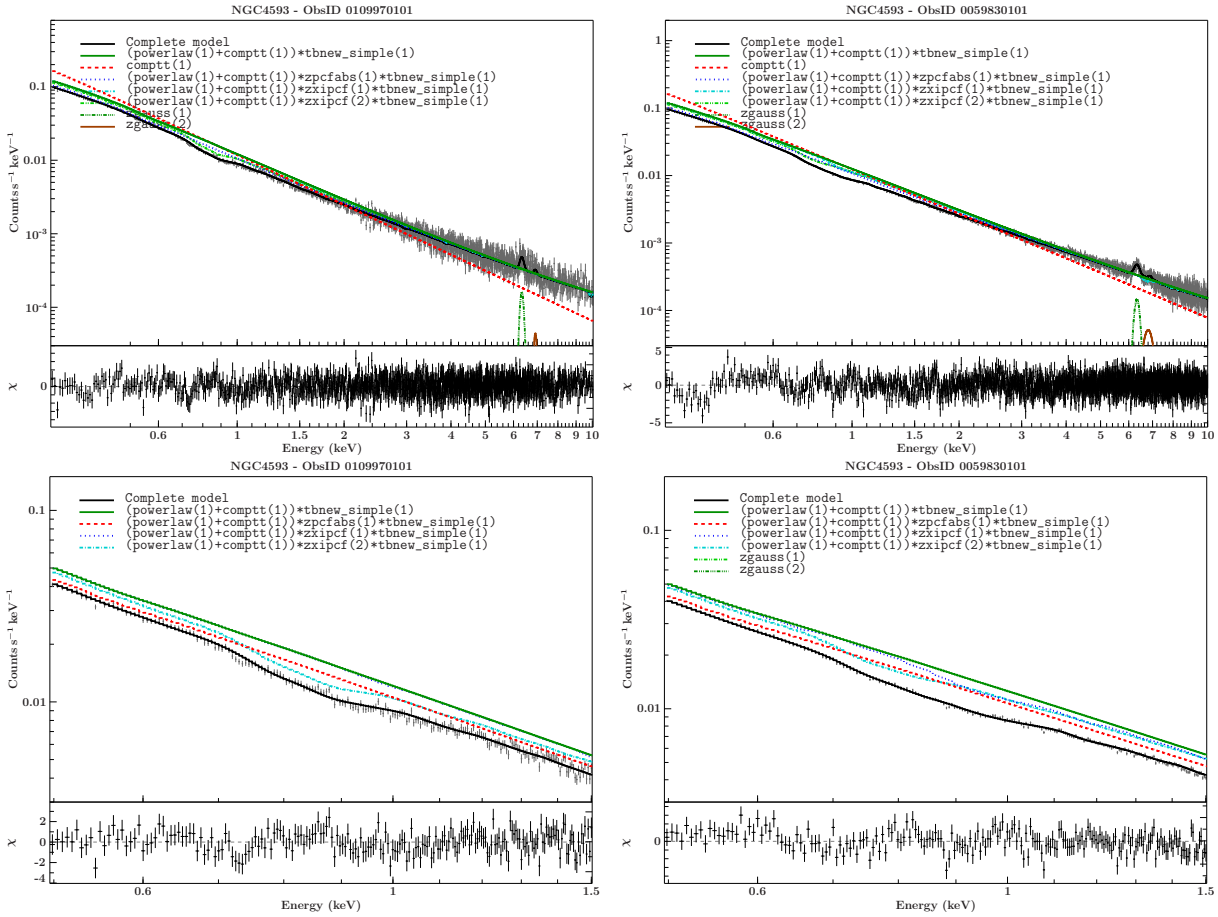

Figure 3.15.: Best-fit model components of the NGC 4593 – *XMM*-spectra (EPIC-pn) from 2000-07-02 and 2002-06-23 in full-range $0.3 - 10$ keV (*top*) and the soft-range $0.5 - 1.5$ keV (*bottom*) for better visualization.

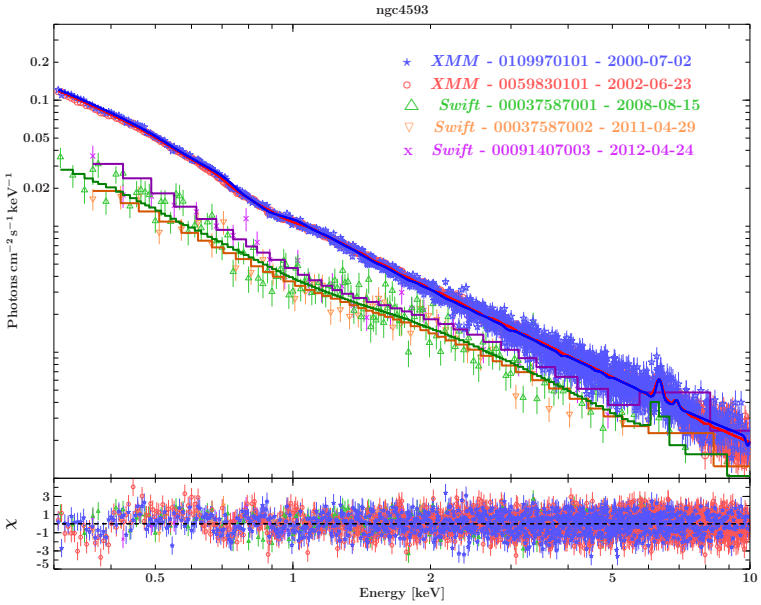

Figure 3.16.: Plot of all five analyzed data-sets recorded with *Swift* (XRT) and *XMM* (EPIC-pn) for NGC 4593.

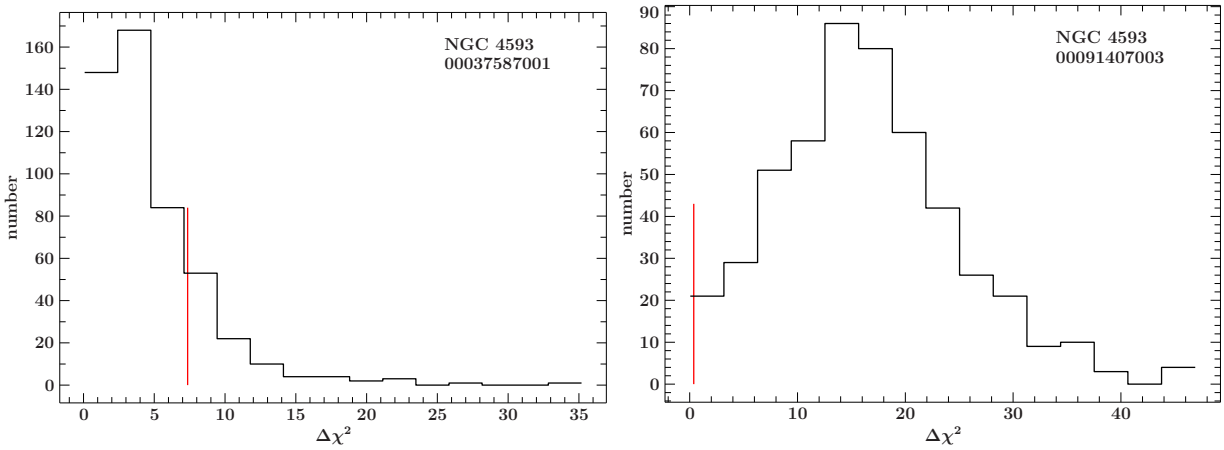

Figure 3.17.: Plots of the $\Delta\chi^2$-distributions for the extreme cases of the obsids 00037587001 and 00091407003. The red vertical line marks the $\Delta\chi^2$-value of fits to the real dataset.

0.418 for the obs-id 00037587002. The observation with the obs-id 00091407003 yields a p-value of even 0.96. That means that the probability for finding larger χ^2 deviations between a partial coverer and a simple absorbed power-law are largest for the last two cases and only very small for the first one with only 9.4 %. Figure 3.17 illustrates those results. In the left panel the distribution is clearly centered around zero deviation between the statistics of both model attempts, where the peak shifts to non-zero values for the last observation in 2012 with the obsid 00091407003. Considering the location of the best-fit $\Delta\chi^2$ of the real data-set (red vertical line) the p-value as being the integral over the distribution from that point on, is largest for the latter case.

3.4.2.3. N_{H}-VARIABILITY STUDY

Proceeding with these results the next step is again the derivation of proper errors using the advantages of contour maps.
In the following I do not show the single contour plots but only the combination of all. In opposite to Fairall 51 where no partial covering by neutral matter can be constrained, here there are two considerable correlations: one between the column density N_{H} and the power-law slope Γ and the other between N_{H} and the covering factor c. The third important correlation between c and Γ does not affect the parameter of interest, N_{H}. The contours for both possible correlating parameter pairs do – in opposite to Fairall 51 - cross each other on the 90 % confidence limit especially within *Swift* and *XMM* observations. Considering that the spectral shape and normalization stay quite unchanged within the observations of each instrument, this is expected. Only the contours between observations of *Swift* and *XMM* stay inconsistent in particular regarding the column density. Figure 3.19 as a final result returns a minimum variability time-scale of 2245 days of ≈ 6 years which is more or less the time spacing of observations between the *XMM* observations from 2000/2002 and the *Swift* ones from 2008/2011/2012. The arrows pointing downwards represent upper limits of the ΔN_{H} which are the upper end of the up-side combined uncertainties for those combinations of N_{H} values, where the value is consistent with zero within the uncertainty.
The development of the N_{H} over time is shown in the right panel. The large error of the first *XMM* data point in 2000 is due to the difficulty of constraining a neutral, cold absorber besides the warm absorbers.

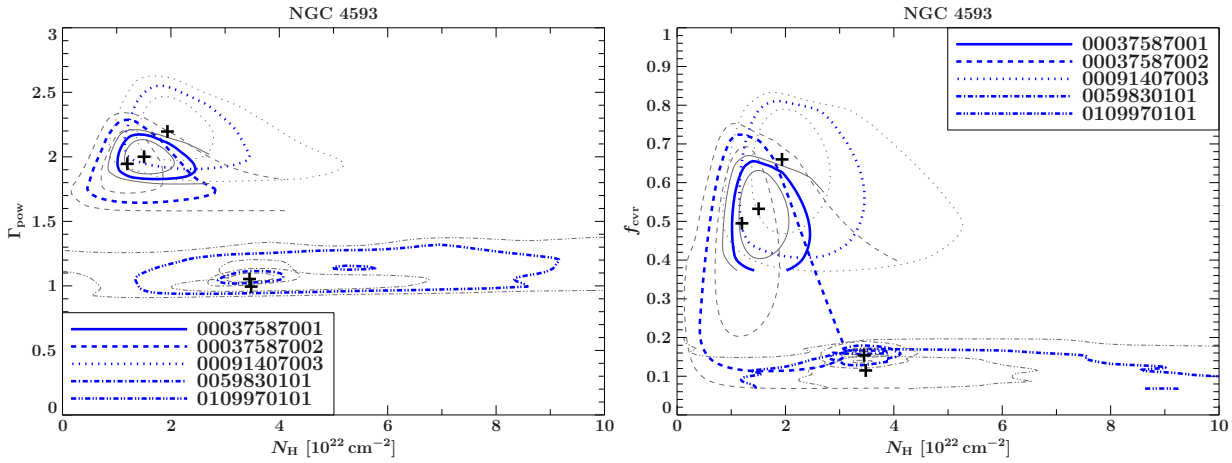

Figure 3.18.: Plot of all interpolated contours for NGC 4593. The blue, thick lines in the middle represent the 90 % contours, the thin, gray lines the 68 % and 99 % contours. *Left:* contour maps for $N_{\rm H}$ and Γ, *right:* for $N_{\rm H}$ and c.

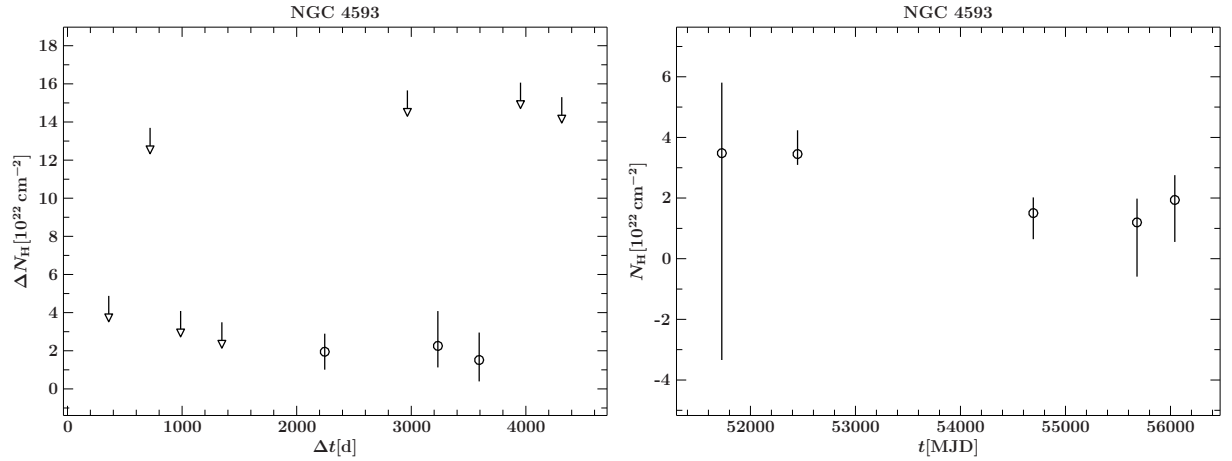

Figure 3.19.: *Left:* $\Delta N_{\rm H}$ over Δt for all possible combinations of observations of NGC 4593, *right:* absolute values of $N_{\rm H}$ with errors plotted over time.

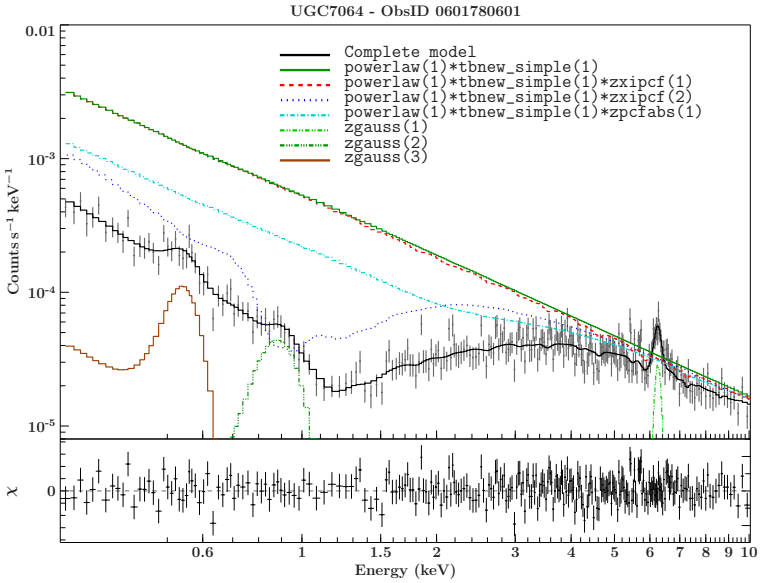

Figure 3.20.: Best-fit model components of the UGC 7064 – *XMM*-spectrum (EPIC-pn) from 2009-12-27 in the full range 0.3 – 10 keV.

3.4.3. UGC 7064

3.4.3.1. Introduction and Observations

Véron-Cetty & Véron (2006) classify UGC 7064 as Sy 1.9 type. I measure a luminosity of $L_X = 4.05 \cdot 10^{42}$ erg/s based on the two observations by *Swift* in 2007 December 29 and *XMM*-Newton in 2009 December 27. The source is amongst those with least flux within my sample but has a distance-independent luminosity comparable to Fairall 51.

3.4.3.2. Spectral Fits

For UGC 7064 no references regarding a model fit of the continuum can be found in the literature. The *XMM*-Newton spectrum is fitted best with the model

```
zxipcf(1)*zxipcf(2)*zpcfabs*powerlaw+zgauss(1)+zgauss(2)+zgauss(3))*tbnew_simple
```

consisting of a power-law attenuated by two warm absorbers, one partial covering cold absorber and the galactic absorption. Three absorption line components can also be constrained. Figure 3.20 nicely reveals the interaction of both an intermediately high ionized ($\xi \approx 4$) warm absorber and a partial covered power-law to form the best-fit model of the *XMM*-Newton observation. The second warm absorber component with a comparatively lower ionization factor of $\xi \approx 1$ does not really affect the initial power-law.

The *Swift* observation from 2007 over-plotted in Fig. 3.21 does not bring enough S/N to constrain such a complex model. An exposure time of 7.6 ks is still not enough facing the low flux. Therefore the second available *Swift* observation with an exposure of only 1.9 ks has to be rejected from the further analysis. The fit model applied to the *Swift* data is again a simple power-law partial covered with neutral, cold matter.

```
(((1-constant)+constant*tbnew_simple_z)*powerlaw+zgauss)*tbnew_simple
```

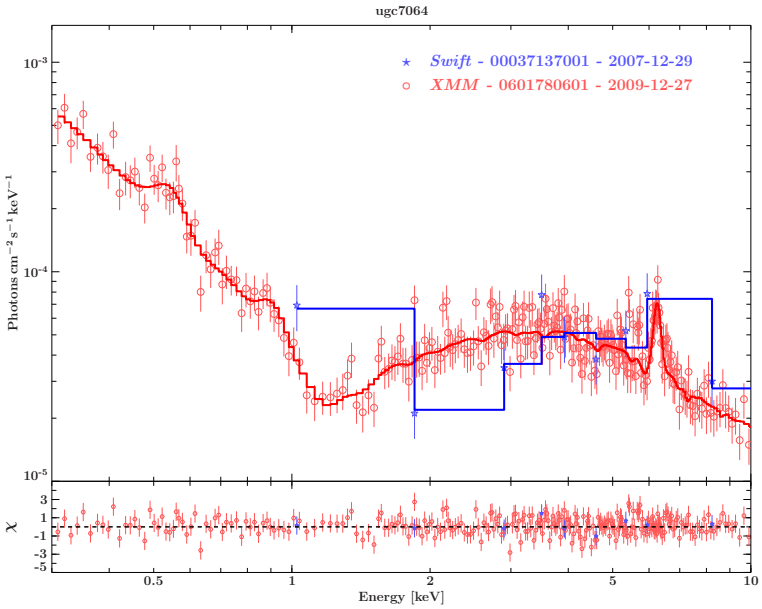

Figure 3.21.: Plot of all five analyzed data-sets recorded with *Swift* (XRT) and *XMM* (EPIC-pn) for UGC 7064.

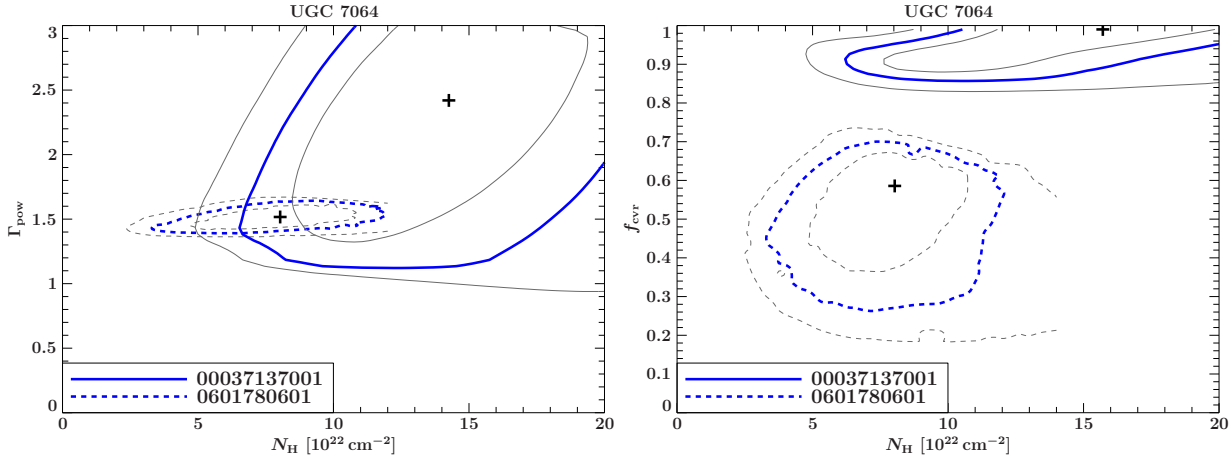

Figure 3.22.: Plot of all interpolated contours for UGC 7064. The blue, thick lines in the middle represent the 90% contours, the thin, gray lines the 68 and 99% contours. *Left:* contour maps for N_H and Γ, *right:* for N_H and c.

3.4.3.3. N_H-VARIABILITY STUDY

As already obvious from Fig. 3.21, no significant N_H variability can be expected. Indeed the contour plots for both possible correlated parameter pairs show a strong consistency of both observations with each other on a 90 % confidence level (Fig. 3.22). Also the $\Delta N_H - \Delta t$ and $N_H - t$ plots support this result as only an upper limit on the N_H-variability can be derived.

3.4.4. NGC 3227

3.4.4.1. Introduction and Observations

NGC 3227 is a nearby Sy 1.5 galaxy (Osterbrock & Martel, 1993) with a redshift of $z = 0.00386$. It was observed twice with *XMM*-Newton in (2000 November 28, 2006 December 3) and seven times with *Swift* in 2008. From those only three can be further processed due to the low S/N ratio of the rest of the spectra. The overall time coverage comprehends time differences from days to years. There are more observations by *Suzaku* in 2008 and *Chandra* in 1999 and 2002. Their analysis is subject of current research. With my model fits I derive the X-ray luminosities in the $0.3 - 10\,\mathrm{keV}$ range to vary between $L_\mathrm{X} = 2.81 \cdot 10^{41}\,\mathrm{erg/s}$ and $L_\mathrm{X} = 1.45 \cdot 10^{42}\,\mathrm{erg/s}$.

3.4.4.2. Spectral Fits

The two ***XMM*-Newton** spectra come along with one strongly absorbed spectrum (obsid 0101040301, Nov. 2000) and one hardly absorbed one with a strong soft excess (obsid 0400270101, Dec. 2006). Both observations are already analyzed by Gondoin et al. (2003) and Markowitz et al. (2009)/Lamer et al. (2003). As for all other sources I built up an independent fit-function following a bottom-top procedure. My independent results, though, turn out to be comparable with those derived in both publications. The observation from 2000 reveals significant absorption in the soft and can be addressed as the low-state comparing all available data in that energy range. In opposite the *XMM*-Newton observation six years later lacks obvious neutral absorption just by examining the spectra (Fig. 3.24). Regarding the other observations, this is clearly the high-state. Starting with the well absorbed observation from the year 2000, a first glance suggests to try a partial coverer as fit model. The high-state observation, however, additionally shows a clear soft excess over the extrapolation of the hard X-ray galactic absorbed power-law (Fig. 3.23, right panel). Ceballos & Barcons (1996) suggest to use a full covering of partially ionized gas instead of the partial coverer of cold, neutral gas. This warm absorber can account for both the soft excess seen in the unobscured high-state as well as notable absorption in the low-state. A combination of both partial, neutral covering and a warm absorber component turns out to form the best-fit model for the low-state, which is also found by Gondoin et al. (2003). The model description in *ISIS* is called:

```
(powerlaw*((1-constant)+constant*tbnew_simple_z)*absori+zgauss)*tbnew_simple
```

In Fig. 3.23 the top figure explicitly plots each additive model component. The blue, dotted line shows the shape of the constrained cold partial coverer with a high covering of $c \approx 0.85$ and a considerable absorption of $N_\mathrm{H} \approx 6.5 \cdot 10^{22}\,\mathrm{cm}^{-2}$. The dashed red line resembles the partially ionized absorber with moderate ionization of $\xi \approx 1.9$ and and $N_\mathrm{H} \approx 1.6 \cdot 10^{22}\,\mathrm{cm}^{-2}$.
For the *XMM*-Newton high state modeling I refer to Markowitz et al. (2009). The argumentation for the model given by

```
((powerlaw(1)+zgauss(1))*tbnew_simple_z(1)+(powerlaw(2)+zgauss(2)))*
zxipcf(1)*zxipcf(2)*tbnew_simple_z(2)*tbnew_simple(1)
```

is best understood by involving Fig. 3.23. Fitting only a power law to the hard X-ray part of the spectrum ($\Gamma \approx 1.43$), the residuals strongly suggest both absorption and a soft excess. The absorption is modeled with a shield of neutral matter ($N_\mathrm{H} \approx 0.40 \cdot 10^{22}\,\mathrm{cm}^{-2}$, blue, dotted line). The residuals suggesting the soft-excess are suppressed by adding a second steeper power-law (red, dashed line) with $\Gamma \approx 2.72$ absorbed by two warm absorber components (green, dotted-dashed lines) as well as one cold absorber ($N_\mathrm{H} \approx 0.08 \cdot 10^{22}\,\mathrm{cm}^{-2}$, turquoise, dotted-dashed line). The initial power-law of the high-state spectrum additionally has a higher normalization than the low-state

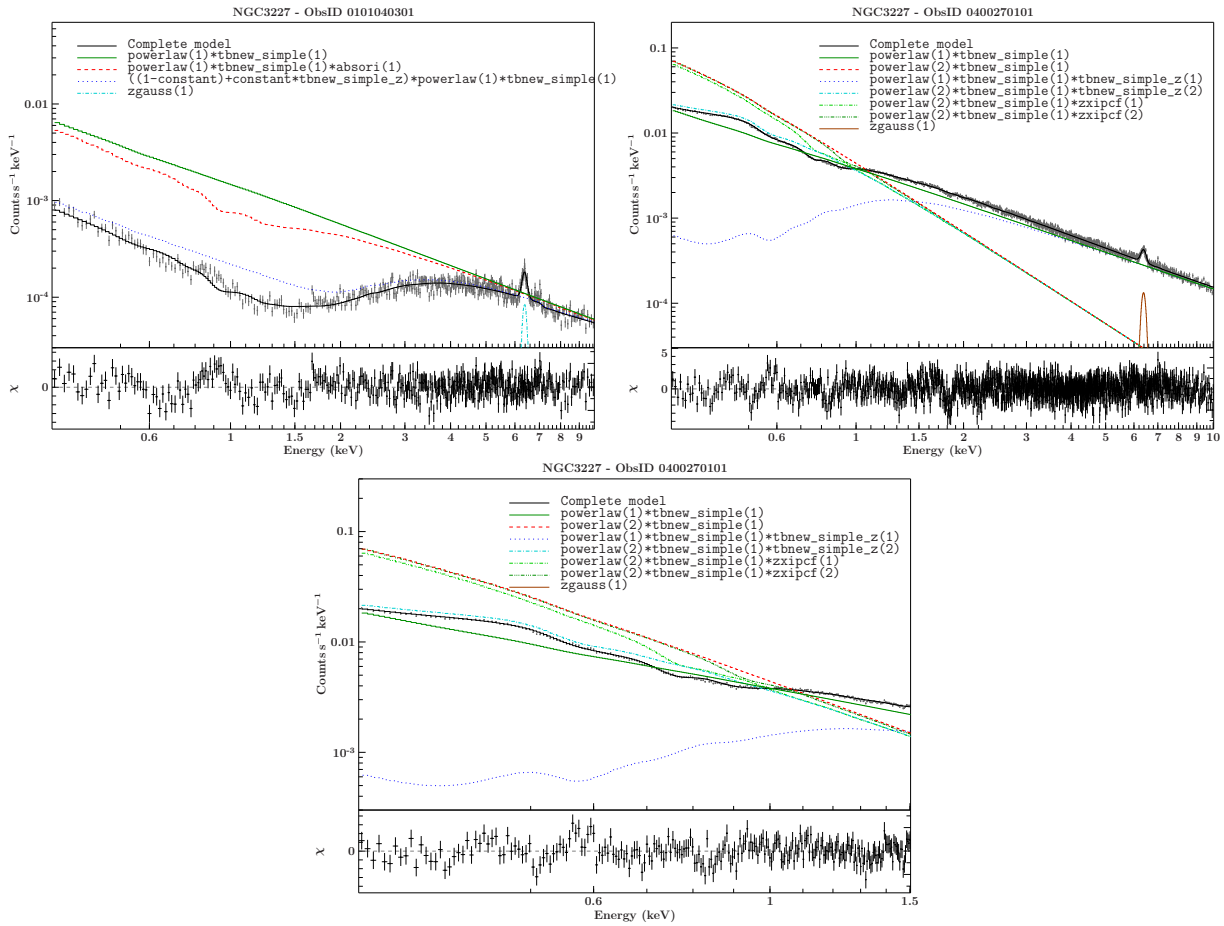

Figure 3.23.: Best-fit model components of the NGC 3277 – *XMM*-spectra (EPIC-pn) from 2000-11-28 and 2006-12-03 in full-range $0.3 - 10$ keV (*top*) and the soft-range $0.5 - 1.5$ keV (*bottom*) of the 2006 observation for better visualization.

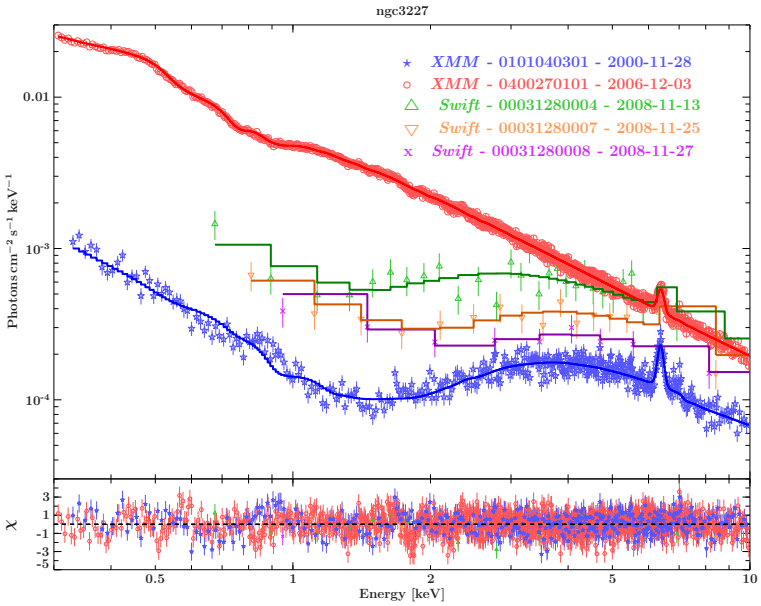

Figure 3.24.: Plot of all five analyzed data-sets recorded with *Swift* (XRT) and *XMM* (EPIC-pn) for NGC 3227.

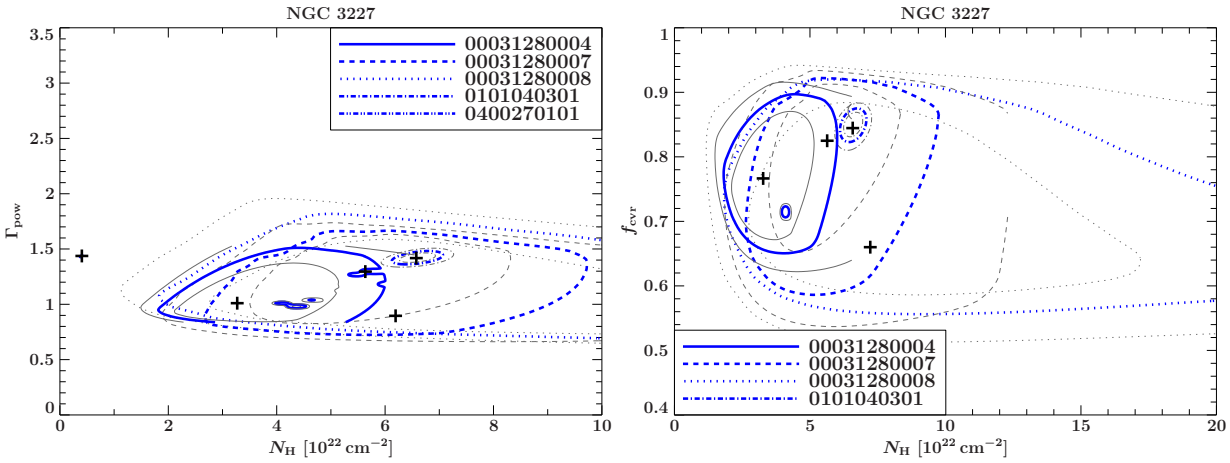

Figure 3.25.: Plot of all interpolated contours for NGC 3227. The blue, thick lines in the middle represent the 90 % contours, the thin, gray lines the 68 % and 99, % contours. *left:* contour maps for N_H and Γ, *right:* for N_H and c.

one. This implies also an increase in the irradiation on structures surrounding the nucleus for the high-state. Higher irradiation again suggests highly ionized gas, which is indeed confirmable with a second warm absorber component of larger ionization ($\xi \approx 3$) accompanied with a lower ionized one ($\xi \approx 1.5 - 1.8$) as occurring in both the low- and high-state observations. For alternative modeling of the soft excess with a black-body or Comptonization as also suggested in the introduction of this thesis and applied to previous data sets, see Markowitz et al. (2009).
Of all seven ***Swift*** observations, all performed in the end of 2008, three can be used for continuum model fitting. The others rule out while being analyzed due to severe problems in constraining the cold N_H. Such as for nearly all *Swift* observations, also here a simple neutral partial covering model

```
(((1-constant)+constant*tbnew_simple_z)*powerlaw+zgauss)*tbnew_simple
```

is applied to the data of the remaining three observations with the obsids 00031280004, 00031280007 and 00031280008. The power-law indices vary around the value derived with *XMM*-Newton ($\Gamma \approx 1.4$) between $\Gamma \approx 1.2$ and 1.8 with appropriate neutral column densities of $N_H \approx 3.3 - 7.6 \cdot 10^{22}$ cm^{-2}. Those are again comparable to the column found for the low-state *XMM*-Newton observation in 2000 ($N_H \approx 6.5 \cdot 10^{22}$ cm^{-2}). Note that if the S/N ratio would be better also in the soft, most likely additional warm absorbers could be constrained. This would in turn lead to a lower column of neutral gas as it is measured with the *Swift* data implying only cold absorption.

3.4.4.3. N_H-VARIABILITY STUDY

It has been shown that variability indeed is present in the spectra. Again, I am interested in a proper statistical constraint of the N_H values and differences between those. The contour plots in Fig. 3.25 are quite interesting. On the one hand they show that many contours cross and thus are consistent with each other. On the other hand the contour sizes differ strongly. *XMM*-Newton contours are in general much smaller than *Swift* ones, simply because parameters can generally be constrained better with *XMM*'s higher effective area. So, absorption variability is expected mainly between both *XMM* spectra and occasionally also between *Swift* and *XMM*. Figure 3.26 supports this first impression. Indeed variability can be statistically constrained for some combinations of spectra. The minimum variability time-scale is 710 days ($\approx$ 2 years). The evolution of measured N_H with time in the right panel shows statistically significant the drop in cold absorption from

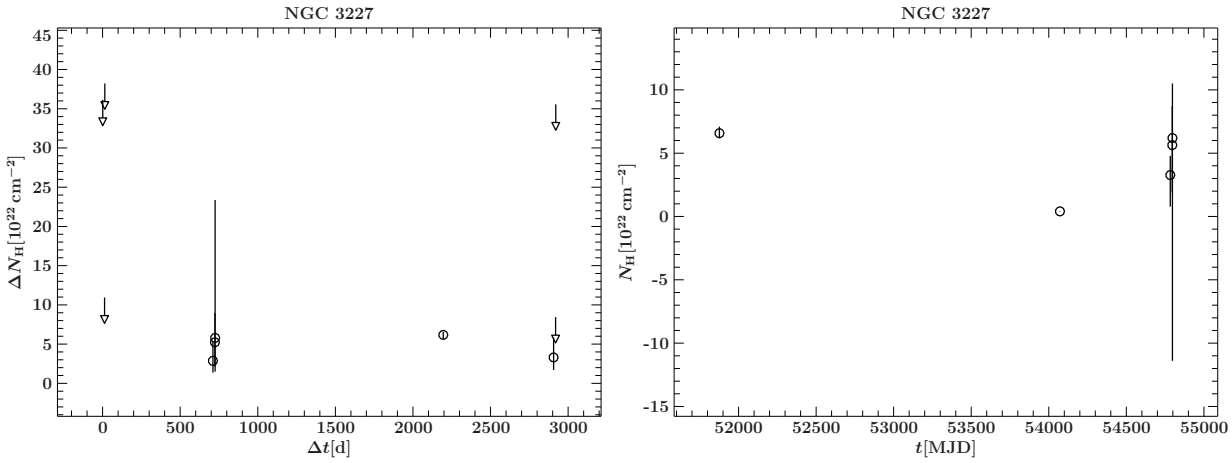

Figure 3.26.: *Left:* $\Delta N_{\rm H}$ over Δt for all possible combinations of observations of NGC 3227, *right:* absolute values of $N_{\rm H}$ with errors plotted over time.

2000 to 2006. The point cloud at the end are the *Swift* observations from 2008 where – due to the large errors and the low S/N ratio – no column density variations can be constrained.

3.4.5. ESO 323-G077

3.4.5.1. Introduction and Observations

ESO 323-G077 is a well absorbed Sy 1.2 galaxy (Véron-Cetty & Véron, 2006) with redshift $z = 0.015$. It was observed once by *XMM*-Newton in 2006 February 7 and three times by *Swift* in 2006 June and August. Only two of three pointings can be further analyzed due to too low data S/N of the first *Swift* observation in 2006 June 28.
Although being hidden behind multiple absorbing layers, no variability can be detected with the here analyzed spectra. However, there is more data available in the archives such as one pointing by *Suzaku* in 2011 July and four more by *Chandra* in 2010 April. As already noted for NGC 4593 and NGC 3227, those observations still have to be analyzed. Model fits to the data reveal a X-ray luminosity of $L_{\rm X} = 4.31 \cdot 10^{42}\,{\rm erg/s}$ in the $0.3 - 10\,{\rm keV}$ range.

3.4.5.2. Spectral Fits

The single ***XMM*-Newton** observation from 2006 (obsid: 0300240501) was in detail examined by Jiménez-Bailón et al. (2008) regarding the blue-shifted emission most likely from a warm absorber. The best-fit model proposed by Jiménez-Bailón et al. (2008) consists of two power laws. To keep consistency with my other models, I successfully constrain a partial covering model further obscured by warm absorber components:

```
(((1-constant)+constant*tbnew_simple_z)*zxipcf(1)*zxipcf(2)*powerlaw+
zgauss(1)+zgauss(2)+zgauss(3))*tbnew_simple
```

The derived warm absorber parameters are, however, consistent with their two-power-law model. The warm absorber component is not further discussed here. See Jiménez-Bailón et al. (2008) for more information. Figure 3.27 again shows the different model components fitted to the data. The partial coverer is appearing clearly with its high covering factor of nearly one displayed as dotted blue line (attenuated power-law) and red dashed line (absorbed power-law). The ***Swift*** spectra

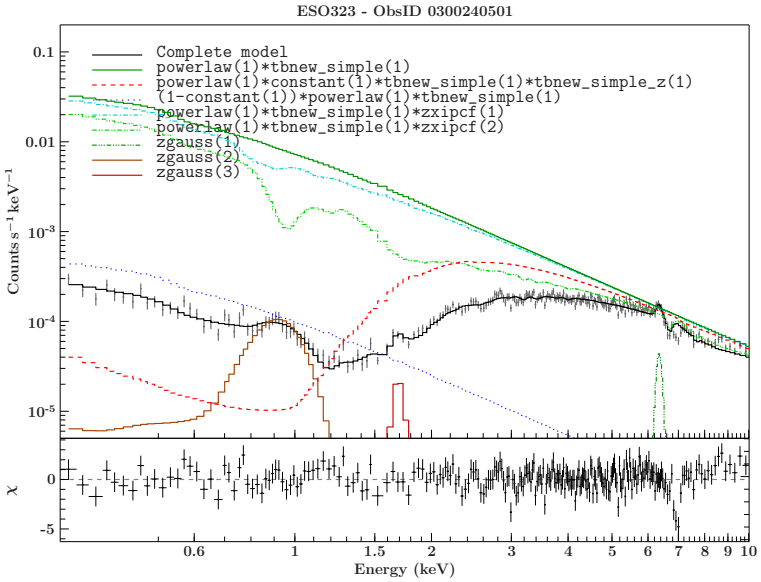

Figure 3.27.: Best-fit model components of the ESO 323-G077 – *XMM*-spectrum (EPIC-pn) from 2006-02-07 in full-range 0.3 – 10 keV.

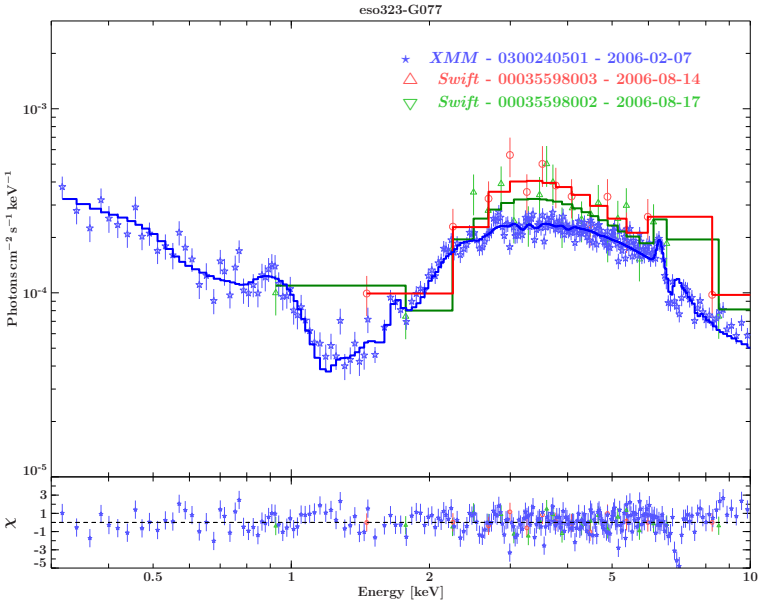

Figure 3.28.: Plot of all three analyzed data-sets recorded with *Swift* (XRT) and *XMM* (EPIC-pn) for ESO 323-G077.

are, however, fitted with a double power-law

```
((powerlaw(1)*tbnew_simple_z+zgauss) + powerlaw(2))*tbnew_simple
```

at this moment. To be consistent with the partial covering model found for the *XMM*-Newton observation, the same model should be also applied for the *Swift* data, most likely without being able to constrain a warm absorber. This will be done in the future work. As Fig. 3.28 shows, this would not change the missing variability in absorption.

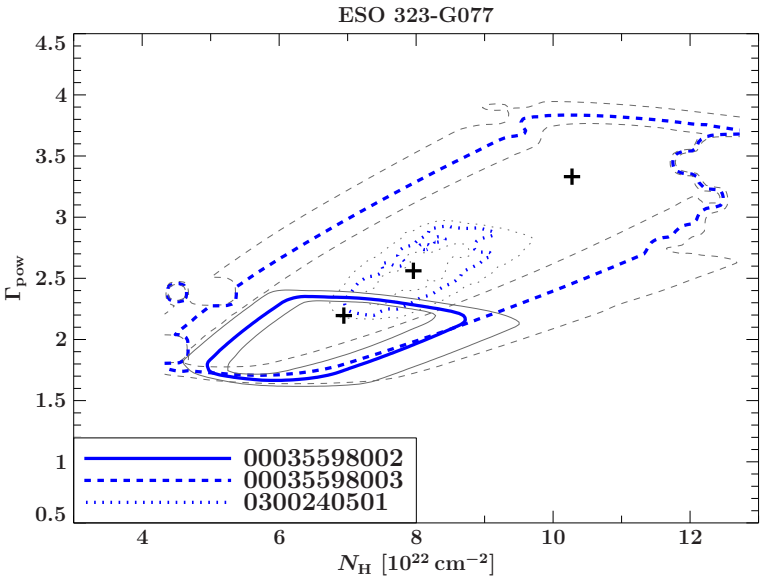

Figure 3.29.: Plot of all interpolated contours for ESO 323-G077. The blue, thick lines in the middle represent the 90 % contours, the thin, gray lines the 68 % and 99 % contours. Plotted are contour maps for N_H and Γ only as the *Swift* model fits do not include a partial coverer.

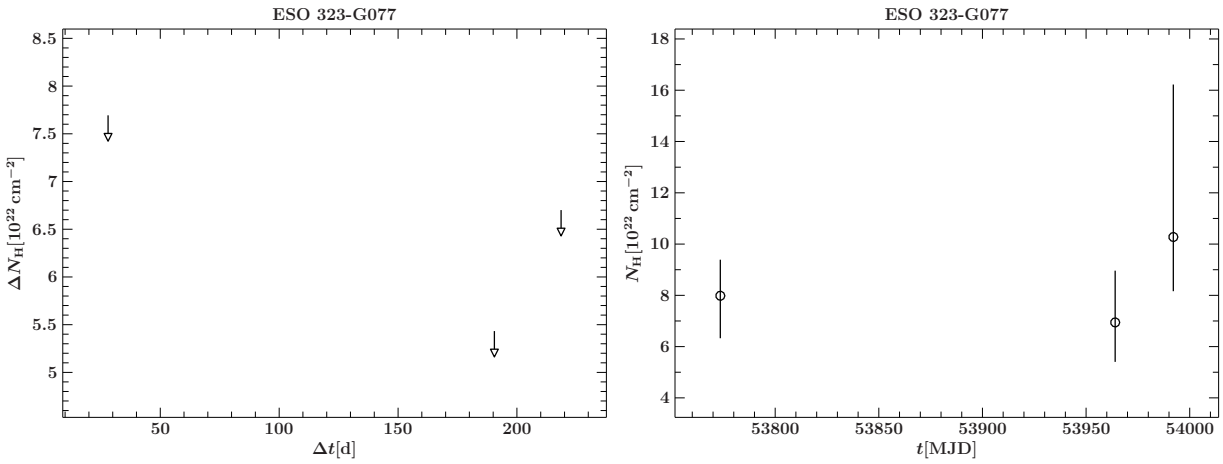

Figure 3.30.: *Left:* ΔN_H over Δt for all possible combinations of observations of ESO 323-G077, *right:* absolute values of N_H with errors plotted over time.

3.4.5.3. N_H-VARIABILITY STUDY

The study on N_H-variability stays simple in this case. Already from the spectra, no variation is seen. This is further backed by the contours in Fig. 3.29. Due to the yet missing partial coverer model for the *Swift* spectra, only this kind of contour-map can be calculated. Also the plots of N_H against time differences as well as N_H against time in Fig. 3.30 do support the result of no variability.

3.4.6. MRK 704

3.4.6.1. Introduction and Observations

Mrk 704 is again a very local Sy 1.2 galaxy classified by (Véron-Cetty & Véron, 2006) with a redshift of $z = 0.029$. It was treated in detail by Matt et al. (2011) for its extreme warm absorber variability between the two subsequent *XMM* observations in 2005 October 21 and 2008 November 2. Furthermore Mrk 704 was observed by *Swift* five times between 2006 and 2011 where only three observations with the largest exposure time and thus data S/N can further be analyzed here. These are observations in 2006 June 14 and September 28 as well as 2007 January 21. The high- and low-state spectra are represented by the *XMM* observations with according X-ray luminosities of $L_{\mathrm{X}} = 1.95 \cdot 10^{43}\,\mathrm{erg/s}$ and $L_{\mathrm{X}} = 3.62 \cdot 10^{43}\,\mathrm{erg/s}$ in the $0.3 - 10\,\mathrm{keV}$ band.

3.4.6.2. Spectral Fits

As the introduction implies, both ***XMM*-Newton** observations from 2005 (obsid: 0300240101) and 2008 (obsid: 0502091601) are well fitted by a warm absorber model of two components each. The observation 0300240101 is additionally absorbed by neutral matter in form of a partial coverer of an intermediate column density ($N_{\mathrm{H}} \approx 6 \cdot 10^{22}\,\mathrm{cm}^{-2}$) and a covering fraction of $c = 0.64$. The complete best-fit model I find turns out to be

```
(zxipcf(1)*zxipcf(2)*zpcfabs*powerlaw+zgauss(1)+zgauss(2))*tbnew_simple
```

The following spectrum taken three years later (obsid: 0502091601) can be fitted only with two warm absorber components plus an additional Comptonized power-law fully without cold, neutral obscuring matter:

```
((powerlaw+comptt)*zxipcf(1)*zxipcf(2)+zgauss)*tbnew_simple
```

The Comptonization component accounts for the clear soft excess present if only a single power-law would be fitted to the hard $2-10\,\mathrm{keV}$ part of the spectrum. Figure 3.31 (left/right panel) shows the model components of both spectra. Remarkable is again that both ionization parameters that are fitted as free parameters stay the same for both spectra (Fig. 3.32) whilst the appropriate column densities vary strongly. This is, as for Fairall 51, nicely explained by the unchanged irradiating luminosity given by the initial power-law staying about at the same normalization and photon index for both observations. The cold partial coverer is also nicely visible in Fig. 3.31 (left panel) as turquoise dotted-dashed line. The analyzed ***Swift*** observations are again fitted with the model of a partial coverer of cold/neutral matter. This is legitimate as Fig. 3.32 shows. The *Swift* observations are situated in time as well as flux between the high- and low-state *XMM*-Newton observations. As Fig. 3.34 (right panel) shows, the N_{H} values of neutral matter decrease from the low-state in 2005 on. The subsequent spectra plotted in Fig. 3.32 show indeed a trend in cold N_{H}. By eye, all *Swift* spectra have the typical "S-shape" of a partial coverer. The only spectrum where this might be uncertain is the one from 2006 June 14 (obsid: 0003559002). A Monte Carlo test as also performed for NGC 4593, however, returns p-values larger than 90 % favoring a partial-covering over a full-covering shield. Still it can not be neglected that there might be some contribution of a warm absorber in that questionable *Swift* observation which simply can not be constrained due to low S/N.

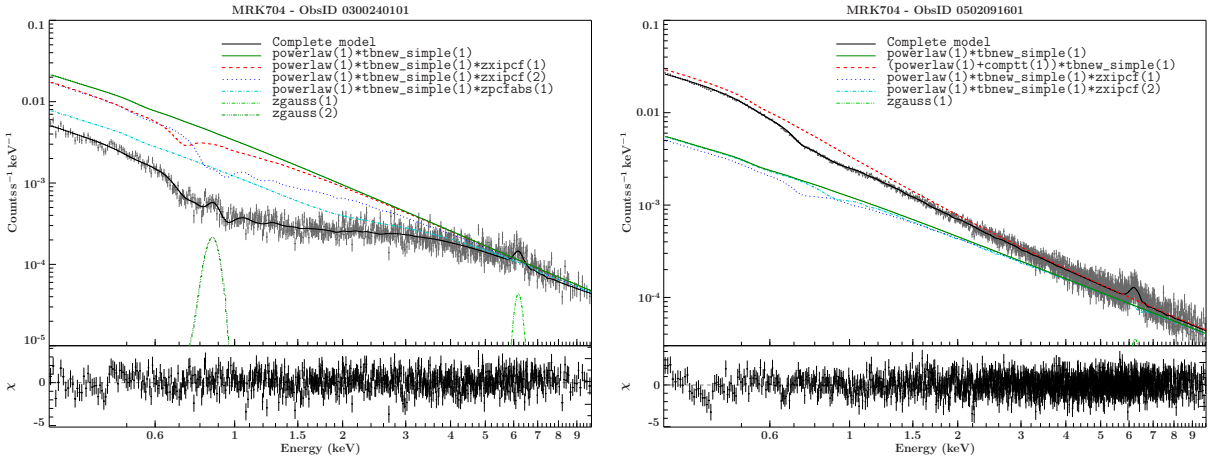

Figure 3.31.: Best-fit model components of the Mrk 704 – *XMM*-spectra (EPIC-pn) from 2005-10-21 and 2008-11-02 in full-range 0.3 – 10 keV.

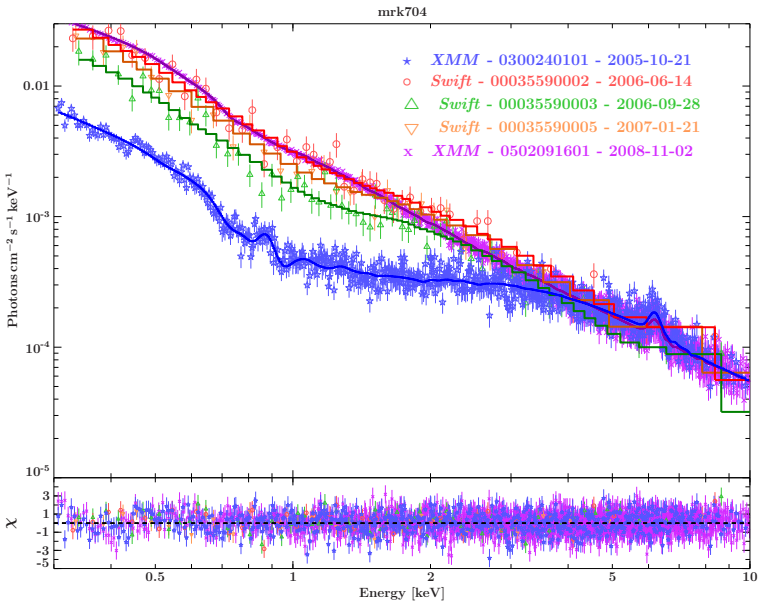

Figure 3.32.: Plot of all five analyzed data-sets recorded with *Swift* (XRT) and *XMM* (EPIC-pn) for Mrk 704.

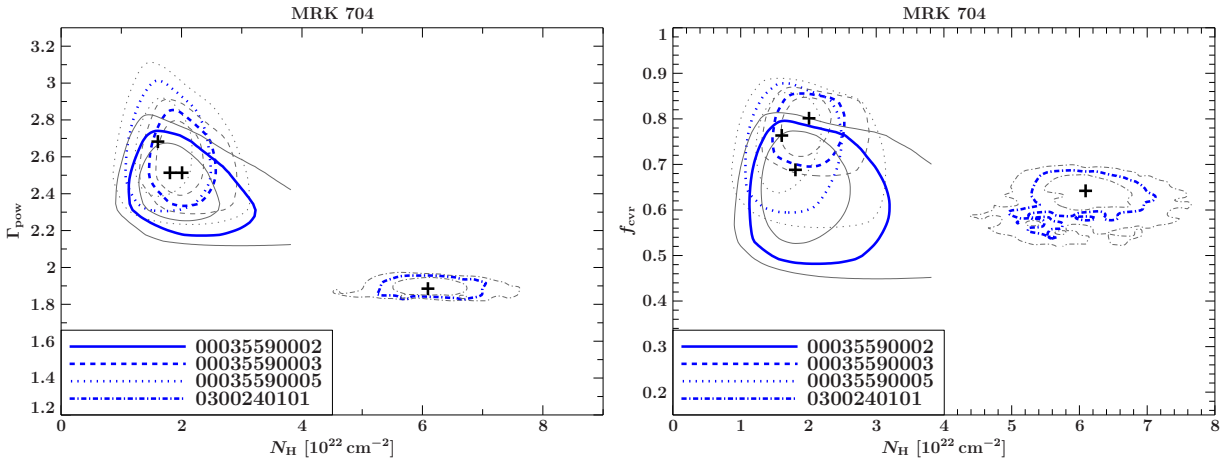

Figure 3.33.: Plot of all interpolated contours for Mrk 704. The blue, thick lines in the middle represent the 90 % contours, the thin, gray lines the 68 % and 99 % contours. *Left:* contour maps for N_H and Γ, *right:* for N_H and c.

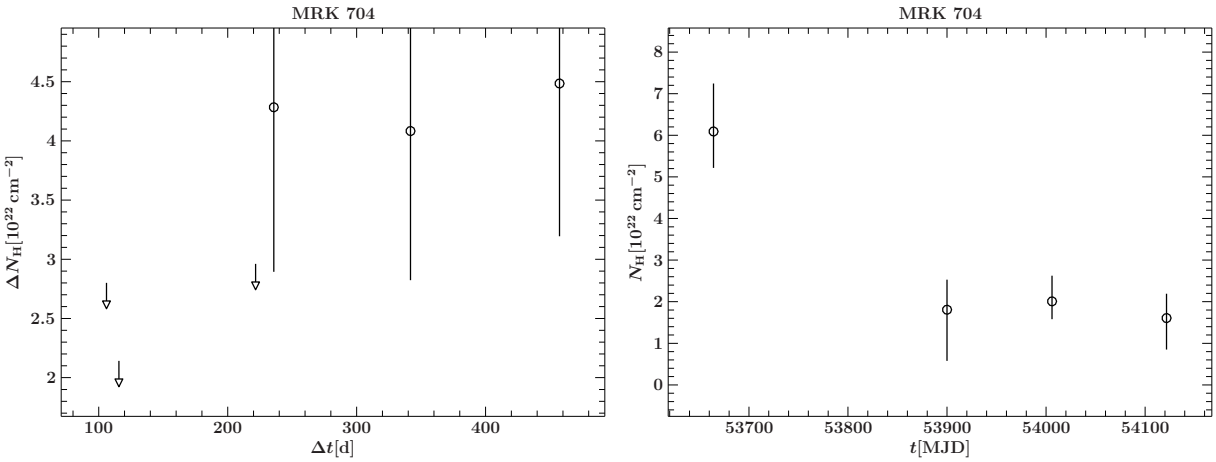

Figure 3.34.: *Left:* ΔN_H over Δt for all possible combinations of observations of Mrk 704, *right:* absolute values of N_H with errors plotted over time.

3.4.6.3. N_H-VARIABILITY STUDY

As implied by my results being consistent with those of Matt et al. (2011), strong variability is present in the archival continuum observations not only in the warm absorber column densities, but also in cold absorption. I concluded in the previous section that the high-state *XMM*-Newton spectrum does not include constrainable cold absorption compared to all other observations of this source. In contrast to Fairall 51, where for all observations no cold obscuration could be determined at all, I can not compare the column density of the lowest ionized warm absorber component of the high state with cold absorber columns of the other spectra because of consistency. Taking a value of zero-N_H would be the way to go, if I could state appropriate uncertainties. Therefore as the contours of all observations suggest in Fig. 3.33, variability can only be shown between the *XMM*-Newton low-state and the subsequent *Swift* pointings. Missing the existing variability between both *XMM*-Newton pointings on a time scale of three years does not imply a disadvantage as the aim is to find the shortest variability timescale, which could not be improved when including the high-state.
The shortest variability time scale is 235 days of around 2/3 years as read off the data for Fig.3.34 (left panel).

3.4.7. MRK 766

3.4.7.1. Introduction and Observations

Mrk 766 was studied in great detail by Miller et al. (2007) and Turner et al. (2007).
Risaliti (2010) and Risaliti et al. (2011) focus on the N_{H} variability They use *XMM*-Newton data taken in six consecutive orbits from 2005 May 23 to June 3. The nearly full time coverage allows one a much more detailed analysis regarding shortly following occultations than I can do it with only some snapshot spectra taken over large time intervals. In turn the named authors have also access to much shorter variability time-scales by construction of the experiment than I do.

3.4.7.2. N_{H}-variability study

Because of the huge amount of work that has already been done for the same purpose with probably the best time coverage on short scales ever reached for one campaign with *XMM*-Newton , I fully rely on the results of Risaliti et al. (2011) for my further analysis and also refer to the above mentioned references for further information on the data analysis.
The result extracted from Risaliti et al. (2011) is a minimum variability time scale of 10 to 20 hours coming along with a ΔN_{H} of $3 \cdot 10^{22}\,\mathrm{cm}^{-2}$.

3.4.8. MRK 1218

3.4.8.1. Introduction and Observations

Mrk 1218 is amongst the sources with least flux in the given sample. It was observed two times by *XMM*-Newton in 2005 April 9 and 2005 October 8. Only the first observation can be further used due to the low data S/N of the latter spectrum.
Also *Swift* pointed to this source at a total of seven times between 2005 and 2007. The same problem of low S/N allows only one of these observations in 2006 October 8 to be properly analyzed.
Both further treated observations are – similar to the case of ESO 323-G077 – not variable at a first glance (see Fig. 3.36). The X-ray luminosity calculated from derived models to the data yield a value of $L_{\mathrm{X}} = 5.33 \cdot 10^{42}\,\mathrm{erg/s}$ in the full $0.3 - 10\,\mathrm{keV}$ range.

3.4.8.2. Spectral Fits

Spectral fits to the ***XMM*-Newton** dataset return a quite simple model to be the best reachable fit for the given low S/N ratio. This is a power-law, partially covered by a neutral shield:

```
powerlaw(1)*zpcfabs(1)*tbnew_simple(1)
```

The same model also holds for the ***Swift*** dataset. The parametric results for N_{H} are consistent with each other inside the 90 % confidence levels of appropriate parameter contours (Fig. 3.37). The model components of the partial coverer for the *XMM*-Newton observation are revealed in Fig. 3.35. A similar shape can be expected for the *Swift* spectrum over-plotted with the *XMM* one in Fig. 3.36.

3.4.8.3. N_{H}-variability study

As already expected, no N_{H}-variability can be found for Mrk 1218 constraining to the two spectra. The *Swift* contours for the N_{H}-Γ parameter pair fully include the contours of the *XMM*-Newton

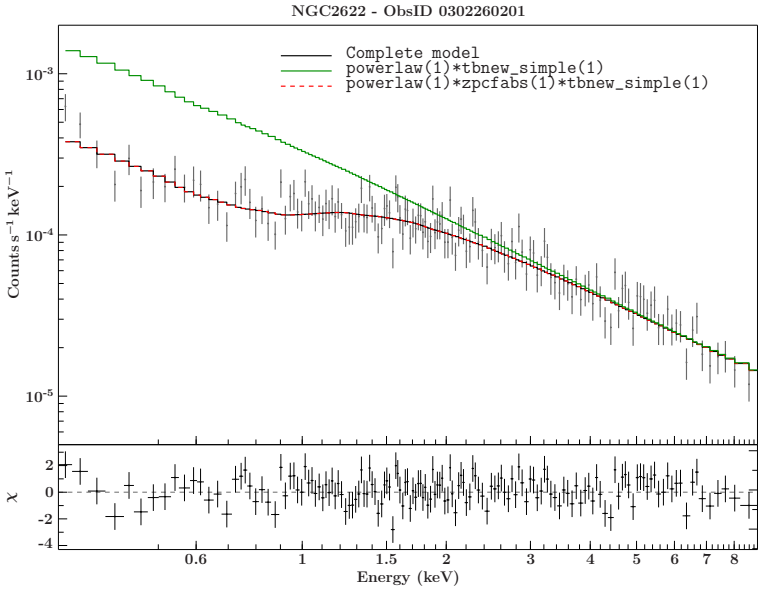

Figure 3.35.: Best-fit model components of the Mrk 1218 – *XMM*-spectrum (EPIC-pn) from 2005-04-09 in full-range 0.3 – 10 keV.

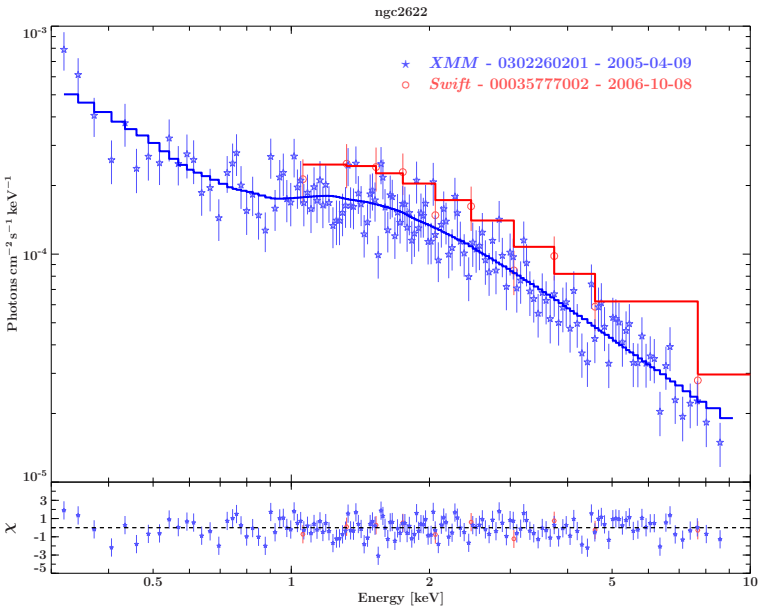

Figure 3.36.: Plot of all three analyzed data-sets recorded with *Swift* (XRT) and *XMM* (EPIC-pn) for MRK 1218.

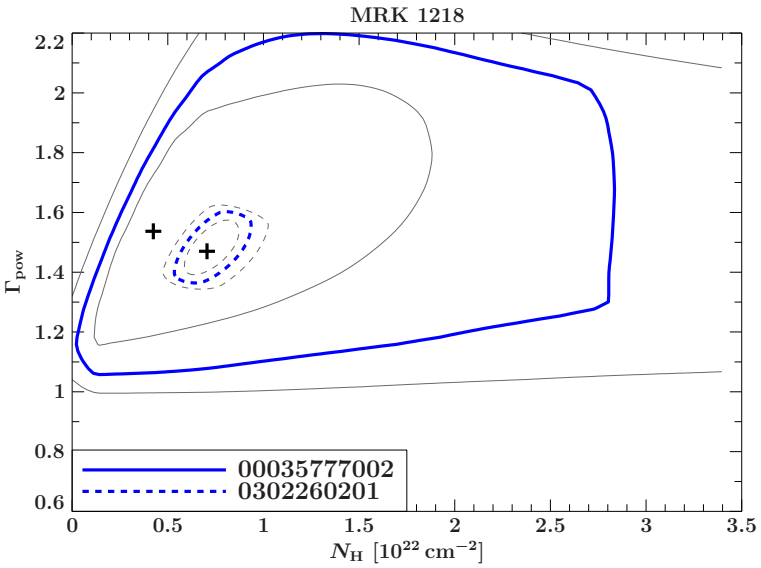

Figure 3.37.: Plot of all interpolated contours for Mrk 1218. The blue, thick lines in the middle represent the 90 % contours, the thin, gray lines the 68 % and 99 % contours. Shown are the contour maps for the parameter pair N_H/Γ.

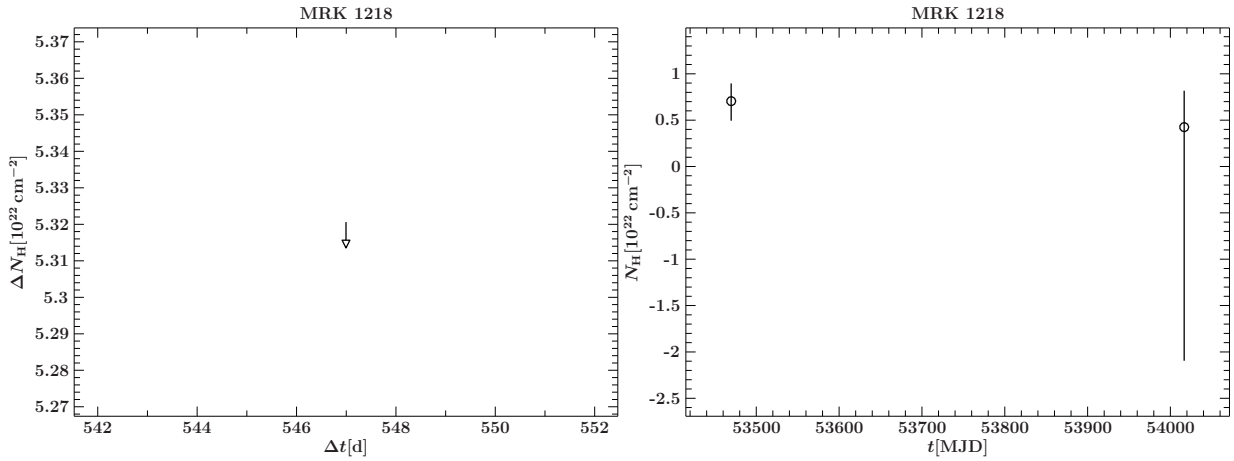

Figure 3.38.: *Left:* ΔN_H over Δt for all possible combinations of observations of Mrk 1218, *right:* absolute values of N_H with errors plotted over time.

observation. This implies such as Fig. 3.38 that no variability can be found based on the given data.

3.5. Discussions and Conclusions

The results until the date of submission of this thesis do provide evidence for N_H variability in over 40 % of the 12 sources in the sample given by Smith et al. (2004). Adding also data of *Suzaku* and *Chandra* that are yet missing in the analysis, the border of 50 % variable sources could be crossed. Furthermore also the control sample of sources that should lack of N_H variability, if the assumed geometrical assumptions of both the morphology of those yet unresolved AGN cores and the line of sight towards them are true, has to be examined in the same kind.
In a next step I combine all results in terms of the shortest variability timescales (Fig. 3.39). This is possible as the basic assumption is that all examined sources are just representatives of the same

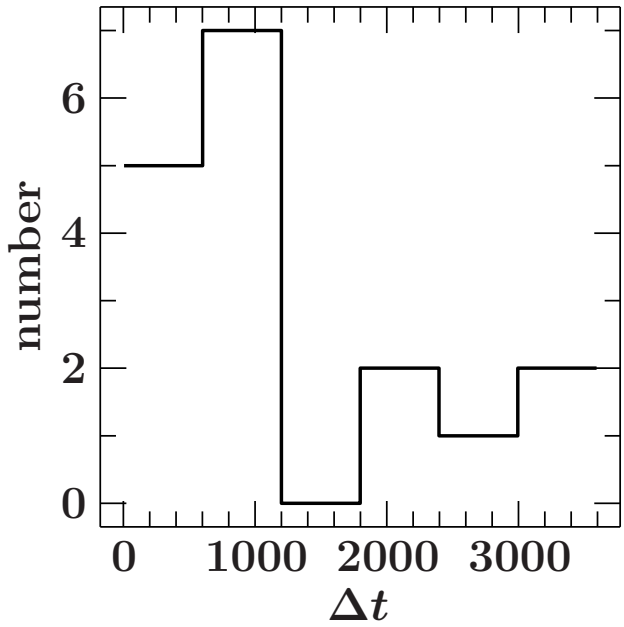

Figure 3.39.: Distribution of all measured variability timescales.

underlying kind of object. As it lies in the nature of the thing, the work with a sample comes along with a worse time coverage compared to the analysis of one source in detail. Therefore I add all the information on time-scales of all sources and use the smallest to derive an upper limit on the distance of the absorber from the central SMBH assuming that the minimal timescale found here is still too long.
Figure 3.39 shows a peak at lower timescales from zero to 1000 days. From the real data for the histogram I find for the shortest time-scale a value of $\Delta t \approx 5$ days. Inserting this time-scale into Eq. 1.45, I find an upper limit for the radial distance of the absorber from the central engine.

3.5.1. Constraints on the location of the absorbers

Based on some simple assumptions presented at the end of Sect. 1.4.2.2 the distance $R = Xr_S$ of the absorber can be determined for the smallest measured variability time-scale. The basic assumption is clouds orbiting the central black hole on Kepler trajectories and obscuring the line of sight in a fraction of the orbit-period. The straight forward ansatz is used for occultation events in Fairall 9 by Lohfink et al. (2012). The time a cloud of radius $r = xr_S$ needs to pass the line of sight with the velocity v is

$$\Delta t \sim 2r/v = 2xX^{1/2}r_S/c. \tag{3.25}$$

Assuming a typical black hole mass of $10^9\,M_\odot$ (Richstone et al., 1998) yielding a Schwarzschild radius of $r_S = 1.48 \cdot 10^{14}$ cm thus yields $\Delta t \approx 9860xX^{1/2}$ s. From my results I find a minimum variability time scale of $\Delta t \approx 5$ days which results in the relation $xX^{1/2} \approx 43.8$. For a cloud to be able to fully cover the compact, with the central X-ray source having a size of about $10r_S$, the spherical cloud must have a minimum diameter of $r \gtrsim 10r_S \approx 1.5 \cdot 10^{14}$ cm or $x \gtrsim 10$ using that the distance of the cloud to the observer is much larger than to the X-ray source. This in turn leads to the necessity of $X \lesssim 19.2$ ($R \lesssim 2.84 \cdot 10^{15}$ cm).
For consistency, I test this result with the formula suggested by Risaliti et al. (2002) (Eq. 1.45). The assumed black hole mass is again $10^9\,M_\odot$ and the smallest variability time scale found $\Delta t \approx 5$ days. The size of the obscuring cloud is also assumed to be $r \gtrsim 10r_S$. For a spherical, uniform cloud its density can be calculated out of the average measured column density of $N_H \approx 5 \cdot 10^{22}\,\mathrm{cm}^{-2}$ and

the expected minimal size of the cloud of $r \gtrsim 1.5 \cdot 10^{14}$ cm to be $\rho \lesssim 3.4 \cdot 10^{7}\,\mathrm{cm}^{-3}$. Eq. 1.45 then yields $R \lesssim 2.6 \cdot 10^{15}$ cm which is consistent with the first result of $R \lesssim 2.84 \cdot 10^{15}$ cm.
We can compare this result with the distance of the Broad Line Region (BLR) being expected much closer to the X-ray source than the surrounding torus. Reverberation mapping yields a distance of the BLR of around 0.1 pc $\approx 3 \cdot 10^{17}$ cm (Peterson, 1993) which is still of about two orders larger than the distance estimated for the smallest variability time-scale in my sample. The reason for that is most likely the nature of the absorber that yields the minimal time scale of 5 days. The source where this is found is Fairall 51, not revealing evidence for cold absorption. The obscuration of all spectra is instead modeled consistently with a warm absorber component of small ionization. But still – those warm absorbing clouds are expected to exist in form of diffuse gas much closer to the X-ray source than the BLR or the torus farther outside. This can explain the resulting relatively low upper limit on the radial distance of the absorber from the black hole of $\approx 10^{15}$ cm. In fact Reynolds & Fabian (1995) conclude that the warm absorber – most likely evaporated gas from, e.g., the outer torus layers driven outwards by radiation pressure (Ashton, 2005) – lies between 10^{15} and 10^{18} cm according to my result.
Even though the absorber responsible for the shortest variability time scales of 5 and 180 days measured for Fairall 51 can rather be located in the warm absorbing gas or the NLR than in the torus layer, the other measured timescales of several hundreds of days can indeed be connected with cold absorbers at distances where the torus is expected.
The second smallest measured time scale according to clear influence of cold absorption is $\Delta t =$ 136 days (Mrk 704). Performing the same calculations as above, the upper limit on the radial distance of the *cold absorber* from the black hole turns out to be $R \lesssim 6.3 \cdot 10^{18}$ cm which is around 2 pc and thus more in agreement with the BLR or even the torus.

3.6. Conclusions and Outlook

Direct spatially resolved measurements of processes taking place in AGN are not possible by now. Even techniques like Very Large Baseline Interferometry in the radio regime going down to some milliarcsecond resolution have no access to the hearts of AGN due to the limiting Synchrotron self absorption. So, all other techniques trying to reveal the detailed geometry of such accreting kernels of active galaxies use indirect methods such as spectroscopy, reverberation mapping and so on. The probably most promising methods of all, accounts for the omnipresent signature of such AGN, namely the variable behavior as it is the natural property of an accreting, dynamical system. Those methods include all kind of study of that variability. Variable obscuration, e.g., is the subject of this work making it possible to learn more about the physical processes and the geometry of those AGN systems. My work clearly shows the variability in absorption of hitherto 5 of 12 polar scattered sources where the measured column densities do confirm the proposal stated by Smith et al. (2004) regarding the geometrically orientation of those sources towards our line of sight while relying on the truth of the Unified Model. On the other hand it is even possible to substantiate the Unified Model by the observational insight gathered in my work.
This work, however, can be driven further by analyzing available data of other satellites (*Suzaku* and *Chandra*) for some sources of my sample. With those data it will at a first glance be possible to find at least 6 sources out of 12 to reveal variable absorption. In addition proposals will be written for the rest of the sources where yet not enough data are available to state variations of whatsoever kind. Furthermore the control sample of equatorial scattered sources, supposed not to be variable, has to be analyzed in the same way to double-check the results gained in this thesis.

Chapter 4

General Conclusions

> *By three methods we may learn wisdom: first, by reflection, which is noblest; second, by imitation, which is easiest; and third by experience, which is the bitterest.*
>
> Confucius, *551–479 BC*

This thesis shall show the importance of polarization for both radio-quiet as well as radio-loud AGN.
In the first part of my thesis I reveal that single dish radio polarimetry offers access to many questions of modern research in **radio-loud AGN**. Although the presented monitoring program F-GAMMA constraints to compact AGN or so called blazars / BL Lacs, I can conclude that even extended radio galaxies such as 3C 111 are able to be studied within such a campaign. The clear advantages are access to multi-wavelength polarimetric information over a long term. Even though the interferometric campaign MOJAVE offers also monthly monitorings, it is more expensive and lacks the potential of studying sources at such a high amount of frequencies as single dish instruments as Effelsberg are in principle able to. This study is constrained to the polarimeters of largest reliability at the two frequencies of 5 GHz and 10 GHz only, however, this work shall serve as one more cornerstone in terms of experience to proceed with other receivers that already are equipped with polarimeters but suffer from problems that now are able to be understood better. Besides technical issues, the science behind single-dish polarimetry offers many new insights regarding questions of long term variability of integrated properties of AGN, structural appearance especially of the underlying magnetic field on large scales, shock formation, evolution and many more.
On the other hand, (optical) polarimetry can also be used indirectly for **radio-quiet AGN** as a tracer for certain kind of objects assuming a geometrical model – the Unified Model of AGN. As the region of interest – the AGN core – is still unresolved, many assumptions on the geometry have to be made based on observational insights on a multi-wavelength basis. The model being broadly accepted is the Unified Model suggesting the accreting system around the black hole to appear in a toroidal shape. The line of sight towards this system is defined by observational characteristics such as assumed variability when watching those sources under a partially obscured line of sight through layers of absorbing gas orbiting the black hole. This assumption on the line of sight is implied by certain properties of optical polarized light. Assuming that this assumption is true, I examine the variability of X-rays propagating on the same (obscured?) line of sight to show that at least 5 of 12 sources in the sample show X-ray variability. Taking into account data of other instruments the border of 6 variable sources (50 %) should be breakable. By the submission of this thesis no reliable conclusion can be made whether the given sample is indeed variable with over half of the sources. I also have to check a sample of sources that is not supposed to be variable

under the given assumption of geometry and in particular the line of sight determined via optical polarization.
Finally I can conclude the vast importance of polarization for the study of AGN in general. Polarization has a character of breaking the geometrical symmetry in every respect. Radio-loud AGN with radio jets being aligned or misaligned with our line of sight appear to be rotational symmetric cone-like structures. Polarimetry of shocked regions gives additional information on the underlying magnetic field as well as structural variability being completely hidden if only studying total power with a single-dish telescope integrating over large fractions of sources that can be spatially resolved with interferometers.
Furthermore the appearing structural symmetry of an AGN that can not be resolved with modern telescopes is also broken by polarization. Optical polarized light reveals a line of sight dependence towards the source if one can assume the same underlying object tried to be described by the Unified Model to be present in all compact, active extragalactic sources such as the content of my sample. However, the statement of morphological models such as the Unified Model of those objects is only possible when being able to find observational differences in line of sights which can in turn be implied by (optical) polarized radiation from the core being scattered towards the observer in different parts of the system revealing differently polarized light. Finding evidence for different line of sights towards the same kind of object implies to use other wavelength, such as X-rays, to further study the morphology. In turn the symmetry breaking character of optical polarization in this radio-quiet case combined with the further test of this asymmetry with X-rays yields an unique opportunity to independently test the Unified Model for its consistency.

Appendix A

Best-Fit Parameters

Table A.1.: Best-fit parameters of all analyzed *Swift*-observations

model component	**Parameter**	**freeze**	**value ± uncertainty**
Fairall 51			
00037809001 - $\chi^2 = 27.59$ - $n_{\mathrm{free}} = 25$			
Warm absorbing zone 1	$N_{\mathrm{H}}\,(\mathrm{cm}^{-2})$	0	$6.3\,^{+0.24}_{-1.60} \times 10^{22}$
	$\log\xi\,(\mathrm{erg\ cm\ s}^{-1})$	1	$0.71\,^{+1.29}_{-0.71}$
	$\mathrm{f_{cvr}}$	1	$1\,^{+0.00}_{-1.00}$
	z	1	$0.014\,^{+9.99}_{-1.01}$
Powerlaw 1	Norm	0	$0.0098\,^{+0.00}_{-0.00}$
	Γ	0	$2.2\,^{+0.06}_{-0.37}$
Galactic absorption	$N_{\mathrm{H}}\,(\mathrm{cm}^{-2})$	1	$0.07\,^{+99.93}_{-10.07} \times 10^{22}$
00037809002 - $\chi^2 = 48.19$ - $n_{\mathrm{free}} = 25$			
Warm absorbing zone 1	$N_{\mathrm{H}}\,(\mathrm{cm}^{-2})$	0	$2.5\,^{+0.27}_{-0.23} \times 10^{22}$
	$\log\xi\,(\mathrm{erg\ cm\ s}^{-1})$	1	$0.71\,^{+1.29}_{-0.71}$
	$\mathrm{f_{cvr}}$	1	$1\,^{+0.00}_{-1.00}$
	z	1	$0.014\,^{+9.99}_{-1.01}$
Powerlaw 1	Norm	0	$0.0036\,^{+0.00}_{-0.00}$
	Γ	0	$1.5\,^{+0.15}_{-0.11}$
Galactic absorption	$N_{\mathrm{H}}\,(\mathrm{cm}^{-2})$	1	$0.07\,^{+99.93}_{-10.07} \times 10^{22}$
NGC 4593			
00037587001 - $\chi^2 = 190.11$ - $n_{\mathrm{free}} = 141$			
Covering Factor	$\mathrm{f_{cvr}}$	0	$0.53\,^{+0.11}_{-0.14}$
Internal cold absorption	z	0	$1.5\,^{+0.63}_{-0.39} \times 10^{22}$
	z	1	$0.009\,^{+9.99}_{-0.01}$ redshift
Powerlaw 1	Norm	0	$0.0082\,^{+0.00}_{-0.00}$
	Γ	0	$2\,^{+0.14}_{-0.15}$
Gauss 1	Norm	0	$8.4\text{e-}05\,^{+0.00}_{-0.00}$
	Energy (keV)	0	$6.2\,^{+0.12}_{-0.00}$ keV
	σ (keV)	1	$0.05\,^{+9.95}_{-0.05}$ keV
	z	1	$0.009\,^{+9.99}_{-1.01}$
Galactic absorption	$N_{\mathrm{H}}\,(\mathrm{cm}^{-2})$	1	$0.019\,^{+99.98}_{-10.02} \times 10^{22}$

Table A.2.: Best-fit parameters of all analyzed *Swift*-observations

model component	**Parameter**	**freeze**	**value ± uncertainty**
00037587002 - χ^2 = 54.61 - $n_{\rm free}$ = 40			
Covering Factor	f_{cvr}	0	$0.51^{+0.19}_{-0.35}$
Internal cold absorption	z	0	$1.2^{+0.82}_{-0.53} \times 10^{22}$
	z	1	$0.009^{+9.99}_{-0.01}$ redshift
Powerlaw 1	Norm	0	$0.0069^{+0.00}_{-0.00}$
	Γ	0	$2^{+0.27}_{-0.28}$
Gauss 1	Norm	0	5e-05 $^{+0.00}_{-0.00}$
	Energy (keV)	0	$6.5^{+0.12}_{-0.28}$ keV
	σ (keV)	1	$0.05^{+9.95}_{-0.05}$ keV
	z	1	$0.009^{+9.99}_{-1.01}$
Galactic absorption	$N_{\rm H}$ (cm^{-2})	1	$0.019^{+99.98}_{-10.02} \times 10^{22}$
00091407003 - χ^2 = 22.29 - $n_{\rm free}$ = 29			
Covering Factor	f_{cvr}	0	$0.67^{+0.13}_{-0.22}$
Internal cold absorption	z	0	$2^{+0.98}_{-0.63} \times 10^{22}$
	z	1	$0.009^{+9.99}_{-0.01}$ redshift
Powerlaw 1	Norm	0	$0.013^{+0.01}_{-0.00}$
	Γ	0	$2.2^{+0.27}_{-0.28}$
Gauss 1	Norm	0	$0.00039^{+0.00}_{-0.00}$
	Energy (keV)	0	$6.2^{+0.25}_{-0.13}$ keV
	σ (keV)	1	$0.05^{+9.95}_{-0.05}$ keV
	z	1	$0.009^{+9.99}_{-1.01}$
Galactic absorption	$N_{\rm H}$ (cm^{-2})	1	$0.019^{+99.98}_{-10.02} \times 10^{22}$
UGC 7064			
00037137001 - χ^2 = 3.98 - $n_{\rm free}$ = 3			
Covering Factor	f_{cvr}	0	$0.98^{+0.02}_{-0.09}$
Internal cold absorption	z	0	$14^{+6.32}_{-5.45} \times 10^{22}$
	z	1	$0.025^{+9.98}_{-0.02}$ redshift
Powerlaw 1	Norm	0	$0.0033^{+0.01}_{-0.00}$
	Γ	0	$2.4^{+0.81}_{-1.17}$
Gauss 1	Norm	0	4.3e-05 $^{+0.00}_{-0.00}$
	Energy (keV)	0	$6.4^{+0.12}_{-0.17}$ keV
	σ (keV)	1	$0.05^{+9.95}_{-0.05}$ keV
	z	1	$0.025^{+9.98}_{-1.02}$
Galactic absorption	$N_{\rm H}$ (cm^{-2})	1	$0.013^{+99.99}_{-10.01} \times 10^{22}$
NGC 3227			
00031280004 - χ^2 = 29.38 - $n_{\rm free}$ = 24			
Covering Factor	f_{cvr}	0	$0.82^{+0.08}_{-0.13}$
Internal cold absorption	z	0	$3.3^{+1.32}_{-0.94} \times 10^{22}$
	z	1	$0.0039^{+10.00}_{-0.00}$ redshift
Powerlaw 1	Norm	0	$0.0036^{+0.00}_{-0.00}$
	Γ	0	$1.2^{+0.31}_{-0.29}$
Gauss 1	Norm	0	$0.0001^{+0.00}_{-0.00}$
	Energy (keV)	0	$6.4^{+0.10}_{-0.10}$ keV
	σ (keV)	1	$0.05^{+9.95}_{-0.05}$ keV
	z	1	$0.0039^{+10.00}_{-1.00}$
Galactic absorption	$N_{\rm H}$ (cm^{-2})	1	$0.02^{+99.98}_{-10.02} \times 10^{22}$

Table A.3.: Best-fit parameters of all analyzed *Swift*-observations

model component	**Parameter**	**freeze**	**value ± uncertainty**
00031280007 - $\chi^2 = 6.50$ - $n_{\rm free} = 11$			
Covering Factor	f_{cvr}	0	$0.8\,^{+0.10}_{-0.19}$
Internal cold absorption	z	0	$6.2\,^{+3.29}_{-2.46} \times 10^{22}$
	z	1	$0.0039\,^{+10.00}_{-0.00}$ redshift
Powerlaw 1	Norm	0	$0.0024\,^{+0.00}_{-0.00}$
	Γ	0	$1.1\,^{+0.37}_{-0.34}$
Gauss 1	Norm	0	8.2e-05 $^{+0.00}_{-0.00}$
	Energy (keV)	0	$6.5\,^{+0.12}_{-0.28}$ keV
	σ (keV)	1	$0.05\,^{+9.95}_{-0.05}$ keV
	z	1	$0.0039\,^{+10.00}_{-1.00}$
Galactic absorption	$N_{\rm H}$ ($\rm cm^{-2}$)	1	$0.02\,^{+99.98}_{-10.02} \times 10^{22}$
00031280008 - $\chi^2 = 2.48$ - $n_{\rm free} = 3$			
Covering Factor	f_{cvr}	0	$0.78\,^{+0.12}_{-0.27}$
Internal cold absorption	z	0	$7.6\,^{+7.17}_{-3.68} \times 10^{22}$
	z	1	$0.0039\,^{+10.00}_{-0.00}$ redshift
Powerlaw 1	Norm	0	$0.0021\,^{+0.00}_{-0.00}$
	Γ	0	$1.2\,^{+0.44}_{-0.45}$
Gauss 1	Norm	0	2.9e-05 $^{+0.00}_{-0.00}$
	Energy (keV)	0	$6.6\,^{+0.00}_{-0.40}$ keV
	σ (keV)	1	$0.05\,^{+9.95}_{-0.05}$ keV
	z	1	$0.0039\,^{+10.00}_{-1.00}$
Galactic absorption	$N_{\rm H}$ ($\rm cm^{-2}$)	1	$0.02\,^{+99.98}_{-10.02} \times 10^{22}$
ESO 323-G077			
00035598002 - $\chi^2 = 15.25$ - $n_{\rm free} = 16$			
Powerlaw 1	Norm	0	$0.01\,^{+0.00}_{-0.01}$
	Γ	0	$2.2\,^{+0.08}_{-0.50}$
Internal cold absorption	z	0	$7\,^{+0.88}_{-1.66} \times 10^{22}$
	z	1	$0.015\,^{+9.98}_{-0.02}$ redshift
Gauss 1	Norm	0	6.1e-05 $^{+0.00}_{-0.00}$
	Energy (keV)	0	$6.4\,^{+0.07}_{-0.06}$ keV
	σ (keV)	1	$0.05\,^{+9.95}_{-0.05}$ keV
	z	1	$0.015\,^{+9.98}_{-1.01}$
Powerlaw 2	Norm	0	5.9e-05 $^{+0.00}_{-0.00}$
	Γ	0	$3\,^{+1.29}_{-1.21}$
Galactic absorption	$N_{\rm H}$ ($\rm cm^{-2}$)	1	$0.08\,^{+99.92}_{-10.08} \times 10^{22}$
00035598003 - $\chi^2 = 4.63$ - $n_{\rm free} = 6$			
Powerlaw 1	Norm	0	$0.034\,^{+0.07}_{-0.03}$
	Γ	0	$2.9\,^{+2.12}_{-1.88}$
Internal cold absorption	z	0	$8.6\,^{+11.43}_{-3.39} \times 10^{22}$
	z	1	$0.015\,^{+9.98}_{-0.02}$ redshift
Gauss 1	Norm	0	$0.0001\,^{+0.00}_{-0.00}$
	Energy (keV)	0	$6.3\,^{+0.25}_{-0.15}$ keV
	σ (keV)	1	$0.05\,^{+9.95}_{-0.05}$ keV
	z	1	$0.015\,^{+9.98}_{-1.01}$
Powerlaw 2	Norm	0	$0.00024\,^{+0.00}_{-0.00}$
	Γ	0	$5\,^{+0.00}_{-4.39}$
Galactic absorption	$N_{\rm H}$ ($\rm cm^{-2}$)	1	$0.08\,^{+99.92}_{-10.08} \times 10^{22}$

Table A.4.: Best-fit parameters of all analyzed *Swift*-observations

model component	**Parameter**	**freeze**	**value ± uncertainty**
Mrk 704			
00035590002 - $\chi^2 = 52.41$ - $n_{\rm free} = 43$			
Covering Factor	$f_{\rm cvr}$	0	$0.68\,^{+0.11}_{-0.16}$
Internal cold absorption	z	0	$1.8\,^{+0.91}_{-0.54} \times 10^{22}$
	z	1	$0.029\,^{+9.97}_{-0.03}$ redshift
Powerlaw 1	Norm	0	$0.0095\,^{+0.00}_{-0.00}$
	Γ	0	$2.5\,^{+0.22}_{-0.23}$
Gauss 1	Norm	0	$4.1\text{e-}05\,^{+0.00}_{-0.00}$
	Energy (keV)	0	$6.6\,^{+0.00}_{-0.40}$ keV
	σ (keV)	1	$0.05\,^{+9.95}_{-0.05}$ keV
	z	1	$0.029\,^{+9.97}_{-1.03}$
Galactic absorption	$N_{\rm H}$ ($\rm cm^{-2}$)	1	$0.03\,^{+99.97}_{-10.03} \times 10^{22}$
00035590003 - $\chi^2 = 73.25$ - $n_{\rm free} = 59$			
Covering Factor	$f_{\rm cvr}$	0	$0.8\,^{+0.06}_{-0.09}$
Internal cold absorption	z	0	$1.9\,^{+0.44}_{-0.35} \times 10^{22}$
	z	1	$0.029\,^{+9.97}_{-0.03}$ redshift
Powerlaw 1	Norm	0	$0.0081\,^{+0.00}_{-0.00}$
	Γ	0	$2.6\,^{+0.20}_{-0.20}$
Gauss 1	Norm	0	$3.6\text{e-}05\,^{+0.00}_{-0.00}$
	Energy (keV)	0	$6.3\,^{+0.32}_{-0.08}$ keV
	σ (keV)	1	$0.05\,^{+9.95}_{-0.05}$ keV
	z	1	$0.029\,^{+9.97}_{-1.03}$
Galactic absorption	$N_{\rm H}$ ($\rm cm^{-2}$)	1	$0.03\,^{+99.97}_{-10.03} \times 10^{22}$
00035590005 - $\chi^2 = 21.62$ - $n_{\rm free} = 26$			
Covering Factor	$f_{\rm cvr}$	0	$0.78\,^{+0.09}_{-0.15}$
Internal cold absorption	z	0	$1.6\,^{+0.59}_{-0.45} \times 10^{22}$
	z	1	$0.029\,^{+9.97}_{-0.03}$ redshift
Powerlaw 1	Norm	0	$0.01\,^{+0.00}_{-0.00}$
	Γ	0	$2.7\,^{+0.28}_{-0.29}$
Gauss 1	Norm	0	$3.7\text{e-}05\,^{+0.00}_{-0.00}$
	Energy (keV)	0	$6.2\,^{+0.40}_{-0.00}$ keV
	σ (keV)	1	$0.05\,^{+9.95}_{-0.05}$ keV
	z	1	$0.029\,^{+9.97}_{-1.03}$
Galactic absorption	$N_{\rm H}$ ($\rm cm^{-2}$)	1	$0.03\,^{+99.97}_{-10.03} \times 10^{22}$
Mrk 1218			
00035777002 - $\chi^2 = 4.00$ - $n_{\rm free} = 6$			
Covering Factor	$f_{\rm cvr}$	0	$0.93\,^{+0.07}_{-0.18}$
Internal cold absorption	z	0	$0.38\,^{+0.48}_{-0.24} \times 10^{22}$
	z	1	$0.029\,^{+9.97}_{-0.03}$ redshift
Powerlaw 1	Norm	0	$0.00056\,^{+0.00}_{-0.00}$
	Γ	0	$1.4\,^{+0.38}_{-0.33}$
Galactic absorption	$N_{\rm H}$ ($\rm cm^{-2}$)	1	$0.028\,^{+99.97}_{-10.03} \times 10^{22}$

Table A.5.: Best-fit parameters of all analyzed *XMM*-observations

model component	**Parameter**	**freeze**	**value ± uncertainty**
Fairall 51			
0300240401 - χ^2 = 1403.54 - $n_{\rm free}$ = 1344			
Warm absorbing zone 1	$N_{\rm H}$ ($\rm cm^{-2}$)	0	$0.62\,^{+0.10}_{-0.14} \times 10^{22}$
	$\log\xi$ (erg cm $\rm s^{-1}$)	0	$0.72\,^{+0.14}_{-0.12}$
	$\rm f_{cvr}$	1	$1\,^{+0.00}_{-1.00}$
	z	0	$0.014\,^{+0.00}_{-0.00}$
Warm absorbing zone 2	$N_{\rm H}$ ($\rm cm^{-2}$)	0	$3.2\,^{+0.39}_{-0.53} \times 10^{22}$
	$\log\xi$ (erg cm $\rm s^{-1}$)	0	$2.3\,^{+0.09}_{-0.13}$
	$\rm f_{cvr}$	1	$1\,^{+0.00}_{-1.00}$
	z	0	$-0.01\,^{+0.00}_{-0.00}$
Powerlaw 1	Norm	0	$0.0087\,^{+0.00}_{-0.00}$
	Γ	0	$1.8\,^{+0.04}_{-0.04}$
Gauss 1	Norm	0	$3.1e\text{-}05\,^{+0.00}_{-0.00}$
	Energy (keV)	0	$6.4\,^{+0.04}_{-0.05}$ keV
	σ (keV)	0	$0.12\,^{+0.05}_{-0.05}$ keV
	z	1	$0.014\,^{+9.99}_{-1.01}$
Gauss 2	Norm	0	$4e\text{-}05\,^{+0.00}_{-0.00}$
	Energy (keV)	0	$1.6\,^{+0.02}_{-0.03}$ keV
	σ (keV)	0	$0.057\,^{+0.06}_{-0.04}$ keV
	z	1	$0\,^{+10.00}_{-1.00}$
Gauss 3	Norm	0	$0.0012\,^{+0.00}_{-0.00}$
	Energy (keV)	0	$0.52\,^{+0.01}_{-0.02}$ keV
	σ (keV)	0	$0.093\,^{+0.02}_{-0.01}$ keV
	z	1	$0\,^{+10.00}_{-1.00}$
Galactic absorption	$N_{\rm H}$ ($\rm cm^{-2}$)	1	$0.07\,^{+99999.93}_{-0.07} \times 10^{22}$
0300240901 - χ^2 = 458.14 - $n_{\rm free}$ = 432			
Warm absorbing zone 1	$N_{\rm H}$ ($\rm cm^{-2}$)	0	$1.7\,^{+0.49}_{-0.44} \times 10^{22}$
	$\log\xi$ (erg cm $\rm s^{-1}$)	1	$0.71\,^{+0.29}_{-0.61}$
	$\rm f_{cvr}$	1	$1\,^{+0.00}_{-1.00}$
	z	0	$0.0048\,^{+0.00}_{-0.01}$
Warm absorbing zone 2	$N_{\rm H}$ ($\rm cm^{-2}$)	0	$11\,^{+1.36}_{-1.05} \times 10^{22}$
	$\log\xi$ (erg cm $\rm s^{-1}$)	0	$2.1\,^{+0.10}_{-0.05}$
	$\rm f_{cvr}$	1	$1\,^{+0.00}_{-1.00}$
	z	0	$0.014\,^{+0.00}_{-0.01}$
Powerlaw 1	Norm	0	$0.0026\,^{+0.00}_{-0.00}$
	Γ	0	$1.6\,^{+0.09}_{-0.08}$
Gauss 1	Norm	0	$2e\text{-}05\,^{+0.00}_{-0.00}$
	Energy (keV)	0	$6.4\,^{+0.03}_{-0.04}$ keV
	σ (keV)	0	$0.09\,^{+0.01}_{-0.05}$ keV
	z	1	$0.014\,^{+9.99}_{-1.01}$
Gauss 2	Norm	0	$3.3e\text{-}05\,^{+0.00}_{-0.00}$
	Energy (keV)	0	$0.85\,^{+0.02}_{-0.02}$ keV
	σ (keV)	0	$0.1\,^{+0.00}_{-0.02}$ keV
	z	1	$0.014\,^{+9.99}_{-1.01}$
Gauss 3	Norm	0	$3.7e\text{-}05\,^{+0.00}_{-0.00}$
	Energy (keV)	0	$0.55\,^{+0.01}_{-0.01}$ keV
	σ (keV)	0	$0.00011\,^{+0.05}_{-0.00}$ keV
	z	1	$0.014\,^{+9.99}_{-1.01}$
Galactic absorption	$N_{\rm H}$ ($\rm cm^{-2}$)	1	$0.07\,^{+99999.93}_{-0.07} \times 10^{22}$

Table A.6.: Best-fit parameters of all analyzed *XMM*-observations

model component	**Parameter**	**freeze**	**value ± uncertainty**
	NGC 4593		
0109970101 - χ^2 = 1336.84 - $n_{\rm free}$ = 1352			
Powerlaw 1	Norm	0	$0.0013\,^{+0.00}_{-0.00}$
	Γ	0	$1\,^{+0.22}_{-0.00}$
Comptonization of soft photons	Norm	0	$0.00049\,^{+0.00}_{-0.00}$
		1	$0.009\,^{+9.99}_{-1.01}$
	T_0 (keV)	1	$0.05\,^{+99.95}_{-0.04}$ keV
	$k_{\rm B}T$ (keV)	0	3.2e+02 $^{+22.33}_{-80.93}$ keV
	τ	0	$0.011\,^{+0.08}_{-0.00}$
		1	$1\,^{+4.00}_{-1.00}$
Partial covering with cold absorption	$N_{\rm H}$ (cm^{-2})	0	$4.1\,^{+3.33}_{-1.73} \times 10^{22}$
	$f_{\rm cvr}$	0	$0.13\,^{+0.05}_{-0.08}$
	z	1	$0.009\,^{+9.99}_{-1.01}$
Warm absorbing zone 1	$N_{\rm H}$ (cm^{-2})	0	$15\,^{+0.00}_{-14.27} \times 10^{22}$
	$\log\xi$ (erg cm s^{-1})	0	$4.2\,^{+0.15}_{-0.69}$
	$f_{\rm cvr}$	1	$1\,^{+0.00}_{-1.00}$
	z	0	-0.32 $^{+0.01}_{-0.01}$
Warm absorbing zone 2	$N_{\rm H}$ (cm^{-2})	0	$0.42\,^{+0.06}_{-0.05} \times 10^{22}$
	$\log\xi$ (erg cm s^{-1})	0	$2.2\,^{+0.08}_{-0.07}$
	$f_{\rm cvr}$	1	$1\,^{+0.00}_{-1.00}$
	z	0	$0.042\,^{+0.01}_{-0.01}$
Gauss 1	Norm	0	4e-05 $^{+0.00}_{-0.00}$
	Energy (keV)	0	$6.4\,^{+0.03}_{-0.03}$ keV
	σ (keV)	0	$0.054\,^{+0.05}_{-0.05}$ keV
	z	1	$0.009\,^{+9.99}_{-1.01}$
Gauss 2	Norm	0	8.5e-06 $^{+0.00}_{-0.00}$
	Energy (keV)	0	$7\,^{+0.09}_{-0.16}$ keV
	σ (keV)	0	$0\,^{+0.20}_{-0.00}$ keV
	z	1	$0.009\,^{+9.99}_{-1.01}$
Galactic absorption	$N_{\rm H}$ (cm^{-2})	1	$0.019\,^{+99999.98}_{-0.02} \times 10^{22}$

Table A.7.: Best-fit parameters of all analyzed *XMM*-observations

model component	**Parameter**	**freeze**	**value ± uncertainty**
0059830101 - χ^2 = 2071.59 - $n_{\rm free}$ = 1841			
Powerlaw 1	Norm	0	$0.001\,^{+0.00}_{-0.00}$
	Γ	0	$1\,^{+0.03}_{-0.00}$
Comptonization of soft photons	Norm	0	$0.0017\,^{+0.00}_{-0.00}$
		1	$0.009\,^{+9.99}_{-1.01}$
	T_0 (keV)	1	$0.05\,^{+99.95}_{-0.04}$ keV
	$k_{\rm B}T$ (keV)	0	$90\,^{+12.38}_{-0.65}$ keV
	τ	0	$0.18\,^{+0.00}_{-0.04}$
		1	$1\,^{+4.00}_{-1.00}$
Partial covering with cold absorption	$N_{\rm H}$ (cm^{-2})	0	$3.3\,^{+0.41}_{-0.40} \times 10^{22}$
	$f_{\rm cvr}$	0	$0.15\,^{+0.01}_{-0.03}$
	z	1	$0.009\,^{+9.99}_{-1.01}$
Warm absorbing zone 1	$N_{\rm H}$ (cm^{-2})	0	$2.1\,^{+0.47}_{-0.40} \times 10^{22}$
	$\log\xi$ (erg cm s^{-1})	0	$3.3\,^{+0.02}_{-0.03}$
	$f_{\rm cvr}$	1	$1\,^{+0.00}_{-1.00}$
	z	0	$-0.0064\,^{+0.00}_{-0.00}$
Warm absorbing zone 2	$N_{\rm H}$ (cm^{-2})	0	$0.24\,^{+0.02}_{-0.02} \times 10^{22}$
	$\log\xi$ (erg cm s^{-1})	0	$2.1\,^{+0.04}_{-0.05}$
	$f_{\rm cvr}$	1	$1\,^{+0.00}_{-1.00}$
	z	0	$0.094\,^{+0.00}_{-0.00}$
Gauss 1	Norm	0	$5.1e{-}05\,^{+0.00}_{-0.00}$
	Energy (keV)	0	$6.4\,^{+0.01}_{-0.01}$ keV
	σ (keV)	0	$0.088\,^{+0.02}_{-0.02}$ keV
	z	1	$0.009\,^{+9.99}_{-1.01}$
Gauss 2	Norm	0	$3.4e{-}05\,^{+0.00}_{-0.00}$
	Energy (keV)	0	$6.9\,^{+0.05}_{-0.05}$ keV
	σ (keV)	0	$0.2\,^{+0.00}_{-0.05}$ keV
	z	1	$0.009\,^{+9.99}_{-1.01}$
Galactic absorption	$N_{\rm H}$ (cm^{-2})	1	$0.019\,^{+99999.98}_{-0.02} \times 10^{22}$
UGC 7064			
0601780601 - χ^2 = 251.59 - $n_{\rm free}$ = 255			
Warm absorbing zone 1	$N_{\rm H}$ (cm^{-2})	0	$5e{+}02\,^{+0.00}_{-374.11} \times 10^{22}$
	$\log\xi$ (erg cm s^{-1})	0	$4.4\,^{+0.65}_{-0.19}$
	$f_{\rm cvr}$	1	$1\,^{+0.00}_{-1.00}$
	z	0	$-0.43\,^{+0.01}_{-0.01}$
Warm absorbing zone 2	$N_{\rm H}$ (cm^{-2})	0	$3.1\,^{+1.34}_{-0.80} \times 10^{22}$
	$\log\xi$ (erg cm s^{-1})	0	$1.3\,^{+0.11}_{-0.24}$
	$f_{\rm cvr}$	1	$1\,^{+0.00}_{-1.00}$
	z	0	$-0.051\,^{+0.02}_{-0.04}$
Partial covering with cold absorption	$N_{\rm H}$ (cm^{-2})	0	$8\,^{+1.97}_{-5.03} \times 10^{22}$
	$f_{\rm cvr}$	0	$0.59\,^{+0.08}_{-0.20}$
	z	1	$0.025\,^{+9.98}_{-1.02}$
Powerlaw 1	Norm	0	$0.00068\,^{+0.00}_{-0.00}$
	Γ	0	$1.5\,^{+0.04}_{-0.10}$
Gauss 1	Norm	0	$9.8e{-}06\,^{+0.00}_{-0.00}$
	Energy (keV)	0	$6.4\,^{+0.03}_{-0.03}$ keV
	σ (keV)	0	$0.066\,^{+0.05}_{-0.07}$ keV
	z	1	$0.025\,^{+9.98}_{-1.02}$
Gauss 2	Norm	0	$1.3e{-}05\,^{+0.00}_{-0.00}$
	Energy (keV)	1	$0.9\,^{+0.02}_{-0.02}$ keV
	σ (keV)	0	$0.074\,^{+0.02}_{-0.02}$ keV
	z	1	$0.025\,^{+9.98}_{-1.02}$
Gauss 3	Norm	0	$1.7e{-}05\,^{+0.00}_{-0.00}$
	Energy (keV)	1	$0.56\,^{+999999.44}_{-0.56}$ keV
	σ (keV)	0	$0\,^{+0.03}_{-0.00}$ keV
	z	1	$0.025\,^{+9.98}_{-1.02}$
Galactic absorption	$N_{\rm H}$ (cm^{-2})	1	$0.013\,^{+99999.99}_{-0.01} \times 10^{22}$

Table A.8.: Best-fit parameters of all analyzed *XMM*-observations

model component	**Parameter**	**freeze**	**value ± uncertainty**
NGC 3227			
0101040301 - χ^2 = 508.25 - $n_{\rm free}$ = 400			
Powerlaw 1	Norm	0	$0.0019\,^{+1.00}_{-0.00}$
	Γ	1	$1.4\,^{+2.58}_{-1.42}$
Covering Factor	$f_{\rm cvr}$	0	$0.85\,^{+0.15}_{-0.85}$
Internal cold absorption	z	0	$6.6\,^{+93.40}_{-6.60} \times 10^{22}$
	z	1	$0.0039\,^{+10.00}_{-0.00}$ redshift
Ionized absorber	Γ	0	$1.4\,^{+2.58}_{-1.42}$
	$N_{\rm H}$ ($\rm cm^{-2}$)	0	$1.6\,^{+98.44}_{-1.56} \times 10^{22}$
	$T_{\rm abs}$ (K)	1	$1.2e{+}05\,^{+880000.00}_{-110000.00}$ K
	ξ	0	$74\,^{+925.85}_{-74.15}$
	z	1	$0.0039\,^{+10.00}_{-1.00}$
	$tFe - abund$	1	$1\,^{+999999.00}_{-1.00}$
Gauss 1	Norm	0	$2.6e{-}05\,^{+1.00}_{-0.00}$
	Energy (keV)	1	$6.4\,^{+999993.61}_{-6.39}$ keV
	σ (keV)	1	$0.05\,^{+9.95}_{-0.05}$ keV
	z	1	$0.0039\,^{+10.00}_{-1.00}$
Galactic absorption	$N_{\rm H}$ ($\rm cm^{-2}$)	1	$0.02\,^{+99.98}_{-10.02} \times 10^{22}$
0400270101 - χ^2 = 1480.68 - $n_{\rm free}$ = 1220			
Powerlaw 1	Norm	0	$0.005\,^{+0.00}_{-0.00}$
	Γ	0	$1.4\,^{+0.01}_{-0.00}$
Gauss 1	Norm	0	$4.3e{-}05\,^{+0.00}_{-0.00}$
	Energy (keV)	0	$6.4\,^{+0.01}_{-0.01}$ keV
	σ (keV)	0	$0.078\,^{+0.01}_{-0.01}$ keV
	z	1	$0.0039\,^{+10.00}_{-1.00}$
Internal cold absorption	z	0	$0.4\,^{+0.00}_{-0.04} \times 10^{22}$
	z	1	$0.0039\,^{+10.00}_{-0.00}$ redshift
Powerlaw 2	Norm	0	$0.0058\,^{+0.00}_{-0.00}$
	Γ	0	$2.7\,^{+0.01}_{-0.03}$
Gauss 2	Norm	0	$1e{-}05\,^{+0.00}_{-0.00}$
	Energy (keV)	1	$0.58\,^{+0.02}_{-0.01}$ keV
	σ (keV)	0	$0.001\,^{+0.04}_{-0.00}$ keV
	z	1	$0.0039\,^{+10.00}_{-1.00}$
Warm absorbing zone 1	$N_{\rm H}$ ($\rm cm^{-2}$)	0	$0.2\,^{+0.00}_{-0.01} \times 10^{22}$
	$\log \xi$ (erg cm $\rm s^{-1}$)	0	$1.5\,^{+0.02}_{-0.06}$
	$f_{\rm cvr}$	1	$1\,^{+0.00}_{-1.00}$
	z	0	$0.055\,^{+0.01}_{-0.00}$
Warm absorbing zone 2	$N_{\rm H}$ ($\rm cm^{-2}$)	0	$0.35\,^{+0.00}_{-0.07} \times 10^{22}$
	$\log \xi$ (erg cm $\rm s^{-1}$)	0	$3\,^{+0.06}_{-0.08}$
	$f_{\rm cvr}$	1	$1\,^{+0.00}_{-1.00}$
	z	0	$0.019\,^{+0.00}_{-0.00}$
Internal cold absorption	z	0	$0.079\,^{+0.00}_{-0.01} \times 10^{22}$
	z	1	$0.0039\,^{+10.00}_{-0.00}$ redshift
Galactic absorption	$N_{\rm H}$ ($\rm cm^{-2}$)	1	$0.02\,^{+99999.98}_{-0.02} \times 10^{22}$

Table A.9.: Best-fit parameters of all analyzed *XMM*-observations

model component	**Parameter**	**freeze**	**value ± uncertainty**
ESO 323-G077			
0300240501 - χ^2 = 309.34 - $n_{\rm free}$ = 226			
Covering Factor	$f_{\rm cvr}$	0	$0.99^{+0.01}_{-0.99}$
Internal cold absorption	z	0	$3.7^{+26.33}_{-3.67} \times 10^{22}$
	z	1	$0.015^{+9.98}_{-0.02}$ redshift
Warm absorbing zone 1	$N_{\rm H}$ (cm^{-2})	0	$1^{+9.00}_{-0.00} \times 10^{22}$
	$\log\xi$ (erg cm s^{-1})	0	$2^{+0.00}_{-1.00}$
	$f_{\rm cvr}$	1	$1^{+0.00}_{-1.00}$
	z	0	$0.015^{+0.00}_{-0.01}$
Warm absorbing zone 2	$N_{\rm H}$ (cm^{-2})	0	$17^{+13.37}_{-14.63} \times 10^{22}$
	$\log\xi$ (erg cm s^{-1})	0	$2.4^{+2.60}_{-1.40}$
	$f_{\rm cvr}$	1	$1^{+0.00}_{-1.00}$
	z	0	$-0.024^{+0.01}_{-0.00}$
Powerlaw 1	Norm	0	$0.011^{+0.00}_{-0.01}$
	Γ	0	$2.2^{+0.66}_{-0.00}$
Gauss 1	Norm	0	$1.3e\text{-}05^{+0.00}_{-0.00}$
	Energy (keV)	0	$6.4^{+0.02}_{-0.04}$ keV
	σ (keV)	0	$0.053^{+0.05}_{-0.02}$ keV
	z	1	$0.015^{+9.98}_{-1.01}$
Gauss 2	Norm	0	$3.7e\text{-}05^{+0.00}_{-0.00}$
	Energy (keV)	0	$0.93^{+0.00}_{-0.02}$ keV
	σ (keV)	0	$0.1^{+0.00}_{-0.00}$ keV
	z	1	$0.015^{+9.98}_{-1.01}$
Gauss 3	Norm	0	$3.4e\text{-}06^{+0.00}_{-0.00}$
	Energy (keV)	0	$1.7^{+0.01}_{-0.02}$ keV
	σ (keV)	0	$2.8e\text{-}08^{+0.03}_{-0.00}$ keV
	z	1	$0.015^{+9.98}_{-1.01}$
Galactic absorption	$N_{\rm H}$ (cm^{-2})	1	$0.08^{+99999.92}_{-0.08} \times 10^{22}$
Mrk 704			
0300240101 - χ^2 = 754.06 - $n_{\rm free}$ = 691			
Warm absorbing zone 1	$N_{\rm H}$ (cm^{-2})	0	$0.27^{+0.16}_{-0.07} \times 10^{22}$
	$\log\xi$ (erg cm s^{-1})	0	$1^{+0.30}_{-0.30}$
	$f_{\rm cvr}$	1	$1^{+0.00}_{-1.00}$
	z	0	$0.1^{+0.00}_{-0.00}$
Warm absorbing zone 2	$N_{\rm H}$ (cm^{-2})	0	$2.4^{+1.27}_{-0.43} \times 10^{22}$
	$\log\xi$ (erg cm s^{-1})	0	$2^{+0.13}_{-0.11}$
	$f_{\rm cvr}$	1	$1^{+0.00}_{-1.00}$
	z	0	$-0.032^{+0.01}_{-0.01}$
Partial covering with cold absorption	$N_{\rm H}$ (cm^{-2})	0	$5.9^{+0.71}_{-0.84} \times 10^{22}$
	$f_{\rm cvr}$	0	$0.64^{+0.04}_{-0.06}$
	z	1	$0.029^{+0.01}_{-1.03}$
Powerlaw 1	Norm	0	$0.0045^{+0.00}_{-0.00}$
	Γ	0	$1.9^{+0.04}_{-0.05}$
Gauss 1	Norm	0	$2.3e\text{-}05^{+0.00}_{-0.00}$
	Energy (keV)	0	$6.4^{+0.06}_{-0.06}$ keV
	σ (keV)	0	$0.16^{+0.01}_{-0.05}$ keV
	z	1	$0.029^{+9.97}_{-1.03}$
Gauss 2	Norm	0	$2.8e\text{-}05^{+0.00}_{-0.00}$
	Energy (keV)	0	$0.89^{+0.01}_{-0.01}$ keV
	σ (keV)	0	$0.013^{+0.02}_{-0.01}$ keV
	z	1	$0.029^{+9.97}_{-1.03}$
Galactic absorption	$N_{\rm H}$ (cm^{-2})	1	$0.03^{+99999.97}_{-0.03} \times 10^{22}$

Table A.10.: Best-fit parameters of all analyzed *XMM*-observations

model component	**Parameter**	**freeze**	**value ± uncertainty**
0502091601 - $\chi^2 = 1451.47$ - $n_{\rm free} = 1432$			
Powerlaw 1	Norm	0	$0.0016\,^{+0.00}_{-0.00}$
	Γ	0	$1.5\,^{+0.10}_{-0.10}$
Comptonization of soft photons	Norm	0	$0.00016\,^{+18.63}_{-0.00}$
		1	$0.029\,^{+9.97}_{-1.03}$
	T_0 (keV)	0	$0.078\,^{+0.00}_{-0.00}$ keV
	$k_{\rm B}T$ (keV)	0	1.7e+02 $^{+26.10}_{-157.97}$ keV
	τ	0	$0.01\,^{+0.04}_{-0.00}$
		1	$1\,^{+4.00}_{-1.00}$
Warm absorbing zone 1	$N_{\rm H}$ (cm^{-2})	0	$0.25\,^{+0.03}_{-0.03} \times 10^{22}$
	$\log\xi$ (erg cm s^{-1})	0	$1.6\,^{+0.07}_{-0.07}$
	$f_{\rm cvr}$	1	$1\,^{+0.00}_{-1.00}$
	z	0	$0.099\,^{+0.00}_{-0.01}$
Warm absorbing zone 2	$N_{\rm H}$ (cm^{-2})	0	$2\,^{+1.08}_{-0.75} \times 10^{22}$
	$\log\xi$ (erg cm s^{-1})	0	$3.2\,^{+0.04}_{-0.05}$
	$f_{\rm cvr}$	1	$1\,^{+0.00}_{-1.00}$
	z	0	$0.03\,^{+0.01}_{-0.01}$
Gauss 1	Norm	0	2.3e-05 $^{+0.00}_{-0.00}$
	Energy (keV)	0	$6.4\,^{+0.00}_{-0.02}$ keV
	σ (keV)	0	$0.19\,^{+0.01}_{-0.04}$ keV
	z	1	$0.029\,^{+9.97}_{-1.03}$
Galactic absorption	$N_{\rm H}$ (cm^{-2})	1	$0.03\,^{+99999.97}_{-0.03} \times 10^{22}$
Mrk 1218			
0302260201 - $\chi^2 = 153.41$ - $n_{\rm free} = 148$			
Powerlaw 1	Norm	0	$0.00045\,^{+0.00}_{-0.00}$
	Γ	0	$1.5\,^{+0.11}_{-0.09}$
Partial covering with cold absorption	$N_{\rm H}$ (cm^{-2})	0	$0.71\,^{+0.24}_{-0.13} \times 10^{22}$
	$f_{\rm cvr}$	0	$0.73\,^{+0.03}_{-0.13}$
	z	1	$0.029\,^{+9.97}_{-1.03}$
Galactic absorption	$N_{\rm H}$ (cm^{-2})	1	$0.028\,^{+99999.97}_{-0.03} \times 10^{22}$

References

Akylas A., Georgantopoulos I., Griffiths R.G., et al., 2002, MNRAS 332, L23

Angelakis E., 2007, Ph.D. thesis, Mathematisch-Naturwissenschaftlichen Fakultaet der Rheinischen Friedrich-Wilhelms-Universitaet Bonn

Angelakis E., Fuhrmann L., Nestoras I., et al., 2010, ArXiv e-prints

Antonucci R., 1993, ARA&A 31, 473

Arnaud K., Smith R., Siemiginowska A., 2011, Handbook Of X-ray Astronomy, Cambridge University Press, Cambridge, UK

Aschenbach B., 1985, Reports on Progress in Physics 48, 579

Ashton C.E., 2005, Ph.D. thesis, Mullard Space Science Laboratory, London

Barlow R., 2004a, ArXiv Physics e-prints

Barlow R., 2004b, ArXiv Physics e-prints

Barthelmy S.D., Barbier L.M., Cummings J.R., et al., 2005, Space Sci. Rev. 120, 143

Beckmann V., Shrader C., 2012, Active Galactic Nuclei, Wiley-Vch, Weinheim

Begelman M.C., Blandford R.D., Rees M.J., 1984, Reviews of Modern Physics 56, 255

Belikov A.V., Hooper D., 2009, Phys. Rev. D 80, 035007

Beuchert T., 2010, *Master's thesis*, Univ. Erlangen-Nuremberg, Dr. Remeis Sternwarte Bamberg, ECAP

Bevington P., Robinson B.K., 2002, Data Reduction and Error Analysis for the Physical Sciences, McGraw-Hill Science

Bianchi S., Guainazzi M., Chiaberge M., 2006, A&A 448, 499

Blandford R.D., Konigl A., 1979, ApJ 232, 34

Blandford R.D., Payne D.G., 1982, MNRAS 199, 883

Blandford R.D., Znajek R.L., 1977, MNRAS 179, 433

Blissett R.J., Cruise A.M., 1979, MNRAS 186, 45

Blustin A.J., Page M.J., Fuerst S.V., et al., 2005, A&A 431, 111

Boettcher M., E. H.D., H. K., 2012, Relativistic Jets from Active Galactic Nuclei, Wiley-Vch, Weinheim, Germany

Braatz J.A., Reid M.J., Humphreys E.M.L., et al., 2010, ApJ 718, 657

Brenneman L.W., Reynolds C.S., Wilms J., Kaiser M.E., 2007, ApJ 666, 817

Burke B.F., Graham-Smith F., 2009, An Introduction to Radio Astronomy, Cambridge University Press, Cambridge, United Kingdom

Burn B.J., 1966, MNRAS 133, 67

Burrows D.N., Hill J.E., Nousek J.A., et al., 2005, Space Sci. Rev. 120, 165

Cash W., 1976, A&A 52, 307

Cash W., 1979, ApJ 228, 939

Ceballos M.T., Barcons X., 1996, MNRAS 282, 493

Chandrasekhar S., 1960, Radiative Transfer, Dover Publications, New York

Chatterjee R., Marscher A.P., Jorstad S.G., et al., 2011, ApJ 734, 43

Conway R.G., Haves P., Kronberg P.P., et al., 1974, MNRAS 168, 137

Costantini E., 2010, Space Sci. Rev. 157, 265

Dauser T., Wilms J., Reynolds C.S., Brenneman L.W., 2010, MNRAS 409, 1534

Davis J.E., 2001, ApJ 548, 1010

de Rosa A., Piro L., Perola G.C., et al., 2007, A&A 463, 903

den Herder J.W., Brinkman A.C., Kahn S.M., et al., 2001, A&A 365, L7

Doeleman S.S., Fish V.L., Schenck D.E., et al., 2012, Science 338, 355

Fabian A.C., Ross R.R., 2010, Space Sci. Rev. 157, 167

Fanaroff B.L., Riley J.M., 1974, MNRAS 167, 31P

Feretti L., Perley R., Giovannini G., Andernach H., 1999, A&A 341, 29

Fiebig D., Wohlleben R., Prata A., Rusch W.V.T., 1991, IEEE Transactions on Antennas and Propagation 39, 774

Freedman W.L., Madore B.F., Scowcroft V., et al., 2012, ApJ 758, 24

García J., Kallman T.R., 2010, ApJ 718, 695

Gehrels N., 1986, ApJ 303, 336

Gehrels N., Chincarini G., Giommi P., et al., 2004, ApJ 611, 1005

George I.M., Fabian A.C., 1991, MNRAS 249, 352

George I.M., Turner T.J., Netzer H., et al., 1998, ApJS 114, 73

Ghisellini G., Haardt F., Matt G., 1994, MNRAS 267, 743

Gondoin P., Orr A., Lumb D., Siddiqui H., 2003, A&A 397, 883

Grossberger C., Kadler M., Wilms J., et al., 2012, Acta Polytechnica 52, 010000

Guainazzi M., Bianchi S., 2007, MNRAS 374, 1290

Haardt F., Maraschi L., 1991, Astrophys. J., Lett. 380, L51

Hanke M., 2007, *Master's thesis*, Univ. Erlangen-Nuremberg, Dr. Remeis Sternwarte Bamberg, ECAP

Hartman R.C., Kadler M., Tueller J., 2008, ApJ 688, 852
Hogbom J.A., Carlsson I., 1974, A&A 34, 341
Holland A.D., Turner M.J., Abbey A.F., Pool P.J., 1996, In: Siegmund O.H., Gummin M.A. (eds.) Society of Photo-Optical Instrumentation Engineers (SPIE) Conference Series, Vol. 2808. Society of Photo-Optical Instrumentation Engineers (SPIE) Conference Series, p.414
Holt S.S., Mushotzky R.F., Boldt E.A., et al., 1980, Astrophys. J., Lett. 241, L13
Homan D.C., 2005, In: J. Romney & M. Reid (ed.) Future Directions in High Resolution Astronomy, Vol. 340. Astronomical Society of the Pacific Conference Series, p.133
Houck J.C., Denicola L.A., 2000, In: Manset N., Veillet C., Crabtree D. (eds.) Astronomical Data Analysis Software and Systems IX, Vol. 216. Astronomical Society of the Pacific Conference Series, p. 591
Jiménez-Bailón E., Krongold Y., Bianchi S., et al., 2008, MNRAS 391, 1359
Jorstad S.G., Marscher A.P., Larionov V.M., et al., 2010, ApJ 715, 362
Jorstad S.G., Marscher A.P., Lister M.L., et al., 2005, AJ 130, 1418
Kadler M., Ros E., Perucho M., et al., 2008, ApJ 680, 867
Kellermann K.I., Moran J.M., 2001, ARA&A 39, 457
Kembhavi, Ajit K., Narlikar, Jayant V., 1999, Quasars and Active Galactic Nuclei, Cambridge University Press, Cambridge, United Kingdom
Knoll G., 2010, Radiation Detection and Measurement, Wiley and sons, USA
Kraus A., 1997, Ph.D. thesis, Mathematisch-Naturwissenschaftlichen Fakultaet der Rheinischen Friedrich-Wilhelms-Universitaet Bonn
Kraus A., Krichbaum T.P., Wegner R., et al., 2003, A&A 401, 161
Krolik J.H., 1999, Active Galactic Nuclei, Princeton University Press, Princeton, New Jersey, USA
Krolik J.H., Begelman M.C., 1988, ApJ 329, 702
Lamer G., Uttley P., McHardy I.M., 2003, MNRAS 342, L41
Lampton M., Margon B., Bowyer S., 1976, ApJ 208, 177
Leahy J.P., Black A.R.S., Dennett-Thorpe J., et al., 1997, MNRAS 291, 20
Lefebvre M., Keeler R.K., Sobie R., White J., 2000, Nuclear Instruments and Methods in Physics Research A 451, 520
Liedahl D.A., Torres D.F., 2005, Canadian Journal of Physics 83, 1177
Lightman A.P., White T.R., 1988, ApJ 335, 57
Linfield R., Perley R., 1984, ApJ 279, 60
Liu R., Pooley G., 1991, MNRAS 249, 343
Lohfink A.M., Reynolds C.S., Mushotzky R.F., Wilms J., 2012, Astrophys. J., Lett. 749, L31
Lumb D.H., Eggel H., Laine R., Peacock A.J., 1996, In: Siegmund O.H., Gummin M.A. (eds.) Society of Photo-Optical Instrumentation Engineers (SPIE) Conference Series, Vol. 2808. Society of Photo-Optical Instrumentation Engineers (SPIE) Conference Series, p.326
Lyutikov M., Pariev V.I., Gabuzda D.C., 2005, MNRAS 360, 869
Markowitz A., Reeves J.N., George I.M., et al., 2009, ApJ 691, 922
Marscher A.P., 1996, In: P. E. Hardee, A. H. Bridle, & J. A. Zensus (ed.) Energy Transport in Radio Galaxies and Quasars, Vol. 100. Astronomical Society of the Pacific Conference Series, p.45
Marscher A.P., 2006, In: P. A. Hughes & J. N. Bregman (ed.) Relativistic Jets: The Common Physics of AGN, Microquasars, and Gamma-Ray Bursts, Vol. 856. American Institute of Physics Conference Series, p.1
Marscher A.P., Gear W.K., 1985, ApJ 298, 114
Marscher A.P., Jorstad S.G., D'Arcangelo F.D., et al., 2008, Nat 452, 966
Mason K.O., Breeveld A., Much R., et al., 2001, A&A 365, L36
Matt G., Bianchi S., Guainazzi M., et al., 2011, A&A 533, A1+
Matt G., Perola G.C., Piro L., 1991, A&A 247, 25
McKernan B., Yaqoob T., Reynolds C.S., 2007, MNRAS 379, 1359
McKinney J.C., 2005, ArXiv Astrophysics e-prints
Meidinger N., Braeuninger H.W., Hartmann R., et al., 1996, In: Siegmund O.H., Gummin M.A. (eds.) Society of Photo-Optical Instrumentation Engineers (SPIE) Conference Series, Vol. 2808. Society of Photo-Optical Instrumentation Engineers (SPIE) Conference Series, p.492
Meier D.L., 2003, New Astronomy Reviews 47, 667
Meier D.L., Koide S., Uchida Y., 2001, Science 291, 84
Mihalas D., 1978, Stellar Atmospheres, Freeman, USA
Miller L., Turner T.J., Reeves J.N., et al., 2007, A&A 463, 131
Mittaz J.P.D., Carrera F.J., Romero-Colmenero E., et al., 1999, MNRAS 308, 233
Moretti A., Campana S., Tagliaferri G., et al., 2004, In: Flanagan K.A., Siegmund O.H.W. (eds.) Society of Photo-Optical Instrumentation Engineers (SPIE) Conference Series, Vol. 5165. Society of Photo-Optical Instrumentation Engineers (SPIE) Conference Series, p.232
Morris D., Whiteoak J.B., 1968, Australian Journal of Physics 21, 493
Müller C., Kadler M., Ojha R., et al., 2011, A&A 530, L11
Mushotzky R.F., Done C., Pounds K.A., 1993, ARA&A 31, 717

Nenkova M., Sirocky M.M., Nikutta R., et al., 2008, ApJ 685, 160
Nousek J.A., Shue D.R., 1989, ApJ 342, 1207
Osterbrock D.E., Martel A., 1993, In: American Astronomical Society Meeting Abstracts, Vol. 25. Bulletin of the American Astronomical Society
Pagani C., Morris D.C., Racusin J., et al., 2007, In: Society of Photo-Optical Instrumentation Engineers (SPIE) Conference Series, Vol. 6686. Society of Photo-Optical Instrumentation Engineers (SPIE) Conference Series
Perley R.A., 1982, AJ 87, 859
Peterson B.M., 1993, PASP 105, 247
Piconcelli E., Jimenez-Bailón E., Guainazzi M., et al., 2005, A&A 432, 15
Popp M., 2004, Ph.D. thesis, Mathematisch-Naturwissenschaftlichen Fakultaet der Rheinischen Friedrich-Wilhelms-Universitaet Bonn
Pounds K., Reeves J., O'Brien P., et al., 2001, ApJ 559, 181
Protassov R., van Dyk D.A., Connors A., et al., 2002, ApJ 571, 545
Puccetti S., Fiore F., Risaliti G., et al., 2007, MNRAS 377, 607
Reynolds C.S., Fabian A.C., 1995, MNRAS 273, 1167
Ricci C., Beckmann V., Audard M., Courvoisier T.J.L., 2010, A&A 518, A47
Richstone D., Ajhar E.A., Bender R., et al., 1998, Nat 395, A14
Risaliti G., 2010, In: IAU Symposium, Vol. 267. IAU Symposium, p.299
Risaliti G., Elvis M., Nicastro F., 2002, ApJ 571, 234
Risaliti G., Nardini E., Salvati M., et al., 2011, MNRAS 410, 1027
Rivers E., Markowitz A., Rothschild R., 2011, Astrophys. J., Lett. 742, L29
Roming P.W.A., Kennedy T.E., Mason K.O., et al., 2005, Space Sci. Rev. 120, 95
Rybicki G.B., Lightman A.P., 2004, Radiative Processes in Astrophysics, Wiley-Vch, Weinheim
Saikia D.J., Salter C.J., 1988, ARA&A 26, 93
Sargent W.L.W., 1977, Astrophys. J., Lett. 212, L105
Schmid C., 2012, Ph.D. thesis, Friedrich-Alexander Universitaet Erlangen
Seyfert C.K., 1943, ApJ 97, 28
Sievers J.L., Hlozek R.A., Nolta M.R., et al., 2013, ArXiv e-prints
Smith J.E., Robinson A., Alexander D.M., et al., 2004, MNRAS 350, 140
Steenbrugge K.C., Kaastra J.S., Blustin A.J., et al., 2003, A&A 408, 921
Tabara H., Inoue M., 1980, A&AS 39, 379
Taylor G.B., Carilli C.L., Perley R.A., 2008, Synthesis Imaging in Radio Astronomy II, Astronomical Society of the Pacific, San Francisco, California
Thompson A.R., Moran J.M., Swenson G.W., 2004, Interferometry and Synthesis in Radio Astronomy, Wiley-Vch, Weinheim, Germany
Tombesi F., Sambruna R.M., Marscher A.P., et al., 2012, ArXiv e-prints
Turlo Z., Forkert T., Sieber W., Wilson W., 1985, A&A 142, 181
Turner M.J.L., Abbey A., Arnaud M., et al., 2001, A&A 365, L27
Turner T.J., Miller L., 2009, A&A Rev. 17, 47
Turner T.J., Miller L., Reeves J.N., Kraemer S.B., 2007, A&A 475, 121
Valtaoja E., Terasranta H., Urpo S., et al., 1992, A&A 254, 71
van Eldik C., 2010, Datenanalyse, Lecture WT 2010 University Erlangen-Nürnberg
Véron-Cetty M.P., Véron P., 2006, A&A 455, 773
Villa G.E., Abbey A.F., Arnaud M., et al., 1996, In: Siegmund O.H., Gummin M.A. (eds.) Society of Photo-Optical Instrumentation Engineers (SPIE) Conference Series, Vol. 2808. Society of Photo-Optical Instrumentation Engineers (SPIE) Conference Series, p.402
Vlahakis N., 2006, In: Miller H.R., Marshall K., Webb J.R., Aller M.F. (eds.) Blazar Variability Workshop II: Entering the GLAST Era, Vol. 350. Astronomical Society of the Pacific Conference Series, p. 169
Vlahakis N., Königl A., 2004, ApJ 605, 656
Wilms J., 2011, Galaxies and Cosmology, Lecture WT 2011 University Erlangen-Nürnberg
Wilms J., 2012, Astrophysical Radiative Processes, Lecture WT 2012 University Erlangen-Nürnberg
Wilms J., Allen A., McCray R., 2000, ApJ 542, 914
Zavala R.T., Taylor G.B., 2002, Astrophys. J., Lett. 566, L9
Zycki P.T., Krolik J.H., Zdziarski A.A., Kallman T.R., 1994, ApJ 437, 597

ACKNOWLEDGEMENTS

I want to thank my supervisors, collaborators and friends. Amongst them

- first of all Prof. Dr. Jörn Wilms (ECAP) and Prof. Dr. Matthias Kadler (Uni Würzburg, ECAP) for supervising my Master thesis, in particular being extemely helpful to answer questions, giving advice of multiple kind, as well as supporting my participation at conferences, schools and travels.

- the supervisors of my former trainee- (now "radio-quiet" Master-) project at the European Space Astronomy Center (ESAC) Anna-Lia Longinotti, Matteo Guainazzi, Giovanni Miniutti and Ignacio de la Calle for making my traineeship possible and offering me a great time in Madrid learning a lot about experimental X-ray astronomy.
  Not to forget serious still enriching friendships that developed with the trainees André, Marc, Aurelie, Prash, Ali, Annika, Edu, Elena, Nat, Sara, Laura, Pablo, Maxime, Tim, Rachel, Ester..., as well as the staff Wouter, Benoit and many others. In particular: thanks to Nat for the great paintings of living AGN still covering my desk, all the guys for awesome nights at Independance Club and Rock and Roll Radio station, Estar-Cafe..., the ESAC-climbing club for great trips to the mountains, Wouter, Annika and Ali for attending the Spanish course with me until the end, André for all the grand conversations, activities and for giving us a lift to ESAC each day, also Marc, e.g., for the nice time and for being able to live at his place, Annika, my former flatmate for the still ongoing friendship, Ali, e.g., for the Pizza at "Ali's place", and so on.

- Alex Markowitz (University of California, San Diego, Center for Astrophysics and Space Sciences) for helpful discussions regarding variability of radio-quiet galaxies.

- Emmanouil (Manolis) Angelakis, Lars Fuhrmann, Ioannis Nestoras and Ioannis Myserlis from the F-GAMMA program at the Max Planck Institut für Radioastronomie, Bonn, for the pleasant and productive collaboration already lasting some years as well as for the friendships that developed with my frequent stays in Bonn. Not to forget the "friend of the telescope" Uwe Bach who has a great helping hand in terms of technical issues regarding the 100-m Effelsberg telescope as well as offering and preparing data for the mosaic maps shown in this thesis. Furthermore Alex Kraus, the director of the telescope, for all the productive discussions and advice regarding radio polarimetry with Effelsberg. Additional thank to many others who enriched my visits in Bonn.

- The group of Prof. Dr. Matthias Kadler from University of Würzburg for the pleasant collaboration, amongst Till Steinbring for long discussions on jet theory.

- Annika Kreikenbohm who I am working close together with in Würzburg since the traineeship for her friendship and all the things we went through.

- The Dr. Remeis-Observatory, Bamberg, my institute, for its charm and folks being an absolutely amazing working group. Explicitely I want to thank my Master-co-strugglers and friends Felicia Krauss and Bastian Falkner, Felicia also for helping out with issues regarding the *Swift*-satellite, Bastian for his General Relatively expertise and his will to listen to the GRT lecture with me as well as being my climbing partner. Furthermore Christoph Grossberger for many discussions about 3C 111, Cornelia (Nela) Müller getting a good friend of mine and also respresenting the Radio Astronomy at the observatory helping out with many

topics especially regarding Very Long Baseline Interferometry, Thommy/Tommy/Thomas Dauser as expert of many kind (*XMM*-Newton, theoretical issues, programming with `ISIS`) for always being very helpful, providing many useful functions, especially `fits_save_fit`, for being a great climbing mate - probably the most passioned climber I ever met - and friend, Refiz Duro for also helping out in many issues of *XMM* and providing useful functions, Moritz Böck for his work done in scripting mainly in the field of fits-images and the useful discussions about jets and statistics, the admins of the observatory for the amazing work they are supplying in order to make the Remeis-observatory to one of the best organized and most productive institutes I ever saw.

- My former room-mates Udhay and Feli/Kathi for the awesome time as "Henke-WG"
- Sabi, a wonderful person making my day on and on.
- And finally those, who this work is dedicated to: my parents Hermia and Roger. I would not have been able to reach this moment of writing the last lines of my thesis without them. They both gave / and give me a lot of strength and love to be able and willing to pursue and live my dreams.

Erklärung

Hiermit erkläre ich, diese Masterarbeit in Eigenarbeit angefertigt zu haben, sofern nicht explizit in Text oder Referenzen vermerkt. Diese Arbeit ist der Universität Erlangen-Nürnberg als Vorraussetzung für den Erhalt des Abschlusses “Master of Science” vorgelegt worden. Ich erkläre, dass diese Arbeit weder partiell noch als Ganzes für den Erhalt eines anderweitigen Abschlusses verwendet wurde und wird.

Erlangen, den 01.03.2013

Tobias Beuchert